UNIVERSITY OF MODENA AND
REGGIO EMILIA

Department of Physics, Informatics and Mathematics

PHD SCHOOL IN
PHYSICS AND NANOSCIENCES

XXXVII Cycle

Localized particles for quantum information and quantum sensing in prototypical semiconductor devices

Advisor:
Prof. Paolo BORDONE

Co-advisors:
Dr. Andrea BERTONI
Dr. Filippo TROIANI

Candidate:
Dr. Gaia FORGHIERI

PhD School Coordinator:
Prof. Marco AFFRONTE

Academic Year 2023-2024

Contents

Table of Contents I

List of Publications and Contributions V

Introduction VII

I Coherent transport in edge-state interferometers in graphene 1

1 Graphene interferometers in the integer quantum Hall regime 5
1.1 Hall interferometers . . . 5
1.1.1 Devices for electronic flying qubits . . . 7
1.1.2 Single-electron sources . . . 10
1.2 Electron quantum optics in graphene . . . 11
1.2.1 Electronic properties of graphene . . . 12
1.2.2 Graphene devices for interferometry . . . 14

2 Numerical simulation of coherent transport with edge states 19
2.1 Description of massless Dirac fermions in graphene . . . 19
2.1.1 Tight-binding model for graphene . . . 19
2.1.2 Linear approximation . . . 21
2.2 Theoretical treatment of the quantum Hall effect in graphene . . . 23
2.2.1 Spinorial eigenfunctions in bulk . . . 23
2.2.2 Landau levels and HIQH effect . . . 25
2.2.3 Edge states in graphene nanoribbons . . . 26
2.3 Time-dependent simulations of edge-state wavepackets . . . 30
2.3.1 State initialization: Gaussian wavepackets . . . 30
2.3.2 Split-step Fourier method in graphene . . . 32

3 Time-resolved Mach-Zehnder interferometry in graphene 37
3.1 Motion of a carrier in graphene nanoribbons . . . 37
3.1.1 Shape and group velocity of the packet . . . 37
3.1.2 Edge states and snake states along a *pn* junction . . . 40
3.1.3 Klein tunneling through an *npn* junction . . . 42
3.2 Building Mach-Zehnder interferometers . . . 43
3.2.1 Quantum point contacts . . . 43
3.2.2 MZI with quantum point contacts . . . 45
3.2.3 MZI with valley beam splitters . . . 48

II Integrated hole-spin qubits and their application for quantum sensing **51**

4 Spin qubits for quantum technologies in solid state devices **55**
4.1 Spin qubits in semiconductor quantum dots . . . 55
4.1.1 The Loss-DiVincenzo scheme . . . 56
4.1.2 Spin-qubit decoherence . . . 59
4.2 Integrated devices in Si and Ge . . . 60
4.2.1 Overview on device design for gate-defined quantum dots . . . 61
4.2.2 Characteristics of hole-spin qubits . . . 65

5 Numerical models to describe hole-spin qubits in Si quantum dots **71**
5.1 Six-band Hamiltonian in Si and Ge . . . 71
5.1.1 Overview on $\mathbf{k}\cdot\mathbf{p}$ method . . . 72
5.1.2 6×6 Luttinger-Kohn Hamiltonian . . . 73
5.1.3 Action of a magnetic field . . . 77
5.2 Numerical diagonalization . . . 79
5.2.1 Harmonic-oscillator basis . . . 80
5.2.2 Adding electric potentials numerically . . . 82
5.2.3 State analysis . . . 83
5.3 Models for single and double quantum dots . . . 85
5.3.1 Confinement potentials . . . 85
5.3.2 Coulomb-induced modifications in the confinement . . . 87
5.4 Definition of the qubit . . . 91
5.4.1 SU(2) algebra . . . 92
5.4.2 Qubit evolution . . . 93

6 Quantum sensing applied to integrated hole-spin qubits in MOSFET technology **101**
6.1 State characterization . . . 101
6.1.1 Coulomb-induced polarization . . . 103
6.2 Static approach to quantum sensing . . . 108
6.2.1 State discrimination through the Helstrom bound . . . 108
6.2.2 Quantum Fisher information for parameter estimation . . . 110
6.2.3 Behaviour of the QFI . . . 113
6.3 Charge-induced effects on qubit manipulation . . . 119
6.3.1 Modification to the Larmor and Rabi frequencies of the qubit . . . 119
6.4 Dynamic approaches to quantum sensing . . . 126
6.4.1 Rabi scheme applied to state discrimination . . . 126
6.4.2 Fisher information on an evolved state . . . 127
6.4.3 Dynamic parameter estimation . . . 131

7 Characterization of single-hole excited states to enhance qubit manipulation **139**
7.1 Generalization to higher dimensionality . . . 139
7.1.1 SU(d) algebra . . . 139
7.1.2 Ququart evolution . . . 142
7.2 Four-level characterization in a SQD . . . 145
7.2.1 Effects of the degree of anisotropy on the manipulation frequencies . . . 146
7.2.2 Band occupation vs. orbital excitation . . . 149
7.2.3 Comparison to the DQD states . . . 153

III Conclusions 157

Conclusions 161

Acknowledgments 165

Bibliography 167

Non puoi dirmi di non farlo
e poi pretendere che non lo faccia

$\sim$ cit. Jimmy

List of Publications and Contributions

The contents of this Thesis were partly published in the following publications:

- *Giant Rabi frequencies between qubit and excited hole states in silicon quantum dots*, **E. Fanucchi**, **G. Forghieri**, A. Secchi, P. Bordone and F. Troiani, arXiv:2411.05526 (Nov 2024) [1]
- *Quantum estimation and remote charge sensing with a hole-spin qubit in silicon*, **G. Forghieri**, A. Secchi, A. Bertoni, P. Bordone, and F. Troiani, Phys. Rev. Res. **5**, 043159 (Nov 2023) [2]
- *Time-dependent transport in Graphene Mach-Zehnder Interferometers*, **G. Forghieri**, P. Bordone, and A. Bertoni, Phys. Rev. B **106**, 165402 (Sep 2022) [3]

Other research activities performed during my PhD will be published in the following paper:

- *Exploring beyond the single-particle regime for hole-spin qubits in germanium*, **G. Forghieri**, A. Secchi, S. Bosco, P. Bordone, F. Troiani and D. Loss, in preparation

During my PhD activity I was Co-supervisor of 2 Bachelor theses and 1 Master thesis concerning the topics of my research:

- **E. Fanucchi**, "Exploiting excited states for the manipulation of hole-spin qubits in silicon Quantum Dots", Master Thesis (University of Modena and Reggio Emilia, Oct 2023) [4]
- **M. Di Mare**, "Studio dell'evoluzione temporale di qubit e ququart sotto l'azione di potenziali esterni", Bachelor Thesis (University of Modena and Reggio Emilia, Oct 2023)
- **S. Bragadini**, "Studio di stati di lacuna in singoli e doppi Quantum Dot in Silicio in presenza di difetto elettrostatico per Qubit integrati di spin", Bachelor Thesis (University of Modena and Reggio Emilia, Oct 2022)

and I was project leader of 1 computational project:

- **IsCb4-GERONIMO - HP10CG99PB**: *GERmanium hOle-spiN qubIts in the Multi-hOle regime*, ISCRA C project on Galileo 100 at CINECA

My PhD experience included a 3-month period abroad:

- 10 Sep 2023 - 17 Dec 2023 at the University of Basel, under the supervision of Prof. Daniel Loss and Dr. Stefano Bosco, for the study of spin qubit systems in semiconductor nanodevices

as well as 2 seminars, participation in 4 conferences and 2 Summer Schools:

- (**seminar**) *Manipulation and encoding of hole-spin qubits using the first-excited doublet in Si devices* University of Modena and Reggio Emilia, Italy, 1 Oct 2024
- (**contributed talk**) *Hole-spin qubits in the single- and few-hole regimes for quantum technologies*, 110th National SIF Congress, Bologna, Italy, 9 - 13 Sep 2024
- (**poster**) *Quantum sensing with hole-spin qubits in quantum dots*, NANOQI'24 Summer School, San Sebastiàn, Spain, 22 - 25 Jul 2024
- (**invited talk**) *Quantum estimation and remote charge sensing with a hole-spin qubit in silicon*, QWEST Kick-off Meeting, Modena, Italy, 6 - 7 Jun 2024

- (**seminar**) *Quantum estimation of a charge distance from a hole-spin qubit in Si quantum dots*, University of Basel, 25 Sep 2023
- (**contributed talk**) *Coherent transport in Mach-Zehnder interferometers in graphene* + (**poster**) *Quantum sensing with hole-spin qubits in quantum dots*, Edison 22, Münster, Germany, 14 - 18 Aug 2023
- (**contributed talk**) *Edge-state interferometers in graphene nanoribbons: a time-dependent modelling*, IWCN2023, Barcelona, Spain, 12 - 16 Jun 2023
- NANOQI'22 Summer School, San Sebastiàn, Spain, 28 Aug - 2 Sep 2022

and the following teaching activity:

- (**10h**) Personal Tutor to student with SLD for the course in *Physics* of the Informatics' Bachelor's Degree, Unimore, Jul 2024
- (**20h**) Teaching Assistant for the course *Physics IB – Fundamental Physics* of the Physics' Bachelor's Degree, Unimore, Mar - May 2024
- (**23h**) Teaching Assistant for the course *Physics II – Electromagnetism* of the Physics' Bachelor's Degree, Unimore, Mar - May 2023
- (**20h**) Teaching Assistant for the course *Mathematical Methods for Physics* of the Physics' Bachelor's Degree, Unimore, Oct - Dec 2022
- (**37h**) Personal Tutor to student with SLD for the course *Mathematical Methods for Physics* of the Physics' Bachelor's Degree, Unimore, Nov 2021 - Feb 2022
- (**24h**) Teaching Assistant for the course *Mathematical Methods for Physics* of the Physics' Bachelor's Degree, Unimore, Oct - Dec 2021

Finally, I participated in the following outreach activity in collaboration with the University of Modena and Reggio Emilia:

- European Researchers' Night, official stand of Unimore, Modena, 30 Sep 2022, 27 Sep 2024
- Modena Play 2024, official stand of Unimore, Modena, 17 - 19 May 2024
- (**educational exhibition**) Italian Quantum Weeks: *Dire l'indicibile*, I Edition (*La sovrapposizione quantistica*, Apr 2022), II Edition (*L'Entanglement quantistico*, Mar - Apr 2023), and III Edition (*Viaggio nella meccanica quantistica*, Apr 2024), Modena
- (**seminar**) Italian Quantum Weeks: Classical and Quantum Random compared, University of Modena and Reggio Emilia, 23 Apr 2024
- (**poster**) Topics of Quantum Information for Applications in Quantum Technologies, Unimore, presentation of the lines of research of the Physics Department, 4 Dec 2023

Introduction

Quantum information processing holds significant long-term potential in several areas, including computation and communication [5, 6]. However, despite the rapid progress of the quantum community, practical realizations are still limited. The main objectives yet to be achieved include the realization of powerful, universal quantum processors with a sufficient number of qubits, and their connection through suitable quantum channels. Promising perspectives in these respects are offered by the use of semiconductor nanostructures, due to their compatibility with classical circuitry and with the advanced manufacturing techniques of modern devices [7].

The first part of this Thesis is devoted to Mach-Zehnder interferometers in the integer quantum Hall regime in graphene, as a possible platform for the implementation of flying qubits [8]. In electron quantum optics, the presence of a strong and tunable Coulomb interaction allows for a straightforward implementation of single- and two-qubit gates. Additionally, the chirality of edge channels forbids back-scattering and allows for long coherence lengths of carriers generated by single-electron sources [9]. In graphene specifically, coherence is further enhanced by the linear dispersion of massless Dirac fermions [10]. In Chapter 1 we analyze the state of the art on flying qubits and their implementation with graphene. In Chapter 2 we show how to treat single carriers in graphene nanoribbons analytically, by taking into account both the sublattice and the valley pseudospins. Then, we explain how to simulate their time-dependent evolution through the split-step Fourier method. In Chapter 3, we characterize the motion of Gaussian electron wavepackets inside graphene nanoribbons, focusing on the behavior of single-particle interferometers. We study implementations with either quantum point contacts or valley beam splitters, the latter being fundamental for valleytronics [11], and analyze the effect of the edge-channel structure on visibility.

In the second part of the Thesis, we study hole-spin qubits integrated into Si-based devices [12, 13]. A significant advantage of this approach is the scalability of foundry-compatible Si devices. Indeed, these offer a high degree of control on qubit integration and manipulation, even at temperatures as high as 4 K [14]. Additionally, noise due to the hyperfine interaction is reduced thanks to the natural abundance of spinless isotopes in Si. Holes specifically show a much larger spin-orbit coupling than electrons, thus allowing for an all-electrical qubit manipulation [15]. The state of the art is illustrated in Chapter 4, while we describe our theoretical framework, based on the Luttinger-Kohn approach, and other models in Chapter 5. In Chapter 6 we report on the possible use of hole-spin qubits for quantum sensing applications, specifically for charge sensing [16]. We exploit the sensitivity of a double quantum dot to the presence and position of a remote charge, and how it is reflected into the qubit state and its characteristic frequencies. We consider either a static or dynamic approach, and generalize our results through a generic two-site Hubbard model. In addition, we find the general expressions of the Fisher information after both a Rabi and Ramsey scheme. Finally, in Chapter 7 we explore the possibility of exploiting the first two states beyond the qubit subspace for manipulation. These states are much more sensitive to the system's degree of anisotropy and are consequently much more tunable, allowing for an enhancement of several orders of magnitude on the qubit's frequencies.

Part I

Coherent transport in edge-state interferometers in graphene

Sovrapposizioni

Siamo frammenti ed inganni del tempo,
Schegge di specchi e capricci del dubbio.
Cascate di luce riflesse ed infrante,
Significati nascosti e rifranti

Siamo comete e siam creste di onde,
Calchiamo percorsi che non conosciamo,
Ci sovrapponiamo e sommiamo e annientiamo
Ma non ci vediamo né riconosciamo

Siamo la vita e la morte e l'ignoto
Le fluttuazioni dell'eco di un sogno,
Siamo e creiamo e sfuggiamo e ridiamo
Poi ci afferriamo, e ricominciamo.

Siamo frequenze dell'indissolubile
Come legate da fili invisibili,
Ed il mio passato modifica il tuo
Perché il tuo futuro si specchia nel mio

Siamo pensieri dell'indefinito,
E siamo infinite possibilità.
Capovolgiamo le nostre incertezze
Nell'assoluto dell'ambiguità

Going through the mirrors requires confronting yourself.
You need guts, you know, to look yourself straight in the eyes,
to see yourself as you are, to dive into your own reflection.

$\sim$ from *The Mirror Visitor: A Winter's Promise*,
by Christelle Dabos

Chapter 1

Graphene interferometers in the integer quantum Hall regime

In the first part of this Thesis, we focus on graphene devices, and their use as building blocks for quantum information processing. Specifically, in this Chapter we introduce the state of the art on graphene devices for electron quantum optics as a possible platform for the implementation of flying qubits. In Sec. 1.1 we introduce interferometers working in the integer quantum Hall regime in conventional semiconductors. Specifically, in Sec. 1.1.1 we list the main device geometries for single- and two-electron interference. In Sec. 1.1.2, we report the main sources of single localized carriers available with the current semiconductor technology. Then, in Sec. 1.2 we give a brief overview of graphene and its use in electron quantum optics. In Sec. 1.2.1 we describe its main electronic properties, with a special focus on the anomalous integer quantum Hall effect that it presents. Finally, in Sec. 1.2.2 we talk about the experimental realization of graphene devices, and specifically of Mach-Zehnder interferometers.

1.1 Hall interferometers

When a current I passing through a conductor is subjected to a magnetic field, a transverse potential difference is formed in what is widely known as the Hall effect. Its quantum equivalent, the quantum Hall effect, occurs in the limit of a strong magnetic field acting at low temperatures on a two-dimensional electronic system. Under these conditions, the transverse Hall resistance is quantized:

$$R_H = \frac{V_H}{I} = \frac{\hbar}{e^2 \nu}\,, \tag{1.1}$$

in which V_H is the transverse Hall potential. The quantity ν can be either an integer or a fraction between small integers: in these cases, we talk respectively of integer quantum Hall (IQH) and fractional quantum Hall (FQH) effects. An example of the geometry of a Hall bar used to study this phenomenon is shown in Fig. 1.1(a), while the typical resistance curves are reported in Fig. 1.1(b). Notice that, in correspondence with each plateau at which the transverse resistance is constant, the longitudinal resistance instead drops to zero. The first demonstration of the IQH effect dates back to 1980 [18], when Von Klitzing et al. observed the resistance curves for a high-mobility 2D electron gas (2DEG) occurring inside the inversion layer of a metal-oxide-semiconductor field-effect transistor (MOSFET) cooled-down at liquid helium temperatures ($\sim$ 4.2 K). After that, several studies have demonstrated the FQH effect by cooling the system to even lower temperatures and considering high mobilities GaAs/AlGaAs heterostructures [19], in which the 2D confinement

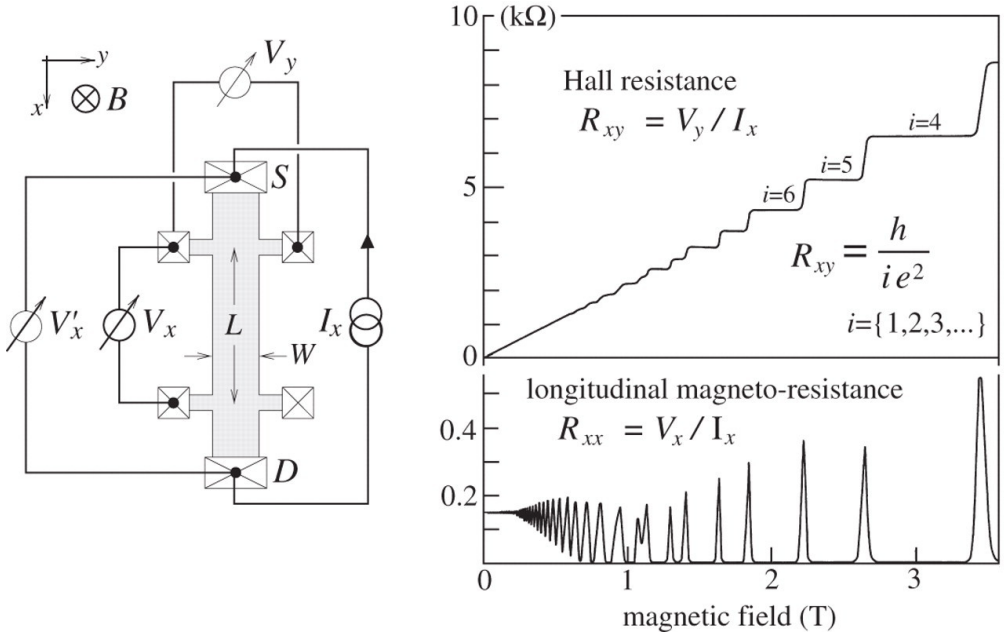


Figure 1.1: (a) Typical Hall bar geometry and electrical set-up for the measurement of the Hall effect under the action of a perpendicular magnetic field of intensity B. L and W are the widths of the bar; V_x and V_y are respectively the longitudinal and transverse potentials measured through the device; I_x and V'_x are respectively the current and potential between the source (S) and drain (D) leads. (b) Hall resistance curves for the transverse/longitudinal resistance R_{xy}/R_{xx}. The plateaus of R_{xy} are labeled by the integer i, corresponding to the quantity ν in the main text. Both panels are taken from [17].

is induced due to the band offset between the interfacing materials.

The quantity ν in Eq. (1.1) can be interpreted as the occupation number of the Landau levels, which make up the discrete eigenenergy spectrum of the 2DEG in the presence of a magnetic field. For a 2DEG with quadratic dispersion, as it is at the bottom of the conduction band of GaAs, each Landau level has energy in bulk equal to:

$$E_n = \hbar\omega_c \left(n + \frac{1}{2}\right), \tag{1.2}$$

where $\omega_c = eB/m^*$ is the cyclotron frequency, m^* being the effective mass of the electron. The degeneracy of each Landau level depends on the ratio between the total magnetic flux passing through a device of area A, $\phi = BA$, and the magnetic flux quantum, $\phi_0 = 2\pi\hbar/e$. Thus, the density of states n_L in a Landau level per unit area is:

$$n_L = \frac{\phi}{\phi_0} \cdot \frac{1}{A} = \frac{eB}{2\pi\hbar}. \tag{1.3}$$

Since both the spacing between Landau levels and their degeneracy increase linearly with B, fewer and fewer Landau levels are occupied as the magnetic field increases or, equivalently, as the carrier density n_S inside the device decreases. From these quantities, one can define the so-called bulk filling factor (FF), $\nu_L = n_S/n_L$. The FF is equivalent to the quantity ν from Eq. (1.1) only when its value is among those allowed by the IQH/FQH effect. Otherwise, the values of ν_L and ν are

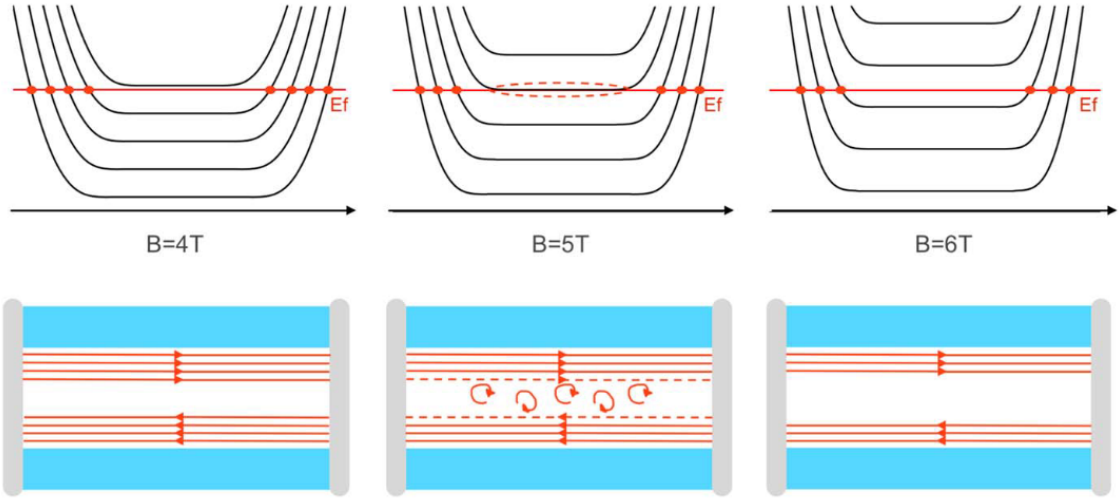


Figure 1.2: (Top) Band structure of the Landau levels (black) and (Bottom) evolution of the edge channels (red arrows) near the physical confinement of the device (blue) at progressively increasing magnetic fields. E_f indicates the Fermi energy and the red dots show the states that are energetically allowed for transport, corresponding to the creation of edge channels. In grey are two metallic leads. The picture is taken from [20].

generally different.

The Landau levels bend in correspondence with confinement conditions felt by the 2DEG, like, for instance, at the edge of a device or next to a potential barrier. The monotonic dispersion that the Landau levels present under these conditions allows for chiral transport through so-called edge channels [21]. The shape of the Landau levels and edge channels is shown for a schematic device in Fig. 1.2. As we can see, the edge channels follow the shape of the device, and allow electrons to move ballistically through them only in a certain direction, thus suppressing back-scattering. This phenomenon is equivalent to the classical skipping orbits, which, rather than being backscattered by an obstacle, allow under certain conditions to go around it by following its profile [22]. The lack of back-scattering explains why the longitudinal resistance drops to zero. Instead, the transverse resistivity is inversely proportional to the number of available edge channels, thus explaining the relation in Eq. (1.1). Only when the bulk states become available for transport, i.e. when $E_F = E_n$ for a certain n, is it possible for electrons to pass from one edge of the device to the other due to perturbations and/or disorder (see the central panel in Fig. 1.2). In this case, the longitudinal resistance shows a peak, as observable in Fig. 1.1, before falling to zero as soon as E_F increases again.

1.1.1 Devices for electronic flying qubits

In quantum computation, the ability to transmit information is of fundamental importance for an endless number of tasks, among which is quantum communication [6]. This field specifically requires the definition of a *flying qubit*, that is, a unit of quantum information that is able to travel from place to place. In order to implement quantum communication, the following two criteria are necessary:

1. The ability to convert stationary qubits into flying qubits and vice versa;

2. The ability to faithfully transmit the flying qubit between specific locations.

These requirements are usually considered alongside the rest of DiVincenzo's criteria [23] (see Chapter 4 for further details). Due to the different nature of stationary and flying qubits, the implementation of the latter is expected to differ greatly from the ones used in local computations. A first example is the vast use of photons in the field of quantum optics [8, 24]. Here, single-qubit gates are straightforwardly implemented thanks to the use of single-photon interferometers. However, two-qubit gates are more difficult to obtain, due to the non-interacting nature of photons. A possible way to create entanglement with photons could rely on a projective measurement, which however is unsuitable for large-scale implementations due to its probabilistic outcome [25]. On the contrary, this difficulty is overcome in electron quantum optics, where the Coulomb interaction can couple two charges and consequently create entanglement. We talk in this case about *charge-based* flying qubits [26, 27]. Although the Coulomb interaction may cause unwanted noise on the electron state from the electromagnetic environment, the previously illustrated chirality inside edge states allows for the carriers to reach coherence lengths in the order of tens of μm [9, 28].

From the considerations above, devices working in the IQH regime are particularly promising in the context of quantum communication. Generally, these devices are operated through the use of source and drain leads at their edge, and with metallic top/bottom gates to control the bulk FF. Additionally, modulation gates can be used to vary ν locally, and consequently modify the profile of edge channels. Thanks to this, one can create physical restrictions in the profile potentials, thus producing so-called quantum point contacts (QPCs). In electron quantum optics, a QPC works as a beam splitter, that is, a semi-transparent mirror which ideally allows for a 50-50% splitting of the incoming state into two channels, thus separating the electronic stream into a transmitted and reflected component (see Sec. 3.2.1 for further details).

In the past years, the versatility of edge channels has allowed for a wide variety of device geometries to be implemented in the IQH regime. The first one demonstrated for electrons, in 1999, is the Hanbury Brown-Twiss interferometer [33, 34]. Its schematic description is reported in Fig. 1.3(a), alongside an example of its implementation in a GaAs/AlGaAs heterostructure in Fig. 1.3(b). The apparatus consists of two independent electron sources, S1 and S2, and four beam splitters, A through D. When the two electronic streams injected through the sources meet the first two beam splitters, A and B, they are each split into two separate paths. Then, at C and D, the two streams meet and interfere. The electrons can then be measured at two of four detectors, D1 through D4. The joint detection probability of two detectors will depend on the interference, that is, on the relative phase accumulated by the electrons inside the interferometer's arms [35].

It is relevant to note that the statistics of the Hanbury Brown-Twiss interferometer are based on the Hong-Ou-Mandel effect [36], which explains the behavior of two identical, counterpropagating particles impinging on the same beam splitter, as illustrated schematically in Fig. 1.3(c). When boson statistics apply, as is the case for photons, the particles are expected to leave the beam splitter on the same side (bunching). The opposite is true for electrons, which, due to fermionic statistics, are expected to leave on opposite sides (antibunching). Deviations from perfect bunching/antibunching signify imperfect indistinguishability between particles, which can consequently be detected and exploited in quantum information protocols. This phenomenon may be due to several sources, among which the Coulomb interaction [30] and the energy dispersion of single carriers. The latter allows the electrons to not violate the Pauli principle for different energy

components. In this case, the antibunching probability depends on the energy overlap between the transmitted and reflected parts of the carrier through the beam splitter [37, 38].

Another fundamental building block for computation with flying qubits is the Mach-Zehnder interferometer (MZI), first demonstrated for electrons in 2003 [31]. Here, as schematically shown in Fig. 1.3(d), a single source of electron (S) creates a stream that meets two subsequent beam splitters, BS1 and BS2, and consequently interferes with itself. The detection probability at D1 and D2 here depends on the Aharonov-Bohm phase accumulated between the two parts of the electronic state along the different paths. This phase, in turn, depends on both the area of the interferometer and the magnetic field acting on the 2DEG (see Sec. 3.2.2 for further details). An example of the implementation of such an interferometer in GaAs/AlGaAs is shown in Fig. 1.3(e). In this kind of interferometers it is crucial to prevent back-scattering at each beam splitter, so that the chirality of the edge states becomes of fundamental importance. Several other geometries have been proposed to further eliminate the problem, for instance by exploiting the interchannel scattering between

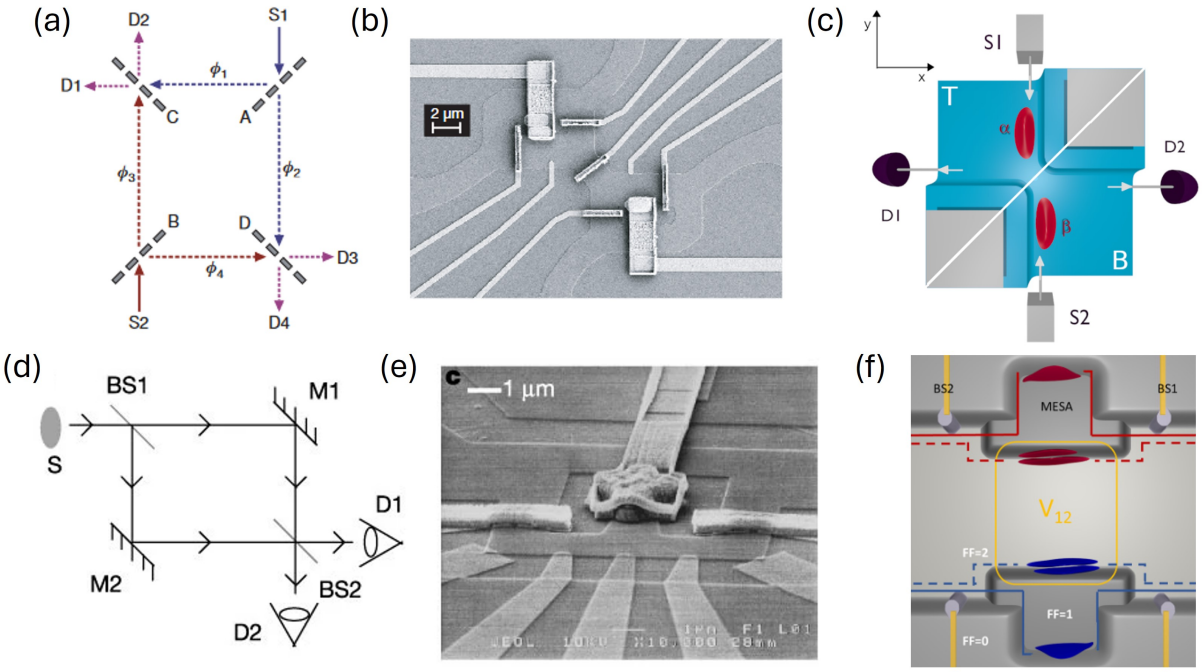


Figure 1.3: Electronic devices working in the IQH regime. (a) Diagram and (b) experimental realization in GaAs/AlGaAs of a Hanbury Brown-Twiss interferometer. S1 and S2 are the electron sources, A through D are beam splitters, and D1 and D2 are detectors; ϕ_{1-4} are the electronic wavefunctions passing through each part of the interferometer. (c) Scheme of an Hong-Ou-Mandel interferometer created with a QPC (blue); α and β are the incoming counterpropagating electrons; T and B are the top and bottom regions of the device. (d) Diagram and (e) experimental realization in GaAs/AlGaAs of a Mach-Zehnder interferometer. S is the source; BS1 and BS2 are beam splitters; and M1 and M2 are completely reflective mirrors. (f) Scheme of a conditional phase shifter realized with two Mach-Zehnder interferometers at FF two in parallel; a potential step (MESA) defines a region at FF one, thus separating the arms of the interferometer and allowing selective Coulomb coupling V_{12}. Panels (a) and (b) are adapted from [29]; panel (c) from [30]; panels (d) and (e) from [31]; panel (f) from [32].

copropagating edge channels at FF higher than one [39, 40]. The multichannel geometry of devices at FF two could also be exploited in the realization of conditional phase shifters (CPSs) [41]. Inside a CPS, entanglement can be created between two flying qubits through the selective action of the Coulomb potential on spatially separated edge channels [32], as illustrated in Fig. 1.3(f).

1.1.2 Single-electron sources

The first experimental implementations of electron interferometry relied on the injection of continuous currents through the Ohmic contacts that define the source and drain of the devices [31, 33, 34]. In these cases, the quantum properties of the system can be obtained through ensemble measurements or by detecting the transmitted current. However, the possibility of injecting localized carriers represents a more direct way to send and control single qubits. This is possible thanks to the current advances in nanotechnology, which allow to generate single electrons with an emission efficiency higher than 99% [42–44], superior even to single-photon sources. Thanks to recent protocols, it thus becomes possible to encode the qubit state directly into the configuration of a wavepacket. For instance, by exploiting its Landau index or the spatial position of the edge channel along which it travels.

Possible single-electron sources are illustrated in Fig. 1.4. The first one was suggested by Levitov et al. in 1996 [48], and is based on the use of a time-dependent perturbation $V(t)$ on the potential acting directly on the source lead of the device. Usually, under these conditions a quasiparticle is produced, made up of a complex superposition of electrons and holes. However, with the use of a properly tuned Lorentzian perturbation as in Fig. 1.4(a), a minimal excitation is produced, called *Leviton*. This particle corresponds to a single electron and no holes, thus possessing a unitary negative charge [45]. Its shape is also Lorentzian in real space. However, the wavepacket is instead highly asymmetric in the energy domain, showing an exponential probability distribution.

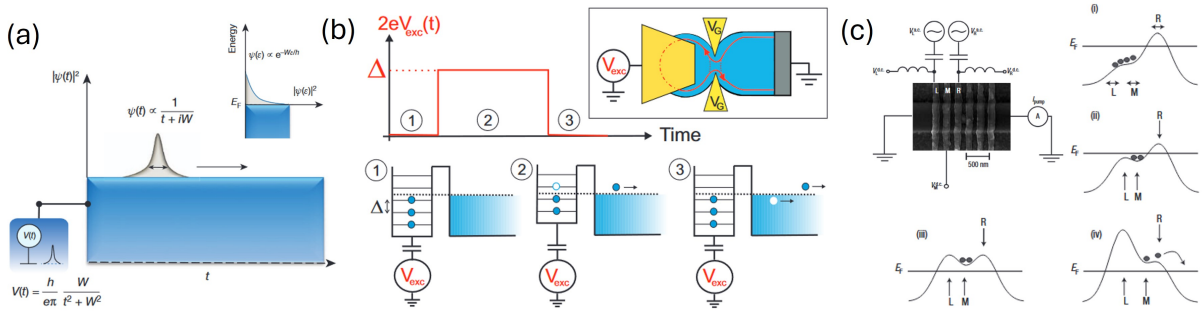


Figure 1.4: Single-electron sources for Hall interferometers. (a) Schematic emission of a Leviton through the application of a Lorentzian perturbation $V(t)$; in grey is the shape of the wavepacket in real space (main panel) and in the energy domain (inset); in blue is the Fermi sea. (b) Protocol for the injection of a Landau quasiparticle by means of a mesoscopic capacitor (inset). V_G are the gate potentials defining the QPC coupled to the quantum dot; the shape of $V_{ext}(t)$ in time (top of the main panel) describes the evolution of the quantum dot (bottom of the main panel). (c) Behavior of a quantum dot pump for the emission of hot electrons. Three leads (L, M, R) form a quantum dot coupled with both the Fermi sea and the 2DEG (top left panel); the manipulation of the quantum dot barriers causes the ejection of single carriers into the device (panels i through iv). The figure in (a) was adapted from [45]; the one from (b) is from [46]; the one from (c) is from [47].

Consequently, it's relatively easy for this wavepacket to lose its coherence in time, especially in systems with quadratic dispersion at the bottom of the conduction band, such as in GaAs/AlGaAs heterostructures. Indeed, in this case, each component of the wavepacket possesses a different group velocity depending on its energy, and the Lorentzian shape is soon lost [32].

An alternative to Levitons, which however does not solve the problem of carrier decoherence, is represented by the use of *mesoscopic capacitors* [49]. These consist of a dynamic quantum dot weakly coupled to a lead, in correspondence with which a single carrier can be injected or absorbed. The coupling can be controlled for instance through a tunable QPC, and by exploiting the Coulomb blockade between the quantum dot and the 2DEG. Specifically, the energy of the quantum dot is periodically shifted above and below the Fermi energy of the 2DEG through a time-dependent bias $V(t)$, as shown in Fig. 1.4(b), thus stimulating the alternated ejection of electrons and holes. The single-electron carrier in this case takes the name of *Landau quasi-particle*, and its shape, contrarily to the Leviton, is exponential in real space and Lorentzian in the energy domain [50].

Inter-channel and intra-channel interactions represent an additional cause of decoherence for Landau quasiparticles [51], which however can be avoided by injecting the carrier at a much larger energy than E_F (hot electron) through a *quantum dot pump* [52]. In this case, a quantum dot is coupled to both an external fermionic bath and the device. By manipulating the confinement potential of the dot in time, as shown in Fig. 1.4(c), one can allow the passage of one or more electrons through the first barrier. Subsequently, the carriers are released into the device by increasing the first barrier much higher than the Fermi level. Specifically, with this method it's possible to generate wavepackets with a Gaussian shape [47], both in real space and in the energy domain. Their symmetry consequently allows them to better retain the wavepacket shape in time with respect to the previous implementations. The main drawback of these sources is the phonon-induced relaxation due to their high injection energy, which can lead to decreased visibility. However, this can be overcome by fine-tuning the carrier energy distribution [53, 54].

That said, single-carrier detection remains a challenging task, due to the high velocity of the single carriers [55]. However, detection efficiencies above 99% can be achieved if the electron interacts with the detector for a sufficiently long timescale, at least of the order of a μs [42, 43]. For instance, particles close to the Fermi sea, like Levitons, can be detected through capacitive coupling to a spin qubit sensitive to charge fluctuations [56]. Alternatively, the electron is made to pass below two surface electrodes, thus generating a voltage signal that can be measured [57]. These kinds of detection do not perturb the state of the flying qubit and enable non-demolition measurements, something that was not possible for single-photon detectors.

1.2 Electron quantum optics in graphene

Graphene has emerged relatively recently in the scientific community as one of the most fascinating and promising materials in modern science and technology. Indeed, despite the simplicity of its structure and it being the basis constituent of common graphite, suspending and isolating a single layer of graphene turned out to be a problem that vexed scientists for decades. Indeed, the first theoretical study on graphene dates back to 1947 [58], but it was only in 2004 that a single layer of graphene was unambiguously produced [59]. Since then, graphene has piqued the interest of many scientific communities, one of its strong points being its structural robustness while still

remaining light and flexible. Additionally, it shows both very high electrical and thermal conductivity [60–62]. Consequently, countless studies have shown its potential, ranging from chemical sensors to biomicroelectronics, from energy harvesting to flexible wearable devices, to name a few [63].

One of the main reasons behind the importance of graphene lies in its peculiar crystalline structure, consisting of a honeycomb lattice. This structure is in turn made possible thanks to the unique properties of carbon. Indeed, as we know from basic chemistry, carbon is the lightest and smallest atom possessing four valence electrons in its neutral form, occupying the second atomic shell. Consequently, the orbitals available for bonding are an s orbital and three p orbitals. When forming covalent bonds with more than one atom, two or more of the valence-shell orbitals are able to hybridize. If all orbitals participate in strong covalent σ-bonds, as it is in diamond, four sp^3-hybridized orbitals are formed, oriented in a tetrahedral geometry at angles of 109.5°. Because of the strength of these bonds, diamond is among the strongest natural materials known to man [64, 65]. Instead, only three orbitals in graphene are sp^2-hybridized, forming three in-plane σ-bonds with the surrounding atoms belonging to the same layer. The remaining, out-of-plane p-orbital forms weaker delocalized π-bonds with the surrounding atoms. These bonds make it possible for two or more layers of graphene to interact with each other through weak Van der Waals interaction, thus creating graphite.

1.2.1 Electronic properties of graphene

While we postpone the analytical treatment of the last valence band and first conduction band of graphene to Chapter 2, here we give a brief overview of the electronic properties and phenomena that are typical in monolayer graphene and of interest in this Thesis. First of all, in Fig. 1.5(a) are reported the band structure and density of states of graphene. As we can see, the in-plane σ-bonds in graphene completely fill a deep σ valence band. Instead, the remaining electrons participating in the out-of-plane π-bonds only half-fill the π valence band. As a consequence, graphene is a zero-gap semiconductor and behaves as a semimetal, with zero density of stated in correspondence of the Fermi energy E_F. Specifically, the last valence band and first conduction band meet at high symmetry points at which the valleys present linear dispersion, leading to a linear density of states near E_F. The analogy with the linear dispersion of photons described by the Dirac equation is apparent. Consequently, low-energy excitations in graphene form 2DEGs of so-called massless Dirac fermions. The only difference is that, instead of traveling at the speed of light, the velocity of Dirac fermion in graphene v_F is approximately 300 times smaller, meaning that the same phenomena from quantum electrodynamics can be observed at much smaller speeds in graphene [66–68].

Dirac fermions show peculiar behaviors with respect to ordinary electrons when subjected to electromagnetic fields. Firstly, they are mostly insensitive to the presence of external electrostatic potentials, due to the so-called Klein paradox [69]. This phenomenon is typical of particles following the relativistic Dirac equation, like photons or acoustic phonons [70]. Specifically, it stems from interference effects between the conduction and valence bands of bulk graphene in the presence of a steep potential barrier. Indeed, although the region under the potential barrier is classically forbidden, the valence band for Dirac-like particles is still available for transport. This allows the particle to be transmitted as a hole with transmission coefficient 1 through the barrier, restoring its electron character as soon as it reaches the other side of the barrier. Due to the phenomenology of this process, the Klein paradox is also usually referred to as Klein *tunneling*, as it resembles the

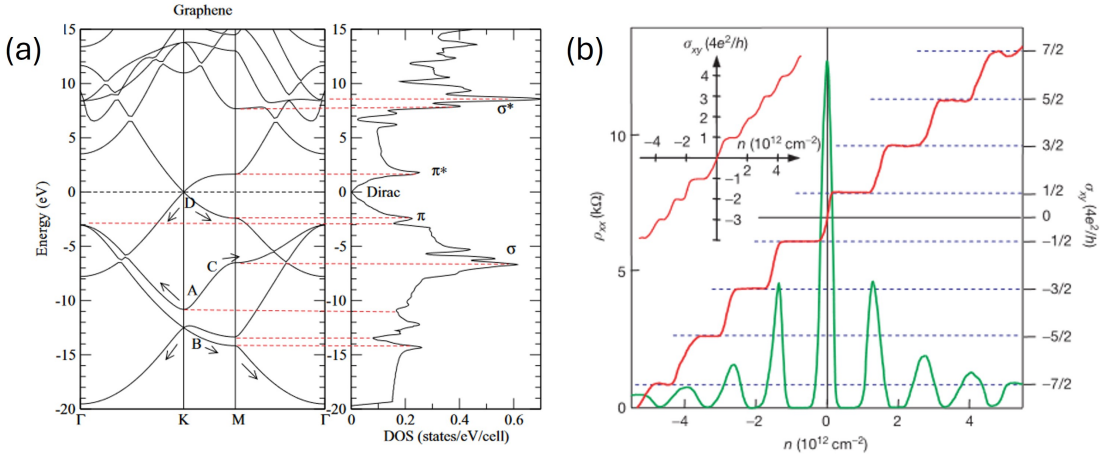


Figure 1.5: Band structure (left) and density of states (right) in the first Brillouin zone of graphene, obtained through *ab initio* calculations. The labels σ, σ^*, π and π^* reference the atomic bonds contributing to each band. (b) Curves of the transverse conductivity σ_{xy} (red) and longitudinal resistivity ρ_{xx} (green) showing half-integer quantum Hall effect in monolayer graphene. The inset shows the usual integer quantum Hall effect in bilayer graphene for comparison. Panel (a) is taken from [78]; panel (b) from [10].

perfect tunneling of a quantum particle through an electrostatic barrier. The occurrence of this phenomenon implies that transport in graphene is particularly immune to potentials created by disorder inside the sample. Indeed, under certain conditions, electrons are immune to localization effects. Consequently, they can usually reach mobilities in the range of $10^{4\div5}\text{cm}^2/\text{V}\cdot\text{s}$ [71–73], even at room temperature, with the possibility of going even higher [74]. At the same time, mean free-path lengths are in the order of a few μm's and possibly higher [59, 75–77].

Half-integer quantum Hall effect

Most interestingly, the 2DEG in monolayer graphene subjected to an external electric field notoriously presents an anomalous half-integer quantum Hall (HIQH) effect [79–82]. This is clearly visible from the curves first observed in Ref. [59] [Fig. 1.5(b)]. Indeed, here the longitudinal conductivity, $\sigma_{xy} = 1/R_H$ is not proportional to an integer number, as it is for the usual IQH effect from Sec. 1.1.1. Instead, it can be written as:

$$\sigma_{xy} = \frac{1}{R_H} = 4\left(n + \frac{1}{2}\right)\frac{e^2}{\hbar}, \tag{1.4}$$

where we recall that n is the Landau level index, which for graphene can be any integer, $n \in \mathbb{Z}$. We will delve into more details into the analytical treatment of this peculiar behavior in Sec. 2.2.2. For now, it suffices to say that massless Dirac fermions in graphene can be localized in momentum space in either one of two inequivalent valleys in the first Brillouin zone. This factor defines a two-fold valley *pseudospin*, on which the Landau levels are degenerate. Adding spin degeneracy, Landau levels overall are four-fold degenerate and possess a SU(4) symmetry. Additionally, since a Landau level falls on the Fermi energy, it is always half-filled at zero carrier density, thus causing the peak in the longitudinal resistivity ρ_{xx} visible in Fig. 1.5(b). Interestingly, the HIQH effect in graphene is also observable at room temperatures [83], thanks to the cyclotron energy being much

higher than in GaAs/AlGaAs (see Sec. 2.2.1).

The usual IQH effect is retrieved as soon as the spin and valley degeneracies are lifted. This can be done in many ways by introducing fields that couple with the respective degrees of freedom, for example through high magnetic fields or interaction effects [84–86]. A significant example is in bilayer graphene, in which the stacking configuration highly influences the inequivalence between the A and B sublattices of graphene. This introduces a gap in the band dispersion, highly tunable by the twisting angle θ_T [87], so that the system becomes an insulator. Consequently, the four-fold degenerate Landau level with $n = 0$ is forced to split into two, two-fold degenerate Landau levels, one below and one above the Fermi energy. Then, an additional degeneracy on the layer degree of freedom in bilayer graphene may cause a total conductivity of $\sigma_{xy} = 4ne^2/\hbar$ [88], so that the usual behavior of the IQH regime is retrieved up to a normalization factor [see the inset in Fig. 1.1(b)]. That said, note that this behavior is also highly dependent on the tilting angle θ_T, and odd-integer quantum Hall effect was also reported in twisted bilayers [89].

Going back to monolayer graphene, the SU(4) symmetry breaking of Landau levels can also directly occur at the edge of nanoribbons [90–93]. These are defined as strips of graphene of finite length, so that the atoms at their edges present unsaturated bonds. As in GaAs/AlGaAs, the Landau levels must bend at the edge of the 2DEG, and in order to do so the Landau level for $n = 0$ splits once again as described above. Specifically, the two states below the Fermi level bend downward and the other two above the Fermi level bend upward. Here however the nature of the Landau level splitting and of the edge states is dependent on the characteristics of the edge: namely, on the sublattice to which the dangling atoms belong to, and the consequent shape of the edge. Specifically, we talk about *zigzag* nanoribbons if all the edge atoms belong to the same sublattice (either A or B), or *armchair* nanoribbons if the atoms belong alternately to different sublattices. In the former case, the edge states possess a well-defined valley pseudospin, while they are in a superposition of the spin degrees of freedom; in the latter case, the opposite is true [90]. We will see all of this in more details later in Sec. 2.2.3.

1.2.2 Graphene devices for interferometry

Synthesis of graphene

Over the decades after its theoretical discovery, many methods have been employed to try and isolate monolayer graphene. The most direct one consists of mechanical exfoliation. In this method, the weak Van der Waals bonds between graphite layers are broken through mechanical stress in order to isolate thin graphitic films. This is also the method first used by Novoselov et al. [59]. The procedure they used is illustrated in Fig. 1.6(a): they started with 1-mm-thick samples of highly oriented pyrolytic graphite (HOPG) and etched 5-μm mesas on its surface. After pressing the mesas on an adhesive layer placed on top of a SiO_2 substrate, the rest of the sample was peeled off with scotch tape. For this reason, this method is also referred to as the *scotch tape method*. The difficulty with this procedure consists of making sure that these films reach single-atom thickness. Consequently, the peeling process is repeated multiple times on the same sample until sufficiently thin crystals are obtained. After additional cleaning procedures, the thin flakes that remained attached to the substrate were then analyzed with optical and atomic force microscopes, and monolayer samples were observed.

Using SiO_2 as a substrate for mechanical exfoliation however causes a significant problem.

Indeed, due to its disordered structure, the obtained graphene samples can be corrugated, thus showing properties that are far from the ones expected from free-standing graphene [95, 96]. As a solution, more recent advances substitute SiO_2 as a substrate with hexagonal boron nitride (hBN) [97–99]. Indeed, hBN is an isomorph of graphite, meaning that it presents the same crystalline structure, with a lattice mismatch as small as 1.7% [100]. Additionally, hBN possesses similar electronic properties to SiO_2, the first one being its large band gap [101], caused by the inequality between the two triangular sublattices that make up its honeycomb structure. Consequently, the use oh hBN as a gate dielectric does not imply any loss of functionality in device integration, while also suppressing corrugation on the graphene sample. In addition, operativity at much higher temperatures and electric fields is made possible, thanks to the much higher energy of the surface phonon modes of hBN with respect to SiO_2 [102]. That said, the sublattice inequivalence in hBN couples to the sublattice pseudospin of carriers in graphene, and consequently introduces a tunable energy gap in graphene as well [103, 104]. This is usually very small, in the order of the tens of meVs, but it suffices to break the valley degeneracy in the Landau level lying on the Fermi level, equivalently as we explained for bilayer graphene in the previous section.

For the sake of completion, we also illustrate other possible techniques for graphene synthesis on other substrates. One example is epitaxial growth on transition metals (most commonly nickel or copper), as illustrated in Fig. 1.6(b). This is possible through the use of chemical vapor deposition of carbon atoms on cleaned metallic crystals [105]. During this procedure, a volatile carbon precursor (e.g. a hydrocarbon or carbon oxide) in vacuum is progressively cooled down, forming graphene islands on the substrate that eventually form a thin graphene film [106]. Alternatively, graphene flakes can originate from bulk carbon impurities in the metal, which are consequently segregated on the surface through annealing. Although these platforms are promising in terms of scalability, the interaction between the graphene layer and the metallic substrate is strong and introduces charge transfer mechanisms that can affect the electronic properties of the sample. Another possibility is consequently to use a carbide substrate instead, as shown in Fig. 1.6(c). SiC specifically has shown encouraging perspectives thanks to its compatibility with modern semiconductor technology. In this case, the substrate undergoes ultrahigh vacuum annealing at high temperature, a process during which Si atoms evaporate from the surface of the substrate and the produced C-rich surface reconstructs into thin graphene films [107]. The number of obtained layers is controlled by tuning the temperature and time of the process. Doing so can lead to sample

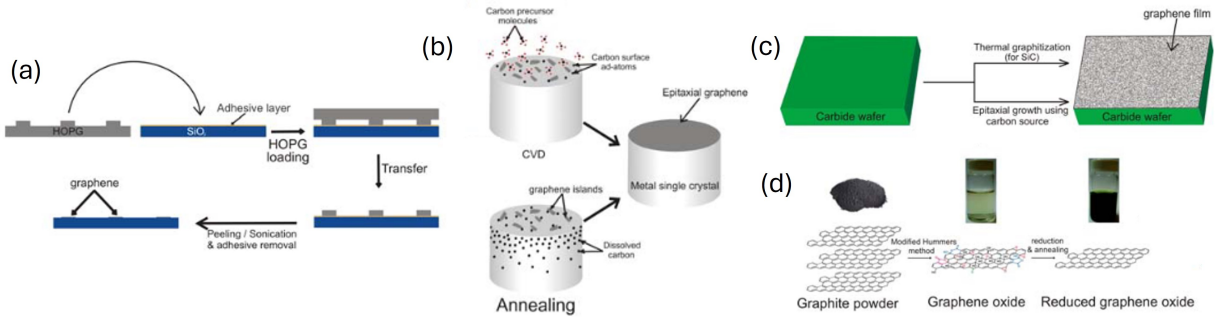


Figure 1.6: Various techniques for graphene synthesis. (a) Mechanical exfoliation on SiO_2. (b) Epitaxial growth on transition metals either by chemical vapor deposition or annealing. (c) Epitaxial growth on carbides through thermal graphitization of SiC or deposition. (e) Chemical synthesis with graphene oxide. The picture was adapted from [94].

properties that are nearly identical to those of free-standing graphene [108].

Lastly, it's worth mentioning that large quantities of graphene can also be produced without the need of a substrate, for instance through the chemical synthesis of graphene oxide [109], as schematically illustrated in Fig. 1.6(d). This method produces high-quality graphene, and could be useful for integrating it in devices through solution processing. However, this road is not usually pursued for the implementation of solid-state devices, since it's more straightforward to directly produce graphene on the desired substrate.

Mach-Zehnder interferometry with graphene devices

Thanks to the peculiar properties of graphene, and the progresses in producing progressively cleaner monolayers, a wide variety of high-quality devices for high-performance electronics can be produced. Specifically, the possibility of reaching the ballistic regime for electrons in the IQH regime makes graphene an excellent platform for electron quantum optics, allowing for a clean observation of quantum coherence and interference. In the remainder of the first part of this Thesis, we will focus on possible ways to implement an MZI in graphene, which we illustrate schematically in Fig. 1.7. Equivalently to what happened in GaAs/AlGaAs devices, the shape of the edge channels used for electronic transport is controlled through electrostatic potentials created by gate electrodes [112]. Consequently, one can create QPCs that are equivalent to those in gapped semiconductors [110], as shown in Fig. 1.7(a). In this case, the optical paths of the MZI can be formed

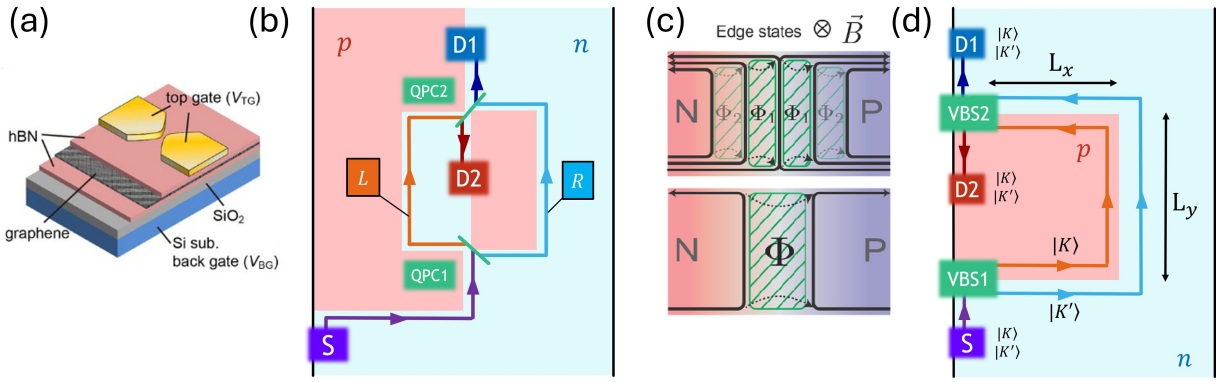


Figure 1.7: (a) Scheme of a QPC implemented in a state-of-the-art graphene monolayer, encapsulated in hBN on a SiO_2 substrate. The potential profile defining the QPC is generated by the top gates (yellow). (b) Schematic representation of a MZI in graphene based on QPCs (QPC1 and QPC2). The edge channels and the transport directions are shown through arrowed lines. S is the electronic source, while D1 and D2 are the detectors. The spatially separated arms of the interferometer are labeled L and R. (c) Edge states propagating along a *pn* junction at high (above) and low (below) carrier densities. The dashed arrows indicate electron scattering in correspondence with the electrostatic barrier. The quantities Φ_i indicate the magnetic flux between various edge states determining the Aharonov-Bohm phase. (d) Schematic representation of a MZI in graphene based on VBSs (VBS1 and VBS2). L_x and L_y are the dimensions of the gate-defined barrier defining the *pn* junction. The labels $|K\rangle$ and $|K'\rangle$ indicate the valley composition of the carrier propagating along each edge channel. The rest of the notation is the same as panel (a). Note that the *n* and *p* regions inside the devices are respectively shown in blue and red in panels (b) and (d), while the colors are inverted in (c). Panel (a) is taken from [110]; (b) and (d) from [3]; and (c) from [111].

on spatially separated potential profiles, as illustrated schematically in Fig. 1.7(b), thus mimicking the interferometers previously illustrated in Sec. 1.1.1.

That said, the introduction of electrostatic potentials in graphene creates regions with different FFs on the two sides of the barrier, as schematically shown in Fig. 1.7(c). Indeed, differently from gapped semiconductors, in graphene holes can be transmitted below a potential barrier, as explained previously in Sec. 1.2.1. Under these conditions, an incoming carrier traveling on the edge of a nanoribbon gets scattered in all the energetically available Landau levels, including those with negative FF [113, 114]. The splitting into different channels consequently occurs without the need for a QPC. At the same time, interchannel scattering between opposite spins is suppressed [113, 115, 116], so that states with different spins behave independently. An Aharonov-Bohm phase can then be defined inside this system for each spin, due to the area enclosed by the edge channels defined along the potential profile. At low carrier density specifically [bottom panel of Fig. 1.7(c)], the only two available channels are the sublevels of the 0-indexed Landau level, which from now on we will call LL_0^+ and LL_0^-. When these are degenerate and overlap, the enclosed area is zero, and so is the Aharonov-Bohm phase. On the contrary, when the valley degeneracy is lifted, the two channels move further away from each other and interference is possible.

The intersection between the gate potential and the edge of the nanoribbon takes the name of valley beam splitter (VBS). Indeed, the two channels $LL_0^{+/-}$ described above, in which the carrier gets scattered, correspond each to a different valley quantum number. The definition of VBSs opens the road to possible encoding and manipulation of information through the valley degree of freedom of electrons in graphene, in what takes the name of *valleytronics* [11]. In this context, a valley interferometer is built through the use of two VBSs, as shown in Fig. 1.7(d) and 1.8. That is, the carrier is first initialized at the edge of an armchair nanoribbon into a superposition state of the two valleys, K and K' [90, 117]. Then, as it meets the first VBS, it gets split into the two valley-resolved edge channels running alongside the barrier. One of these is located in the n region and populated by an electron-like state, and the other is in the p region, populated by a hole-like state. Then, the channels are reunited at the other edge of the potential barrier, where a second VBS is located, and the carrier interferes with itself. Notice that the inter-level splitting can also occur in the first kind of MZI from Fig. 1.7(b). Inside here, it can cause detrimental effects, among which the back-scattering below the electrostatic gates [118–122]. However, the occurrence of VBSs and their behavior can be finely controlled by tuning the gap in the graphene sample [123], and consequently, in clean enough monolayers, this effect could be removed.

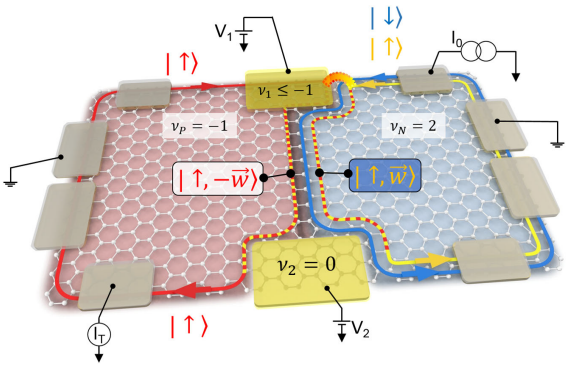


Figure 1.8: Example of a valley interferometer in graphene. In grey are the Ohmic contacts defining the manipulating potentials. In yellow are the gates defining the behavior of VBSs. Interchannel scattering conserves the spin (↑ / ↓) and is only possible at the edge of the nanoribbon. Here the valley index is labeled as $w/-w$. The picture is taken from [114].

Up until now, interferometers built with VBSs have mostly been demonstrated using delocalized currents [112–114, 124–126]. Visibilities up to 98% were achieved [113, 114], much higher than those obtainable in MZIs implemented in GaAs/AlGaAs heterostructures. However, not as

much progress has been made in the interferometry of single localized carriers. Indeed, contrary to conventional semiconductors, the negligible gap of graphene makes it nearly impossible to create electrical pumps through dynamically coupled quantum dots. Only recently, the generation of Leviton-like excitations in graphene has been demonstrated experimentally [127]. Similarly as we illustrated in Sec. 1.1.2, this required the application of a time-dependent Lorentzian voltage $V(t)$ on the source lead. Specifically, through fine-tuning of the gate potentials, Assouline et al. were able to obtain both one- and two-electron injection in graphene with the absence of electron-hole pairs. This definitively opens the possibility of on-demand single- and few-particle interferometry in graphene. In view of this, in the next two Chapters we will focus on the coherent evolution of localized carriers. Since we know that the shape of the wavepacket does not influence interference phenomena significantly [32], our focus will be on Gaussian wavepackets, which we expect to better preserve their shape in time.

He deals the cards to find the answer
The sacred geometry of chance
The hidden law of a probable outcome
The numbers lead a dance

$\sim$ from *Shape of my Heart*, by Sting

Chapter 2

Numerical simulation of coherent transport with edge states

In this Chapter we describe the analytical and theoretical models employed in the time-dependent simulations of transport in graphene nanoribbons. In Sec. 2.1 we study the theory behind massless Dirac fermions in graphene, starting with the tight-binding model in Sec. 2.1.1 and obtaining the linear approximation of the Hamiltonian in the valley and sublattice degrees of freedom in Sec. 2.1.2. We then analyze the IQH effect in Sec. 2.2, from how to find the eigenfunctions of the Hamiltonian in bulk in Sec. 2.2.1, to describing the Landau levels in Sec. 2.2.2, and then looking at the behavior of edge states in an armchair nanoribbon in Sec. 2.2.3. In Sec. 2.3, we describe how to initialize and simulate the dynamics of electronic wavepackets. We show how to build Gaussian wavepackets of edge states in Sec. 2.3.1, along with how to use the wavepacket method to analyze the wave function at the end of the evolution. Finally, we explain the split-step Fourier method used to evolve the state of the carrier in Sec. 2.3.2, taking account of both the coupled valley and sublattice degrees of freedom of the wave function.

2.1 Description of massless Dirac fermions in graphene

2.1.1 Tight-binding model for graphene

The crystalline structure of monolayer graphene (see Fig. 2.1(a)) consists of a triangular lattice with lattice vectors $\mathbf{a} = a(1,0)$ and $\mathbf{b} = a(1/2, \sqrt{3}/2)$. The unit cell presents two carbon atoms: the first at $(0,0)$ belonging to sublattice A, and the second at $\mathbf{d} = a(0, 1/\sqrt{3})$ belonging to sublattice B. The lattice parameter is $a = \sqrt{3}A$, with $A = 1.422\dot{A}$ being the carbon-carbon bond length [130]. Considering only nearest-neighbor hopping, the tight-binding Hamiltonian in second-quantization form for a single layer of graphene reads:

$$\hat{H} = -t \sum_{i \in A} \sum_{\delta} (\hat{a}_i^\dagger \hat{b}_{i+\delta} + \hat{b}_{i+\delta}^\dagger \hat{a}_i), \tag{2.1}$$

where $\hat{a}_i^\dagger$, $\hat{a}_i$ are the creation and annihilation operators that create/annihilate a particle on site i belonging to sublattice A; $\hat{b}_{i+\delta}^\dagger$, $\hat{b}_{i+\delta}$ create/annihilate a particle on site $i+\delta$ belonging to sublattice B; and $t = 2.7eV$[130] is the hopping parameter. The quantity δ runs on the three possible nearest-neighbor vectors,

$$\delta_1 = a(0, 1/\sqrt{3}), \quad \delta_2 = \frac{a}{2}(1, -1/\sqrt{3}), \quad \delta_3 = \frac{a}{2}(-1, -1/\sqrt{3}). \tag{2.2}$$

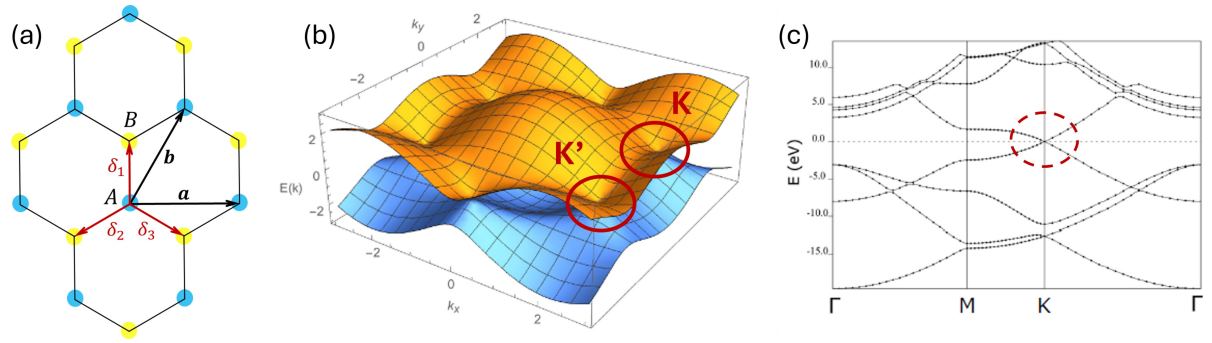


Figure 2.1: (a) Honeycomb lattice in graphene, made of two interpenetrating triangular lattices A and B, with unit vectors $\mathbf{a}$ and $\mathbf{b}$. The three nearest-neighbour vectors are δ_1, δ_2 and δ_3. (b) Electronic band structure of the last valence band (blue) and first conduction band (orange) in the First Brillouin Zone of graphene. The K and K' valleys are pointed out by red circles. (c) Band structure of monolayer graphene found through *ab initio* simulations with DFT using Quantum ESPRESSO [128]. The presence of the Dirac cone is highlighted with a red circle. Panel (b) is taken from [129].

In order to represent the Hamiltonian in Eq. (2.1) in momentum space, and being the system periodic, we use the Fourier expansion of the creation/annihilation operators:

$$\hat{a}_i^\dagger = \frac{1}{\sqrt{N/2}} \sum_{\mathbf{k}} e^{i\mathbf{k}\cdot\mathbf{r}_i} \hat{a}_{\mathbf{k}}^\dagger, \quad \hat{a}_i = \frac{1}{\sqrt{N/2}} \sum_{\mathbf{k}} e^{-i\mathbf{k}\cdot\mathbf{r}_i} \hat{a}_{\mathbf{k}}, \tag{2.3}$$

where $\hat{a}_{\mathbf{k}}^\dagger/\hat{a}_{\mathbf{k}}$ create/annihilate a particle with crystal momentum $\mathbf{k}$. Similarly for $\hat{b}_{i+\delta}^\dagger/\hat{b}_{i+\delta}$, which will be written as a function of $\hat{b}_{\mathbf{k}}^\dagger/\hat{b}_{\mathbf{k}}$, only replacing $\mathbf{r}_i \to \mathbf{r}_i + \delta$. In Eq. (2.3), $N/2$ is the number of atoms of each sublattice. By replacing the formulas from Eq. (2.3) into Eq. (2.1) and using the equality

$$\sum_{i\in A} e^{i(\mathbf{k}-\mathbf{k}')\cdot\mathbf{r}_i} = \frac{N}{2}\delta_{\mathbf{k}\mathbf{k}'}, \tag{2.4}$$

with $\delta_{\mathbf{k}\mathbf{k}'}$ being the Kronecker delta, the Hamiltonian becomes:

$$\begin{aligned} \hat{H} &= -\frac{t}{N/2} \sum_{i\in A} \sum_{\delta} \sum_{\mathbf{k}\mathbf{k}'} (e^{i\mathbf{k}\cdot\mathbf{r}_i} e^{-i\mathbf{k}'\cdot(\mathbf{r}_i+\delta)} \hat{a}_{\mathbf{k}}^\dagger \hat{b}_{\mathbf{k}'} + H.c.) = \\ &= -t \sum_{\delta} \sum_{\mathbf{k}} (e^{-i\mathbf{k}\cdot\delta} \hat{a}_{\mathbf{k}}^\dagger \hat{b}_{\mathbf{k}} + e^{i\mathbf{k}\cdot\delta} \hat{b}_{\mathbf{k}}^\dagger \hat{a}_{\mathbf{k}}), \end{aligned} \tag{2.5}$$

where $H.c.$ stands for *Hermitian conjugate*. The obtained Hamiltonian operator is now diagonal on the momentum degree of freedom. Consequently, in the following we can consider $\mathbf{k}$ as a parameter, obtaining a 2 by 2 momentum-dependent Hamiltonian $\hat{H}(\mathbf{k})$, written on the basis of the sublattice degrees of freedom (A, B):

$$\hat{H}(\mathbf{k}) = -t \begin{pmatrix} 0 & f_{\mathbf{k}} \\ f_{\mathbf{k}}^* & 0 \end{pmatrix}, \tag{2.6}$$

$$f_{\mathbf{k}} = \sum_{\delta} e^{-i\mathbf{k}\cdot\delta} = e^{i\frac{a}{2}\frac{k_y}{\sqrt{3}}} \left[e^{-i\frac{\sqrt{3}}{2}ak_y} + 2\cos\left(\frac{a}{2}k_x\right) \right]. \tag{2.7}$$

The eigenvalues of the Hamiltonian in Eq. (2.6) as a function of the **k**-vector give the shape of the last valence band and first conduction band of monolayer graphene:

$$E_{\pm}(\mathbf{k}) = \pm t\sqrt{f_{\mathbf{k}}^{*} f_{\mathbf{k}}} = \pm t\sqrt{1 + 4\cos^2\left(\frac{a}{2}k_x\right) + 4\cos\left(\frac{a}{2}k_x\right)\cos\left(\frac{\sqrt{3}}{2}ak_y\right)}\,. \tag{2.8}$$

The bands in Eq. (2.8) are shown in Fig. 2.1(b). As seen from the picture, there are a total of six points at the edge of the first Brillouin zone at which the valence and conduction bands touch and $E_{\pm} = 0$. These points are called *Dirac points*. Only two of these points,

$$\mathbf{K} = \frac{2\pi}{a\sqrt{3}}\left(\frac{1}{\sqrt{3}}, 1\right), \quad \mathbf{K}' = \frac{2\pi}{a\sqrt{3}}\left(-\frac{1}{\sqrt{3}}, 1\right), \tag{2.9}$$

which we refer to as K and K' valleys, are independent: the other four are all equivalent to either K or K' in one of the adjacent Brillouin zones belonging to the reciprocal lattice. Due to the shape of the last valence band and first conduction band, the energy gap in pure suspended monolayer graphene is zero, although presenting zero density of states at $E = 0$. Consequently, this makes monolayer graphene behave as a semimetal, as previously mentioned in Sec. 1.2.1.

2.1.2 Linear approximation

As highlighted in Fig. 2.1(c), the bands in graphene near the Dirac points present a linear dispersion. Indeed, if we define a relative wave vector with respect to the valley K (K') as $\mathbf{q} = \mathbf{k} - \mathbf{K}(\mathbf{K}')$, for small enough values of $q = |\mathbf{q}|$ the function $f_{\mathbf{q}}$ found through Eq. (2.7) approximates to:

$$f_{\mathbf{q}} \approx \frac{3a}{2}(+q_x - iq_y) \quad (K), \tag{2.10}$$

$$f_{\mathbf{q}} \approx \frac{3a}{2}(-q_x - iq_y) \quad (K'), \tag{2.11}$$

and the energy $E_{\pm}(\mathbf{q})$ from Eq. (2.8) approximates to

$$E_{\pm}(\mathbf{q}) \approx \hbar v_F\sqrt{q_x^2 + q_y^2} = \hbar v_F q\,, \tag{2.12}$$

where $v_F = \frac{3at}{2}\cdot\frac{1}{\hbar}$ is the Fermi velocity. Particularly, when replacing the approximated expression of $f_{\mathbf{q}}$ into Eq. (2.6), the Hamiltonian takes the form of the Dirac Hamiltonian for massless particles:

$$\hat{H}(\mathbf{q}) = \hbar v_F\begin{pmatrix} 0 & -q_x + iq_y \\ -q_x - iq_y & 0 \end{pmatrix} = \hbar v_F(-q_x\hat{\sigma}_1^{AB} - q_y\hat{\sigma}_2^{AB}) \quad (K), \tag{2.13}$$

$$\hat{H}(\mathbf{q}) = \hbar v_F\begin{pmatrix} 0 & +q_x + iq_y \\ +q_x - iq_y & 0 \end{pmatrix} = \hbar v_F(+q_x\hat{\sigma}_1^{AB} - q_y\hat{\sigma}_2^{AB}) \quad (K'), \tag{2.14}$$

which means that carriers near the Fermi energy in graphene behave equivalently to relativistic particles, from which comes the name Dirac fermions introduced in Sec. 1.2.1. In Eqs. (2.13-2.14), $\hat{\sigma}_{1/2}^{AB}$ are the first two Pauli matrices on the *sublattice isospin* basis (A/B).

For small values of q, where the linear approximation is valid, an electron can be located in momentum space either near the K or K' valley. Consequently, one can define an additional quantum

number in terms of the valley pseudospin (K/K'). In total, the Hamiltonian can be rewritten as a 4×4 operator, block-diagonal on the valley degree of freedom:

$$\begin{aligned}\hat{H}(\mathbf{q}) =& \hbar v_F \begin{pmatrix} 0 & -q_x + iq_y & 0 & 0 \\ -q_x - iq_y & 0 & 0 & 0 \\ 0 & 0 & 0 & +q_x + iq_y \\ 0 & 0 & +q_x - iq_y & 0 \end{pmatrix} = \\ =& \hbar v_F (-q_x \hat{\sigma}_1^{AB} \otimes \hat{\sigma}_3^{KK'} + q_y \hat{\sigma}_2^{AB} \otimes \hat{\mathbb{1}}) \,, \end{aligned} \tag{2.15}$$

where $\hat{\sigma}_3^{KK'}$ is the third Pauli matrix on the valley pseudospin (K/K'). Within this formalism, the eigenvector of $\hat{H}$ is the electronic wave function of the system, and is represented by a four-component spinor,

$$\hat{H}(\mathbf{q})\Psi(\mathbf{r}) = E(\mathbf{q})\Psi(\mathbf{r}), \tag{2.16}$$

$$\Psi(\mathbf{r}) = \left(\psi_A^K(\mathbf{r}), \psi_B^K(\mathbf{r}), \psi_A^{K'}(\mathbf{r}), \psi_B^{K'}(\mathbf{r})\right)^T, \tag{2.17}$$

where Eq. (2.16) is the Dirac equation for massless Dirac fermions. Since the four-dimensional Dirac Hamiltonian of Eq. (2.15) is block-diagonal in the valley degree of freedom, its most generic solution will be a linear combination of the wave functions $\Psi^K(\mathbf{r})$ and $\Psi^{K'}(\mathbf{r})$, located in the K and K' valleys respectively:

$$\Psi^K(\mathbf{r}) = \left(\psi_A^K(\mathbf{r}), \psi_B^K(\mathbf{r}), 0, 0\right)^T \quad \Psi^{K'}(\mathbf{r}) = \left(0, 0, \psi_A^{K'}(\mathbf{r}), \psi_B^{K'}(\mathbf{r})\right)^T, \tag{2.18}$$

$$\Psi(\mathbf{r}) = \alpha e^{i\mathbf{K}\cdot\mathbf{r}}\Psi^K(\mathbf{r}) + \beta e^{i\mathbf{K}'\cdot\mathbf{r}}\Psi^{K'}(\mathbf{r}) \,. \tag{2.19}$$

The factors α and β are two generic complex coefficients such that $|\alpha|^2 + |\beta|^2 = 1$. The relative exponential phase factors come from the different points $\mathbf{K}$ and $\mathbf{K}'$ in the first Brillouin zone around which $\mathbf{k}$ is expanded.

The Hamiltonian in Eq. (2.15) is antisymmetric under chiral symmetry:

$$\hat{\Gamma}\hat{H}\hat{\Gamma} = -\hat{H}, \quad \hat{\Gamma} = \begin{pmatrix} \hat{\sigma}_3^{AB} & 0 \\ 0 & \hat{\sigma}_3^{AB} \end{pmatrix}, \tag{2.20}$$

with $\hat{\sigma}_3^{AB}$ being the z Pauli matrix on the sublattice isospin. This means that each solution with energy E has a particle-hole conjugate with energy $-E$. As a consequence, the electronic wave function must be normalized separately on each sublattice,

$$\int d\mathbf{r}\; \psi_\mu^K(\mathbf{r})\psi_\mu^{K'}(\mathbf{r}) = \frac{1}{2}, \quad \mu = A, B \,. \tag{2.21}$$

Opening a gap in graphene

The tight-binding Hamiltonian for massless Dirac fermions built in Eq. (2.13) and (2.14) includes terms proportional to the x and y Pauli matrices in the sublattice basis. It is possible to also introduce a term proportional to $\hat{\sigma}_3^{AB}$: this adds two components of opposite signs on the diagonal of $\hat{H}$. Taking as an example the K valley:

$$\hat{H}(\mathbf{q}) = \begin{pmatrix} M & \hbar v_F(-q_x + iq_y) \\ \hbar v_F(-q_x - iq_y) & -M \end{pmatrix} = \hbar v_F(-q_x \hat{\sigma}_1^{AB} - q_y \hat{\sigma}_2^{AB}) + M\hat{\sigma}_3^{AB} \,. \tag{2.22}$$

We will call M a mass term, for reasons that will be clear below. In the tight-binding formalism, Eq. (2.22) is obtained from Eq. (2.13) by adding the following term:

$$\hat{H}_z = M\left(\sum_{i\in A}\hat{N}_{A,i} - \sum_{j\in B}\hat{N}_{B,j}\right) \tag{2.23}$$

with $\hat{N}_{A,i} = \hat{a}_i^\dagger\hat{a}_i$ and $\hat{N}_{B,j} = \hat{b}_j^\dagger\hat{b}_j$. This means introducing specific on-site potential terms that discriminate atoms from the two sublattices, A and B. It's reasonable to introduce a similar term in systems where the two sublattices are made up of different atoms, for example in hBN (see Sec. 1.2.2 for further details). The main consequence of having $M \neq 0$ is a modification in the band dispersion near the Dirac points from Eq. (2.12):

$$E_\pm(\mathbf{q}) \approx \pm\hbar v_F\sqrt{q_x^2 + q_y^2 + \left(\frac{M}{\hbar v_F}\right)^2}\,. \tag{2.24}$$

Therefore, a gap is introduced at $\mathbf{k} = 0$ between the valence $(-)$ and conduction $(+)$ bands:

$$E_g = 2M\,, \tag{2.25}$$

and the bands present a curvature different from zero, however small it may be. The name 'mass term' comes from the subsequent introduction of an effective mass,

$$m_\pm^{eff} = \left(\frac{1}{\hbar^2}\frac{\partial^2 E_\pm(\mathbf{q})}{\partial q^2}\bigg|_{\mathbf{q}=0}\right)^{-1} \approx \pm\frac{M}{v_F^2}\,. \tag{2.26}$$

It has been experimentally shown that graphene can present a gap, despite the equivalence of sublattices A and B [98, 131–133]. This may be because of the impurity of the samples, the substrates they are grown on, or any other field that may couple to the sublattice degree of freedom. The Hamiltonian in Eq. (2.22) is a way to take account of these effects.

2.2 Theoretical treatment of the quantum Hall effect in graphene

In order to study graphene under the effect of an external magnetic field, one can focus on solving the Dirac equation for the K valley, thus dealing with a 2×2 eigenvalue problem. This can be done since the total Hamiltonian is block-diagonal in the valley degree of freedom. The calculations for K' valley are equivalent under a reflection $q_x \to -q_x$. Note that in our treatment we neglect the real spin degree of freedom. However, it has been shown that interchannel scattering is suppressed for opposite spins [115]. Thus, states with opposite spins behave independently of each other and do not interfere. Consequently, the results of our simulations are valid separately for any value of the spin.

2.2.1 Spinorial eigenfunctions in bulk

For the moment, let's set $M = 0$. In the presence of a magnetic field $\mathbf{B} = B\hat{\mathbf{z}}$ perpendicular to the graphene monolayer, the Dirac Hamiltonian transforms under the Peierls substitution, $\mathbf{q} \to$

$\mathbf{q} + e\mathbf{A}/\hbar$, $\mathbf{A}$ being the vector potential. Choosing the Landau gauge, $\mathbf{A} = B(0, x, 0)$, the system's Hamiltonian becomes:

$$\hat{H}(\mathbf{q}, \mathbf{r}) = \hbar v_F \begin{pmatrix} 0 & -q_x + i(q_y + \frac{eBx}{\hbar}) \\ -q_x - i(q_y + \frac{eBx}{\hbar}) & 0 \end{pmatrix} . \tag{2.27}$$

The eigenvalue problem for this Hamiltonian has general solution $\Psi^K(\mathbf{r}) = (\psi_A^K(\mathbf{r}), \psi_B^K(\mathbf{r}))^T$. In order to solve the eigenvalue problem we replace the wave vector operator with its representation in real space, $\mathbf{q} = -i\nabla$, and choose an appropriate *ansatz*. We start by considering the following form for the eigenfunction:

$$\psi_\mu^K(\mathbf{r}) = e^{iq_y y}\phi_\mu^K(x), \quad \mu = A, B, \tag{2.28}$$

$$\Phi^K(x) = \begin{pmatrix} \phi_A^K(x) \\ \phi_B^K(x) \end{pmatrix} , \tag{2.29}$$

which is separable and has the shape of a plane wave with wave vector q_y in the y direction. By doing so, the Dirac equation can be reduced to an effective one-dimensional eigenvalue problem for the spinor $\Phi^K(x)$.

$$\begin{aligned} &\hbar v_F \begin{pmatrix} 0 & i\frac{\partial}{\partial x} + \frac{\partial}{\partial y} + i\frac{eBx}{\hbar} \\ i\frac{\partial}{\partial x} - \frac{\partial}{\partial y} - i\frac{eBx}{\hbar} & 0 \end{pmatrix} e^{iq_y y} \begin{pmatrix} \phi_A^K(x) \\ \phi_B^K(x) \end{pmatrix} = E e^{iq_y y} \begin{pmatrix} \phi_A^K(x) \\ \phi_B^K(x) \end{pmatrix} \\ \rightarrow\ & iv_F \begin{pmatrix} 0 & \hbar\frac{\partial}{\partial x} + \hbar q_y + eBx \\ \hbar\frac{\partial}{\partial x} - \hbar q_y - eBx & 0 \end{pmatrix} \begin{pmatrix} \phi_A^K(x) \\ \phi_B^K(x) \end{pmatrix} = E \begin{pmatrix} \phi_A^K(x) \\ \phi_B^K(x) \end{pmatrix} . \end{aligned} \tag{2.30}$$

At this point, we can define the magnetic length,

$$l_m = \sqrt{\hbar/eB} , \tag{2.31}$$

and introduce a set of ladder operators:

$$\hat{a} = \frac{l_m}{\sqrt{2}} \left(\frac{1}{l_m^2}(x - x_0) + \frac{\partial}{\partial x} \right) , \qquad \hat{a}^\dagger = \frac{l_m}{\sqrt{2}} \left(\frac{1}{l_m^2}(x - x_0) - \frac{\partial}{\partial x} \right) , \tag{2.32}$$

$$\left[\hat{a}, \hat{a}^\dagger \right] = \mathbb{1} . \tag{2.33}$$

In particular, $x_0 = -\frac{\hbar q_y}{eB}$ is a spatial translation and is coupled to the wave vector q_y. By inserting these creation and annihilation operators into the effective Hamiltonian introduced in Eq. (2.30) we get

$$\hat{H} = \hbar\omega_c \begin{pmatrix} 0 & i\hat{a} \\ -i\hat{a}^\dagger & 0 \end{pmatrix} , \tag{2.34}$$

with $\omega_c = \frac{\sqrt{2}v_F}{l_m}$ defined as the cyclotron energy. The corresponding result for the K' valley has the creation and annihilation operators' positions switched:

$$\hat{H} = \hbar\omega_c \begin{pmatrix} 0 & i\hat{a}^\dagger \\ -i\hat{a} & 0 \end{pmatrix} . \tag{2.35}$$

Eventually, $\Phi^K(x)$ and $\Phi^{K'}(x)$ are solutions of the following systems of equations:

$$(K) \quad \begin{cases} i\hbar\omega_c \hat{a}\phi_B^K(x) = E\phi_A^K(x) \\ -i\hbar\omega_c \hat{a}^+\phi_A^K(x) = E\phi_B^K(x) \end{cases} , \qquad (K') \quad \begin{cases} i\hbar\omega_c \hat{a}^+\phi_B^{K'}(x) = E\phi_A^{K'}(x) \\ -i\hbar\omega_c \hat{a}\phi_A^{K'}(x) = E\phi_B^{K'}(x) \end{cases} . \tag{2.36}$$

We can now replace the expression of ϕ_A^K ($\phi_B^{K'}$) in the second (first) equation of the system corresponding to valley K (K'):

$$(K) \quad \begin{cases} \phi_A^K(x) = i\hbar\omega_c \hat{a}\phi_B^K(x)/E \\ \hbar^2\omega_c^2 \hat{N}\phi_B^K(x) = E^2\phi_B^K(x) \end{cases}, \qquad (K') \quad \begin{cases} \hbar^2\omega_c^2 \hat{N}\phi_A^{K'}(x) = E^2\phi_A^{K'}(x) \\ \phi_B^{K'}(x) = -i\hbar\omega_c \hat{a}\phi_A^{K'}(x)/E \end{cases}, \tag{2.37}$$

which allows us to define the number operator $\hat{N} = \hat{a}^\dagger\hat{a}$. From Eq. (2.37) we see now that the components $\phi_B^K(x)$ (in the K valley) and $\phi_A^{K'}$ (in the K' valley) obey the eigenvalue problem of a harmonic oscillator, and as such are the eigenfunctions ϕ_n, associated to quantum number n, of the number operator $\hat{N}$. The second component of the spinor is obtained by applying the annihilation operator on the first one, so that it is the $(n-1)$th eigenfunction of the same harmonic oscillator. For $n \neq 0$ the eigenstates are:

$$\Phi_n^K(x) = \frac{1}{\sqrt{2}}\begin{pmatrix} \phi_{n-1}(x-x_0) \\ \phi_n(x-x_0) \end{pmatrix}, \quad \Phi_n^{K'}(x) = \frac{1}{\sqrt{2}}\begin{pmatrix} \phi_n(x-x_0) \\ \phi_{n-1}(x-x_0) \end{pmatrix}. \tag{2.38}$$

The factor of $\frac{1}{\sqrt{2}}$ comes from imposing that the set of eigenstates in Eq. (2.38) be an orthonormal set:

$$\langle \Phi_n^{K/K'} | \Phi_m^{K/K'} \rangle = \frac{1}{2}\left(\langle \phi_n | \phi_m \rangle + \langle \phi_{n-1} | \phi_{m-1} \rangle\right) = \frac{1}{2}(\delta_{n,m} + \delta_{n-1,m-1}) = \delta_{n,m}\,, \tag{2.39}$$

with $n, m \neq 0$, where we used the orthonormality of the eigenstates of the harmonic oscillator:

$$\langle \phi_n(x) | \phi_m(x) \rangle = \delta_{n,m}. \tag{2.40}$$

The only exception is for $n = 0$, where one of the two components becomes null and the wave function is completely localized on sublattice B for the K valley and A for the K' valley. In order to have normalized states, the normalization factor is now equal to one:

$$\Phi_0^K = \begin{pmatrix} 0 \\ \phi_0(x-x_0) \end{pmatrix}, \qquad \Phi_0^{K'} = \begin{pmatrix} \phi_0(x-x_0) \\ 0 \end{pmatrix}, \tag{2.41}$$

$$\langle \Phi_0^{K/K'} | \Phi_0^{K/K'} \rangle = \langle \phi_0 | \phi_0 \rangle = 1\,, \tag{2.42}$$

however, this does not change the fact that $\Phi_0^{K/K'}$ are still orthogonal to all other states with $n > 0$:

$$\langle \Phi_0^{K/K'} | \Phi_n^{K/K'} \rangle = \langle \phi_0 | \phi_n \rangle = 0\,, \tag{2.43}$$

so that we can generalize the orthonormality condition in Eq. (2.39) for all $n, m \in \mathbb{N}$.

2.2.2 Landau levels and HIQH effect

We saw how the eigenvalue problems of the Hamiltonians in Eq. (2.34) and (2.35) can be reduced to solving the eigenvalue problem of a harmonic oscillator. From the same argument, we find the values of the quantized energies. The following equation for ϕ_B^K (equivalently for $\phi_A^{K'}$), extracted from Eq. (2.36),

$$\hbar^2\omega_c^2 \hat{N}\phi_B^K(x) = E^2\phi_B^K(x) \tag{2.44}$$

tells us that the square values of the energies are eigenvalues of the number operator $\hat{N}$. As such they are proportional to the quantum number n:

$$E_n^2 = \hbar^2\omega_c^2 n \rightarrow E_n = \pm\hbar\omega_c\sqrt{n}\,. \tag{2.45}$$

The values shown in Eq. (2.45) now correspond to the energies of the Landau levels in bulk graphene. Notice that these present a few main differences from the Landau levels of the usual quantum Hall effect that occurs in traditional GaAs/AlGaAs heterostructures. Firstly, there is no zero point energy, and $E_0 = 0$ for quantum number $n = 0$. Secondly, the energy of the system is allowed to be negative and presents no lower bound, so that there is an infinite number of states with negative energy[1]. Furthermore, the actual energy of the system is not directly proportional to n but to its square root. Because of this, the separation between Landau levels is not constant as it is for other 2DEG (e.g. in GaAs/AlGaAs heterostructures), but instead decreases as the absolute value of the energy increases. Last but not least, each value of the energy is degenerate not only in the spin degree of freedom but also in the valley pseudospin. Because of this, each Landau level presents a total fourfold degeneracy and SU(4) symmetry. This last characteristic specifically explains the typical HIQH effect in graphene mentioned in Sec. 1.2.1. Indeed, considering that the four eigenvalues for $n = 0$ lie on the Fermi energy ($E_0 = 0$), half of them will be occupied at neutral conditions, while the other half will be available for transport. As the energy of an injected carrier inside the device reaches E_n, the subsequent states will become available four at a time, giving rise to an occupation number:

$$\nu = 4\left(n + \frac{1}{2}\right), \tag{2.46}$$

which ultimately explains the formula of the quantized Hall conductivity in graphene, previously introduced in Eq. (1.4).

When we also introduce a mass term M to the system, as seen in Section (2.1.2), the Hamiltonians for the K and K' valley from Eq. (2.34) and (2.35) are modified as follows:

$$\hat{H} = \begin{pmatrix} M & i\hbar\omega_c\hat{a} \\ -i\hbar\omega_c\hat{a}^\dagger & -M \end{pmatrix} \quad (K), \tag{2.47}$$

$$\hat{H} = \begin{pmatrix} M & i\hbar\omega_c\hat{a}^\dagger \\ -i\hbar\omega_c\hat{a} & -M \end{pmatrix} \quad (K'). \tag{2.48}$$

Although this does not change the eigenfunctions of $\hat{H}$, it does change their eigenvalues:

$$E_n = \pm\sqrt{\hbar^2\omega_c^2 n + M^2}, \tag{2.49}$$

so that the Landau levels for $n = 0$ (LL_0^+ and LL_0^-) split. The energy gap between them is still $E_g = 2M$, as in the tight-binding model without a magnetic field. This aspect is fundamental for nanodevices with implementation in valleytronics, as previously explained in Sec. 1.2.2. In fact, the consequence of Eq. (2.49) is that for $n = 0$ (and only for $n = 0$) the valley degeneracy of LL_0 is lifted, and states belonging to the two valleys can be distinguished: one will be positive (K) while the other one will be negative (K').

2.2.3 Edge states in graphene nanoribbons

The calculations in the previous sections are valid in 'bulk' graphene, i.e. considering an infinite layer with no bounds: the situation changes when treating graphene ribbons. A graphene ribbon

[1] This is equivalent to what happens for the solution of the Dirac equation for relativistic particles: here, instead of having a Dirac sea of antiparticles with negative energies, we have holes occupying the valence band below the reference value of the Fermi energy of graphene.

is defined by an infinite length in one direction and a limited width L in the other, and the edges of the ribbon are made up of unsaturated carbon atoms presenting only two bonds. Depending on the orientation of the lattices, the edges of the ribbon can either be zigzag-shaped or armchair-shaped, as illustrated in Fig. 2.2(a). In the first case, the terminating unsaturated atoms of an edge all belong to the same sublattice, let's say lattice A. Depending on the number of vertical strips of the ribbon, the atoms of the second edge may belong either to the same sublattice A or to the other, B. In the armchair case instead, each edge consists of alternating atoms from both sublattices: half of them will be A and the other half will be B.

The specifics of the calculations and the shape of the electronic wave functions in each case are determined by the boundary conditions that need to be introduced. Let's first briefly consider the zigzag case: if the terminating atoms of one edge belong to sublattice A, this means that there's a phantom strip of B atoms just outside the ribbon in which the wave function must vanish. This introduces a boundary condition such that the B-component of the wave function goes to zero at the edge. Vice versa, the A-component should go to zero if the boundary atoms belong to the B sublattice. This solution does not admix the valley degrees of freedom, meaning that the solutions of the eigenvalue problem maintain the K/K' valley as a good quantum number. The specific calculations for the zigzag ribbon are reported in Ref. [90]. Our calculations from now on will follow instead the case of the armchair ribbon in the IQH effect, since it follows directly from the calculations of the previous sections and is more interesting in the scope of valleytronics.

Let's consider an infinite armchair ribbon in the y direction, with finite width L_x in the x direction. More specifically, let's define two boundaries at positions $x_L = 0$ and $x_R = L_x$. Since the boundary atoms belong to both the A and B sublattices, the boundary conditions require that the

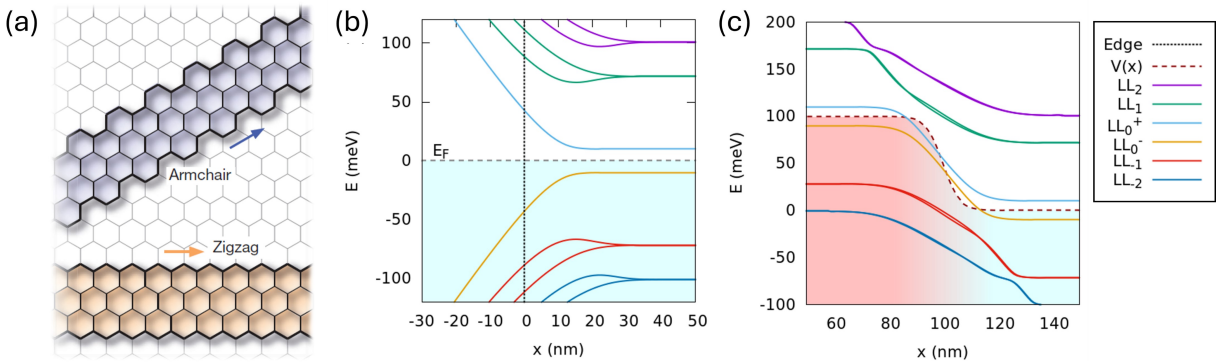


Figure 2.2: (a) Comparison between armchair and zigzag nanoribbons in monolayer graphene. (b) Landau levels at the edge of an armchair nanoribbon defined in $x \in [0, 200]$ nm in the presence of a magnetic field $B = 5$ T orthogonal to the nanoribbon and a mass-induced energy gap $E_g = 20$ meV. The vertical dotted line indicates the position of the edge. The blue region represents energies below the Fermi energy. (c) Landau levels far from the edges and in the proximity of an electrostatic barrier with height $\Delta V = 100$ meV and slope $S = 0.33\,\mathrm{nm}^{-1}$, with same magnetic field and gap as in (b). The red dashed line shows the potential profile along x; the red and blue regions represent respectively the p and n regions of the junction. Panel (a) was taken from [134]; panels (b) and (c) were taken from [3].

total electronic wave function of the system vanishes on both sublattices at each edge:

$$\begin{cases} \psi_A(0,y) = 0 \\ \psi_B(0,y) = 0 \\ \psi_A(L_x,y) = 0 \\ \psi_B(L_x,y) = 0 \end{cases} . \tag{2.50}$$

Here the components of spinor $\Psi(x,y)$ are a specific combination [117] of the solutions of the effective one-dimensional Hamiltonians for the K and K' valleys:

$$\begin{cases} \psi_A(x,y) = \frac{1}{\sqrt{2}} \left(e^{i\mathbf{K}\cdot\mathbf{r}} \psi_A^K(x,y) - i e^{i\mathbf{K'}\cdot\mathbf{r}} \psi_A^{K'}(x,y) \right) \\ \psi_B(x,y) = \frac{1}{\sqrt{2}} \left(i e^{i\mathbf{K}\cdot\mathbf{r}} \psi_B^K(x,y) + e^{i\mathbf{K'}\cdot\mathbf{r}} \psi_B^{K'}(x,y) \right) \end{cases} . \tag{2.51}$$

In this way, it naturally follows that the conditions in Eq. (2.50) become:

$$\begin{cases} \psi_A^K(0,y) = i\psi_A^{K'}(0) \\ \psi_B^K(0,y) = i\psi_B^{K'}(0) \\ \psi_A^K(L_x,y) = i e^{i(K'_x - K_x)L_x} \psi_A^{K'}(L_x) \\ \psi_B^K(L_x,y) = i e^{i(K'_x - K_x)L_x} \psi_B^{K'}(L_x) \end{cases} , \tag{2.52}$$

where we used the fact that $K_y = K'_y$ to simplify the exponential phase factor in y. Notice that the states in Eq. (2.51) are no longer defined by the valley quantum number, since they are a complete superposition of the states in the K and K' valley. Because of this, it is said that the boundary conditions of an armchair ribbon impose an admixing of the valleys.

The way to treat the particular conditions in Eq. (2.52) numerically consists in working in an extended real space $x \in [-L_x, L_x]$. We need to define a two-component spinor in the sublattice quantum number, $\varphi(x,y)$, built as a function of the K valley and K' valley spinors:

$$\varphi(x,y) = \begin{cases} e^{iK_x x} \Psi^K(x,y) & 0 \leq x \leq L_x \\ e^{iK'_x x} \Psi^{K'}(-x,y) & -L_x \leq x < 0 \end{cases} . \tag{2.53}$$

In practice, $\varphi(x,y)$ is equal to the solution in the K valley for positive values of x, and it is specular to the one in the K' valley for negative values of x. The boundary conditions previously imposed for $\Psi(x,y)$ now directly translate to $\varphi(x,y)$ being continuous in $x = 0$ and periodic in $[-L_x, L_x]$:

$$\varphi(L_x,y) = \varphi(-L_x,y) . \tag{2.54}$$

Because of how it is defined, this wave function is the eigenvalue of a 2×2 Hamiltonian in the sublattice degree of freedom, which follows from combining the effective Hamiltonians in Eq. (2.13) and (2.14). Remember that the $\Psi^{K'}$ component is mirrored in the x direction, such that $q_x \to -q_x$ in Eq. (2.14). The relative phase factors with respect to K_x and K'_x are taken into account when considering the actual wave vector $\mathbf{k}$ in the expression instead of the relative one $\mathbf{q}$ introduced for the calculations in the previous sections. We also need to take account of the specular nature of the whole space in $[-L_x, L_x]$, so that $x \to |x|$. For the most general case, we set $M \neq 0$ and introduce an external electric potential $V(|x|,y)$ as a diagonal term in the Hamiltonian. That said, the final eigenvalue problem for $\varphi(x,y)$ becomes:

$$\begin{pmatrix} V(|x|,y) + M & \hbar v_F \left(-k_x + ik_y\right) \\ \hbar v_F \left(-k_x - ik_y\right) & V(|x|,y) - M \end{pmatrix} \begin{pmatrix} \varphi_A(x,y) \\ \varphi_B(x,y) \end{pmatrix} = E \begin{pmatrix} \varphi_A(x,y) \\ \varphi_B(x,y) \end{pmatrix} . \tag{2.55}$$

After discussing how to treat the boundary conditions of a graphene armchair ribbon, we can now introduce the magnetic field $\mathbf{B} = B\hat{\mathbf{z}}$ and proceed in the same way we did for bulk graphene. As such, we use again the Landau gauge $\mathbf{A} = B(0, |x|, 0)$, where the absolute value must be introduced to take account of the specular nature of the problem in the x direction. We perform the Peierls substitution in the Hamiltonian, $\mathbf{k} \to \mathbf{k} + e\mathbf{A}/\hbar$:

$$\hat{H} = \begin{pmatrix} V(|x|, y) + M & \hbar v_F \left(-k_x + ik_y + i\frac{eB|x|}{\hbar}\right) \\ \hbar v_F \left(-k_x - ik_y - i\frac{eB|x|}{\hbar}\right) & V(|x|, y) - M \end{pmatrix} . \tag{2.56}$$

Then, we consider a separable *ansatz* for $\varphi(x, y)$ with a plane wave on the y direction:

$$\varphi_\mu(x, y) = e^{ik_y y}\varphi_\mu(x), \quad \mu = A, B, \tag{2.57}$$

$$\varphi(x) = \begin{pmatrix} \varphi_A(x) \\ \varphi_B(x) \end{pmatrix} , \tag{2.58}$$

with the x-component continuous in the whole space and periodic in $[-L_x, L_x]$:

$$\varphi(L_x) = \varphi(-L_x). \tag{2.59}$$

Eventually if the potential V is separable,

$$V(|x|, y) = V_x(|x|) + V_y(y) , \tag{2.60}$$

the equation in Eq. (2.55) transforms into an effective one-dimensional problem for $\varphi(x)$:

$$\begin{pmatrix} V_x(|x|) + M & iv_F \left(\frac{\partial}{\partial x} + \frac{1}{l_m^2}(|x| - x_0)\right) \\ iv_F \left(\frac{\partial}{\partial x} - \frac{1}{l_m^2}(|x| - x_0)\right) & V_x(|x|) - M \end{pmatrix} \begin{pmatrix} \varphi_A(x) \\ \varphi_B(x) \end{pmatrix} = E \begin{pmatrix} \varphi_A(x) \\ \varphi_B(x) \end{pmatrix} . \tag{2.61}$$

When the electron is located far enough from the ribbon edges, i.e. when the center of the wave function x_0 is located in 'bulk', and the potential is zero, the solutions of Eq. (2.61) are similar to the ones shown in Eq. (2.38), (2.41), and (2.49), valid for an infinite monolayer of graphene with $M \neq 0$. Instead, as illustrated in Fig. 2.2(b), the eigenvalues (and eigenfunctions) start to change as soon as the electron moves towards the edges of the ribbon: in this case we talk about edge states. Here the Landau levels, which presented no dispersion in bulk, are bent and their energies start depending on k_y, the wave vector along y, which in turn is coupled to the x coordinate,

$$x = -\frac{\hbar k_y}{eB} . \tag{2.62}$$

Because of this dispersion, the edge states now present a group velocity that is proportional to the slope of the bands,

$$v_g(k) = -\frac{1}{\hbar}\frac{\partial E(k_y)}{\partial k_y} . \tag{2.63}$$

The sign of v_g depends on whether the bands are above or below the Fermi energy: in fact, a Landau level with positive energy will bend upwards, while one at negative energy will bend downwards. This brings an opposite sign to v_g depending on whether we consider the propagation of an electron or a hole along the edges. Reasonably, under the presence of $\mathbf{B}$ particles with opposite charges will move in opposite directions.

Fig. 2.2(c) shows us that the bands bend also when in the presence of an additional potential term along x. However, the potential $V(x)$ only introduces a local shift of the Fermi energy, and both bands bend the same way, thus implying the same transport direction both for negative and positive carriers. We will see later in Chapter 3 what this implies for carrier dynamics. Specifically, in our simulations we introduce a smooth Fermi-like potential barrier:

$$V(x) = V_0 + \Delta V \frac{1}{e^{-Sx} + 1}, \tag{2.64}$$

where V_0 is an arbitrary reference value, ΔV is the height of the barrier, and S is its slope. This kind of potential better reproduces realistic barriers present in actual devices [135, 136], rather than a sharp one. This can be seen by fitting the potential obtained from realistic simulations with the formula in Eq. (2.64), as is shown in Fig. 2.3. Indeed, although the sharpness of the barrier can be controlled by the distance of the top gate from the device [113, 126], it is almost impossible to completely eliminate the smoothness of the potential profile and the phenomena causing it [126].

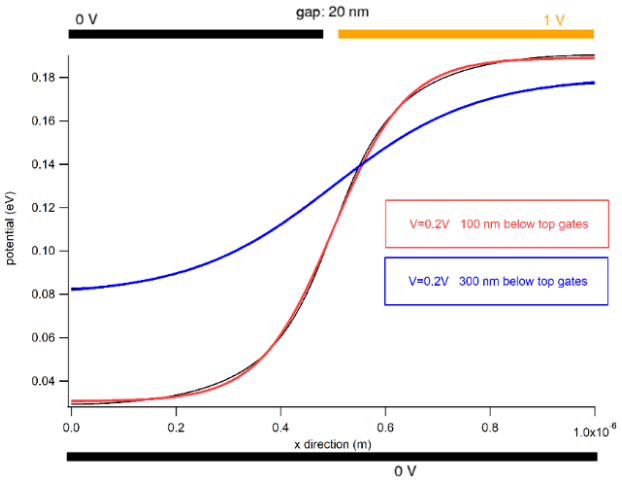


Figure 2.3: Profile of the potential barrier obtained through self-consistent Poisson simulations (black) compared to a Fermi-like barrier (red/blue), for two different distances between the graphene nanoribbon and the top gates.

2.3 Time-dependent simulations of edge-state wavepackets

2.3.1 State initialization: Gaussian wavepackets

To simulate single-carrier dynamics inside a device implemented in graphene nanoribbons, we need to define a localized wavepacket as the initial state of our particle. Looking at the *ansatz* in Eqs. (2.57-2.58), we see that a single edge state is represented by a plane wave along the y direction, $e^{ik_y y}$, and is delocalized. Consequently, in order to build a localized packet, we need to consider a linear combination of multiple edge states. Considering a carrier injected in the n-th Landau level, the particle's initial state can thus be defined as:

$$\varphi_n(x,y) = \frac{1}{\sqrt{2\pi}} \int dk F(k_y) \varphi_{n,k_y}(x) e^{ik_y y}. \tag{2.65}$$

where $F(k_y)$ is a generic weight function defining the shape of the packet in momentum space. From this moment on we will focus on the case for $n = 0$, corresponding to the occupation of only the Landau levels closest to the Fermi energy. In a region in which the Landau levels have an approximately linear dispersion, e.g. for $x_0 < 0$ (see Fig. 2.2(b)), the weight function $F(k_y)$ has the same shape as the distribution of the packet in energy, $F(E)$. Within this region, the group velocity defined in Eq. (2.63) is also approximately constant for every k_y-component, meaning that the dispersion of the wavepacket is suppressed compared to other regions with non-linear dispersion of the bands. Additionally, in the following we will choose a Gaussian weight function, which, according to previous equivalent studies on edge states in GaAs/AlGaAs heterostructures [32, 40, 137] preserves its shape in time more efficiently rather than, say, a Lorentzian or exponential

distribution. Additionally, this shape accurately reproduces carriers injected by various single-electron sources for semiconductor-based flying qubits, such as those produced by quantum dot pumps [8, 46, 47, 138, 139]. The chosen weight function is:

$$F(k_y) = \sqrt[4]{\frac{2\sigma^2}{\pi}} e^{(-\sigma^2(k_y-k_0)^2)} e^{-ik_y y_0}\,, \tag{2.66}$$

where y_0 is the initial position of the wavepacket in real space, and k_0 is the central wave vector of the weight function in momentum space. Notice that from the formula above we can define $\sigma_k = 1/\sqrt{2}\sigma$ as the standard deviation in momentum space. In first approximation, considering that the shape of the edge states along x only slightly changes depending on the value of k, the shape of the wavepacket along y is given by the Fourier transform of the weight function in Eq. (2.66), and consequently possesses a Gaussian shape with real-space standard deviation σ. Additionally, remembering from Eq. (2.62), the values of the real-space coordinate x and momentum k_y are coupled, meaning that in first approximation we can associate the weight function in Eq. (2.66) to a wavepacket centered along the x direction around position $x_0 = -\frac{hk_0}{eB}$.

Note that in order for the initialization of the wavepacket to be applicable in these terms, the carrier must be localized completely in a region in which $V(|x|, y)$ is translationally invariant with respect to the y direction. Indeed, the shape $\varphi_{n,k_y}(x)$ of the wavepacket along x present in Eq. (2.65), is evaluated numerically as the solution of the 1D eigenvalue problem in Eq. (2.61), in which the quantity of $V_x(|x|)$ is the shape of the total potential at fixed $y = y_0$. Consequently, in order for $\varphi_{n,k_y}(x)$ to remain an eigenfunction of the 1D Hamiltonian of the system for the whole extension of the wavepacket in y, we must have $V(|x|, y) \equiv V_x(|x|)$ in the whole region in which the carrier is initialized.

Wave packet method for the analysis of the wave function

At any point during the evolution of the particle, the wavepacket may undergo scattering processes that modify its weight function to a new one, $F'(k_y)$, meaning that the final wavepacket can be rewritten as:

$$\varphi'_n(x, y) = \frac{1}{\sqrt{2\pi}} \int dk F'(k_y) \varphi_{n,k_y}(x) e^{ik_y y}\,. \tag{2.67}$$

Specifically, let's consider an elastic scattering process in which the energy of the carrier is conserved, meaning $F(E) = F'(E)$. In this scenario, the carrier can be either transmitted or reflected, so that we can define the weight functions of the respective parts as $F'_T(k_{y,T})$ and $F'_R(k_{y,R})$. The values of $k_{y,T}$ and $k_{y,R}$ are the wave vectors corresponding to energy E for each parts. Notice that, depending on the potential landscape that the transmitted and reflected parts of the packet feel, the values of $k_{y,T}$ and $k_{y,R}$ may generally differ from one another and from the initial wave vector k_y. The transmission and reflection probabilities for energy E are then defined respectively as

$$T(E) = \frac{|F'_T(k_{y,T})|^2}{|F(k_y)|^2}\,, \quad R(E) = \frac{|F'_R(k_{y,R})|^2}{|F(k_y)|^2}\,, \tag{2.68}$$

for which the condition for energy conservation imposes $T(E) + R(E) = 1$. In order to find the transmitted and reflected weight functions we resort to the so-called wave packet method [140], which consists of the Fourier analysis of the final state of the carrier. Specifically, we start by performing the Fourier transform of the final state $\varphi(x, y)$ along the y direction alone, basically by

projecting the state on a plane wave along y. Considering without loss of generality the transmitted wavepacket:

$$\begin{aligned}\tilde{\varphi}_T(x,k_{y,T}) =& \frac{1}{\sqrt{2\pi}}\int dy e^{-ik_{y,T}y}\varphi_T(x,y) = \\ =& \int dk F'_T(k_y)\varphi_k(x)\frac{1}{2\pi}\int dy e^{i(k_{y,T}-k)} = \\ =& \int dk F'_T(k_y)\varphi_k(x)\delta(k_{y,T}-k) = \\ =& F'_T(k_{y,T})\varphi_{k_{y,T}}(x)\,. \end{aligned} \tag{2.69}$$

Finally, we project the obtained function on the edge state $\varphi_{k_{y,T}}(x)$, which is normalized to one:

$$\int dx \varphi^*_{k_{y,T}}(x)\tilde{\varphi}_T(x,k_{y,T}) = F'_T(k_{y,T})\int dx \varphi^*_{k_{y,T}}(x)\varphi_{k_{y,T}}(x) = F'_T(k_{y,T})\,. \tag{2.70}$$

2.3.2 Split-step Fourier method in graphene

Once the initial state of the system is defined, its temporal evolution is obtained by integrating the time-dependent Schrödinger equation, which for a generic, spinless wave function $\Psi(\mathbf{r})$ reads:

$$\frac{\partial}{\partial t}\Psi(\mathbf{r};t) = -\frac{i}{\hbar}H\Psi(\mathbf{r};t)\,. \tag{2.71}$$

Calling $\Psi(\mathbf{r};t_0)$ the electronic wave function at an initial time t_0, the final wave function at time $t_0+\Delta t$ is obtained through the application of an evolution operator $U(\Delta t)$:

$$\Psi(\mathbf{r};t_0+\Delta t) = U(\Delta t)\Psi(\mathbf{r};t_0)\,, \tag{2.72}$$

which depends on the Hamiltonian of the system. In our case, since $\hat{H}$ is independent of time, the expression of $\hat{U}(\Delta t)$ becomes:

$$U(\Delta t) = e^{-\frac{i}{\hbar}H\Delta t}\,. \tag{2.73}$$

At this point, in order to apply this evolution operator numerically one can exploit the split-step Fourier method. This procedure is usually carried out and is well known for systems described by one-component wave functions. However, the system of graphene nanoribbons that we study is described by a spinor on the sublattice isospin basis, and the usual split-step method needs to be adapted accordingly, as explained below.

The electronic wave function we want to evolve in time is $\varphi(x,y)$, introduced in Eq. (2.53). This is the eigenfunction of the 2×2 non-diagonal block Hamiltonian of Eq. (2.56) in the sublattice basis. This can be written as the sum of specific diagonal and off-diagonal terms:

$$\begin{aligned}\hat{H} =& V(|x|,y)\begin{pmatrix}1&0\\0&1\end{pmatrix} + M\begin{pmatrix}1&0\\0&-1\end{pmatrix} - \hbar v_F k_x\begin{pmatrix}0&1\\1&0\end{pmatrix} - \hbar v_F\left(k_y+\frac{|x|}{l_m^2}\right)\begin{pmatrix}0&-i\\i&0\end{pmatrix} = \\ =& V(|x|,y)\hat{\mathbb{1}} + M\hat{\sigma}_3^{AB} - \hbar v_F k_x\hat{\sigma}_1^{AB} - \hbar v_F k_y\hat{\sigma}_2^{AB} - \frac{\hbar v_F}{l_m^2}|x|\,\hat{\sigma}_2^{AB} = \\ =& \hat{V} + \hat{T}_x + \hat{T}_y + \hat{V}_B\,. \end{aligned} \tag{2.74}$$

In Eq. (2.74), $\hat{\sigma}_1^{AB}$, $\hat{\sigma}_2^{AB}$ and $\hat{\sigma}_3^{AB}$ are the Pauli matrices on the sublattice isospin and l_m is the magnetic length from Eq. (2.31). The operator $\hat{V}$ is a diagonal potential term, which includes both the

diagonal potential term, $V(|x|,y)\hat{\mathbb{1}}$, and the mass term $M\hat{\sigma}_3^{AB}$. $\hat{T}_x$ and $\hat{T}_y$ are the kinetic operators in the x and y directions respectively, and are linear in k_y and k_x. Finally, $\hat{V}_B$ takes the name of magnetic potential: it only appears in the presence of an external magnetic field, is linear in $|x|$, and is directly proportional to B.

Notice that both kinetic operators in Eq. (2.74) only depend on the wave vector components, k_x and k_y respectively. This means that there is no coupling between the wave vectors and the spatial coordinates, in contrast to what happened for 2DEG in gapped materials. In the latter case in fact, the parabolic dispersion of the bands introduced the square of $(k_y + \frac{eBx}{\hbar})$ and consequently a double product proportional to $k_y x$ in the Hamiltonian. This does not happen in the case of graphene because of the absence of the square: that is to say, because the bands have linear dispersion near the Dirac cones.

Following from Eq. (2.74), the Trotter-Suzuki factorization tells us that for an infinitesimal time-step δt the wave function $\varphi(x,y;t)$ evolves with the following approximation of $\hat{U}(\delta t)$:

$$\varphi(x,y;t+\delta t) = \hat{U}(\delta t)\varphi(x,y;t) \tag{2.75}$$

$$\hat{U}(\delta t) = e^{-\frac{i}{\hbar}\hat{H}\delta t} = F^{-1}e^{-\frac{i}{\hbar}\hat{T}_x\delta t}e^{-\frac{i}{\hbar}\hat{T}_y\delta t}Fe^{-\frac{i}{\hbar}\hat{V}_B\delta t}e^{-\frac{i}{\hbar}\hat{V}\delta t} + \mathcal{O}(\delta t^2)\,, \tag{2.76}$$

where F is the two-dimensional Fourier transform,

$$F\varphi(x,y) \equiv \frac{1}{2\pi}\int_{-\infty}^{+\infty} e^{-i\mathbf{k}\cdot\mathbf{r}}\varphi(x,y)\,d\mathbf{r} = \tilde{\varphi}(k_x,k_y)\,, \tag{2.77}$$

used to apply the kinetic operators directly in momentum space, where the k_x and k_y operators are diagonal. F^{-1} is the inverse Fourier transform, used to go back to real space:

$$F^{-1}\tilde{\varphi}(k_x,k_y) \equiv \frac{1}{2\pi}\int_{-\infty}^{+\infty} e^{i\mathbf{k}\cdot\mathbf{r}}\tilde{\varphi}(k_x,k_y)\,d\mathbf{k} = \varphi(x,y)\,. \tag{2.78}$$

Looking at Eq. (2.76), the exponentiation of the block-diagonal potential operator is trivial:

$$\begin{aligned}\exp\left(-\frac{i}{\hbar}\hat{V}\delta t\right) &= \exp\begin{pmatrix} -\frac{i}{\hbar}(V(|x|,y)+M)\delta t & 0 \\ 0 & -\frac{i}{\hbar}(V(|x|,y)-M)\delta t\end{pmatrix} = \\ &= \begin{pmatrix} e^{-\frac{i}{\hbar}(V(|x|,y)+M)\delta t} & 0 \\ 0 & e^{-\frac{i}{\hbar}(V(|x|,y)-M)\delta t}\end{pmatrix}.\end{aligned} \tag{2.79}$$

On the contrary, the exponentiation of the magnetic potential and kinetic terms is less trivial, and results in non-diagonal operators:

$$\exp\left(-\frac{i}{\hbar}\hat{V}_B\delta t\right) = \exp\begin{pmatrix} 0 & \frac{v_F}{l_m^2}|x|\,\delta t \\ -\frac{v_F}{l_m^2}|x|\,\delta t & 0\end{pmatrix} = \begin{pmatrix} \cos\left(\frac{v_F}{l_m^2}|x|\,\delta t\right) & \sin\left(\frac{v_F}{l_m^2}|x|\,\delta t\right) \\ -\sin\left(\frac{v_F}{l_m^2}|x|\,\delta t\right) & \cos\left(\frac{v_F}{l_m^2}|x|\,\delta t\right)\end{pmatrix}; \tag{2.80}$$

$$\exp\left(-\frac{i}{\hbar}\hat{T}_y\delta t\right) = \exp\begin{pmatrix} 0 & v_F k_y\delta t \\ -v_F k_y\delta t & 0\end{pmatrix} = \begin{pmatrix} \cos\left(v_F k_y\delta t\right) & \sin\left(v_F k_y\delta t\right) \\ -\sin\left(v_F k_y\delta t\right) & \cos\left(v_F k_y\delta t\right)\end{pmatrix}; \tag{2.81}$$

$$\exp\left(-\frac{i}{\hbar}\hat{T}_y\delta t\right) = \exp\begin{pmatrix} 0 & iv_F k_x\delta t \\ iv_F k_x\delta t & 0\end{pmatrix} = \begin{pmatrix} \cos\left(v_F k_x\delta t\right) & i\sin\left(v_F k_x\delta t\right) \\ i\sin\left(v_F k_x\delta t\right) & \cos\left(v_F k_x\delta t\right)\end{pmatrix}. \tag{2.82}$$

Now that we have defined the shape of the evolution operators, let's look more in detail at each step of the Trotter-Suzuki factorization. First, we apply the block-diagonal operator in Eq. (2.79) to the spinor wave function $\varphi(x,y)$: since the operator is block-diagonal on the sublattice degree of freedom, the A and B components evolve separately.

$$\begin{pmatrix} \varphi'_A(x,y) \\ \varphi'_B(x,y) \end{pmatrix} = \begin{pmatrix} e^{-\frac{i}{\hbar}(V(|x|,y)+M)\delta t} & 0 \\ 0 & e^{-\frac{i}{\hbar}(V(|x|,y)-M)\delta t} \end{pmatrix} \begin{pmatrix} \varphi_A(x,y;t) \\ \varphi_B(x,y;t) \end{pmatrix}$$

$$\rightarrow \begin{cases} \varphi'_A(x,y) = e^{-\frac{i}{\hbar}(V(|x|,y)+M)\delta t}\varphi_A(x,y;t) \\ \varphi'_B(x,y) = e^{-\frac{i}{\hbar}(V(|x|,y)-M)\delta t}\varphi_B(x,y;t) \end{cases} \tag{2.83}$$

The second step then consists of applying the magnetic potential operator in Eq. (2.80), which is non-diagonal in the sublattice basis. Because of its shape, now the evolutions of φ_A and φ_B are coupled. In other words, the shape of one component at the end of the step also depends on the shape of the other at the previous step:

$$\begin{cases} \varphi''_A(x,y) = \cos\left(\frac{v_F}{l_m^2}|x|\,\delta t\right)\varphi'_A(x,y) + \sin\left(\frac{v_F}{l_m^2}|x|\,\delta t\right)\varphi'_B(x,y) \\ \varphi''_B(x,y) = \cos\left(\frac{v_F}{l_m^2}|x|\,\delta t\right)\varphi'_B(x,y) - \sin\left(\frac{v_F}{l_m^2}|x|\,\delta t\right)\varphi'_A(x,y)\,. \end{cases} \tag{2.84}$$

At this point, both components of the wave functions are transformed in momentum space with a two-dimensional Fourier transform:

$$\begin{cases} \tilde{\varphi}_A(k_x,k_y) = \frac{1}{2\pi}\int_{-\infty}^{+\infty} e^{-i\mathbf{k}\cdot\mathbf{r}}\varphi''_A(x,y)\,d\mathbf{r} \\ \tilde{\varphi}_B(k_x,k_y) = \frac{1}{2\pi}\int_{-\infty}^{+\infty} e^{-i\mathbf{k}\cdot\mathbf{r}}\varphi''_B(x,y)\,d\mathbf{r} \end{cases} \tag{2.85}$$

and the kinetic operators in Eq. (2.81-2.82) can be applied. These are also non-diagonal in the sublattice basis, thus coupling once again the A and B components of the spinor. For the kinetic operator in k_y:

$$\begin{cases} \tilde{\varphi}'_A(k_x,k_y) = \cos\left(v_F k_y \delta t\right)\tilde{\varphi}_A(k_x,k_y) + \sin\left(v_F k_y \delta t\right)\tilde{\varphi}_B(k_x,k_y) \\ \tilde{\varphi}'_B(k_x,k_y) = \cos\left(v_F k_y \delta t\right)\tilde{\varphi}_B(k_x,k_y) - \sin\left(v_F k_y \delta t\right)\tilde{\varphi}_A(k_x,k_y) \end{cases} ; \tag{2.86}$$

and for the kinetic operator in k_x:

$$\begin{cases} \tilde{\varphi}''_A(k_x,k_y) = \cos\left(v_F k_x \delta t\right)\tilde{\varphi}'_A(k_x,k_y) + i\sin\left(v_F k_x \delta t\right)\tilde{\varphi}'_B(k_x,k_y) \\ \tilde{\varphi}''_B(k_x,k_y) = \cos\left(v_F k_x \delta t\right)\tilde{\varphi}'_B(k_x,k_y) - i\sin\left(v_F k_x \delta t\right)\tilde{\varphi}'_A(k_x,k_y) \end{cases} . \tag{2.87}$$

Finally, the system is brought back to real space and the wave function at time $t+\delta t$ is obtained.

$$\begin{cases} \varphi_A(x,y;t+\delta t) = \frac{1}{2\pi}\int_{-\infty}^{+\infty} e^{i\mathbf{k}\cdot\mathbf{r}}\tilde{\varphi}''_A(k_x,k_y)\,d\mathbf{k} \\ \varphi_B(x,y;t+\delta t) = \frac{1}{2\pi}\int_{-\infty}^{+\infty} e^{i\mathbf{k}\cdot\mathbf{r}}\tilde{\varphi}''_B(k_x,k_y)\,d\mathbf{k} \end{cases} \tag{2.88}$$

Overall, the shape of the operators in Eq. (2.81-2.82) implies that the evolution of the components of $\varphi(x,y)$ on the two sublattices A and B cannot be separated. It is then of fundamental importance to carry out the evolution of both components at the same time.

The Trotter-Suzuki factorization in Eq. (2.76) can then be modified by splitting the initial evolution in $\hat{V}$ into two half-steps, at the beginning and at the end of the formula:

$$\hat{U}(\delta t) = e^{-\frac{i}{\hbar}\hat{V}\frac{\delta t}{2}}F^{-1}e^{-\frac{i}{\hbar}\hat{T}_x\delta t}e^{-\frac{i}{\hbar}\hat{T}_y\delta t}Fe^{-\frac{i}{\hbar}\hat{V}_B\delta t}e^{-\frac{i}{\hbar}\hat{V}\frac{\delta t}{2}} + \mathcal{O}(\delta t^3)\,. \tag{2.89}$$

This way the error induced by the approximation reduces from $\mathcal{O}(\delta t^2)$ to $\mathcal{O}(\delta t^3)$. Eventually, after N infinitesimal steps, the final wave function at time $t + N\delta t$ would read:

$$\begin{aligned}\varphi(x,y;t+N\delta t) &= \hat{U}(\delta t)^N \varphi(x,y;t) \simeq \\ &\simeq (e^{-\frac{i}{\hbar}\hat{V}\frac{\delta t}{2}} F^{-1} e^{-\frac{i}{\hbar}\hat{T}_x \delta t} e^{-\frac{i}{\hbar}\hat{T}_y \delta t} F e^{-\frac{i}{\hbar}\hat{V}_B \delta t} e^{-\frac{i}{\hbar}\hat{V}\frac{\delta t}{2}})^N \varphi(x,y;t)\,; \end{aligned} \tag{2.90}$$

or equivalently, for a lower number of intermediate steps:

$$\begin{aligned}\varphi(x,y;t+N\delta t) &\simeq \\ &\simeq e^{-\frac{i}{\hbar}\hat{V}\frac{\delta t}{2}} (F^{-1} e^{-\frac{i}{\hbar}\hat{T}_x \delta t} e^{-\frac{i}{\hbar}\hat{T}_y \delta t} F e^{-\frac{i}{\hbar}\hat{V}_B \delta t} e^{-\frac{i}{\hbar}\hat{V}\delta t})^N e^{+\frac{i}{\hbar}\hat{V}\frac{\delta t}{2}} \varphi(x,y;t)\,. \end{aligned} \tag{2.91}$$

Discretization conditions

In Sec. 2.2.3 we saw that for the numerical simulation of a graphene nanoribbon of finite width L_x along x we require an extended simulated real space of width $2L_x$. Therefore, it is useful to define a total number $2N_x$ of grid points in the x coordinate in real space. Defining also L_y and N_y as the length of the ribbon and number of grid points along y, the real-space grids are given as

$$\begin{cases} x_i = -L_x + i\delta x\,, & i = 1,...,2N_x \\ y_i = -L_y/2 + i\delta y\,, & i = 1,...,N_y \end{cases}, \tag{2.92}$$

with $\delta x = L_x/N_x$, $\delta y = L_y/N_y$. Consequently, the reciprocal space coordinates are also quantized as follows:

$$\begin{cases} k_{x,i} = k_{x,min} + i\delta k_x\,, & i = 1,...,2N_x \\ k_{y,i} = k_{y,min} + i\delta k_y\,, & i = 1,...,N_y \end{cases}, \tag{2.93}$$

in which $\delta k_x = 2\pi/2L_x$, $\delta k_y = 2\pi/L_y$, and $k_{x,min} = -\pi/\delta x$, $k_{y,min} = -\pi/\delta y$. The numerical treatment of edge states in armchair nanoribbons also requires periodical boundary conditions along x. These are directly applied inside of our simulations, both along x and y, thanks to the application of the fast Fourier transform algorithm implemented to perform the discrete Fourier transforms [141].

Due to the coupling between coordinates x and k_y seen in Eq. (2.62), each grid point x_i is associated with a wave vector. Consequently, in the presence of a magnetic field, the definition of the real-space and reciprocal-space grid must obey the following additional requirements:

- The wave vector associated to the maximum value of $x = L_x$ is $\bar{k}_{y,max} = eBL_x/\hbar$. Consequently, in order to have an accurate numerical representation in the whole simulated region along x, we must have that $\bar{k}_{y,max} < k_{y,max} = -k_{y,min}$. This in turn imposes a condition on the maximum grid step in y:

$$\delta y < \frac{\hbar\pi}{eBL_x}\,. \tag{2.94}$$

- Since the characteristic length of the system is the magnetic length l_m defined in Eq. (2.31), the grid steps δx and δy must be both smaller than l_m. Otherwise, the eigenstates of the 1D Hamiltonian in Eq. (2.61) found numerically will not represent the edge states accurately.

Additionally, other conditions must apply for the convergence of the split-step Fourier method described in the previous Section:

- In order to accurately describe the physical phenomena occurring inside the device, the time step δt must be much shorter than any time scale of the system's Hamiltonian.
- The exponent of the evolution operators in Eq. (2.76) must be small enough with respect to the period of the exponential, i.e. 2π, so that

$$\delta t \ll \frac{2\pi\hbar}{V_{max}}\,. \tag{2.95}$$

  The previous condition guarantees that every exponent is correctly defined, thanks to the Virial theorem [142].

- The grid steps δx and δy must be smaller than the spatial variations of the wave function, in order for the discretized Fourier transform to be accurate. In other terms, the values of $k_{x,max}$ and $k_{y,max}$ must be higher than the largest wave-vector components of the wavepacket.

In conclusion, the code we implemented starts by numerically finding the eigenstates of the effective one-dimensional Hamiltonian in Eq. (2.61). The partial derivatives are represented through finite difference methods, specifically with the trapezoidal method, and the resulting Hamiltonian, a 2×2 block matrix represented on a grid of $2N_x$ points, is diagonalized using the library ARPACK, which is ideal for dealing with sparse matrices specifically. Then, the linear combination of said eigenstates from Eq. (2.67) is performed on a discretized set of k, and the obtained state is evolved for N steps with the procedure described in Sec. 2.3.2. In the latter passage, the discrete Fourier transforms are performed through the routines of the FFTW library. Finally, the final state is analyzed through the wavepacket method, in which we once again use the ARPACK library to diagonalize the effective one-dimensional Hamiltonian at the final position of the wavepacket. The simulations reported in the next Chapter were performed serially; however, the sections of the code that implement each step of the time evolution, including the fast Fourier transform, can be easily parallelized through the use of the OpenMP library.

The memory required by a single run is relatively low, and consequently allows to simulate large systems with contained computational resources. Indeed, the procedure illustrated above in this Chapter requires the allocation of the two 2D complex wave functions making up the spinor from Eq. (2.53), as well as at least one copy for each, necessary to perform the operations in Eqs. (2.83-2.88). Using double-precision floating-point numbers, this corresponds to a total of $4 \times 2N_x \times N_y \times 16$ bytes: consequently, a reference run with $N_x = 800$ and $N_y = 1600$ occupies ~ 164 MB. For the same reference simulation, the diagonalization of the effective Hamiltonian in Eq. (2.61), used in the construction of the wave function in Eq. (2.65) and for the wavepacket method, takes ~ 3 s for each value of k_y from Eq. (2.93) with an Intel(R) Xeon(R) processor E3-1241 v3 @ 3.50 GHz. As for the dynamical evolution as described in Eqs. (2.89-2.91) with the same parameters and processor, the simulation of 1 ps with a typical time-step value of $\delta t = 5 \cdot 10^{-16}$ s (i.e. $N = 2 \cdot 10^3$ steps) takes approximately half an hours.

Every hundred years, a little bird comes
and sharpens its beak on the diamond mountain.
And when the entire mountain is chiseled away,
the first second of eternity will have passed.

$\sim$ The Twelfth Doctor in *Heaven Sent*,
Doctor Who, S9E11

Chapter 3

Time-resolved Mach-Zehnder interferometry in graphene

In this Chapter we look at the numerical results of our time-dependent simulations of coherent transport in graphene nanoribbons. We start in Sec. 3.1 with the description of single-carrier dynamics, by first analyzing its evolution along the armchair edge in Sec. 3.1.1. In Sec. 3.1.2 we characterize the edge-state vs. snake-state regimes along *pn* junctions in the presence of gate-induced barriers, and in Sec. 3.1.3 we report the observation of Klein tunneling. We then describe the behavior of MZIs in graphene in Sec. 3.2. Specifically, in Sec. 3.2.1 we characterize the behavior of QPCs created through electrostatic barriers, by studying its transmission and reflection curves. We use these QPCs to build an interferometer in Sec. 3.2.2, and study the visibility of Aharonov-Bohm oscillations subjected to phase averaging. Finally, in Sec. 3.2.3 we consider a MZI built with VBSs, and focus on the effect of the shape of the edge channels on the interferometer's visibility.

3.1 Motion of a carrier in graphene nanoribbons

3.1.1 Shape and group velocity of the packet

In this Section we aim at characterizing the evolution of the shape of the wavepacket in time, and the conditions to obtain a high group velocity. For these and all subsequent simulations we fix the magnetic field to $B = 5\,\mathrm{T}$; then, here we momentarily fix the mass term $M = 0\,\mathrm{meV}$. We also fixed $\delta x = \delta y = 0.5\,\mathrm{nm}$, small enough to guarantee a good discretization, but suitable for simulating realistic scales. All other parameters were set by following the guidelines in Sec. 2.3.2. As explained in the previous Chapter, we initialize the electronic wavepacket by building a Gaussian linear combination of edge states, as seen in Eqs. (2.65) and (2.66). Numerically, the sum is limited to the interval $k_y \in [k_0 - 3\sigma_k; k_0 + 3\sigma_k]$. We choose to initialize the wave function mostly in the first Landau level above the Fermi energy, in a region in which there is no potential and close to the edge of the armchair nanoribbon. In this way, we simulate the injection of a carrier at the edge through single-electron sources, as explained in Sec. 1.1.2. An example of the wavepacket built with this method is shown in Fig. 3.1. Here are also highlighted the energies of each edge state used for the linear combination, and the corresponding x, which, as seen in Eq. (2.62), is linked to the $\mathbf{k}$-vector of the state along y. Note that, as previously explained in Sec. 2.2.3, the wavepacket is made up of two components, one for each sublattice A and B; and additionally, the representation space is $[0; L]$ for the K component and $[-L; 0]$ for the K' component.

In Fig. 3.2(a) we report the evolution of different wavepackets during a time period of 0.5 ps along the edge of the armchair nanoribbon (y direction). As we can see, the evolution depends mainly on two factors: the central position of the wavepacket, x_0, linked to the central wave vector k_0 of the distribution in momentum space; and the real-space standard deviation σ of the wave-packet, linked to σ_k and, consequently, to the range of k_y considered for the Gaussian combination of edge states. We see that either when x_0 is high ($x_0 \geq 0$ nm) or σ is small the packet loses its shape: it spreads non-symmetrically and, as shown in Fig. 3.2(b), its maximum significantly decreases. This behavior is perfectly explained by looking at the band dispersion in momentum space [see Fig. 2.2(b) for reference]. Indeed, each of the components of the wavepacket corresponds to a specific value of the momentum k_y, and consequently to an energy $E(k_y)$. The shape of the wavepacket is maintained in time only if all edge states making up the packet have similar group velocity, v_g, defined as the derivative of the Landau level at point k_y [see Eq. (2.63)]. That is, when the energy region occupied by the packet in momentum space corresponds to a linear dispersion of the first Landau level. Otherwise, the components of the wavepacket

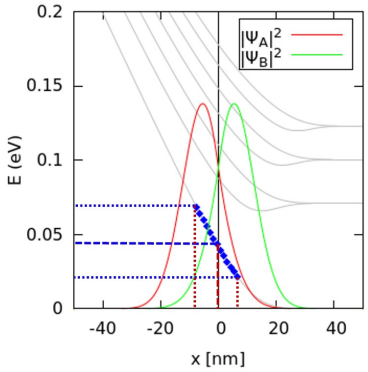


Figure 3.1: Electronic wavepacket initialized with central position at $x_0 = 0$ nm and $\sigma = 30$ nm. In red/green are the A/B sublattice components; in grey the Landau levels; in blue the energies of the k_y-vectors used in the Gaussian combination. The vertical black line at $x = 0$ nm shows the edge of the nanoribbon.

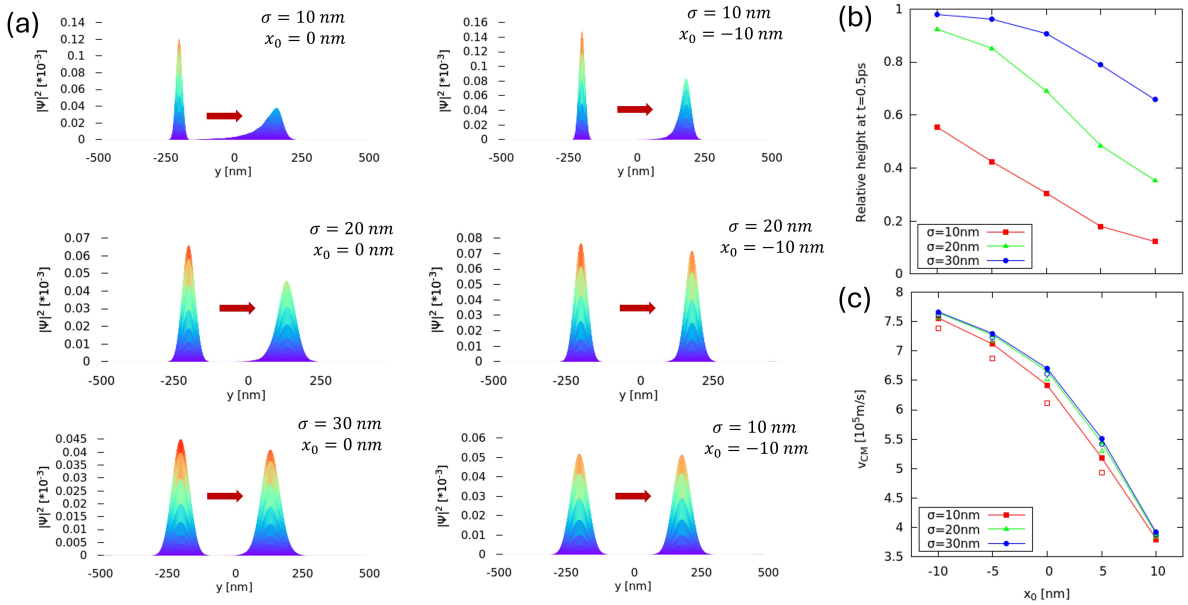


Figure 3.2: (a) Shape of the wavepackets at $t = 0.5$ ps compared to its initial shape at $t = 0$, for different x_0 and σ. (b) Height of the center of the wavepacket at $t = 0.5$ ps relative to its initial height at $t = 0$. (c) Velocity of the center of mass of the wavepackets evaluated as in Eq. (3.1) (full dots) for $t = 0.5$ ps and $t_0 = 0$ ps, compared to the velocities obtained from a linear fit of the bands (empty dots) in the considered k_y-interval for the Gaussian combination.

σ (nm)	x_0 (nm)	$v_{fit} \pm \delta v_{fit}$ (10^5 m/s)	$\delta v_{fit}/v_{fit}$ (%)	v_{CM} (10^5 m/s)	Relative height (%)
10	10	3.8 ± 0.2	5.318	3.813	12.26
10	5	4.93±0.18	3.74	5.186	18.00
10	0	6.11±0.14	2.263	6.419	30.54
10	-5	6.87±0.09	1.369	7.114	42.41
10	-10	7.80±0.06	0.8136	7.558	55.38
20	10	3.84±0.18	4.795	3.889	35.31
20	5	5.30±0.15	2.764	5.448	48.47
20	0	6.52±0.09	1.364	6.657	69.04
20	-5	7.17±0.05	0.767	7.269	85.2
20	-10	7.57±0.03	0.4609	7.649	92.31
30	10	3.88±0.16	4.215	3.919	65.79
30	5	5.42±0.12	2.271	5.513	78.88
30	0	6.61±0.07	1.082	6.703	90.73
30	-5	7.11±0.04	0.6085	7.294	96.16
30	-10	7.60±0.03	0.3692	7.663	97.92

Table 3.1: Numerical values of the velocity of the wavepackets, either from the linear fit of the bands in the considered interval for the Gaussian combination or from the evaluation of the center of mass, and the relative height after $t = 0.5$ ps with respect to $t = 0$, for different values of x_0 and σ.

will proceed all at different speeds, and the initial Gaussian will broaden. The relation between the linearity of the band dispersion and the packet broadening is clearly visible in Table 3.1 as well. Indeed, the smaller the relative error on the slope of the bands in the considered interval, and the higher the relative height maintained by the packet after 0.5 ps. Overall, we observe good shape retention only for $\sigma \geq 30$ nm and negative values of x_0. Note that a negative x_0 doesn't mean that the wavepacket is localized outside of the ribbon, but only that the edge states are highly localized on the edge and that their shape is much different from the one in bulk.

The slope of the bands is strictly related to the velocity of the wavepacket in our time-dependent simulations. One possible way to measure such velocity in a laboratory is to resort, for example, to *weak* measurements on Bohmian trajectories [143, 144]. However, the identification of a measurable velocity goes beyond the scope of this Thesis. Consequently, we will limit ourselves to a numerical estimation of the wavepacket velocity through the definition of the velocity of its center of mass along y, evaluated as

$$v_{CM}(t) = \frac{\int dx \int dy |\Psi(\mathbf{r};t)|^2 y - y_0}{t - t_0}. \tag{3.1}$$

The quantity defined in Eq. (3.1) is reported in Fig. 3.2(c) and Table 3.1 for various values of x_0 and σ. We see that the closer the wavepacket is to the bulk, the slower it moves. Indeed, this is the same case in which the Gaussian broadens and part of the wavepacket is 'left behind'. Equivalently, the group velocities of part of the edge states forming the wavepacket are smaller due to the curvature of the first Landau level when approaching the bulk, and they lower the overall value of the center-of-mass velocity. On the contrary, as x_0 decreases, v_{CM} approaches the limit value of the linear slope of the first Landau level far from the bulk, and is more and more similar to the value of the slope v_{fit} obtained from a linear fit of the bands.

After these considerations, in all following simulations we choose a real-space broadening of our Gaussian wavepacket equal to $\sigma = 30\,nm$. This value allows for the good retention of the wavepacket shape in time without requiring excessive dimensions of the device into which it is injected. The energy broadening of such packet is $\sigma_E \simeq 7.63\,\text{meV}$, meaning an energy interval of 45.8 meV, consisting of three standard deviations around the central energy E_0. With this broadening, the particle can be directly injected into the device at FF one at the chosen value of $B = 5\,\text{T}$.

3.1.2 Edge states and snake states along a *pn* junction

Now we can pass to describing the motion of the wavepacket along *pn* junctions. Through the time-resolved evolution of a localized wavepacket in this context we aim at exposing the similarities and differences in behavior with respect to previous studies on delocalized currents [116, 135, 136, 146–152]. Junctions are included inside our simulations through an external potential acting on the 2DEG in graphene, and whose profile is built either through step-like functions or through Fermi-like barriers (previously introduced in Sec. 2.64). In the following, we will refer to p and n regions respectively as regions with potential $V_p > E_{max}$ and $V_n < E_{min}$, where E_{max} and E_{min} are the maximum and minimum energies of the wavepacket.

In Fig. 3.3 we can see the semi-classical description of a single carrier traveling along a *pn* junction. Looking at Fig. 3.3(a), in the n region of the device the Dirac cone is below the chemical potential, since the energy of the wavepacket is completely above the potential V_n. Consequently, the carrier behaves as an electron, i.e. with an effective negative charge. On the contrary, in the p region, the Dirac cone is completely above the chemical potential, being the energy of the wavepacket lower than V_p. Thus, the carrier behaves as a hole, i.e. with an effective positive charge. Due to this behavior, the carrier experiences opposite Lorentz forces at the two sides of the junction, and acquires an oscillating motion with net transport from one side of the device to the other, as shown schematically in Fig. 3.3(b). The specific paths obtained in this situation also take the name of *snake states* due to their shape. The cyclotron radius in each region is [149]:

$$r_c = \frac{|\mathbf{q}|}{eB} = \frac{|E - V|}{v_F eB}\,, \tag{3.2}$$

where E is the energy of the classical carrier and $\mathbf{q}$ is the momentum of the carrier, which near the

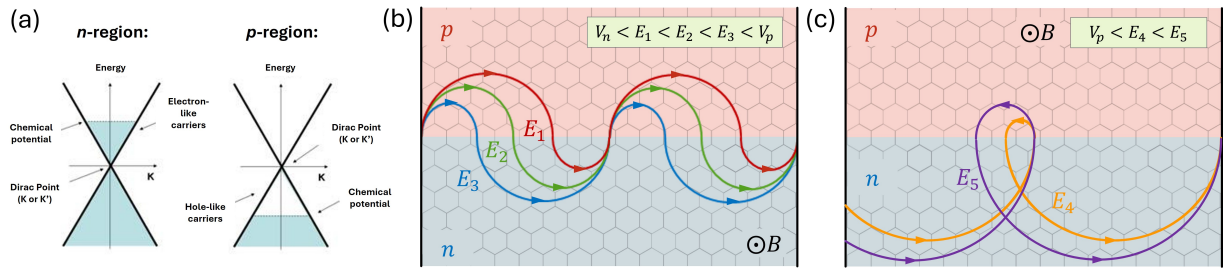


Figure 3.3: (a) Diagram of the Dirac cones below and above the Fermi energy respectively inside a n- and p-region, with an indication of the type of carrier in each case. (b,c) Schematic representation of Snake states along the potential barrier of a *pn* junction in the presence of a magnetic field $\mathbf{B}$. In panel (b), the energy of the carrier is fixed between the potentials $V_n < V_p$ of each region, while in (c) it's above V_p. Panel (a) is adapted from [145]

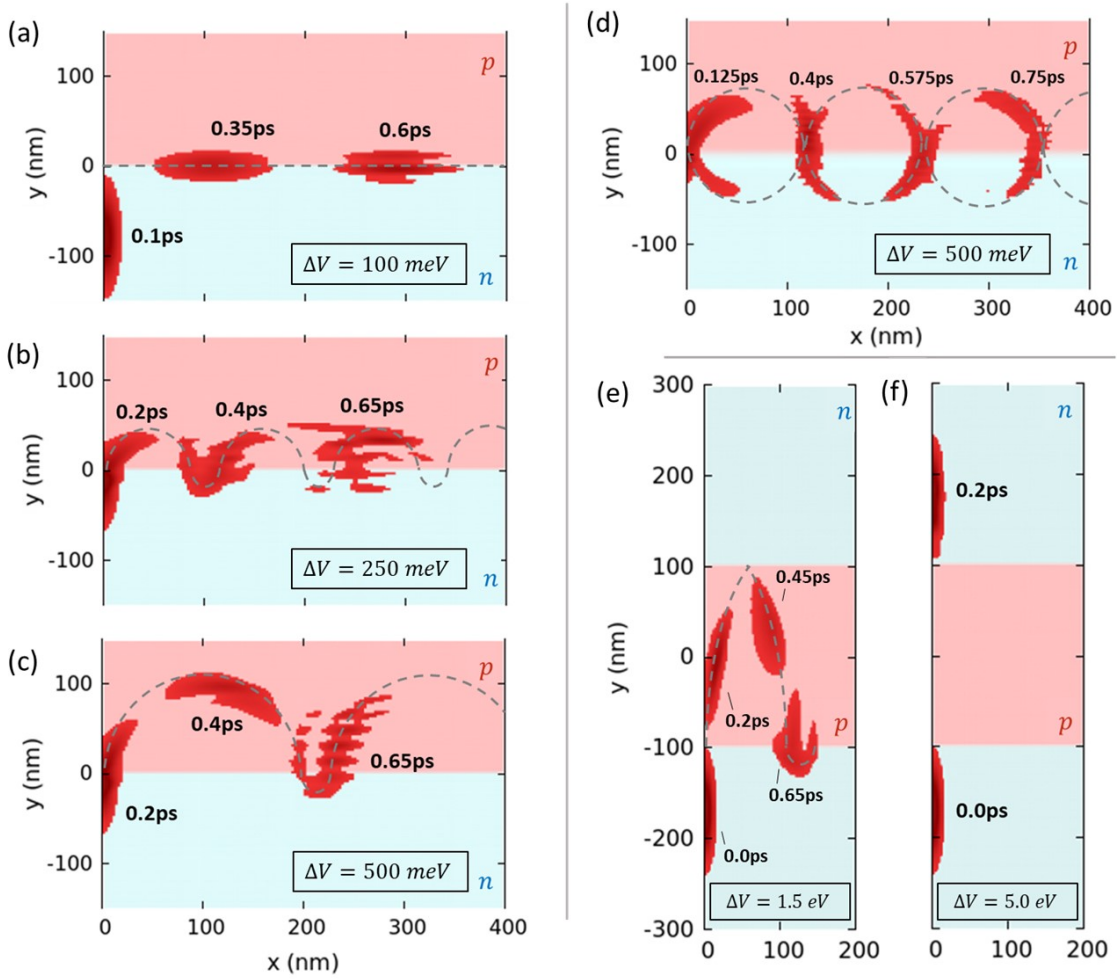


Figure 3.4: Stills from the time-dependent evolution of Gaussian wavepackets (in red). See Ref. [153] for the complete animations. In bold are the times at which each still was taken. The height of the potential barrier between the p region (red) and n region (blue) in each case is ΔV. The dashed grey lines are guides for the eyes. (a-c) Evolution along a sharp barrier when the central energies of the wavepacket are (a) $E^0 = 51.4\,\text{meV}$ and (b,c) $E^0 = 77.5\,\text{meV}$. (d) Evolution along a smooth barrier with slope $S = 0.33\,\text{nm}^{-1}$ [see Eq. (2.64)], with central energy of the wavepacket $E^0 = 241\,\text{meV}$. (e,f) Evolution along an npn junction characterized by width $\Delta y = 200\,\text{nm}$ and sharp barriers, with central energy of the wavepacket $E^0 = 77.5\,\text{meV}$. The picture is taken from [3].

Fermi energy is $\mathbf{q} = |E - V|/v_F$ thanks to the linear approximation of the Dirac cones. Summing the cyclotron radius in both regions gives

$$r_{c,n} + r_{c,p} = \frac{E - V_n}{v_F eB} + \frac{V_p - E}{v_F eB} = \frac{\Delta V}{v_F eB}\,, \tag{3.3}$$

where $\Delta V = V_p - V_n$ is the height of the potential barrier. Consequently, the sum of the two radii does not depend on the energy of the carrier, but only on the height of the barrier. In other words, the net velocity at which the carrier is transported along the pn junction is the same for every carrier. The same result is also valid for a carrier with energy E higher than V_p. In fact, in this case, the carrier behaves as an electron in both regions and, as illustrated in Fig. 3.3(c), the radius in the

Fig. 3.4	(a)	(b)	(c)	(d)	(e)	(f)
p-region	0.386	1.37	3.36	2.06	11.3	39.1
n-region	0.408	0.616	0.616	1.92	0.616	0.616

Table 3.2: Ratios r_c/l_m for the cases reported in Fig. 3.4. The reference panel from (a) to (f) for each simulation is reported in the first row; the labels p- and n-region refer to the corresponding red and blue regions in Fig. 3.4. The picture is taken from [3].

p region needs to be subtracted from the one in the n region:

$$r_{c,n} - r_{c,p} = \frac{E - V_n}{v_F eB} + \frac{E - V_p}{v_F eB} = \frac{\Delta V}{v_F eB}\,. \tag{3.4}$$

As with all things quantum, the semiclassical treatment is only valid when the characteristic lengths describing the quantum phenomena of the system are much smaller than the classical ones. In this case, the discriminating quantity is the ratio between the cyclotron radius introduced in Eq. (3.2) and the magnetic length of the system, previously defined in Eq. (2.31):

$$\frac{r_c}{l_m} = \frac{|E_0 - V|}{v_F\sqrt{\hbar eB}}\,, \tag{3.5}$$

where E_0 here is the central energy of the wavepacket. Indeed, when we simulate our Gaussian combination of edge states traveling along a sharp, step-like pn junction [Fig. 3.4(a-c)], we clearly observe a transition between two regimes as we change the value of $|E_0 - V|$. For all simulations in Fig. 3.4, the values of r_c/l_m are reported in Table 3.2. First, when the potential barrier is small enough and $l_m \gg r_c$ [Fig. 3.4(a)] the carrier goes on as an edge state along the junction and remains highly localized along the barrier. Then, the carrier starts penetrating the barrier more and more as ΔV increases and $r_c \gtrsim l_m$ [Fig. 3.4(b,c)], and snake states are observed.

Note that in the first cases in Fig. 3.4(a-c) we said that the potential barrier is sharp and step-like. However, a smoother potential barrier better reproduces the experimental conditions of realistic devices. Indeed, the slope of the barrier depends on the distance between the top gate and the nanoribbon [126], and though it is possible to increase the sharpness of the barrier by decreasing this distance [113, 126], it is impossible to completely eliminate all processes that smoothen the junction [126]. Thus, in Fig. 3.4(d) we simulate a Fermi-like barrier as introduced in Eq. (2.64) and with slope $S = 0.33\,\mathrm{nm}^{-1}$. Here we see that an additional phenomenon occurs: the finite width of the barrier causes the packet to be partially reflected back every time that it hits the barrier. This was also reported in previous studies on delocalized currents [135, 136]. Particularly, once the incident angle is fixed (here 90°), the reflection coefficient increases with the width of the barrier. Here, by setting the ratio r_c/l_m to be similar in both regions, the observed skipping orbits are the same on both sides of the barrier and overlap.

3.1.3 Klein tunneling through an npn junction

The last frames in Fig. 3.4(e,f) show the phenomenon of the Klein paradox, typical of Dirac fermions in graphene and, more in general, of particles with Dirac-like behavior [69, 70], as introduced in Sec. 1.2.1. Specifically, we choose to simulate npn junctions by using potential barriers with a short length along the y direction, Δy. For these simulations we consider sharp barriers for simplicity. Notice that the finite dimension of the nanoribbon along x in the IQH regime introduces

an energy gap between the conduction and valence states at the edge of the device (see Fig. 2.2 in the previous Chapter), even in the absence of a mass term M in the Hamiltonian. Consequently, the term *tunneling* becomes in this case more appropriate for the description of the phenomenon, due to the occurrence of true potential barriers felt by the propagating particle. Now, by fixing $r_c/l_m \gg 1$ in the p region and a cyclotron radius $r_c > \Delta y$, two things can happen. In the first case [Fig. 3.4(e)], for relatively low values of ΔV, the carrier penetrates the barrier and reaches the other side of the barrier. At this point, the direction of transport is prohibited along the junction, due to the chirality of edge states, and the carrier is reflected back. Once it reaches the initial n region again, the Lorentz force curves its trajectory and makes it enter the barrier again, and the motion goes on until the packet reaches the other side of the ribbon. Overall, net transport occurs along the side of the ribbon, but it's much slower than in the previous cases.

In the second case [Fig. 3.4(f)], with high ΔV, Klein tunneling occurs and the packet instantaneously tunnels through the barrier. The carrier now proceeds along the initial edge of the ribbon and there is no net transport along the side of the ribbon. As briefly mentioned in Sec. 1.2.1, this phenomenon can be explained through a process of interference between all possible Landau levels available for transport, which in the literature is also referred to as an *equilibration* process [67, 113, 115, 119, 148, 149, 154–156]. Indeed, the incident carrier can scatter elastically among all the energetically-available hole-like Landau levels below the barrier: the higher the barrier, the more levels are available. Consequently, the carrier will penetrate further and further, thanks to the slope of all the Landau levels, until it scatters so deep inside the barrier that Landau levels of the opposite junction become available for transport. Since the latter levels present opposite slopes, the carrier can no longer transport along the junction and it needs to proceed along the edge. Although this phenomenon is well documented in graphene with delocalized currents [67, 148, 149, 155, 156], we are not aware of experimental observations for single particles as well.

3.2 Building Mach-Zehnder interferometers

3.2.1 Quantum point contacts

Let's first look at the behavior of QPCs created with physical restrictions of the potential landscape, which is an important block to build one of the MZIs previously illustrated in Sec 1.2.2. To prevent unwanted scattering processes between many hole-like Landau levels below the potential barrier, we work in the edge-state regime for which $r_c/l_m \ll 1$. For these simulations we fix $\Delta V = 100\,\text{meV}$ and $M = 0\,\text{meV}$. The behavior of a QPC is schematically illustrated in Fig. 3.5(a). The initial packet (I) travels along the potential profile in the direction of transport allowed by the chirality of the system, and meets the QPC. Here, only two paths are available, again because of chirality, and the packet splits. Part of it is transmitted (T) along the potential barrier on the left, and the other is reflected (R) and forced to travel along the barrier on the right. Each component of the wavepacket has specific reflection and transmission coefficients depending on its wave vector. The empirical formula is [137, 157]:

$$\begin{bmatrix} r(k) \\ t(k) \end{bmatrix} = \frac{1}{\sqrt{e^{\pm\beta(k-k_{QPC})}+1}}, \tag{3.6}$$

where β and k_{QPC} are parameters of the QPC depending on its characteristics: namely, the width L_{QPC}, the height ΔV of the potential barrier, and its slope S. Specifically, in the k_y-intervals we considered to build our packet, the band dispersion is nearly linear, meaning that the same formula

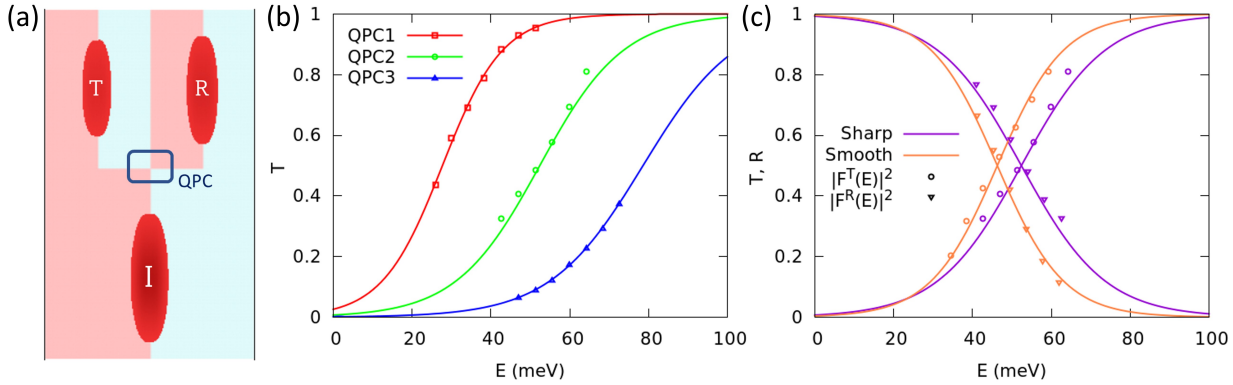


Figure 3.5: (a) Schematic evolution of a wavepacket scattered through a QPC. The potential barrier is shown in red. The label 'I' indicates the initial wavepacket before meeting the QPC; 'T' and 'R' are respectively the transmitted and reflected parts. (b) Transmission curves for three QPCs with width $L_{QPC} = 5\,\text{nm}$ (QPC1), $L_{QPC} = 0\,\text{nm}$ (QPC2) and $L_{QPC} = -5\,\text{nm}$ (QPC3). We show the numerical data obtained from the projection of the transmitted wave function φ^T (dots) and the fit through Eq. (3.7) (continuous line). The data was obtained for wavepackets of central energy 58.2 meV (QPC1), 49.8 meV (QPC2) and 41.8 meV (QPC3). (c) Transmission and reflection curves of QPC2 compared between sharp and smooth barrier with slope $S = 0.33\,\text{nm}^{-1}$ [see Eq. (2.64)]. We show the numerical data obtained from the projection of the transmitted wave function φ^T (dots) and the fit through Eq. (3.7) (continuous line). The central energy of the wavepacket is 49.8 meV. The picture is taken from [3].

also applies to the energies:

$$\begin{bmatrix} r(E) \\ t(E) \end{bmatrix} = \frac{1}{\sqrt{e^{\pm\alpha(E-E_{QPC})}+1}}\,, \tag{3.7}$$

where $\alpha = \beta/v_F$ and $E_{QPC} = v_F k_{QPC}$. Thanks to the setup in Fig. 3.5(a), we can find the weights $F^{T/R}(E)$ for the two parts of the packet through the wave packet method explained in Sec. 2.3.1. These can be related to the reflection/transmission coefficients in Eq. (3.7) through the energy-resolved reflection/transmission probability:

$$R(E) = |r(E)|^2 = \frac{|F^R(E)|^2}{|F(E)|^2}\,, \qquad T(E) = |t(E)|^2 = \frac{|F^T(E)|^2}{|F(E)|^2}\,, \tag{3.8}$$

where $F(E)$ are the Gaussian weights of the incoming wavepacket. The overall percentage of reflection and transmission of a packet going through a QPC can then be found by integrating $R(E)$ and $T(E)$.

Numerical fits of $R(E)$ and $T(E)$ with the analytical formulas are reported in Fig. 3.5(b) and (c) for various QPCs; data on the reflected/transmitted wavepackets are reported in Table 3.3. We chose to simulate three QPCs with different widths: an open one (QPC1, $L_{QPC} = 5$ nm), a closed one where the potential barriers touch (QPC2, $L_{QPC} = 0$ nm), and a final one with overlapping barriers (QPC3, $L_{QPC} = -5$ nm). Transmission is possible in the last case as well, thanks to the availability of hole-like states below the barrier, which allow for Klein tunneling through a short enough barrier (see the previous description in Sec. 3.1.3). This is in contrast with the behavior of QPCs in GaAs/AlGaAs heterostructures [20, 137, 157], or in general in semiconductor devices. Indeed, in those conditions the band gap is too large and hole states are not available for transport,

x_0 (nm)	E_0 (meV)	S (nm^{-1})	QPC	$R-T$ (%)	x_R (nm)	x_T (nm)	E_R (meV)	E_T (meV)
-4.72	58.2	∞	1	7.82-92.18	-0.977	-2.359	53.45	58.49
-4.72	58.2	∞	2	39.78-60.22	-1.470	-2.778	55.24	60.00
-4.72	58.2	∞	3	82.92-17.08	-2.035	-3.447	57.29	62.43
-2.36	49.8	∞	1	13.32-86.68	1.145	-0.121	45.77	50.37
-2.36	49.8	∞	2	55.19-44.81	0.591	-0.657	47.78	52.31
-2.36	49.8	∞	3	90.49-9.51	0.171	-1.215	49.30	54.34
-2.36	49.8	0.33	1	9.11-90.89	1.609	-0.116	43.98	50.08
-2.36	49.8	0.33	2	41.39-58.61	0.962	-0.659	46.23	51.98
-2.36	49.8	0.33	3	81.40-18.60	0.347	-1.473	48.37	54.82
-2.36	49.8	0.1	1	0.59-99.41	6.970	0.056	34.76	49.65
-2.36	49.8	0.1	2	12.72-87.28	5.758	-0.090	37.11	49.96
-2.36	49.8	0.1	3	19.71-80.29	4.128	-0.720	40.27	51.26
0	41.8	∞	1	22.16-77.84	3.003	1.951	39.04	42.86
0	41.8	∞	2	68.67-31.33	2.511	1.428	40.82	44.76
0	41.8	∞	3	93.61-6.39	2.273	1.090	41.68	45.98

Table 3.3: Data regarding the reflection and transmission through various QPCs for different central position x_0 and central energy E_0 and different slopes S of the potential barriers. We report the percentages of the reflected (R) and transmitted (T) wavepackets, and their centers and average energies obtained through a Gaussian fit centered around the half-height point of the reference barrier for each path.

so the electronic wavepacket is forced to continue its path away from the barrier. That said, one can see that the transmission shifts to higher energies as the QPC closes, meaning that the packet needs higher and higher energy to transmit beyond the barrier. This is also clear from the central energies of the reflected and transmitted wavepackets, which progressively increase for QPC1, 2 and 3. Consequently, consistently with the shape of the Landau levels near a barrier, the central positions in real space of the wavepackets decrease.

The opposite behavior is observed when gradually reducing the slope of the potential barrier: as S decreases, the shape of the reflection and transmission curves slightly changes, and the 50% values shift towards lower energies. Consequently, the effective width of the QPC felt by the wavepacket increases. Indeed, although the half-height width of the QPC, namely L_{QPC}, may be the same, the transmission probability increases, the central energies of the reflected and transmission parts decrease, and their central position slightly shifts away from the center of the barrier.

3.2.2 MZI with quantum point contacts

Now that we have characterized QPCs in the IQH regime inside graphene nanoribbons, we can start building our first MZI, which is based on the scheme reported in Fig. 1.7(a). Here, after the packet is split by the first QPC, the two parts travel spatially separated paths (L/R) along two parallel barriers, and meet again at the second QPC, where they can interfere. In our simulations we choose to keep the arms of this interferometer far away from the nanoribbon edges, since previous studies reported on the detrimental effects of the ribbon edges and the presence of back-scattering under the gates [118–122]. Instead, studies performed in edgeless geometries allow for extremely

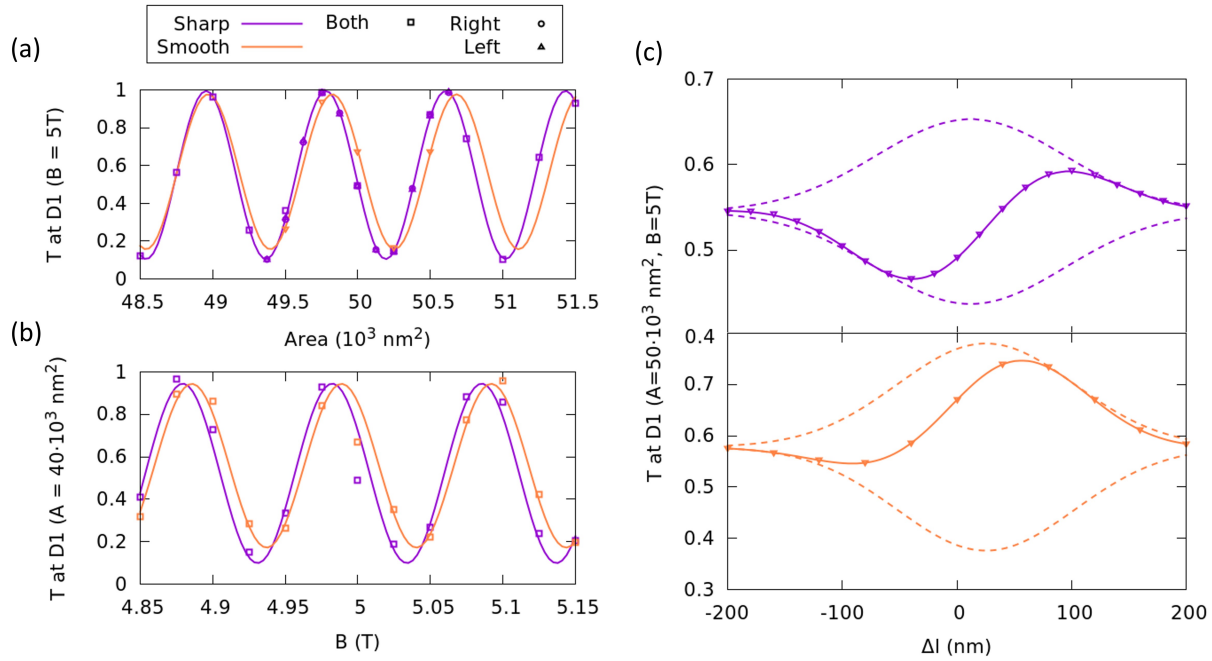


Figure 3.6: Detection probability at D1 for the MZI shown in Fig. 1.7(a). The points are the numerical data, and the solid line is the fit. The curves are obtained with either a sharp barrier (purple) or a smooth barrier (orange) with slope $S = 0.33\,\mathrm{nm}^{-1}$ [see Eq. (2.64)]. (a) Aharonov-Bohm oscillations for a fixed magnetic field $B = 5\,\mathrm{T}$ and varying the area enclosed by the arms of the interferometers. The area was changed by modifying either the length of both arms ('Both') or one at a time ('Left' and 'Right'). (b) Aharonov-Bohm oscillations for fixed area $A = 40 \cdot 10^3\,\mathrm{nm}^2$ and varying the magnetic field. (c) Phase averaging on Aharonov-Bohm oscillations when fixing both the magnetic field $B = 5\,\mathrm{T}$ and the area $A = 50 \cdot 10^3\,\mathrm{nm}^2$, and modifying the path difference Δl. The dashed lines show the Gaussian modulation. The picture is taken from [3].

clean measurements [158, 159]. Once again we choose to work in a regime with $r_c/l_m \ll 1$, by setting $\Delta V = 100\mathrm{meV}$ and $M = 0\,\mathrm{meV}$. Additionally, we select the closed QPC2 introduced in the previous section, with $L_{QPC} = 0$ nm. Then, we set the wavepacket initialization in order to have an approximate $43 - 57\,\%$ splitting into the $L - R$ paths in the case of a sharp barrier ($S \to \infty$) or a $44 - 56\,\%$ splitting when $S = 0.33\,\mathrm{nm}^{-1}$. This is done in order to ensure a non-negligible interference between the parts of the wavepacket reflected/transmitted after the first QPC.

In various reported interferometry experiments with delocalized currents [112–114, 119, 125, 160, 161], the transmission probability T_{D1} of detecting a signal at D1 is completely determined by the Aharonov-Bohm phase,

$$\Delta\theta = \frac{e\Phi}{\hbar}\,, \tag{3.9}$$

related to the magnetic flux $\Phi = AB$ through the area A enclosed by the two paths of the interferometer. Consequently, T_{D1} presents Aharonov-Bohm oscillations when varying either the area of the interferometer or the magnetic field acting on the system:

$$T_{D1} = T_0 + \Delta T \sin\left[\frac{eAB}{\hbar} + \theta_0\right]\,, \tag{3.10}$$

where T_0 is the average transmission through the interferometer and $2\Delta T = T_{D1}^{max} - T_{D1}^{min}$ is the visibility. This is also true in our simulations, specifically when the two paths L/R present approximately the same length. This is shown both for sharp and smooth barriers in Fig. 3.6(a) and (b), where we fit the numerical T_{D1} by varying respectively the values of the area or the magnetic field of the system. All trials show a variation below 0.5 % from the expected period, except for when varying A with smooth barriers. This may be due to the area not being perfectly defined in the presence of barriers of finite sizes. Alternatively, discrepancies may occur due to the spatial spread of the packet, or to its central positions $x_{R/L}$ being slightly shifted from the center of the barriers and adding an additional phase. Still, these errors are negligible since we simulate situations in which the flux is already 50 to 60 times the unit flux $\Phi_0 = e/\hbar$. Other than that, the obtained visibilities are approximately 81 % and 73 % respectively for the sharp and smooth barriers. These are both very high, considering that they correspond to 98.8 % and 95 % of the maximal obtainable visibilities given the QPC splittings. Ideally, this means that under $50-50$ % splitting conditions we should observe visibilities close to 100 %, coherently with literature [113, 114].

The main difference in behavior with respect to delocalized currents consists in the phenomenon of phase averaging [39, 162], which is only present when the carrier is spatially localized. Basically, when the two parts of the carrier travel paths of different lengths, they may not arrive at the end of the interferometer at the same time, and the interference is limited by the spatial overlap of the two packets at the second QPC. Overall, when we introduce a difference in the optical length between the two paths, $\Delta l = l_R - l_L$, the transmission T_{D1} is modified in two ways: the first is the addition of an additional phase, $2\pi\Delta l/L$, where L is the period of the oscillations due to Δl. The second is a Gaussian modulation, equivalent to the convolution of the two Gaussian shapes of the packets traveling the R/L paths:

$$F^{avg}(\Delta l) = (F^R * F^L)(\Delta l) = Ce^{-\frac{(\Delta l-\Delta l_0)^2}{4(\sigma_R^2+\sigma_L^2)}}, \tag{3.11}$$

where $\sigma_{R/L}$ are the real space broadenings of the packets in the y direction and C is a normalization factor. In the last formula, Δl_0 is an additional path discrepancy, mainly due to the centers $x_{R/L}$ of each part of the packet being generally displaced from the barrier, leading to effectively different paths even at $\Delta l = 0$. The transmission probability at D1 overall becomes:

$$T(\Delta l) = T_0 + F^{avg}(\Delta l)\cdot\Delta T\sin\left[\frac{eA|\mathbf{B}|}{\hbar} + \frac{2\pi\Delta l}{L} + \theta_0\right]. \tag{3.12}$$

The phase averaging occurring in our simulations is evident from Fig. 3.6(c), in which we fixed the area and magnetic field and only varied the relative paths of the arms of the interferometer. The curves of the transmission probabilities clearly possess an oscillating behavior modulated by a Gaussian, as highlighted by the fit with the numerical formula in Eq. (3.12) and by the comparison with the Gaussian modulation in Eq. (3.11). Eventually, when $|\Delta l| \gg 0$, the packets reach the second QPC at separate times and don't interfere, causing the signal received at D1 to no longer oscillate. As is clear by now, this phenomenon is detrimental to the visibility of the interferometer, and needs to be taken into account when dealing with localized carriers. An important detail to notice from Fig. 3.6(c) is the shift of the Gaussian modulation between the curves corresponding to a sharp versus a smooth barrier. Respectively these modulations are centered around $\Delta l_0^{sharp} \simeq 12\,\text{nm}$ and $\Delta l_0^{smooth} \simeq 25\,\text{nm}$. This is mainly due to the slope of the bands in the smooth case being lower than the one in the sharp case, and consequently causing a slower group velocity: $v_g^{smooth} = 6.97\cdot10^5\,\text{m/s}$ instead of $v_g^{sharp} = 7.25\cdot10^5\,\text{m/s}$. Because of this, when using smooth barriers the intrinsic delay increases.

E_g (meV)	x_0 (nm)	E_0 (meV)	S (nm^{-1})	R-T (%)	x_R (nm)	x_T (nm)	E_R (meV)	E_T (meV)
5	-2.07	48.84	∞	52.97-46.83	0.520	0.101	49.06	48.54
10	-2.07	48.84	∞	55.92-43.66	0.673	-0.163	49.53	48.48
10	-2.07	48.84	0.5	56.79-42.69	0.756	-0.244	49.42	48.17
10	-2.07	48.84	0.33	57.55-41.78	0.523	-0.336	49.49	48.06
10	-2.07	48.84	0.25	58.32-40.78	0.967	-0.450	49.62	47.99
10	-2.07	48.84	0.1	63.05-34.82	-0.260	-2.823	54.67	51.19
20	-4.14	56.78	∞	61.58-37.32	-1.091	-2.863	57.95	55.67
20	-2.07	48.84	∞	61.52-37.41	0.875	-0.819	50.94	48.70
20	-2.07	48.84	0.33	64.73-33.95	1.214	-1.184	51.11	48.13
20	0.00	42.71	∞	61.56-37.19	2.710	1.004	44.55	42.20

Table 3.4: Data regarding the reflection and transmission through various VBSs for different gap energy E_g central position x_0 and central energy E_0 and different slopes S of the potential barriers. We report the percentages of the reflected (R) and transmitted (T) wavepackets, and their centers and average energies obtained through a Gaussian fit centered around the half-height point of the reference barrier for each path. Data is partially taken from [3].

3.2.3 MZI with valley beam splitters

Finally, we build an MZI built with VBSs and characterize its functional regime. The operation of this interferometer is illustrated in Fig. 1.7(b). The difference with respect to the previous interferometer is that the two arms of the interferometer walk along the same barrier, and the wavepacket does not get split into two spatially separated components. On the contrary, the overall wavepacket reaches the first VBS and is split into its valley components, Ψ^K and $\Psi^{K'}$. This is thanks to the valley-degeneracy lifting along the zigzag direction between states $LL_0^{+/-}$, and the scattering between energetically available levels occurring in the proximity of a potential barrier [113]. Then the two parts of the packet recombine at the second VBS and interfere. In our setup, instead of running the potential barrier along the full nanoribbon width [77, 112–114], we built the interferometers' arms so that they curve back to the first edge of the ribbon. In this way, two VBSs are generated along the same edge, and we are able to tune the length of the interferometer's arms by changing the dimensions L_x and L_y of the potential generated by the gate. For these simulations, once again we fix $\Delta V = 100\,\text{meV}$ in order to have $r_c/l_m \ll 1$. Then, we set the mass term $M \neq 0\,\text{meV}$, in order to lift the $LL_0^{+/-}$ degeneracy at the barrier.

We begin our analysis by first characterizing the reflected and transmitted parts of the localized wavepacket after the first VBS. In this context, we will refer to the K component, occupying LL_0^- below the barrier, as the transmitted component, and to the K' component, occupying LL_0^+ above the barrier, as the reflected component. The data of this analysis is reported in Table 3.4: note that the splitting percentages (R-T) don't sum up to 100% due to some unwanted scattering into other energetically available Landau levels. Contrarily to transmission and reflection probabilities in QPCs, here R and T do not depend on the energy of the wavepacket, as is visible by comparing results for different x_0 and E_0. Instead, R and T are only affected by the value of the mass term and the slope of the barrier, namely, the only terms that affect the distance in momentum space between the LL_0^+ and LL_0^- levels in the proximity of a potential barrier. Indeed, the larger the energy gap $E_g = 2M$ is or the lower the potential slope S is, the farther away are LL_0^+ and LL_0^- from each other. Consequently, it's more difficult for each component of the packet to be transmitted below the bar-

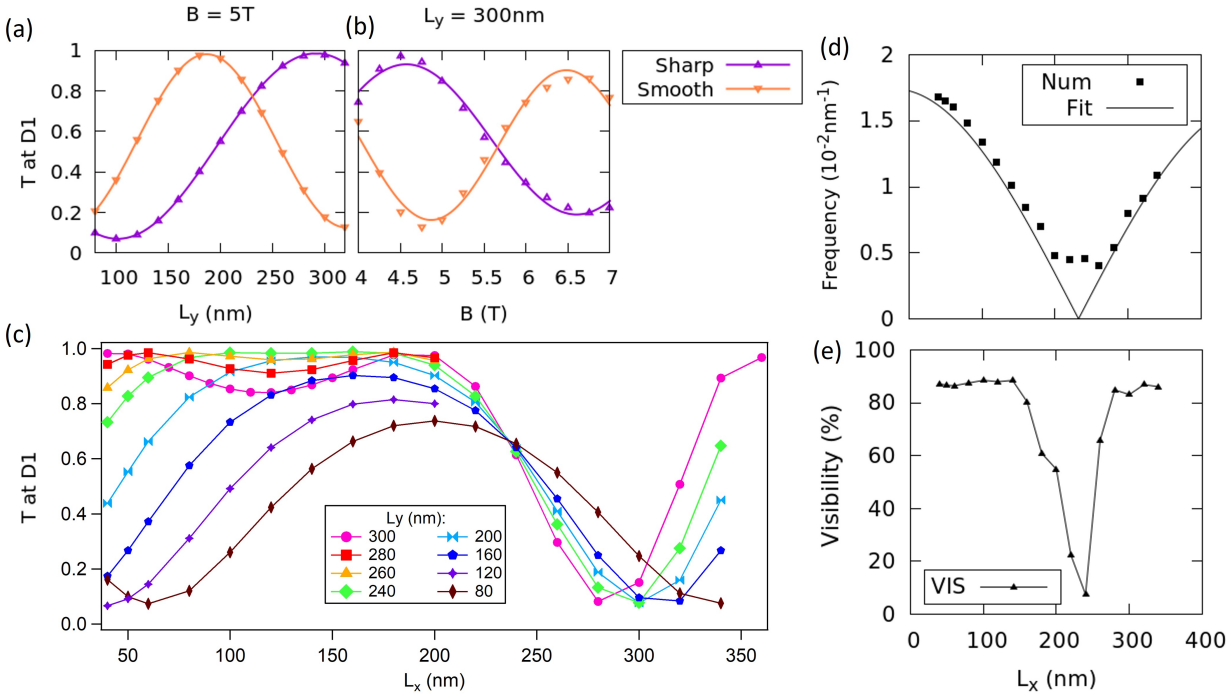


Figure 3.7: (a)-(c) Detection probability at D1 of the MZI shown in Fig. 1.7. The points are the numerical data, and the solid line is the fit. We use both a sharp barrier and one with slope $S = 0.33\,\mathrm{nm}^{-1}$, respectively labeled 'Sharp' and 'Smooth'. (a) Aharonov-Bohm oscillations at fixed magnetic field $B = 5\,\mathrm{T}$ and length of the gate along x, $L_x = 50\,\mathrm{nm}$, while varying L_y. (b) Aharonov-Bohm oscillations at fixed gate lengths L_x and L_y with varying magnetic field B. (c) Transmission curves with sharp barrier for different L_y, observed by varying L_x at fixed $B = 5\,\mathrm{T}$. (d)-(e) Respectively frequency and visibility of the Aharonov-Bohm oscillations obtained with sharp barrier for various L_x, observed by varying L_y at fixed $B = 5\,\mathrm{T}$. The picture is taken from [3].

rier, and the transmission probability decreases. The ideal $50-50\,\%$ splitting probability would be recovered in the limit $M \to 0\,\mathrm{meV}$, for which the two $LL_0^{+/-}$ levels are degenerate and their distance in momentum space is zero. Overall, we confirm previous results valid for delocalized currents [126], showing that interference phenomena in an MZI built with VBSs are significantly affected only by the electrostatic setup of the device.

At this point, we are ready to characterize the behavior of the overall interferometer. We choose a case with $\sim 44-56\,\%$ splitting after the first VBS in the presence of a sharp barrier, and $\sim 44-56\,\%$ for a smooth barrier with $S = 0.33\,\mathrm{nm}^{-1}$, and measure the probability T_{D1} of detecting the carrier at detector D1. Importantly, in this interferometer the paths of the K and K' components both follow the same potential profile, and always stay at a distance of the order of a few nanometers from each other [see Table 3.4]. Consequently, the difference in path length is negligible and no phase averaging occurs. This means that T_{D1} will follow the original formula describing Aharonov-Bohm oscillations in Eq. (3.10). Here, the area of the interferometer is given approximately by

$$A = 2L_x\delta_x + L_y\delta_y\,, \tag{3.13}$$

where δ_x and δ_y are respectively the distance between the channels along the x and y directions.

Figs. 3.7(a) and (b) show the Aharonov-Bohm oscillations fixing one length of the interferometer, L_x, and varying either the their length L_y or the magnetic field B acting on the system. The visibilities obtained respectively for the sharp and smooth barriers are $\Delta T \simeq 86.7\,\%$ and $\simeq 77.3\,\%$ in Fig. 3.7(a) and $\simeq 66\,\%$ and $69\,\%$ in Fig. 3.7(b). In the latter case, however, the sinusoidal fit agrees less with the data, and the fitting variables are less reliable. This is probably caused by the magnetic field slightly changing the Landau level dispersion and thus the separation of $LL_0^{+/-}$ along the barrier. This would consequently affect the first VBS and introduce an additional dependency on the oscillations. Looking at the formula for the area in Eq. (3.13), the value of the period L_y^T of the oscillations in Fig. 3.7(a) allows us to find, at fixed L_x, the value of δ_y. These turn out to be $\delta_y \simeq 2.17\,\text{nm}$ and $\simeq 3.08\,\text{nm}$ in the sharp and smooth cases, respectively. Coherently with Table 3.4, the separation between $LL_0^{+/-}$ increases as the slope of the barrier decreases. The values of δ_y we found are much smaller than those usually observed in MZI with VBS from literature [113, 114, 126], which are usually in the order of 50 nm and higher. However, the discrepancy is due to the specific regime that we chose in order to simulate localized wavepackets, and is consistent with the results from another study in a similar system [163]. We note that we were also able to reach a value of δ_y as high as 12 nm, however, these conditions implied a very small value of the transmission probability after the first VBS, of approximately $\simeq 5\,\%$.

We then study the value of T_{D1} as a function of L_x in Fig. 3.7(c), for various values of L_y. We can firstly see that the observed oscillations present a behavior far from the sinusoidal one we could see in Fig. 3.7(a) and (b). We were able to lead this back to a variation in the channel distance depending on L_x. Indeed, by analyzing the Aharonov-Bohm oscillations as a function of L_y, like in Fig. 3.7 but for different values of L_x, we obtained frequencies oscillating as the absolute value of a sinusoid, as reported in Fig. 3.7(d). Importantly, these frequencies mimic the ones expected through the formula $f = eB|\delta_y|/\hbar$, by replacing δ_y with the distance between the spatial centers of Ψ^K and $\Psi^{K'}$ along L_y. Indeed, this is also another way to evaluate the channel distance δ_y along the armchair direction. Consequently, we found a periodicity of $L_x^T \simeq 992\,\text{nm}$ in the behavior of δ_y, and were able to observe the channels crossing along y for certain values of L_x. Specifically, it's in correspondence with these points that the frequencies differ from the expected ones: this is due to δ_y being close to zero, causing the energy broadening of the packets to affect the oscillations. Fig. 3.7(e) further confirms the channels crossing through a drop in visibility, which otherwise stays more or less constant throughout the whole simulated interval. Indeed, when $\delta_y = 0$ the area enclosed by the arms of the interferometers along L_y is null, and the value of L_y does not affect the interference between the K and K' components.

In conclusion, we hypothesize that the distance between edge channels in graphene interferometers based on VBSs is not constant throughout the whole interferometer. On the contrary, our results suggest that the channels are only straight along the armchair direction parallel to the nanoribbon edge, i.e. along y in our simulations. Instead, they oscillate along the zigzag direction orthogonal to the armchair edge of the nanoribbon, in our case x. This oscillation is of the order of a few nanometers, which means that it did not produce significant effects in previous implementations, in which the channel distance was equal to or higher than 50 nm [113, 114]. Instead, we could observe the channels crossing along x thanks to the smaller separation we fixed between them.

Part II

Integrated hole-spin qubits and their application for quantum sensing

Indeterminazione

La possibilità si impone con violenza
L'assoluto è l'ambiguità della certezza
Le osservabili che stregano mondi nascosti
In salti azzardati, inferenze e interazioni
L'assurdità che costringe l'assodato al silenzio

Onde che subiscono il forzato annientamento
In una assoluta mancanza di riferimenti
Scontri di specchi che si infrangono in luce
Con schianti e spaventevoli stonature
Si distruggono in agonizzante silenzio

La separazione cede allo straziante ricordo
Il passato incombe in indelegabili aberrazioni
Che disprezzano il disordine della causalità
In apparenze di accorate dipendenze
Ma il tempo appesantisce la cadenza del silenzio

L'accuratezza non soddisfa la bellezza del caos
La costrizione delle differenze si moltiplica in fracassanti arabeschi
La presenza è costretta infinitamente in circolazioni d'assenze
L'intuizione in vizi di correzioni che la privano di senso
E la conoscenza ne determina il silenzio

Così ci trasciniamo in vibrazioni di sogni
E poi sussurriamo parole d'inganno
Non ci capiamo ma ci comprendiamo
Per parole effimere
E tutto sommato restiamo in silenzio

We demand rigidly defined areas of doubt and uncertainty!

∼ from *The Hitchhicker's Guide to the Galaxy*,
by Douglas Adams

Chapter 4

Spin qubits for quantum technologies in solid state devices

In the second part of this Thesis, we study prototypical systems of integrated hole-spin qubits for scalable quantum computing. Specifically, in this Chapter we give an overview of the state of the art on the implementation of spin qubits with semiconductor technology. In Sec. 4.1 we illustrate the general requirements for qubit implementation, focusing on the scheme proposed by Loss and DiVincenzo (Sec. 4.1.1), and defining possible decoherence processes (Sec. 4.1.2). Then, in Sec. 4.2 we describe the possible integration of spin qubits in Si- and Ge-based devices: in Sec. 4.2.1 we list the most recent advancements in terms of device architectures; while in Sec. 4.2.2 we identify the characteristics of hole-spin qubits and their differences with respect to electrons.

4.1 Spin qubits in semiconductor quantum dots

Qubits are the fundamental building blocks of quantum computing. Unlike their classical equivalent, the bits, qubits can exist in any superposition state between 0 and 1, and as such live in a two-dimensional Hilbert space and can be written as:

$$|\psi_q\rangle = \alpha|0\rangle + \beta|1\rangle\,, \tag{4.1}$$

with $\alpha, \beta \in \mathbb{C}$ so that $|\alpha|^2 + |\beta|^2 = 1$. The implementation of a qubit can be realized through any quantum system which satisfies the so-called DiVincenzo's criteria [23]:

1. The qubits must be *well characterized*. This means that one must be able to identify two orthogonal states $|0\rangle$ and $|1\rangle$ that constitute the basis of the two-dimensional Hilbert space in which the qubit lives. Additionally, one must be able to generate entanglement between qubits. That is, it must be possible to build an n-qubit state which is not the product of the states of each qubit, and instead lives in a 2^n-dimensional Hilbert space.

2. The experimenter must have the ability to *initialize* the state of the qubits to a fiducial reference state, such as $|0\rangle^n$. The reason for this comes from the need to know the state of the qubit register at the beginning of a computation. A method to achieve this is for example by cooling the system to the ground state $|0\rangle$ of each qubit, or through a projective measurement.

3. The qubits must possess *longer coherence times* than the typical gate times. Decoherence processes influence the state of the qubit in ways that cannot be controlled, for example by coupling its 2-dimensional subspace to a higher dimensional Hilbert space. The latter can

be either represented by levels above the qubit subspace, or by the external environment. This ultimately undermines the quantum properties of the system and results in the loss of the information encoded in it. Consequently, quantum operations must be performed before this information is lost.

4. The experimenter needs to be able to implement a *universal set* of quantum gates. Indeed, quantum computation requires that the state of the n qubits could be evolved to any possible state of their 2^n-dimensional Hilbert space through unitary transformations U. This problem reduces to the possibility of implementing a finite set of gates, which in turn can be combined into any n-qubit transformation. This set usually includes a certain number of single-qubit gates, and a single two-qubit gate to generate entanglement.

5. It must be possible to operate projective measurements on the state of the qubits. This is necessary if one wants to know the results of a computation. The reliability of a measurement is measured in terms of quantum efficiency, and depends on how well we can measure the state of $j < n$ qubits without changing the state of the rest of the quantum computer. Although an efficiency of 100% is not possible to achieve, it can be progressively increased, for example by repeating the calculations and measurements multiple times.

Two additional criteria regard the possibility of implementing quantum communication through the use of flying qubits, as previously described in Sec. 1.1.1.

There is potentially an infinite number of quantum systems that can be harnessed for the implementation of a qubit under the criteria illustrated above. The most promising ones include photons [164], cold atoms [165], superconducting qubits [166], and many more, each one offering unique advantages in terms of manipulation and coherence. Here we focus on one of the most natural implementations of the qubit into the spin degree of freedom of a quantum system. We talk in this case about *spin qubits* [13]. The kind of spin qubit is first of all determined by the number of spins used to encode the qubit. First, the Loss-DiVincenzo (LD) qubit [12] uses the *up* and *down* spin states of a single electron or quasi-particle, and is controlled through oscillating electromagnetic fields. A second implementation extends the same concept to multiple spins, by encoding the qubit into the singlet ($|S\rangle$, spin antisymmetric) and triplet ($|T_0\rangle$, spin symmetric) states generated by the exchange interaction (singlet-triplet qubit, ST_0) [167]. A third kind of spin qubit, unlike the previous two, allows for complete control using only the exchange interaction (exchange-only qubit, EO) [168]. This classification is extremely simplistic. Indeed, a wide variety of flavors exist for each of these macro-categories, depending on the number and species of particles considered; the kind of site used for single- or multi-site arrangements; and gate implementation.

4.1.1 The Loss-DiVincenzo scheme

In this Thesis, we will consider an implementation of the LD qubit very similar to the scheme first proposed by Loss and DiVincenzo in 1998 [12, 23]. In their scheme, they identified the states $|0\rangle$ and $|1\rangle$ of the qubits with the intrinsic spin-1/2 degree of freedom of an electron:

$$|0\rangle \equiv |\Downarrow\rangle \ , \quad |1\rangle \equiv |\Uparrow\rangle \ , \tag{4.2}$$

which in turn is confined in an isolated site, namely a quantum dot. In these systems, which can be effectively compared to 'artificial atoms', the quasi-0D confinement induces the quantization of the energy levels and localized wave functions that are analogous to atomic orbitals [169]. A

possible way to obtain a quantum dot is to exploit the confinement due to the band structure of low-dimensional 2D or 1D nanostructures, and further confining the particle in all other directions through electrostatic potentials generated by metallic gates. We talk in this case of *gate-defined* quantum dots. A more in-depth review of the implementations of gate-defined quantum dots for spin-qubits is reported in Sec. 4.2.1, with a special focus on Si- and Ge-based devices.

Single- and two-qubit gates

In presence of a magnetic field $\mathbf{B}$, the effective single-spin Zeeman Hamiltonian becomes:

$$H_Z = g^* \mu_B \mathbf{B} \cdot \mathbf{S}\,, \tag{4.3}$$

where μ_B is Bohr's magneton, and $\mathbf{S}$ is the electron spin. The quantity g^* is the effective g-factor, which in principle depends on the orientation of the magnetic field. This is usually taken into account by defining a g-tensor $\hat{g}$ [170], which can be more or less isotropic depending on the considered implementation (see Sec. 4.2.2). For a given field orientation $\mathbf{b} = \mathbf{B}/B$, we have $g^* = |\hat{g}\mathbf{b}|$.

Looking at Eq. (4.3), it's clear that single-qubit operations can straightforwardly be translated to the time-dependent control of either $\mathbf{B}$ or g^*. Over the years, this has been done in several different ways. The most direct one is based on electron spin resonance (ESR) [171–173], and consists of applying a combination of static and oscillating magnetic fields: the first one lifts the spin degeneracy, and the second one induces a transition between the spin states. In the original LD scheme

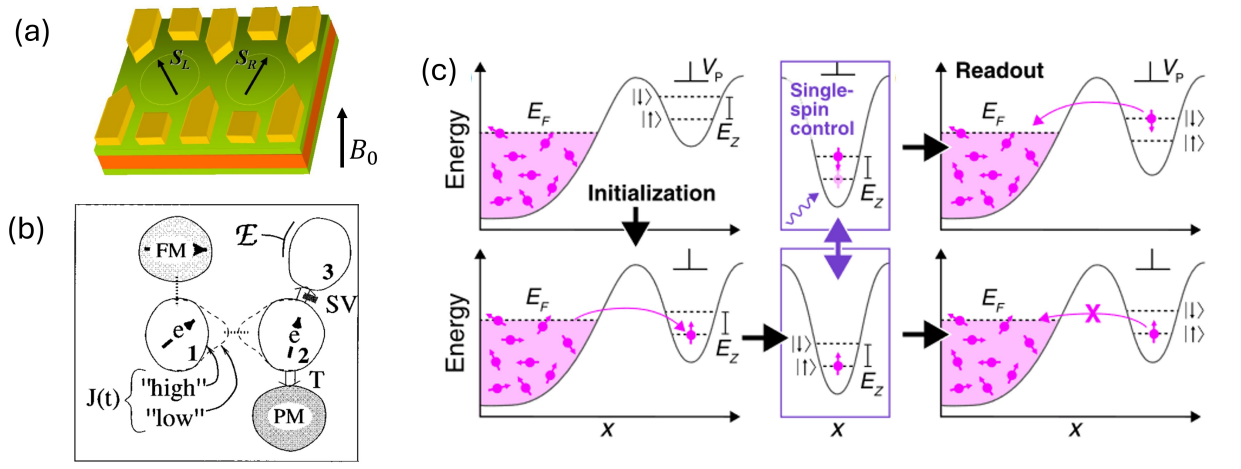


Figure 4.1: (a) Schematic representation of two LD spin qubits in gate-defined quantum dots. In green and orange are the layers of the heterostructure defining the 2DEG. In yellow are the metallic top gates defining the in-plane confinement of the dots. The action of a magnetic field $\mathbf{B}_0$ is necessary for the functioning of the qubits. (b) Original proposal by Loss and DiVincenzo, illustrating the interdot coupling for two-qubit gates through the control of the interdot barrier, either 'high' (continuous line) or 'low' (dashed line). FM/PM and SV are respectively ferromagnetic/paramagnetic elements and a 'spin valve', used for control and initialization/read-out. E is a fermionic bath. (c) Detailed procedures of initialization/read-out by coupling the quantum dot with the fermionic bath and using the Pauli spin blockade. E_Z is the Zeeman splitting induced by a static magnetic field, while V_P is the potential pulse used to the qubit energy levels above or below the Fermi energy E_F. Panels (a) and (c) are adapted from [13]; panel (b) is taken from [12].

[12], manipulation on a specific qubit could be turned on and off by lowering the barrier between the quantum dot of the qubit and a ferromagnetic dot made of ferromagnetic ordered material [see Fig. 4.1(b)]. This method however is not ideal, since oscillating magnetic fields are difficult to localize on single sites. This problem can be circumvented by using oscillating electric fields, which instead are easier to produce using local gates. However, this requires either magnetic-field gradients [174], or that the system naturally possesses spin-orbit coupling (SOC) [175], so that electron dipole spin resonance (EDSR) can occur (see Sec. 4.2.2 for further details).

Within this scheme, two-qubit gates are governed by the exchange interaction between spins $\mathbf{S}_i$ and $\mathbf{S}_j$ localized on neighboring sites. This process is illustrated schematically in Fig. 4.1(b): by controlling the barrier between the two dots, one can define a regime in which the interaction is turned on ('low' barrier) or off ('high' barrier). This process defines a time-dependent tunneling parameter $t_0(t)$ between the dots, which, when the barrier is low, allows for the two spin states to partially overlap. Under these conditions, the arising singlet and triplet states are energetically separated by the *exchange coupling*, $J(t) = 4t_0^2(t)/u$, with u the charging energy of a single dot. This term is sometimes referred to as kinetic exchange. Indeed, it leads back to the fact that two electrons in the singlet state are allowed to move back and forth between sites, while the same motion is forbidden for the triplet states. The term $J(t)$ describes the interaction between spins by entering the two-spin Heisenberg Hamiltonian:

$$H_{H,ij}(t) = J(t)_{ij}\mathbf{S}_i \cdot \mathbf{S}_j \,. \tag{4.4}$$

With this time-dependent Hamiltonian, one can straightforwardly create entanglement between adjacent spins, for example by performing SWAP or XOR gates [12]. Specifically, one can directly manipulate the value of J over time by varying the same gate voltages that are used for the definition of the quantum dots, for example through pulse or AC fields [173].

Qubit definition, initialization and read-out

The procedures described for the implementation of single- and two-qubit gates satisfy the 4th DiVincenzo criterion listed above. All other requirements are also met under specific conditions. For example, the qubits are well characterized (1st criterion) as long as the other energy states inside the quantum dot can be ignored. This condition implies that (i) the energy splitting ΔE between the qubit states and the first higher energy state is much higher than the thermal energy $k_B T$, with k_B the Boltzmann constant; and (ii) that the time scales of all operations are longer than $\hbar/\Delta E$. In this way, all transitions involving higher levels are avoided.

As for state initialization (2nd criterion), a possible approach could be to wait for the spin state to decay to its lower energy state through thermalization processes. However, this method is extremely time-consuming and does not ensure high enough fidelity. Instead, the initial proposal by Loss and DiVincenzo [12] considered spin-selective paramagnetic elements to which the qubit spin could tunnel, and a positively operator-valued measurement (POVM) on the spin would consist of measuring the magnetization induced by the spin. Alternatively, a spin-dependent, switchable 'spin valve', as they called it, could be used [see Fig. 4.1(b)]. In practice, this approach is translated into the use of the Pauli spin blockade, a method that consists of connecting the quantum dot to an external fermionic bath in a way that allows only the lower-energy spin-down state to tunnel into the quantum dot. This process is illustrated in Fig. 4.1(c): here, the action of a high enough static magnetic field must induce a Zeeman splitting $E_Z = g\mu_B B$ much higher than the electron

thermal energy $k_B T_e$. Consequently, short (~ 100 ps) time-dependent pulses V_P lower the quantum dot energy so that only the down state of the qubit is below the Fermi energy of the bath. In this way, an electron with spin down could tunnel from the bath to the dot, while the same process is forbidden for electrons with spin up.

Similarly for read-out (5th criterion), the system is brought again into the same configuration, and now only the spin-up state has a high enough energy to allow tunneling into the fermionic bath. Following a charge measurement on the reservoir, one is able to infer whether the electron has tunneled or not. Consequently, the outcome tells whether the spin state of the electron was up or down, and effectively implements a POVM. This technique, also called Elzerman read-out from its first experimental demonstration [176], usually requires high magnetic fields, especially in systems with modest g-factors such as GaAs, and low-temperature regimes. This method also requires that the read-out be done on quantum dots that are adjacent to a fermionic bath, so that read-out on central dots would require an additional transport of the spin state at the edge of the array. Finally, one must pay additional attention to the tunneling rate, which must be high enough to avoid spin relaxation and low enough compared to the charge measurement bandwidth.

4.1.2 Spin-qubit decoherence

In quantum computation one needs to perform a potentially long series of elementary operations that constitute a quantum algorithm. The accuracy of these operations, and consequently of the results of the computation, is undermined by the finite lifetimes of the qubit and by the errors induced by them [177]. Furthermore, the errors build up as the number of operations increases, so that they become extremely relevant for most existing algorithms. This issue is usually addressed through quantum error correction techniques [178], which are able to partially remove errors from the computations. However, these procedures must correct errors faster than they occur, which is only possible if the probability of an error occurring falls below a specific rate for each operation. This is also called the *fault-tolerance threshold* [179–181]. Moreover, this level of accuracy comes with a price, since it normally requires a large redundancy in the number of physical qubits required. Consequently, it's of fundamental importance to first and foremost address the specific phenomena that induce errors in the system, by trying to possibly remove them or, at least, minimize their effect.

This brings us to the final requirement for the implementation of a qubit, which is the necessity for long coherence times (3rd criterion). As previously mentioned, decoherence phenomena come from any unwanted interaction between the qubit and its surroundings. These phenomena define the lifetime of the qubit, after which its encoded information gets erased and can no longer be retrieved. In simple terms, the coherence time can be extracted from an experiment by looking at the time after which oscillations caused by quantum superposition can no longer be observed [182]. A spin qubit in the LD scheme can undergo a wide range of different decoherence processes, which however can all be studied through the introduction of an *envelope function* describing the decrease in population contrast. In first approximation indeed we can write the occupation probability of state $|1\rangle$ as:

$$p_1 = q(t) p_{1,coh} + \frac{1}{2}[1 - q(t)]\,, \tag{4.5}$$

where $p_{1,coh}$ is the occupation probability in the coherent case (i.e. with no decoherence), and the shape of $q(t)$ in time is determined by the specific process. Specifically, we can mainly distinguish

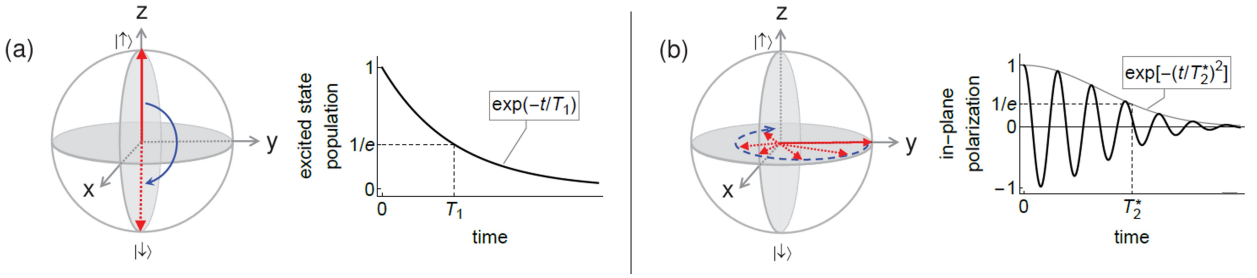


Figure 4.2: (a) Schematization of a relaxation decaying process of a qubit represented on the Bloch sphere (left panel), and relative exponential decay in the population of state $|1\rangle$ (right panel), characterized by characteristic lifetime T_1. (b) Dephasing decaying process as represented on the Bloch sphere (left panel) and relative decay in the Ramsey oscillations (right panel), characterized by lifetime T_2^*. The left panels of both (a) and (b) are taken from [188], while the right panels are from [182].

two categories. The first one involves the relaxation of the qubit to the ground state, usually attributed to thermalization or, for spin qubits, to transverse fluctuating magnetic fields [182]. This process, also referred to as *longitudinal relaxation*, is illustrated in Fig. 4.2(a), and corresponds to a decay in the qubit energy, with subsequent decrease (increase) in the population of state $|1\rangle$ ($|0\rangle$). The characteristic coherence time in this case is referred to as T_1, and the envelope function is usually found to decay exponentially.

The second category of decoherence processes, also called *tranverse relaxation*, relates instead to a phase change of the state along the equator, as is illustrated in Fig. 4.2(b). These processes are defined by the times T_2, and usually show Gaussian decays. For spin qubits, these decays are prevalently due to the hyperfine interaction with the fluctuating nuclear spins inside the device [183] (see Sec. 4.2.1 for further details). The parameter T_2 can be further distinguished into two categories. Firstly, T_2^{Rabi} is the lifetime of the coherent oscillations induced by driving pulses, and can be measured through a Rabi scheme [184] by applying pulses of varying time t and measuring the outcome probability of state $|1\rangle$ as a function of t. Secondly, T_2^* is the inhomogeneous dephasing time during free evolution. This is instead measured through a Ramsey experiment [185], in which the qubit is initialized as a $50-50\%$ superposition of states $|0\rangle$ and $|1\rangle$, and is then measured again after a free precession of time τ. The coherence time can be usually increased by trying to protect the spin qubit through various protocols. Among these, the simplest one is the Hahn-echo protocol [186], which resets the qubit state by rotating it of an angle of π in the middle of the free evolution. The resulting lifetime after this protocol, T_2^{Echo}, can be several orders of magnitude larger than T_2^* [182, 187].

As is clear by now, the coherence times of a qubit impose an upper limit for the timescale of the computation, and can consequently be used to make qualitative comparisons between different implementations of the qubit. We will see later how this translates to our system of interest.

4.2 Integrated devices in Si and Ge

Among the most promising platforms for the implementation of spin qubits in quantum computing are semiconductor devices based on Si and Ge. The key advantage of these materials is

the possibility to rely on well-established manufacturing techniques which, especially for Si, have been refined over decades for the semiconductor industry [181]. This compatibility allows for the potential integration of spin qubits with classical electronics, facilitating the integration of quantum processors alongside modern technology. These aspects would make spin qubit devices not only cost-effective, but in principle also as scalable as the conventional chips of classical computation, facilitating the realization of dense arrays of spin qubits [189, 190]. The latter is a factor that is essential if one aims at building functioning quantum computers. Indeed, the implementation of complex quantum algorithms and the necessary procedures of quantum error correction would require the use of millions of qubits [191].

Another consequence of the compatibility of Si and Ge devices with modern technology is the high degree of tunability and control of spin qubits. Thanks to this, all quantum computational tasks have now reached fidelities above the fault-tolerant threshold in all quantum computational tasks. Indeed, single- and double-qubit gates have reached a fidelity higher than respectively 99.9% [179, 192, 193] and 99.5% [180, 181], while initialization and read-out reach respectively 97.5% [180, 194] and 99% [194–196]. An extremely important detail is that these fidelities are also maintained at temperatures of the order of a few K [14, 197–200], much higher than those of a few mK's required for the operability of other qubits [166]. This means that operating spin qubits requires instead an easier cooling process, thus reducing the need for complex and expensive cryogenic systems, which are usually cumbersome and require significant resources to operate. In addition to all of this, spin qubits show great compatibility also with other quantum platforms, from photonic qubits [201, 202] to superconducting qubits [203, 204], to topological systems [204, 205], and more.

4.2.1 Overview on device design for gate-defined quantum dots

That said, there have been many challenges in translating modern semiconductor information technology for applications in quantum computation. First of all, while devices for classical computation rely mainly on the charge degree of freedom and on the transport properties of electrons, spin qubits are based on the behavior of a single electron trapped in a quantum dot. Consequently, adaptations are needed if one wants to adopt the standard transistor technology. We see below how this translates into the fabrication of spin-qubit devices, by giving a brief overview of the principal designs of Si- and Ge-based devices that are currently employed for the implementation of spin qubits. These devices are all schematically illustrated in Fig. 4.3.

As mentioned in Sec. 4.1.1, LD spin qubits can be implemented inside gate-defined quantum dots built within heterojunctions that define 1D and 2D nanostructures, the electronic structure of which can be optimized to find suitable quality and operational regimes. In this sense, two of the most important quantities that are taken into account to determine the performance of the device are electron/hole mobility and percolation density. The first is strictly related to the particle's effective mass, which in turn is determined by the band curvature in the Brillouin zone. The mobility μ can be measured through the classical Hall effect [206], and is highly dependent on the carrier density n/p (respectively for electrons/holes) inside the channel. Indeed, as n or p increase, the long-range Coulomb scattering with impurities gets increasingly screened, until only short-range scattering is permitted and the mobility saturates. Since μ gives an idea of disorder in the crystal, it indirectly becomes a good indicator of the presence of possible noise sources for spin qubits as well. The second quantity that we mentioned, the percolation density n_p/p_p, is related to the

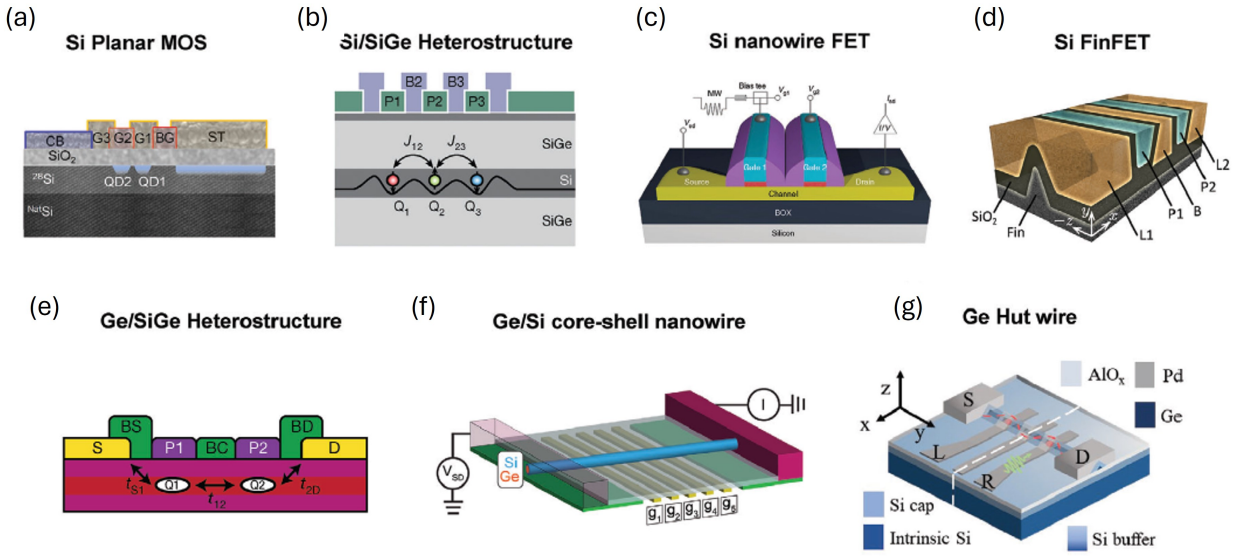


Figure 4.3: Schematic cross-sections of several Si-based (top row) and Ge-based (bottom row) devices. See the main text for their description. (a) Si planar MOS [208]; (b) Si/SiGe heterostructure [209]; (c) Si nanowire FET [210]; (d) Si FinFET [211]; (e) Ge/SiGe heterostructure [212]; (f) Ge/Si core-shell nanowire [213]; (g) Ge hut wire [214]. The panels were adapted from [215].

metal-insulator transition at low carrier densities in 2DEG/2DHG (2D Hole Gas), and is obtained through the analysis of the longitudinal conductivity [207]. The value of n_P/p_P is indicative of disorder at very low densities and without screening, i.e. in the regime of interest when considering the isolation of single particles in quantum dot systems. Consequently, it's as relevant for spin qubits as the charge mobility, if not even more.

The first category of gate-defined quantum dots are *planar* quantum dots. In this case, a 2DEG or 2DHG is confined in a quantum well along the growth direction of a layered semiconductor heterostructure. This *out-of-plane* confinement is created at the interface between materials due to the offset between the conduction or valence bands, respectively for electron- or hole-spin qubits. The remaining, *in-plane* confinement, is created by gates positioned on top of the device. The first Si-based device of this kind is schematically illustrated in Fig. 4.3(a). It consists of a planar metal-oxide-semiconductor (MOS) device, in which a layer of SiO_2 is thermally oxidated on top of Si [216–218] and creates an approximately triangular confinement. In this device, there's close to no mismatch between the two lattices involved, so the strain effects felt by the confined particle are negligible. The main advantage for electron-spin qubits in this structure is that the six-fold degeneracy of the conduction band minimum, usually detrimental for quantum computation, is removed. The valley splitting can be tuned through electrical means to be as high as 0.8 meV [219, 220], and allows for operation at temperatures of 1 K and higher [199, 221]. However, the atomic mismatch between Si and SiO_2 creates defects at the interface, which limit the mobility of the channel (around $10^4\,\mathrm{cm^2V^{-1}s^{-1}}$) [218, 222] and may produce electrical noise that reduces the fidelity of qubit gates [223, 224].

On the contrary, in Si/SiGe and Ge/SiGe heterostructures [Fig. 4.3(b), (e)] the particle is localized in a strained layer, made of Si or Ge, enclosed between two relaxed $Si_{1-x}Ge_x$ layers. The whole

structure is grown on a Si substrate, usually by means of reduced pressure chemical vapor deposition [226], and can be separated from the metallic gates on top thanks to an additional semiconductor layer. The concentration x of Ge is constant in the upper layer, while in the bottom layer it gradually increases from the Si substrate, in order to reduce the density of dislocations [222]. In addition, since here the 2DEG/2DHG is usually located much farther away from the gate-oxide interface with respect to MOS devices, the particles present a mobility of around one or more orders of magnitude larger ($\sim 10^5\,\mathrm{cm^2V^{-1}s^{-1}}$ for electrons in Si and $\sim 10^6\,\mathrm{cm^2V^{-1}s^{-1}}$ for holes in Ge), as well as low percolation density ($\sim 10^{10}\,\mathrm{cm^{-2}}$) [227–230]. On the other hand, the valley splittings are significantly reduced for electrons ($\lesssim 200\,\mu\mathrm{eV}$) [227]. Ge/SiGe heterostructures particularly show very promising perspectives for the implementation of large arrays of hole-spin qubits, with recent works demonstrating a 4-qubit array [225] (see Fig. 4.4), a 16-qubit array [231], and the possibility of multilayer stacking [232].

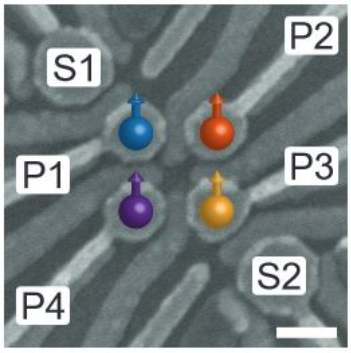


Figure 4.4: Scanning electron microscope of a 4-qubit array implemented in a Ge/SiGe heterostructure. Each qubit (colored arrows) is defined under a plunger gate (P1-4) and can be measured through charge sensors (S1-2). The scale bar is 100 nm long. The picture was taken from [225].

Other Si- and Ge-based devices are obtained from 1D structures. For example, a Si nanowire can be built through etching techniques directly on top of a foundry-compatible silicon-on-insulator (SOI) device [210]. This creates a channel that connects a source and a drain, thus effectively creating a field-effect transistor (FET) [see Fig. 4.3(c)]. The gates here create confinement along the direction of the channel, and trap either electrons or holes depending on the type of doping atoms at the source and drain. In this device, the electron's valley splitting can be as high as 0.7 meV [233]. Similarly, particles can be localized in the channel of a nano-scaled MOSFET [189] or a FinFET [Fig. 4.3(d)]. In the latter case, in a device with a triangular cross-section a hole-spin qubit has recently been implemented and operated at 4 K [14]. Generally, in these devices, both electron- and hole-spin qubits show very high performance [7, 189] as well as extremely long coherence times [182]. Holes are also widely implemented in Ge/Si core-shell nanowires created with vapor liquid solid methods [Fig. 4.3(f)]. In these systems, the hole is confined in the Ge core, and its performances and electronic properties, among which the mobility, are highly tunable by controlling the growth direction, reaching values as high as $\mu \sim 4 \cdot 10^4\,\mathrm{cm^2V^{-1}s^{-1}}$ at 4 K [234]. Finally, self-assembled Ge hut wires with triangular cross-sections can be grown on top of Si wafers by means of molecular beam epitaxy [235, 236]. These wires are fully strained, and present properties more similar to those of planar structures than to quantum wires [235, 237].

Hyperfine interaction and isotopic purification

Other than device design, there are several other properties that may not affect standard transistors, while instead crucially limiting the development of quantum technology with spin qubits. For instance, one of the main challenges in this sense is the sensitivity of localized spins to noise caused by the surrounding environment, which undermines spin coherence. That is why, as briefly

mentioned in Sec. 4.1.2, the most relevant cause of decoherence for spin qubits is the hyperfine interaction, which couples the spin of the qubit with the nuclear spins of the material. The interaction Hamiltonian between one electron and many nuclear spins consists of three terms [183]. The first one is the Fermi contact interaction between the carrier's spin and the nuclear spins; the second couples the latter to the electric current due to the carrier's orbital momentum; and the third is the dipole interaction between spins. Although this Hamiltonian shows a quite complicated shape, its projection on the 2D subspace of the spin qubit returns an effective hyperfine interaction Hamiltonian:

$$H_{hf} = \mathbf{h} \cdot \mathbf{S}\,, \tag{4.6}$$

where $\mathbf{h}$ takes the name of Overhauser field. By comparing the shape of this Hamiltonian with Eq. (4.3), it's clear to see that $\mathbf{h}$ can be viewed as an effective magnetic field. Just like for the effective g-tensor, its value may be more or less isotropic depending on the considered spin-qubit implementation and device characteristics [238] (see Sec. 4.2.2 for further details on our system of interest).

Historically, the need to reduce the hyperfine interaction was the reason why Si and Ge have replaced GaAs and other III-V group materials for implementing spin qubits in semiconductor devices. Indeed, the stable isotopes of gallium (^{69}Ga and ^{71}Ga) and arsenic (^{75}As) that make up GaAs devices all show a nuclear spin of 3/2 [240]. Instead, natural mixtures of IV-group elements present a natural abundance of stable spinless isotopes. For silicon, the isotopes ^{28}Si (92,2%) and ^{30}Si (3,1%) possess zero spin, while only ^{29}Si (4.7%) has a spin of 1/2 [240, 241]. The spinless isotopes of germanium instead are ^{70}Ge (20,5%), ^{72}Ge (27,5%), ^{74}Ge (36,5%) and the slightly radioactive ^{76}Ge (7,76%), while only ^{73}Ge (7.75%) shows a spin of 9/2 [226, 240].

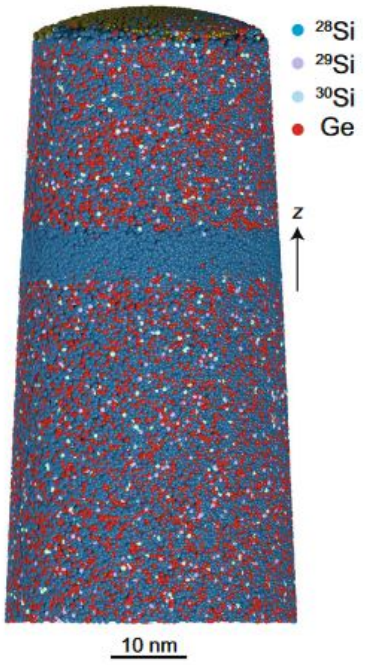


Figure 4.5: Atom-probe tomography of a ^{28}Si/SiGe heterojunction. The picture was taken from [239].

In addition, the hyperfine interaction inside Si and Ge heterostructures can be even further reduced through isotopic purification. The procedure that is used in this case is illustrated in Fig. 4.6 for a ^{28}Si/^{28}SiO$_2$ interface, but is equivalent for other Si heterostructures as well as for Ge [218, 226, 242]. It starts with a silicon-tetrafluoride gas composed of the natural mixture of Si isotopes, which undergoes centrifuge separation to increase the percentage of ^{28}Si to 99.92%, with a remaining ^{29}Si concentration of 0.08%. Subsequently, the gas is reduced to obtain high purity ^{28}SiH$_4$. Finally, a layer of ^{28}Si is deposited through chemical vapor deposition. Figure 4.5 shows the atomic composition of a ^{28}Si/SiGe heterostructure, in which we can clearly observe the isotopically enriched layer of ^{28}Si in correspondence of the quantum well occupied by the 2DEG/2DHG [239]. Since the percentage of all other isotopes is close to none in that region, so is the number of nuclear spins that can interact with the spin qubit, and the hyperfine interaction felt by the confined particle is extremely low. Consequently, the electron/hole mobilities, the valley splittings, and most importantly qubit coherence are all significantly increased [218, 239, 243, 244].

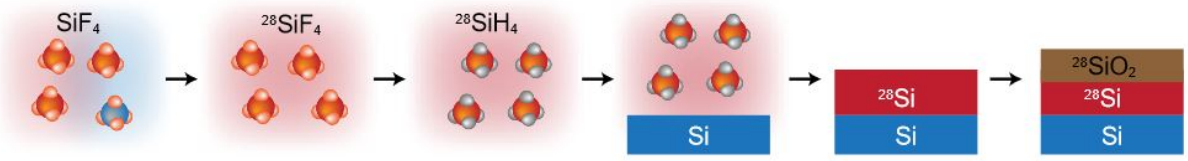


Figure 4.6: Schematic procedure for the production of a $^{28}Si/^{28}SiO_2$ interface, as described in the main text. ^{29}Si atoms are in blue, ^{28}Si in red, F in orange and H in grey. The panels are taken from [218].

4.2.2 Characteristics of hole-spin qubits

Now that we have given a general description of the possible devices used to implement spin qubits, for the rest of this Thesis we will focus on hole-spin qubits, that is, on encoding the qubit in the state of a particle at the top of the valence band. The first advantage with respect to electrons is that the top of the valence band is located at a single point in the Brillouin zone, i.e. Γ. In this way, hole-spin qubits do not present the difficulty of dealing with the six-fold valley degeneracy typical of electron-spin qubits. In addition to that, the bottom of the conduction band in bulk Si and Ge is contributed by s orbitals, while the top of the valence band by p orbitals. Since the gate-defined quantum dots are usually tens of nanometers in size, the same composition is maintained in first approximation also by the states of a confined electron and hole, respectively. Consequently, since p orbitals show a node at the position of the atomic nuclei, the contact interaction entering the hyperfine Hamiltonian in Eq. (4.6) is much lower for holes with respect to electrons, and noise is expected to reduce. That said, there are many other consequences arising from the composition of hole states, often fundamental in describing the behavior of holes and in tuning and exploiting them for an efficient implementation of spin qubits.

Spin-orbit coupling

Being the orbital momentum of p orbitals equal to $l = |\mathbf{l}| = 1$, the hole states at the top of the valence band are necessarily influenced by the atomic SOC. That is, the relativistic interaction between a particle's spin and its motion inside the potential generated by the atomic nucleus. The rules of momentum composition of quantum mechanics tell us that the total angular momentum of holes at the top of the valence bands, $\mathbf{j} = \mathbf{l} + \mathbf{s}$, can be in modulus either $j = |\mathbf{j}| = 3/2$ or $1/2$. Consequently, we can identify a total of three sub-bands making up the valence band at Γ, as also shown by *ab initio* calculations [see Fig. 4.7(a)]: the heavy-hole (HH) bands, with $j = 3/2$ and $j_z = \pm 3/2$; the light-hole bands, $j = 3/2$ and $j_z = \pm 1/2$; and the split-off bands, $j = 1/2$ and $j_z = \pm 1/2$. Without the $\mathbf{l} \cdot \mathbf{s}$ interaction due to the atomic SOC, these bands would all be degenerate. Instead, the SOC introduces an energy splitting between the quartet of HH+LH bands and the SO band, called Δ_{SO} [Fig. 4.7(b)]. Since in Si this parameter is $\Delta_{SO} = 44\,\text{meV}$, the SO band contributes significantly to the hole states at the top of the valence bands. Instead, the splitting in Ge is much larger, $\Delta_{SO} = 290\,\text{meV}$, and the description of hole states is usually simplified by only treating the HH and LH bands, degenerate at Γ.

Additional SOC effects arise due to the breaking of the inversion symmetry. These are mainly distinguished into two categories: the Dresselhaus effect [175] and the Rashba effect [248]. The former is related to the bulk inversion asymmetry (BIA), which is absent in Si and Ge. Instead, the

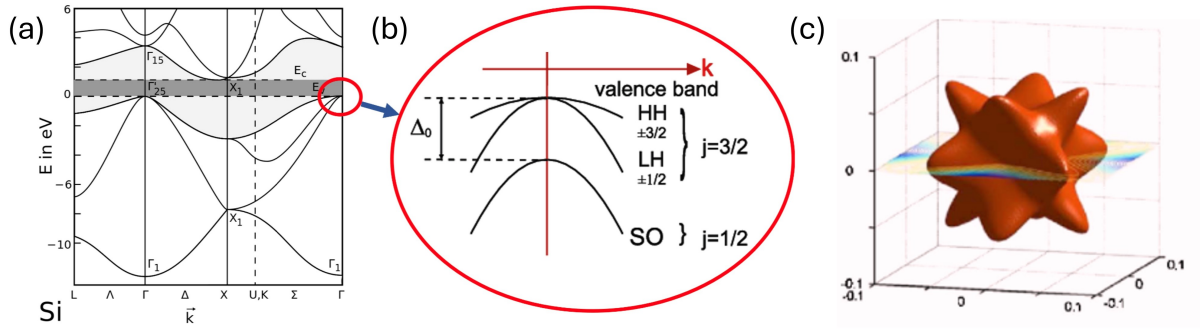


Figure 4.7: (a) Band structure in the first Brillouin zone of Si obtained through *ab initio* calculations. (b) Schematic diagram of the top of the Si and Ge valence band. (c) 3D equienergy surface at 25 meV for the top of the valence band of Si. Panel (a) was taken from [245]; panel (b) from [246]. Panel (c) from [247].

latter comes from the structural inversion asymmetry (SIA). In low-dimensional systems, such as the 2D interfaces, 1D nanostructures and 0D quantum dots implemented in the Si- and Ge-based devices illustrated in Sec. 4.2.1, the SIA can be introduced through the action of electrostatic fields along the confining directions [249]. Consequently, the Rashba SOC introduces a straightforward dependence of the hole state on the macroscopic degrees of freedom of the system, which makes it possible to electrically manipulate the hole-spin qubit through EDSR. Additionally, the spin-charge hybridization caused by the high SOC of holes allows for spin-photon interactions (SPI). These, in turn, make it possible to use cavity quantum electrodynamics as a means to couple distant dots [250], thus significantly increasing the feasibility of large-scale spin-qubit networks. Moreover, the electric dipole can be further increased through the use of a double quantum dot (DQD) rather than a single quantum dot (SQD) [251].

All of this translates into a significant advantage with respect to electron-spin qubits. Indeed, electrons show natural SOC effects that are much weaker than holes. Consequently, if one wants to achieve the same performance through the use of ESDR and SPI, an additional synthetic SOC must be introduced. The usual way to do this implies the use of a micromagnet [174], which causes an inhomogeneous magnetic field in the system. However, this increases the complexity of the experimental apparatus required for qubit manipulation, and is consequently unfavorable for large-scale integration. On the other hand, SOC is a double-edged sword for hole-spin qubits, since it also increases the sensitivity to several noise sources, such as charge-noise [252] and phonon-assisted relaxation [253]. That said, one can carefully tune the electrostatic confinement by choosing appropriate structural geometries and magnetic field orientations, in order to find so-called *sweet spots* [15, 254]. That is, an optimal regime can be reached, in which the hole state can be manipulated efficiently while minimizing the susceptibility to noise. In this way, long coherence times were found, up to several μs [14, 182, 254] [see Fig. 4.8(a)].

Band mixing

As shown by Fig. 4.7(c), the top of the valence band in Si is anisotropic, and similarly for Ge, though to a lower extent [247]. This means that the curvature of HH and LH bands, and conse-

quently their effective mass, is different along different crystallographic directions. In all cases, the hole mass is lighter than the one usually found for electrons in the same systems, consequently implying the possibility of reaching much higher mobilities [228]. Specifically, the LH bands show a lighter effective mass with respect to the HH bands along the crystallographic axis $\mathbf{z} \parallel [001]$, parallel to the growth direction in most heterostructures (out-of-plane). However, along the orthogonal directions (in-plane), the effective mass is instead lighter in the HH bands. From these considerations, we can imagine that the band mixing of hole states can be appropriately tuned through the relative confinement strengths of the implemented quantum dot. For instance, hole-spin qubits in planar quantum dots show a highly predominant HH nature [255]. Indeed, here the in-plane confinement is usually weaker than the out-of-plane one, so that the hole will more easily occupy those states that have a higher out-of-plane mass. This is even truer in strained systems, in which the strain Hamiltonian induces an additional HH/LH energy splitting that increases the LH energy with respect to the HH [256]. On the contrary, quantum dots in 1D nanowires present much stronger confinement in two directions rather than one, and consequently show a great degree of HH/LH mixing, highly dependent on the growth direction and gate confinement [257]. Here a particularly strong kind of Rashba coupling is present, called direct Rashba spin-orbit interaction (DRSOI). This comes from the coupling between HH and LH states, and remains significant even in the presence of strain [258].

The anisotropy of the HH and LH bands is also reflected in the effective g-factor defined in Eq. (4.3). Indeed, contrarily to the roughly constant value of g^* for electrons, the same quantity for holes is instead highly dependent on the orientation of the magnetic field [Fig. 4.8(b)]. This is especially true in planar quantum dots, since the HH bands are much more anisotropic than the LH ones [259]. In this case, the primary magnetic axis of the g-tensor $\hat{g}$ is usually oriented along the direction of the strongest confinement (out-of-plane). That said, the HH/LH mixing makes it pos-

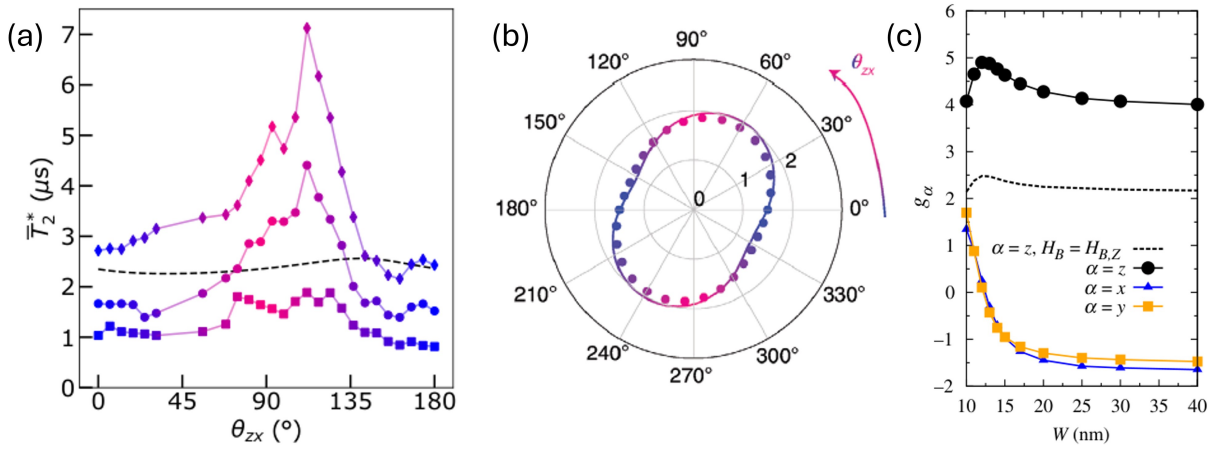


Figure 4.8: (a) Mean inhomogeneous dephasing time $\bar{T}_2^*$ and (b) g-factor for a hole-spin qubit in a Si nanowire FET, as a function of the angle θ_{zx} defining the magnetic field orientation. The dashed black line in (a) is the calculated time due to hyperfine interactions; the dots and solid line in (b) correspond respectively to measured and calculated results. (c) g-factor as a function of the channel width W inside a FDSOI p-MOSFET implemented in a Si/SiO_2 device. The dashed line only considers Zeeman contributions and neglects paramagnetic and diamagnetic terms in the system's Hamiltonian. Panels (a) and (b) are taken from [254]; panel (c) from [189].

sible instead to tune the anisotropies of $\hat{g}$ in a more controlled manner through the gate voltages or the device geometry [Fig. 4.8(c)], and, as mentioned before, find sweet spots for the operation of spin qubits [189, 254, 257]. For instance, comparisons between electron- and hole-spin qubits in Si MOS devices show a modulation of the g-factor that is six orders of magnitude larger for holes with respect to electrons [15].

Our device of choice

In the following Chapters we will focus on hole-spin qubits implemented with foundry-compatible complementary MOS (CMOS) technology in Si, in the scope of the IQubits project [2, 189, 255, 260–262]. Previous works [189, 263] demonstrated the operability of a hole-spin qubit in a commercial 22-nm fully-depleted silicon-on-insulator (FDSOI) MOSFET, as illustrated in Fig. 4.9(a), with g-factor highly tunable through the magnetic field orientation and channel width [Fig. 4.8(c)] and Rabi frequencies of the order of 100 MHz [189]. The dot confinement in this device is reported in Fig. 4.9(b): an out-of-plane electric field is generated through the action of a back gate at the bottom of the device (V_B). As explained above, this is necessary to manipulate the hole spin electrically through the Rashba SOC. The manipulation pulses are applied as a perturbation on the potential generated by the top-gates, used for the in-plane confinement along the channel length (V_G).

For simplicity of the numerical treatment, we will focus on a more planar structure, similar to those previously described in reference to Fig. 4.3(a), maintaining however the same confinement strengths as those simulated in our device of reference from [189]. Consequently, the only significant difference will be the shape of the confinement along one of the in-plane directions. However,

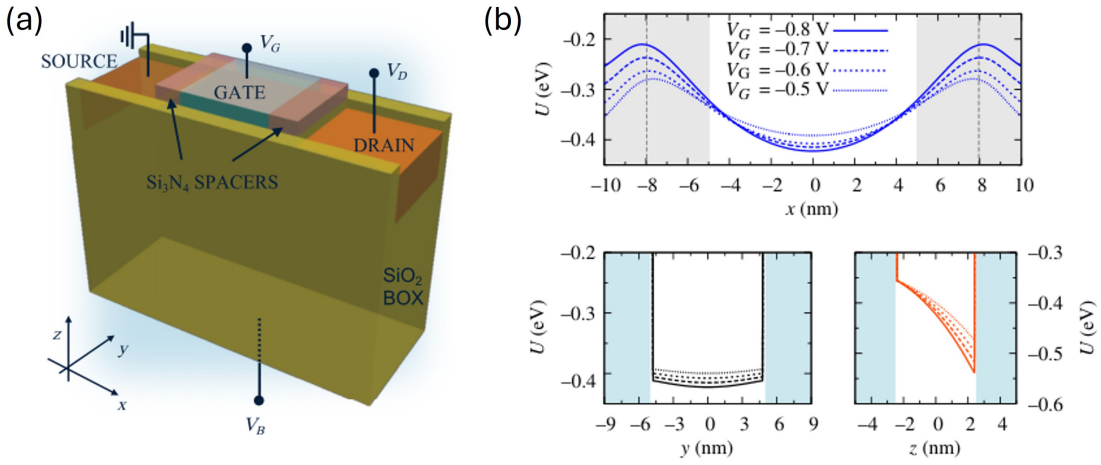


Figure 4.9: (a) Schematic representation of a FDSOI p-MOSFET transistor implemented in a Si/SiO_2 heterostructure. V_g is the potential of the metallic gate defining the confinement along the length of the channel. V_D is the potential applied on the drain with respect to the source. V_B is the back-gate potential. (b) Profiles of the confinement potentials defining the quantum dot along the coordinate axes: $y = z = 0$ for the top panel; $x = z = 0$ for the bottom left panel; $x = y = 0$ for the bottom right panel. The grey areas in the top panel show the source and drain regions, delimited by nitride spacers approximately at $5\,\text{nm} \leq |x| \leq 8\,\text{nm}$. The light blue areas in the bottom panels indicate the SiO_2 box. Both figures are taken from [189].

as we will show in the later chapters, the shape alone does not influence the hole state characteristics significantly, and the results on the figures of merit that we studied can be generalized [2]. Lastly, although we focus on unstrained Si-based devices, note that our numerical method can be extended to also treat Ge-based devices [255], as well as strained heterostructures with any shape of the confinement potential [262].

From time to time, I would gaze up at the stars after a night shift
and think that they looked like a glowing desert,
and I myself was a poor child abandoned in the desert...
I thought that life was truly an accident among accidents in the universe.

$\sim$ from *The Three-Body Problem*, by Cixin Liu

Chapter 5

Numerical models to describe hole-spin qubits in Si quantum dots

In this Chapter we describe the methods that we used to find the eigenstates of a hole in a Si quantum dot, and to model the behavior of the hole-spin qubit we consider. The first part, Sec. 5.1, illustrates the theory on the basis of the Hamiltonian we considered in our simulations. Our analysis starts in Sec. 5.1.1 from a review of the $\mathbf{k}\cdot\mathbf{p}$ method; then, Sec. 5.1.2 focuses on the 6×6 Luttinger-Kohn Hamiltonian for the valence band of Si and Ge, with SOC and an external potential. In Sec. 5.1.3 we explain how to break the time-reversal symmetry by introducing a constant magnetic field. Then, in the second part of the Chapter, Sec. 5.2, we explain the numerical methods used to diagonalize the described Hamiltonian. Specifically, Sec. 5.2.1 illustrates the chosen harmonic-oscillator basis, and Sec. 5.2.2 shows how to add a generic external potential. Sec. 5.2.3 focuses on the methods adopted for numerical analysis of the hole eigenstates. The third part of the Chapter, Sec. 5.3, introduces the confinement potentials used to describe SQDs and DQDs (Sec. 5.3.1) and their modification in the presence of an external charge in the device (Sec. 5.3.2). Finally, in Sec. 5.4, we describe the effective 2D system of the qubit. In Sec. 5.4.1 we define the SU(2) algebra, in which belong all operators acting on the qubit. We end with Sec. 5.4.2, with the analysis of the time-dependent evolution of the qubit, describing the state manipulation due to a driving pulse through the rotating wave approximation.

5.1 Six-band Hamiltonian in Si and Ge

Let's start the theoretical description of this Chapter by recalling the basic treatment of crystalline solids. Specifically, Si and Ge both present the same crystalline structure as diamond, i.e. an FCC lattice with a diatomic basis. Specifically, the positions of the two atoms of the basis are:

$$\mathbf{a}=(0,0,0),\quad \mathbf{b}=\frac{a}{4}(1,1,1), \tag{5.1}$$

where a is the lattice constant of the crystal, being $a=0.5431$ nm in Si and $a=0.5658$ nm in Ge. We define the basis vectors of the lattice as:

$$\mathbf{d_1}=\frac{a}{2}(0,1,1),\quad \mathbf{d_2}=\frac{a}{2}(1,0,1),\quad \mathbf{d_3}=\frac{a}{2}(1,1,0), \tag{5.2}$$

so that a generic lattice point can be written as:

$$\mathbf{R}\equiv\frac{a}{2}(n_2+n_3,n_1+n_3,n_1+n_2), \tag{5.3}$$

where $n_1, n_2, n_3 \in \mathbb{Z}$. At this point, we can write the Schrödinger equation for an electron inside of the system:

$$H\Psi_{n\mathbf{k}}(\mathbf{r}) = E_n(\mathbf{k})\Psi_{n\mathbf{k}}(r), \tag{5.4}$$

where the n is the band index of the electron and $\mathbf{k}$ is its crystalline wave vector. When no external potential is acting on the system, the Hamiltonian in Eq. (5.4) consists of a kinetic term and the atomic potential:

$$H = \frac{\mathbf{p}^2}{2m_0} + V(\mathbf{r}). \tag{5.5}$$

Specifically, the latter possesses the same periodicity of the lattice, so that we can write:

$$V(\mathbf{r} + \mathbf{R}) = V(\mathbf{r}). \tag{5.6}$$

Thanks to the periodic nature of the Hamiltonian, we can apply Bloch's theorem [264] and rewrite $\Psi_{n\mathbf{k}}(\mathbf{r})$ as a Bloch function, that is, the product of a plane wave $e^{i\mathbf{k}\cdot\mathbf{r}}$ and a periodic function $u_{n\mathbf{k}}(\mathbf{r})$ with the same periodicity of the crystal lattice:

$$\Psi_{n\mathbf{k}}(\mathbf{r}) = e^{i\mathbf{k}\cdot\mathbf{r}}u_{n\mathbf{k}}(\mathbf{r}), \tag{5.7}$$

$$u_{n\mathbf{k}}(\mathbf{r} + \mathbf{R}) = u_{n\mathbf{k}}(\mathbf{r}). \tag{5.8}$$

Note that while the plane wave part only depends on the wave vector $\mathbf{k}$, the periodic function also depends on the band index n. Recall that the Bloch's functions satisfy the following properties:

$$\langle \Psi_{n\mathbf{k}} | \Psi_{n'\mathbf{k}'} \rangle \equiv \int_{cell} dV \Psi^*_{n\mathbf{k}}(\mathbf{r})\Psi_{n'\mathbf{k}'}(\mathbf{r}) = \delta_{nn'}\delta(\mathbf{k} - \mathbf{k}'), \tag{5.9}$$

$$\langle u_{n\mathbf{k}} | u_{n'\mathbf{k}'} \rangle \equiv \int_{cell} d\Omega u^*_{n\mathbf{k}}(\mathbf{r})u_{n'\mathbf{k}'}(\mathbf{r}) = \delta_{nn'}\frac{\Omega}{(2\pi)^3}, \tag{5.10}$$

where Ω is the volume of the unitary cell in the crystal.

5.1.1 Overview on $\mathbf{k}\cdot\mathbf{p}$ method

We can now start describing the $\mathbf{k}\cdot\mathbf{p}$ perturbation theory used to find the band structure of Si and Ge. By inserting the expression of the Bloch function from (5.7) into (5.4), and remembering that $\mathbf{p} = -i\hbar\nabla$, one gets:

$$\begin{aligned} He^{i\mathbf{k}\cdot\mathbf{r}}(\mathbf{r})u_{n\mathbf{k}}(\mathbf{r}) =& \left[\frac{-\hbar^2}{2m_0}\nabla^2 + V(r)\right]e^{i\mathbf{k}\cdot\mathbf{r}}u_{n\mathbf{k}}(\mathbf{r}) = \\ =& e^{i\mathbf{k}\cdot\mathbf{r}}\left[\frac{\hbar^2k^2}{2m_0}u_{n\mathbf{k}}(\mathbf{r}) - \frac{\hbar^2}{m_0}i\mathbf{k}\cdot\nabla u_{n\mathbf{k}}(\mathbf{r}) - \frac{\hbar^2}{2m_0}(\nabla^2 u_{n\mathbf{k}}(\mathbf{r})) + V(\mathbf{r})u_{n\mathbf{k}}(\mathbf{r})\right] = \\ =& e^{i\mathbf{k}\cdot\mathbf{r}}E_n(\mathbf{k})u_{n\mathbf{k}}(\mathbf{r})\,. \end{aligned} \tag{5.11}$$

Consequently, by multiplying the two terms of the last equality on the left by $e^{-i\mathbf{k}\cdot\mathbf{r}}$, one obtains an effective equation for the function $u_{nk}(\mathbf{r})$:

$$H(\mathbf{k})u_{n\mathbf{k}}(\mathbf{r}) = \epsilon(\mathbf{k})u_{n\mathbf{k}}(\mathbf{r})\,, \tag{5.12}$$

$$H(\mathbf{k}) \equiv H + H_{\mathbf{k}\cdot\mathbf{p}}\,, \tag{5.13}$$

in which we defined

$$H_{\mathbf{k}\cdot\mathbf{p}} = \frac{\hbar}{m_0}\mathbf{k}\cdot\mathbf{p}\,, \tag{5.14}$$

$$\epsilon_n(\mathbf{k}) = E_n(\mathbf{k}) - \frac{\hbar^2\mathbf{k}^2}{2m_0}\,. \tag{5.15}$$

The equation obtained in Eq. (5.12) is the so-called $\mathbf{k}\cdot\mathbf{p}$ equation. Specifically, note that the whole Hamiltonian $H(\mathbf{k})$ is now the sum of the unperturbed Hamiltonian and the $\mathbf{k}$-dependent term $H_{\mathbf{k}\cdot\mathbf{p}}$. The effective energy $\epsilon_n(\mathbf{k})$ at the right side of the equation depends on $\mathbf{k}$ as well and presents parabolic dispersion.

Perturbation theory at Γ

For small values of $\mathbf{k}$ the term $H_{\mathbf{k}\cdot\mathbf{p}}$ becomes much smaller than H, meaning that it can be considered as a perturbative term. Thus, we can rewrite the eigenfunctions of Eq. (5.12) near the Γ-point in the Brillouin zone through an expansion on the eigenfunctions of the unperturbed Hamiltonian. Specifically, considering the $\mathbf{k}\cdot\mathbf{p}$ equation at $\mathbf{k}=0$, for which $H(\mathbf{k}=0)=H$:

$$Hu_{n0}(\mathbf{r}) = \epsilon_{n0}u_{n0}(\mathbf{r})\,, \tag{5.16}$$

the eigenfunctions $u_{n0}(\mathbf{r})$ form a complete set of periodic functions, and constitute a basis characterized by the band index n with the following normalization conditions:

$$\langle u_{n0}|u_{n'0}\rangle = \int d\Omega u^*_{n0}u_{n'0} = \delta_{nn'}\frac{\Omega}{(2\pi)^3}\,. \tag{5.17}$$

According to perturbative theory, the first-order expansion of $u_{n\mathbf{k}}$ in $H_{\mathbf{k}\cdot\mathbf{p}}$ reads, in ket notation:

$$|u_{n\mathbf{k}}\rangle \cong |u_{n0}\rangle + \sum_m \frac{\langle u_{m0}|\hat{H}_{\mathbf{k}\cdot\mathbf{p}}|u_{n0}\rangle}{\epsilon_{n0}-\epsilon_{m0}}|u_{n0}\rangle, \tag{5.18}$$

while the second-order expansion of $\epsilon_{n\mathbf{k}}$ is:

$$\epsilon_{n\mathbf{k}} \cong \epsilon_{n0} + \langle u_{n0}|\hat{H}_{\mathbf{k}\cdot\mathbf{p}}|u_{n0}\rangle + \sum_{m\neq n}\frac{|\langle u_{m0}|\hat{H}_{\mathbf{k}\cdot\mathbf{p}}|u_{n0}\rangle|^2}{\epsilon_{n0}-\epsilon_{m0}}\,. \tag{5.19}$$

The last formula allows us to recover the band dispersion near the Γ-point, and consequently quantities such as the effective mass of holes and electrons inside the bulk material.

5.1.2 6×6 Luttinger-Kohn Hamiltonian

Ideally, one would like to represent the $\mathbf{k}\cdot\mathbf{p}$ Hamiltonian on the whole complete set of functions $u_{n0}(\mathbf{r})$. In this way, one could directly diagonalize the matrix

$$\langle u_{n0}|\hat{H}_{\mathbf{k}\cdot\mathbf{p}}|u_{n'0}\rangle \tag{5.20}$$

to obtain the exact solutions to the problem. However, it is not realistically possible to consider an infinite number of indices to represent an operator numerically. Instead, it is necessary to limit the treatment to a truncated basis of $u_{n0}(\mathbf{r})$. This approximation is possible when the considered set of indices n corresponds to a sufficiently isolated set of bands, and must be valid at least in the

proximity of the Γ-point where the $\mathbf{k}\cdot\mathbf{p}$ method holds. The simplest case considers a single band, and is useful to describe the conduction band of many semiconductors. Instead, to describe the hole states in Si and Ge we need to focus on the top of the valence band at Γ. Here, as we previously saw with Fig. 4.7, the valence band is made up of three separate bands, all of which present a maximum at Γ. These bands come from a combination of the p orbitals of the atomic valence shell. Consequently, they possess an orbital angular momentum $l = |\mathbf{l}| = 1$ and are each characterized by a different quantum number $l_z = 0, \pm 1$. Additionally, each band is spin-degenerate ($s = 1/2$, $s_z = \pm 1/2$), so that the whole set is made up of six bands:

$$\{|u_{n0}\rangle\} \rightarrow \{|l_z, s_z\rangle\} = \left\{\left|1, \frac{1}{2}\right\rangle, \left|1, -\frac{1}{2}\right\rangle, \left|0, \frac{1}{2}\right\rangle, \left|0, -\frac{1}{2}\right\rangle, \left|-1, \frac{1}{2}\right\rangle, \left|-1, -\frac{1}{2}\right\rangle\right\}. \tag{5.21}$$

These bands are a good set to represent the $\mathbf{k}\cdot\mathbf{p}$ Hamiltonian both for group-IV semiconductors with diamond structure (i.e. Si and Ge) and for III-V semiconductors with zincblende structure (e.g. GaAs, AlAs, ...). Indeed, the band gap between the first conduction band and the Fermi energy is of at least a few eV's (e.g. 1.12 eV for Si and 0.66 eV for Ge at 300 K [265]), and the other valence bands below are even further away.

Spin-orbit term

The Hamiltonian $H(\mathbf{k})$ in Eq. (5.12) does not take into account the interaction between the spin of the hole and its orbital degrees of freedom, namely the SOC previously introduced in Sec. 4.2.2. The SOC comes from a non-relativistic limit of the Dirac equation, for which one needs to perform the following substitution:

$$\mathbf{p} \rightarrow \mathbf{p} + \frac{\hbar}{4m_0c^2}[\hat{\sigma} \times \nabla V(\mathbf{r})] \tag{5.22}$$

with $\hat{\sigma} = (\hat{\sigma}_1, \hat{\sigma}_2, \hat{\sigma}_3)$ the vector of Pauli matrices on the spin degree of freedom, m_0 the free electron mass and c the speed of light in vacuum. After the substitution, the spin-orbit Hamiltonian entering the $\mathbf{k}\cdot\mathbf{p}$ Hamiltonian from Eq. (5.14) is:

$$\hat{H}_{SO} = \frac{\hbar^2}{4m_0^2c^2}\mathbf{k}\cdot[\hat{\sigma} \times \nabla V(\mathbf{r})], \tag{5.23}$$

In IV and III-V group semiconductors, this term is non-negligible and significantly affects the band structure at the Γ-point, and consequently the state of the hole close to the Fermi energy. Consequently, we need to include it in our treatment.

Since the spin-orbit Hamiltonian mixes the spin and angular degrees of freedom, it is now more convenient to consider the quantum numbers of the total angular momentum $\mathbf{j} = \mathbf{l} + \mathbf{s}$ to define the basis set of our problem. Consequently, we need to map the previously defined set $\{|l_z, s_z\rangle\}$ into $\{|j, m\rangle\}$, where $j = |\mathbf{j}|$ and $m = j_z$ is the projection of j along the z axis:

$$\{|l_z, s_z\rangle\} \rightarrow \{|j, m\rangle\}, \tag{5.24}$$

This can be done by applying the composition rules of quantum angular momenta, and by using the Clebsch-Gordan coefficients to perform the basis transformation. Specifically, the combination of $l = 1$ and $s = 1/2$ gives a quartet of states with $j = 3/2$ and a doublet with $j = 1/2$, so that we have:

$$\{|j, m\rangle\} = \left\{\left|\frac{3}{2}, \frac{3}{2}\right\rangle, \left|\frac{3}{2}, \frac{1}{2}\right\rangle, \left|\frac{3}{2}, -\frac{1}{2}\right\rangle, \left|\frac{3}{2}, -\frac{3}{2}\right\rangle, \left|\frac{1}{2}, \frac{1}{2}\right\rangle, \left|\frac{1}{2}, -\frac{1}{2}\right\rangle\right\}. \tag{5.25}$$

As previously explained in Sec. **??**, the quartet is formed by two bands with $m = \pm 3/2$ (HH bands), and two bands with $m = \pm 1/2$ (LH bands). The two bands of the doublet have $m = \pm 1/2$ (SO bands). On this basis, the spin-orbit Hamiltonian is diagonal, and its effect on the band structure at Γ is to shift the SO bands of a quantity Δ_{SO} below the HH and LH bands. The value of Δ_{SO} is 44.0 meV in Si and 290 meV in Ge.

At this point, we can write the whole Hamiltonian in Eq. (5.13), with the addition of the spin-orbit term in Eq. (5.23), on the $\{|j,m\rangle\}$ basis defined in Eq. (5.25). Its matrix elements are evaluated as:

$$H_{(jm,j'm')}(\mathbf{k}) = \langle j,m|\hat{H}(\mathbf{k})|j',m'\rangle = \int dr u^*_{jm,0}(\mathbf{r})\hat{H}(\mathbf{k})u_{j'm',0}(\mathbf{r})\,, \tag{5.26}$$

and the resulting 6×6 Hamiltonian is [266]:

$$\hat{H}(\mathbf{k}) = \begin{pmatrix} P+Q & -S & R & 0 & -\frac{1}{\sqrt{2}}S & \sqrt{2}R \\ -S^* & P-Q & 0 & R & -\sqrt{2}Q & \sqrt{\frac{3}{2}} \\ R^* & 0 & P-Q & S & \sqrt{\frac{3}{2}}S^* & \sqrt{2}Q \\ 0 & R^* & S^* & P+Q & -\sqrt{2}R^* & -\frac{1}{\sqrt{2}}S^* \\ -\frac{1}{\sqrt{2}}S^* & -\sqrt{2}Q & \sqrt{\frac{3}{2}}S & -\sqrt{2}R & P+\Delta_{SO} & 0 \\ \sqrt{2}R^* & \sqrt{\frac{3}{2}}S^* & \sqrt{2}Q & -\frac{1}{\sqrt{2}}S & 0 & P+\Delta_{SO} \end{pmatrix} \tag{5.27}$$

where P, Q, R and S are kinetic terms:

$$P(\mathbf{k}) = \frac{\hbar^2}{2m_0}\gamma_1(k_x^2+k_y^2+k_z^2)\,, \tag{5.28}$$

$$Q(\mathbf{k}) = \frac{\hbar^2}{2m_0}\gamma_2(k_x^2+k_y^2-2k_z^2)\,, \tag{5.29}$$

$$R(\mathbf{k}) = \frac{\hbar^2}{2m_0}\sqrt{3}[-\gamma_3(k_x^2-k_y^2)+2i\gamma_2 k_x k_y)]\,, \tag{5.30}$$

$$S(\mathbf{k}) = \frac{\hbar^2}{2m_0}2\sqrt{3}\gamma_3(k_x-ik_y)k_z\,. \tag{5.31}$$

The quantities γ_1, γ_2 and γ_3 from the previous expressions are the so-called Luttinger parameters, and define the curvature of the bands near the Γ-point along the crystal directions chosen as reference, which in our calculations are [255]:

$$\mathbf{x} \parallel [110]\,, \quad \mathbf{y} \parallel [\bar{1}10]\,, \quad \mathbf{z} \parallel [001]\,. \tag{5.32}$$

Their values are specific for each crystal: for Si they are $\gamma_1 = 4.285, \gamma_2 = 0.339$ and $\gamma_3 = 1.446$; for Ge $\gamma_1 = 13.38, \gamma_2 = 4.24$ and $\gamma_3 = 5.69$. Note that at this point the n-th eigenstate of the 6×6 Hamiltonian in Eq. (5.27) can be expressed as a linear combination on the $\{|j,m\rangle\}$ basis, with constant coefficients:

$$\Phi_n(\mathbf{r}) = \sum_{j,m}\eta_n^{jm}u_{jm,0}(\mathbf{r})\,. \tag{5.33}$$

Envelope-function theory

An external, slowly varying electric potential can now be introduced into the Hamiltonian found in Eq. (5.27) through the theory developed by Luttinger and Kohn, which they used to study the effective motion of electrons and holes in periodic fields [267]. Specifically, the definition of a quantum dot inside our system requires the addition of a confinement potential, $V_c(\mathbf{r})$, whose matrix elements on the $\{|j,m\rangle\}$ are:

$$\langle jm|\hat{V}_c|j'm'\rangle = \int d\mathbf{r}\, u_{jm,0}(\mathbf{r})^* V_c(\mathbf{r}) u_{j'm',0}(\mathbf{r})\,. \tag{5.34}$$

Since both functions $u_{jm,0}(\mathbf{r})^*$ and $u_{j'm',0}(\mathbf{r})$ are periodic with the same periodicity as the lattice, their product can be written through a Fourier expansion restricted to the wave vectors $\mathbf{K}_l$ that are part of the crystal's dual lattice:

$$u^*_{jm,0}u_{j'm',0} = \sum_l B_l^{jm,j'm'} e^{-i\mathbf{K}_l\cdot\mathbf{r}}\,. \tag{5.35}$$

Here, the coefficients $B_l^{jm,j'm'}$ are defined as:

$$B_l^{jm,j'm'} = \frac{1}{\Omega}\int_{cell a} d\mathbf{r}\, e^{-i\mathbf{K}_l\cdot\mathbf{r}} u_{jm,0}(\mathbf{r})^* u_{j'm',0}(\mathbf{r})\,, \tag{5.36}$$

and are independent from both $\mathbf{k}$ and $\mathbf{r}$. By replacing Eq. (5.35) into (5.34) we obtain:

$$\langle jm|\hat{V}_c|j'm'\rangle = \int d\mathbf{r}\, V_c(\mathbf{r}) \sum_l B_l^{jm,j'm'} e^{-i\mathbf{K}_l\cdot\mathbf{r}} dr = (2\pi)^3 \sum_l B_l^{jm,j'm'} \mathcal{U}(\mathbf{K}_l)\,, \tag{5.37}$$

where $\mathcal{U}(\mathbf{K}_l)$ is the Fourier transform of $V_c(\mathbf{r})$ evaluated at $\mathbf{k} = \mathbf{K}_l$:

$$\mathcal{U}(\mathbf{k}) = \frac{1}{(2\pi)^3}\int d\mathbf{r}\, V_c(\mathbf{r}) e^{-i\mathbf{K}_l\cdot\mathbf{r}} dr\,. \tag{5.38}$$

Under the hypothesis that $V_c(\mathbf{r})$ is slowly varying in space, its Fourier transform decays fast in momentum space, so that $U(\mathbf{k}) \approx 0$ for $\mathbf{k} \gg 0$. Specifically, we can affirm that every $U(\mathbf{K}_l)$ with $l \neq 0$ is negligible with respect to $U(\mathbf{0})$. Thus, we can write the following approximation:

$$\langle jm|\hat{V}_c|j'm'\rangle \simeq (2\pi)^3 B_0^{jm,j'm'} \mathcal{U}(\mathbf{0})\,. \tag{5.39}$$

At this point, note that the basis functions $u_{jm,0}$ are orthogonal [see Eq. (5.17)], so that from the definition of the coefficients in Eq. (5.36) we can rewrite $B_0^{jm,j'm'}$:

$$B_0^{jm,j'm'} = \frac{1}{\Omega}\int_{cell} d\mathbf{r}\, u_{jm,0}(\mathbf{r})^* u_{j'm',0}(\mathbf{r}) dr = \frac{1}{(2\pi)^3}\delta_{jj'}\delta_{mm'}\,, \tag{5.40}$$

where $\delta_{jj'}$ and $\delta_{mm'}$ are Kronecker delta's on the j and m degrees of freedom. Therefore, once we replace the last expression into (5.39), we see that the representation of $V_c(\mathbf{r})$ is diagonal on the $\{|j,m\rangle\}$ basis, meaning that it does not couple bands with different quantum numbers. Consequently, we can add its contribution to the total Hamiltonian simply by adding it on the diagonal:

$$\hat{H}(\mathbf{k},\mathbf{r}) = \begin{pmatrix} P+Q & -S & R & 0 & -\frac{1}{\sqrt{2}}S & \sqrt{2}R \\ -S^* & P-Q & 0 & R & -\sqrt{2}Q & \sqrt{\frac{3}{2}} \\ R^* & 0 & P-Q & S & \sqrt{\frac{3}{2}}S^* & \sqrt{2}Q \\ 0 & R^* & S^* & P+Q & -\sqrt{2}R^* & -\frac{1}{\sqrt{2}}S^* \\ -\frac{1}{\sqrt{2}}S^* & -\sqrt{2}Q & \sqrt{\frac{3}{2}}S & -\sqrt{2}R & P+\Delta_{SO} & 0 \\ \sqrt{2}R^* & \sqrt{\frac{3}{2}}S^* & \sqrt{2}Q & -\frac{1}{\sqrt{2}}S & 0 & P+\Delta_{SO} \end{pmatrix} + V_c(\mathbf{r})\hat{\mathbb{1}}\,. \tag{5.41}$$

Note that we have introduced a term that is spatially dependent on the real-space coordinate $\mathbf{r}$. Because of this, the 6-dimensional solution written in Eq. (5.33) that was the eigenstate of the Hamiltonian in Eq. (5.27) will now have components that depend on $\mathbf{r}$ and, just like the potential, are slowly varying in space:

$$\Phi_n(\mathbf{r}) = \sum_{j,m} \phi_n^{jm}(\mathbf{r}) u_{jm,0}(\mathbf{r}) \,, \tag{5.42}$$

where the components $\phi_n^{jm}(\mathbf{r})$ are also called *envelope functions*. Another notation frequently used in these cases is to write the eigenstate as a six-component space-dependent spinor on the band degrees of freedom:

$$\Phi_n(\mathbf{r}) = \begin{pmatrix} \phi_n^{\frac{3}{2},\frac{3}{2}}(\mathbf{r}) \\ \phi_n^{\frac{3}{2},\frac{1}{2}}(\mathbf{r}) \\ \phi_n^{\frac{3}{2},-\frac{1}{2}}(\mathbf{r}) \\ \phi_n^{\frac{3}{2},-\frac{3}{2}}(\mathbf{r}) \\ \phi_n^{\frac{1}{2},\frac{1}{2}}(\mathbf{r}) \\ \phi_n^{\frac{1}{2},-\frac{1}{2}}(\mathbf{r}) \end{pmatrix} . \tag{5.43}$$

5.1.3 Action of a magnetic field

Up to this point, we have only introduced an electrostatic potential inside of our Hamiltonian. The next step is to introduce the magnetic field $\mathbf{B}$, which is necessary to lift the degeneracies inside of our system.

Time-reversal operator

Before describing the way in which we introduce a magnetic field, let's first briefly recall the concept of time reversal in quantum mechanics, i.e. how the equations of motion of a quantum particle behave under the transformation $t \to -t$. For a spinless system only in the presence of an electrostatic potential, the Schrödinger equation is:

$$i\hbar \frac{\partial \psi(\mathbf{r},t)}{\partial t} = \left[-\frac{\hbar^2}{2m}\nabla^2 + V(\mathbf{r}) \right] \psi(\mathbf{r},t) \,. \tag{5.44}$$

If we apply the transformation $t \to -t$ on Eq. (5.44), we see that the sign of the time-derivative on the left side changes. Therefore, the state $\psi(\mathbf{r},-t)$ is not a solution of the same Schrödinger equation as $\psi(\mathbf{r},t)$. Instead, we need to add an additional complex conjugation: this changes $i \to -i$ on the left-hand side of the equation and recovers the initial equation, which now has solution $\psi^*(\mathbf{r},-t)$. Overall, this means that the time-reversal transformation acts on a quantum state as:

$$\Theta : \; \psi(\mathbf{r},t) \to \psi_r(\mathbf{r},t) = \psi^*(\mathbf{r},-t) \,, \tag{5.45}$$

where we refer to $\psi_r(r,t)$ as the time-reversed state. We can write the same concept for operator $\hat{\Theta}$ in ket notation:

$$|\psi_r(t)\rangle = \hat{\Theta} \, |\psi(t)\rangle \; . \tag{5.46}$$

Since the norm must be conserved under time-reversal, $\hat{\Theta}$ satisfies the following property:

$$\hat{\Theta}^\dagger \hat{\Theta} = \hat{\mathbb{1}} \,. \tag{5.47}$$

Furthermore, $\hat{\Theta}$ is an antilinear operator, since it acts on a complex number as a complex conjugation:

$$\hat{\Theta}c = c^*\hat{\Theta}\,, \quad c \in \mathbb{C}\,. \tag{5.48}$$

Therefore, the time-reversal operator is *antiunitary*. This means that it can be rewritten as the product of a unitary operator, $\hat{U}$, and the complex conjugation operator, $\hat{K}$:

$$\hat{\Theta} = \hat{U}\hat{K}\,. \tag{5.49}$$

Additionally, its action on bras is not the same as the one of a linear operator. Indeed, $\langle\psi(t)|\,\hat{\Theta}^\dagger$ is antilinear, and to recover the linearity of the action of a bra on a ket one must introduce an additional complex conjugation and write:

$$\left(\langle\psi_1(t)|\,\hat{\Theta}\right)|\psi_2(t)\rangle = \left[\langle\psi_1(t)|\left(\hat{\Theta}\,|\psi_2(t)\rangle\right)\right]^*\,. \tag{5.50}$$

Kramers degeneracy

Let's now look at how our system behaves under time reversal. All operators with a classical equivalent transform under time reversal just as they do in classical mechanics. For instance:

$$\hat{\Theta}^\dagger\hat{x}\hat{\Theta} = \hat{x}\,, \quad \hat{\Theta}^\dagger\hat{\mathbf{p}}\hat{\Theta} = -\hat{\mathbf{p}}\,, \quad \hat{\Theta}^\dagger\hat{\mathbf{l}}\hat{\Theta} = -\hat{\mathbf{l}}\,, \quad \hat{\Theta}^\dagger\hat{l}_z\hat{\Theta} = -\hat{l}_z\,, \tag{5.51}$$

From the transformations of the orbital angular momentum $\hat{\mathbf{l}}$ and its component $\hat{l}_z$ we can assume that the both the spin operators $\hat{\mathbf{s}} = \frac{\hbar}{2}\hat{\boldsymbol{\sigma}}$ and $\hat{s}_z = \frac{\hbar}{2}\hat{\sigma}_3$ and the total angular momentum operators $\hat{\mathbf{j}}$ and $\hat{m}$ behave in the same way:

$$\hat{\Theta}^\dagger\hat{\mathbf{s}}\hat{\Theta} = -\hat{\mathbf{s}}\,, \quad \hat{\Theta}^\dagger\hat{s}_z\hat{\Theta} = -\hat{s}_z\,, \quad \hat{\Theta}^\dagger\hat{\mathbf{j}}\hat{\Theta} = -\hat{\mathbf{j}}\,, \quad \hat{\Theta}^\dagger\hat{m}\hat{\Theta} = -\hat{m}\,. \tag{5.52}$$

Therefore, we can straightforwardly extend the definition of the time-reversal operator to particles with spin. Specifically, by looking at its action on the momentum operators, as well as the property from Eq. (5.49), we can generally write

$$\hat{\Theta} = e^{-i\pi\hat{j}_y}\hat{K}\,. \tag{5.53}$$

An interesting property follows from Eq. (5.53). Indeed, by squaring the time-reversal operator, we get:

$$\hat{\Theta}^2 = e^{-i\pi\hat{j}_y}\hat{K}e^{-i\pi\hat{j}_y}\hat{K} = e^{-i2\pi\hat{j}_y}\hat{K}^2 = (-1)^{2j}\,, \tag{5.54}$$

where we used the fact that $i\hat{j}_y$ has real matrix elements and $\hat{K}^2 = \hat{\mathbb{1}}$. Consequently, for integer momenta we have $\hat{\Theta}^2 = \hat{\mathbb{1}}$, while for half-integer momenta $\hat{\Theta}^2 = -\hat{\mathbb{1}}$. Combining this with Eq. (5.47), one gets $\hat{\Theta}^\dagger = \hat{\Theta}$ for integer spins and $\hat{\Theta}^\dagger = -\hat{\Theta}$ for half-integer spins.

Overall, the Hamiltonian we found in Eq. (5.41) only presents time-reversal invariant terms. Indeed, it only depends on the spatial coordinates and quadratically on the momentum. Thus, the Hamiltonian operator commutes with $\hat{\Theta}$,

$$\left[\hat{H}(\mathbf{k},\mathbf{r}),\hat{\Theta}\right] = 0\,, \tag{5.55}$$

and our system in the absence of an external magnetic field presents time-reversal symmetry. Under these conditions and for half-integer spins, Kramers' theorem states that every eigenvalue of the Hamiltonian is doubly degenerate and that the eigenstates are organized in *Kramers pairs*, or

Kramers doublets. Indeed, from Eq. (5.55), it follows that for any eigenvector $|v\rangle$ of $\hat{H}$ with eigenvalue e the vector $|v_r\rangle = \hat{\Theta}|v\rangle$ is also an eigenvector of $\hat{\Theta}$ corresponding to the same eigenvalue:

$$\hat{H}|v_r\rangle = \hat{H}\hat{\Theta}|v\rangle = \hat{\Theta}\hat{H}|v\rangle = e\hat{\Theta}|v\rangle = e|v_r\rangle\ , \tag{5.56}$$

And from $\hat{\Theta}^\dagger = -\hat{\Theta}$ it follows that $|v_r\rangle$ is orthogonal to $|v\rangle$:

$$\langle v_r|v\rangle = (\langle v|\hat{\Theta}^\dagger)|v\rangle = \left[\langle v|(\hat{\Theta}^\dagger|v\rangle)\right]^* = \left[\langle v|(-\hat{\Theta}|v\rangle)\right]^* = -\left[\langle v|v_r\rangle\right]^* = -\langle v_r|v\rangle \tag{5.57}$$

$$\rightarrow \quad \langle v_r|v\rangle = 0\,. \tag{5.58}$$

Magnetic terms in the Hamiltonian

To break the Kramers degeneracy, we must introduce into the Hamiltonian in Eq. (5.41) terms that are not time-reversal invariant. This is possible when introducing a static magnetic field acting on the system. Indeed, first of all, the Zeeman-Bloch Hamiltonian depends on the angular and spin momenta [170], which are both quantities that do not commute with the time-reversal operator:

$$\hat{H}_{ZB} = -(3\kappa+1)\mu_B\mathbf{B}\cdot\hat{\mathbf{I}} + g_0\mu_B\mathbf{B}\cdot\hat{\mathbf{s}}\,. \tag{5.59}$$

In Eq. (5.59), μ_B is Bohr's magneton, g_0 is the free-electron g-factor, and κ is the g-factor in Si ($\kappa = -0.42$) or Ge ($\kappa = 3.41$). Secondly, we perform the Peierls substitution,

$$\mathbf{k} \longrightarrow \mathbf{k} + \frac{e}{\hbar}\mathbf{A}\,, \tag{5.60}$$

in which $\mathbf{A}$ is the vector potential, which we represent by fixing the symmetric gauge:

$$\mathbf{A} = -\frac{1}{2}\mathbf{r}\times\mathbf{B} = -\frac{1}{2}(yB_z - zB_y, zB_x - xB_z, xB_y - yB_x)\,. \tag{5.61}$$

Recall that this gauge-fixing procedure does not modify the measurable quantities of the system described by our Hamiltonian in Eq. (5.41). That said, the introduction of the vector potential $\mathbf{A}$ modifies the $\mathbf{k}$-dependent terms of our Hamiltonian in Eq. (5.41), namely the expressions of P, Q, R and S from Eqs. (5.28-5.31). By doing so, it introduces a paramagnetic contribution linear in $\mathbf{B}$ ($\hat{H}_p$), and a diamagnetic contribution quadratic in $\mathbf{B}$ ($\hat{H}_d$). The former is also linear in $\mathbf{k}$, meaning that it does not commute with the time-reversal operator.

In conclusion, the total Hamiltonian describing a single hole at the top of the valence band in Si and Ge in the presence of static electric and magnetic fields becomes:

$$\hat{H}_{tot}(\mathbf{k},\mathbf{r}) = \hat{H}(\mathbf{k},\mathbf{r}) + \hat{H}_{ZB} + \hat{H}_p(\mathbf{k},\mathbf{r}) + \hat{H}_d(\mathbf{r})\,, \tag{5.62}$$

and since both the Zeeman-Bloch term and the paramagnetic terms break the time-reversal symmetry, all degeneracy between Kramers pairs is lifted.

5.2 Numerical diagonalization

We now study the numerical way to diagonalize the complete Hamiltonian in Eq. (5.62) and find its eigenstates. Particularly, notice that $\hat{H}_{tot}$ depends on both the real space coordinates $\mathbf{r}$ and the

momentum $\mathbf{k}$. The latter can be represented in real space as a derivative, i.e. $\mathbf{k} = -i\nabla$. Consequently, the envelope functions characterizing the spinor in Eq. (5.43) are the solution of six coupled and mixed differential equations. From a numerical point of view, a possible choice would be to represent everything on the real space coordinates, and write the derivatives with one of the finite-difference methods (e.g. forward/backward Euler method, the trapezoidal method, and so on). However, these methods introduce an error dependent on the grid steps, e.g. $\mathcal{O}(\delta x^n)$ along x, with n the order of approximation. Instead, there is a better method that we can approach in order to eliminate these discretization errors, and it is to choose a representation basis on which both the real space coordinates and the momenta are represented exactly.

5.2.1 Harmonic-oscillator basis

The solution comes from choosing the basis of the eigenstates of a three-dimensional harmonic oscillator (HO). This method has been described in previous works by the research group of the IQubits project [2, 189, 255, 260]. Let's start with a brief recap on the problem of the quantum HO. The three-dimensional HO potential is the sum of three separate 1D potentials:

$$V^{HO}(\mathbf{r}) = \sum_{\alpha} V_{\alpha}^{HO}(\alpha) = \frac{1}{2}\sum_{\alpha} \kappa_{\alpha}\alpha^2, \tag{5.63}$$

where $\alpha = x, y, z$ are the three spatial directions and κ_{α} the elastic constants of each component. Note that in general κ_{α} may be different for each direction, thus forming an anisotropic potential. The Hamiltonian of a particle moving inside $V^{HO}(\mathbf{r})$ with effective masses m_x, m_y and m_z along the three directions is:

$$H^{HO}(\mathbf{k}, \mathbf{r}) = T(\mathbf{k}) + V^{HO}(\mathbf{r}) = \sum_{\alpha} \left[\frac{\hbar^2}{2m_{\alpha}} k_{\alpha}^2 + \frac{1}{2}\kappa_{\alpha}\alpha^2 \right]. \tag{5.64}$$

The eigenvalue problem of this Hamiltonian can be solved by defining ladder operators for each α:

$$\hat{a}_{\alpha} = \frac{1}{\sqrt{2}}(\tilde{\alpha} + i\tilde{k}_{\alpha}), \quad \hat{a}_{\alpha}^{\dagger} = \frac{1}{\sqrt{2}}(\tilde{\alpha} - i\tilde{k}_{\alpha}), \tag{5.65}$$

where $\tilde{\alpha}$ and $\tilde{k}_{\alpha}$ are the renormalized coordinate and momentum operators,

$$\tilde{\alpha} = \sqrt{\frac{m_{\alpha}\omega_{\alpha}}{\hbar}}\hat{\alpha}, \quad \tilde{k_{\alpha}} = \sqrt{\frac{1}{m_{\alpha}\hbar\omega_{\alpha}}}\hat{k}_{\alpha}, \tag{5.66}$$

and $\omega_{\alpha} = \sqrt{\kappa_{\alpha}/m_{\alpha}}$ is the HO frequency. The following commutation rules hold for each direction:

$$\left[\hat{a}_{\alpha}, \hat{a}_{\alpha}^{\dagger}\right] = \mathbb{1}, \tag{5.67}$$

and operators for different directions always commute with each other.

With the use of the ladder operators in Eq. (5.65) one rewrites the operator of the HO Hamiltonian from Eq. (5.64) as

$$\hat{H}^{HO} = \sum_{\alpha} \hbar\omega_{\alpha} \left(\hat{a}_{\alpha}\hat{a}_{\alpha}^{\dagger} + \frac{1}{2} \right), \tag{5.68}$$

and finds its eigenvalues and eigenfunctions. These are characterized by a quantum number n_α for each direction, which we can organize in a three-dimensional tuple $\mathbf{n}^{HO} = (n_x^{HO}, n_y^{HO}, n_z^{HO})$. Being the Hamiltonian separable, the total eigenvalues are the sum of the ones for each α:

$$E_{\mathbf{n}^{HO}} = \sum_\alpha E_{n_\alpha^{HO}} = \sum_\alpha \hbar\omega_\alpha \left(n_\alpha^{HO} + \frac{1}{2}\right), \quad n_\alpha^{HO} = 0, 1, 2, \dots, \tag{5.69}$$

and the eigenfunctions are the product of each eigenfunction:

$$\varphi_{\mathbf{n}^{HO}}(\mathbf{r}) = \prod_\alpha \varphi_{n_\alpha^{HO}}(\alpha) = \prod_\alpha \frac{\exp\left[-\frac{1}{2}\left(\frac{\alpha}{l_\alpha}\right)^2\right]}{\left(\sqrt{\pi} 2^{n_\alpha^{HO}} n_\alpha^{HO}! l_\alpha\right)^{1/2}} \mathrm{He}_{n_\alpha^{HO}}\left(\frac{\alpha}{l_\alpha}\right), \tag{5.70}$$

in which

$$\mathrm{He}_{n_\alpha^{HO}}(\alpha) = (-1)^{n_\alpha^{HO}} e^{\alpha^2} \frac{d^{n_\alpha^{HO}}}{d\alpha^{n_\alpha^{HO}}} e^{-\alpha^2} \tag{5.71}$$

are the physicist's Hermite polynomials and

$$l_\alpha = \sqrt{\frac{\hbar}{m_\alpha \omega_\alpha}} \tag{5.72}$$

is the characteristic length of each 1D oscillator. As previously mentioned, we choose the eigenvalues written in Eq. (5.70) as our computational basis. In ket notation, we can write:

$$\left\{\left|\mathbf{n}^{HO}\right\rangle\right\} = \left\{\left|n_x^{HO} n_y^{HO} n_z^{HO}\right\rangle\right\}, \tag{5.73}$$

in which $\left|\mathbf{n}^{HO}\right\rangle$ is the eigenvector of the total 3D HO and $\left|n_\alpha^{HO}\right\rangle$ is the one of the 1D component along α; note that $\left|n_x^{HO} n_y^{HO} n_z^{HO}\right\rangle$ is shorthand for $\left|n_x^{HO}\right\rangle \otimes \left|n_y^{HO}\right\rangle \otimes \left|n_z^{HO}\right\rangle$.

Operator representation

Now that we have chosen our basis, we can rewrite the operators composing the Hamiltonian in Eq. (5.62) on this representation. Specifically, by inverting the formulas in Eqs. (5.65) and (5.66), one can write the coordinate and momentum operators in terms of ladder operators:

$$\hat{\alpha} = \sqrt{\frac{\hbar}{2m_\alpha\omega_\alpha}}(\hat{a}_\alpha^\dagger + \hat{a}_\alpha), \quad \alpha = x, y, z, \tag{5.74}$$

$$\hat{k}_\alpha = i\sqrt{\frac{m_\alpha\omega_\alpha\hbar}{2}}(\hat{a}_\alpha^\dagger - \hat{a}_\alpha), \quad \alpha = x, y, z. \tag{5.75}$$

At the same time, the ladder operators are exactly represented on the basis in Eq. (5.73). Indeed, their action on the basis vectors along their same direction is:

$$\hat{a}_\alpha |n_\alpha^{HO}\rangle = \sqrt{n_\alpha^{HO}} |n_\alpha^{HO} - 1\rangle, \tag{5.76}$$

$$\hat{a}_\alpha^\dagger |n_\alpha^{HO}\rangle = \sqrt{n_\alpha^{HO} + 1} |n_\alpha^{HO} + 1\rangle, \tag{5.77}$$

so that in matrix representation their elements can be written as:

$$\langle n_\alpha^{HO}|\hat{a}_\alpha|m_\alpha^{HO}\rangle = \sqrt{m_\alpha^{HO}}\delta_{n_\alpha^{HO},m_\alpha^{HO}-1}, \tag{5.78}$$

$$\langle n_\alpha^{HO}|\hat{a}_\alpha^\dagger|m_\alpha^{HO}\rangle = \sqrt{m_\alpha^{HO}+1}\delta_{n_\alpha^{HO},m_\alpha^{HO}+1}\,. \tag{5.79}$$

Overall, by combining Eqs. (5.74,5.75) with Eqs. (5.78,5.79), one finds the exact representation of the coordinates and momenta on the basis of $\{|n_\alpha^{HO}\rangle\}$:

$$\langle n_\alpha^{HO}|\hat{\alpha}|m_\alpha^{HO}\rangle = \sqrt{\frac{\hbar}{2m_\alpha\omega_\alpha}}(\sqrt{m_\alpha^{HO}+1}\delta_{n_\alpha^{HO},m_\alpha^{HO}+1} + \sqrt{m_\alpha^{HO}}\delta_{n_\alpha^{HO},m_\alpha^{HO}-1})\,, \tag{5.80}$$

$$\langle n_\alpha^{HO}|\hat{k}_\alpha|m_\alpha^{HO}\rangle = i\sqrt{\frac{m_\alpha\omega_\alpha\hbar}{2}}(\sqrt{m_\alpha^{HO}+1}\delta_{n_\alpha^{HO},m_\alpha^{HO}+1} - \sqrt{m_\alpha^{HO}}\delta_{n_\alpha^{HO},m_\alpha^{HO}-1})\,. \tag{5.81}$$

These can be straightforwardly extended to the complete basis $\{|\mathbf{n}\rangle\}$ since the operators defined along α are delta's in all other directions. For instance, for $\hat{x}$:

$$\langle n_x^{HO}n_y^{HO}n_z^{HO}|\hat{x}|m_x^{HO}m_y^{HO}m_z^{HO}\rangle = \langle n_x^{HO}|\hat{x}|m_x^{HO}\rangle\delta_{n_y^{HO}m_y^{HO}}\delta_{n_z^{HO}m_z^{HO}}\,. \tag{5.82}$$

Overall, the choice of this basis does not introduce errors in the representation of the coordinates and momenta that enter the definition of our $\mathbf{k}\cdot\mathbf{p}$ Hamiltonian. However, we still have to limit the set of basis vectors and truncate the basis to a finite number N_α^{HO} among all directions, due to the impossibility of dealing numerically with infinite matrices. Therefore, we define the intervals for each quantum number as

$$n_x^{HO}\in[0,N_x^{HO}-1]\,,\quad n_y^{HO}\in[0,N_y^{HO}-1]\,,\quad n_z^{HO}\in[0,N_z^{HO}-1]\,, \tag{5.83}$$

so that the total number of basis vectors will be $N_{tot}^{HO}=N_x^{HO}\times N_y^{HO}\times N_z^{HO}$.

5.2.2 Adding electric potentials numerically

At this point, the last step for building the Hamiltonian from Eq. (5.62) in the HO basis is to represent the external confining electric potential. Let's start with the same harmonic potential written in Eq. (5.63): since it is separable and a simple function of the coordinates, it can be written exactly on the HO basis. Specifically, let's look at the diagonal contribution to the Hamiltonian in Eq. (5.62) which is common to all its diagonal elements, namely the sum of the external potential and P:

$$\hat{P}+\sum_\alpha\hat{V}_\alpha^{HO} = \sum_\alpha\left(\frac{\hbar}{2m_{eff}^P}\hat{k}_\alpha^2+\frac{1}{2}\kappa_\alpha\hat{\alpha}^2\right) = \sum_\alpha\hbar\omega_\alpha^P\left[\hat{a}_\alpha^P(\hat{a}_\alpha^P)^\dagger+\frac{1}{2}\right]\,, \tag{5.84}$$

where we used the same procedure used to find Eq. (5.73), and the HO frequencies are evaluated through the P contribution to the effective mass, that is:

$$m_{eff}^P = \frac{m_0}{\gamma_1}\,. \tag{5.85}$$

The operator in Eq. (5.84) is diagonal on the HO basis characterized by the frequencies ω_α^P, with matrix elements

$$\left\langle n_x^{HO} n_y^{HO} n_z^{HO} | (\hat{P} + \hat{V}^{HO}) | m_x^{HO} m_y^{HO} m_z^{HO} \right\rangle = \left[\sum_\alpha \hbar\omega_\alpha^P \left(n_\alpha^{HO} + \frac{1}{2} \right) \right] \times \prod_\alpha \delta_{n_\alpha^{HO} m_\alpha^{HO}} \,. \tag{5.86}$$

Consequently, in our implementation of the code, the harmonic potential is automatically included inside of the Hamiltonian alongside all the other terms. However, the external potential may generally have a much more complicated shape in space and not have simple dependencies on the real space coordinates. In this case, the most general way with which to introduce the confining potential V_c is through the explicit evaluation of its matrix elements through integrals in real space. Note that if the HO potential is automatically inside of the Hamiltonian, it must be removed from the actual confining potential while evaluating its matrix elements:

$$\begin{aligned} &\langle n_x^{HO} n_y^{HO} n_z^{HO} | (\hat{V}_c - \sum_\alpha \hat{V}_\alpha^{HO}) | m_x^{HO} m_y^{HO} m_z^{HO} \rangle = \\ &\quad = \int\int\int dx\, dy\, dz\, \varphi_{n_x^{HO}}(x) \varphi_{n_y^{HO}}(y) \varphi_{n_z^{HO}}(z) \left[V_c(\mathbf{r}) - \sum_\alpha V_\alpha^{HO}(\alpha) \right] \varphi_{m_x^{HO}}(x) \varphi_{m_y^{HO}}(y) \varphi_{m_z^{HO}}(z) \,. \end{aligned} \tag{5.87}$$

This operation is performed on a finite real space grid of $N_x^{grid} \times N_y^{grid} \times N_z^{grid}$ points and may require significant computational resources. Luckily, when the external potential is separable the situation simplifies. Indeed, one can rewrite

$$V_c(\mathbf{r}) = \sum_\alpha V_{c,\alpha}(\alpha) \,, \tag{5.88}$$

and calculate the integrals for each component one at a time. For instance in x:

$$\begin{aligned} &\langle n_x^{HO} n_y^{HO} n_z^{HO} | (\hat{V}_{c,x} - \hat{V}_x^{HO}) | m_x^{HO} m_y^{HO} m_z^{HO} \rangle = \\ &\quad = \delta_{n_y^{HO} m_y^{HO}} \delta_{n_z^{HO} m_z^{HO}} \int dx\, \varphi_{n_x^{HO}}(x) \left[V_{c,x}(x) - V_x^{HO}(x) \right] \varphi_{m_x^{HO}}(x) \,, \end{aligned} \tag{5.89}$$

the problem reduces to a one-dimensional integral on only N_x^{grid} grid points, and is consequently much lighter to implement. Equivalently for the other coordinates.

5.2.3 State analysis

The diagonalization of the numerical Hamiltonian as implemented in the previous Sections produces eigenvectors which are the representation on the HO basis of the six envelope functions forming the spinor in Eq. (5.43). For simplicity of notation, from now on we will identify the band degrees of freedom (j, m) with the index b:

$$\left| \phi_n^b \right\rangle = \sum_{\{\mathbf{n}^{HO}\}} \eta_{n,\mathbf{n}^{HO}}^b \left| \mathbf{n}^{HO} \right\rangle \,, \quad n = 1, 2, \dots \,, \tag{5.90}$$

where $\eta_{n,\mathbf{n}^{HO}}^b$ are the elements of the eigenvectors in the HO basis. The envelope function for the b band can then be rewritten in real space through a linear combination of the HO states:

$$\phi_n^b(\mathbf{r}) = \sum_{n_x^{HO}} \sum_{n_y^{HO}} \sum_{n_z^{HO}} \eta_{n,\mathbf{n}^{HO}}^b \varphi_{n_x^{HO}}(x) \varphi_{n_y^{HO}}(y) \varphi_{n_z^{HO}}(z) \,. \tag{5.91}$$

Now, if we want to perform an analysis on these states, there are a few quantities that we can evaluate.

Band occupation

The first is the occupation probability of each band, evaluated as the norm of the envelope function corresponding to such a band. Using Eq. (5.90):

$$p_b = \left\langle \phi_n^b \middle| \phi_n^b \right\rangle = \sum_{\{\mathbf{n}^{HO}\}} \left| \eta^b_{n,\mathbf{n}^{HO}} \right|^2 , \tag{5.92}$$

in which we used the orthogonality of the HO basis. Notice that these probabilities sum to one due to the normalization of the spinor $|\Phi_n\rangle$ from Eq. (5.43) constituting the Hamiltonian's eigenstates:

$$\sum_b p_b = \sum_b \left\langle \phi_n^b \middle| \phi_n^b \right\rangle = \left\langle \Phi_n \middle| \Phi_n \right\rangle = 1 . \tag{5.93}$$

State parity

Then, we can evaluate the expectation value over state n of the parity operators, whose definition is:

$$P_\alpha : \quad \alpha \to -\alpha , \quad \alpha = x, y, z . \tag{5.94}$$

Such expectation value can be evaluated as the sum of the contributions from each band,

$$\langle P_\alpha \rangle_n = \sum_b \langle P_\alpha \rangle_n^b , \tag{5.95}$$

which in turn can be evaluated through Eq. (5.90):

$$\langle P_\alpha \rangle_n^b = \left\langle \phi_n^b \middle| P_x \middle| \phi_n^b \right\rangle = \sum_{\{\mathbf{n}^{HO}\}} \sum_{\{\mathbf{m}^{HO}\}} (\eta^b_{n,\mathbf{n}^{HO}})^* \eta^b_{n,\mathbf{m}^{HO}} \left\langle \mathbf{n}^{HO} \middle| P_\alpha \middle| \mathbf{m}^{HO} \right\rangle = \sum_{\{\mathbf{n}^{HO}\}} \left| \eta^b_{n,\mathbf{n}^{HO}} \right|^2 (-1)^{n_\alpha^{HO}} , \tag{5.96}$$

where we used the parity and orthogonality of the HO eigenstates. The same steps can be easily generalized to the total parity operator:

$$P_{tot} : \quad (x, y, z) \to (-x, -y, -z) , \tag{5.97}$$

for which

$$\langle P_{tot} \rangle_n^b = \sum_{\{\mathbf{n}^{HO}\}} \left| \eta^b_{n,\mathbf{n}^{HO}} \right|^2 (-1)^{n_x^{HO} + n_y^{HO} + n_z^{HO}} . \tag{5.98}$$

The results from Eqs. (5.96) and (5.98) give us an idea of the odd/even nature of the hole states with respect to the axes and the origin of the system. Indeed, we know that the total parity is always between 1 and -1. For P_α:

$$| \langle P_\alpha \rangle_n | \leq \left| \sum_b \langle P_\alpha \rangle_n^b \right| = \left| \sum_b \sum_{\{\mathbf{n}^{HO}\}} \left| \eta^b_{n,\mathbf{n}^{HO}} \right|^2 (-1)^{n_\alpha^{HO}} \right| \leq \sum_b \sum_{\{\mathbf{n}^{HO}\}} \left| \eta^b_{n,\mathbf{n}^{HO}} \right|^2 = \left\langle \Phi_n \middle| \Phi_n \right\rangle = 1 , \tag{5.99}$$

and similarly for P_{tot}, where once again we used the normalization of the hole spinor. Consequently, the closer the expectation value of one parity operator is to 1 (-1), the more even (odd) the nature of the state is with respect to the respective axis or the origin.

Matrix elements

Finally, one can evaluate braket products including the action of external operators $\hat{O}$, which correspond to the matrix elements of $\hat{O}$ between two hole states. For simplicity, we consider operators that do not depend on the band degree of freedom, meaning that they do not couple different bands. Once again, we use Eq. (5.90) to write:

$$O_{nm} = \langle \Phi_n | \hat{O} | \Phi_m \rangle = \sum_b \left\langle \phi_n^b \right| \hat{O} \left| \phi_m^b \right\rangle = \sum_b \sum_{\{\mathbf{n}^{HO}\}} \sum_{\{\mathbf{m}^{HO}\}} (\eta^b_{n,\mathbf{n}^{HO}})^* \eta^b_{m,\mathbf{m}^{HO}} \left\langle \mathbf{n}^{HO} \right| \hat{O} \left| \mathbf{m}^{HO} \right\rangle . \quad (5.100)$$

Here the evaluation of the last equation reduces to the calculation of the matrix elements of $\hat{O}$ on the HO basis, which can be performed through an integral in real space:

$$\left\langle \mathbf{n}^{HO} \right| \hat{O} \left| \mathbf{m}^{HO} \right\rangle = \int d\mathbf{r}\, \varphi_{n_x^{HO}}(x) \varphi_{n_y^{HO}}(y) \varphi_{n_z^{HO}}(z) O(\mathbf{r}) \varphi_{m_x^{HO}}(x) \varphi_{m_y^{HO}}(y) \varphi_{m_z^{HO}}(z) . \quad (5.101)$$

In conclusion, we have explained how to numerically encode the Hamiltonian of a single hole at the top of the valence band in Si and Ge quantum dots, as described in Eq. (5.62). This Hamiltonian is a 6×6 block Hamiltonian represented on a basis made of $N_x^{HO} \times N_y^{HO} \times N_z^{HO}$ HO eigenstates, which we diagonalize numerically using the LAPACK library. Once the eigenvectors and eigenenergies are obtained, state analysis is performed and they are recombined in real space. The sections of the code that implement the evaluation of the integrals in Eq. (5.87), the diagonalization of the Hamiltonian in Eq. (5.62), and the analysis of the states through Eqs. (5.91), (5.92), (5.96), (5.98) and (5.100) were parallelized through the use of the OpenMP library.

Using double-precision floating-point numbers, the heaviest quantities in terms of computational resources are the complex elements of the Hamiltonian in Eq. (5.62) and its eigenvectors on the HO basis. Combined, these require a total of $2(6 \times N_x^{HO} \times N_y^{HO} \times N_z^{HO})^2 \times 16$ bytes. For a reference run with $N_x^{HO} = 14$, $N_y^{HO} = 10$ and $N_z^{HO} = 14$, this corresponds to ~ 4.4 GB. At the same time, each band-resolved complex eigenfunction in real space, computed optionally by the code through Eq. (5.91), requires an allocated memory of $6 \times N_x^{grid} \times N_y^{grid} \times N_z^{grid} \times 16$ bytes, meaning that reference values of $N_x^{grid} = 221$, $N_y^{grid} = 221$ and $N_z^{grid} = 61$ correspond to ~ 0.28 GB. As for the simulation times, the numerical diagonalization of the above-mentioned Hamiltonian considering the specified simulation parameters takes approximately 10 minutes with 4 OpenMP threads and with an Intel(R) Xeon(R) Silver 4214 processor @ 2.20 GHz. Instead, under the same conditions the numerical evaluation of the operatorial representation from Eq. (5.87), or alternately the evaluation of the matrix elements in Eq. (5.100), takes approximately 25 minutes.

5.3 Models for single and double quantum dots

5.3.1 Confinement potentials

In order to simulate SQDs and DQDs we need to introduce specific potentials $V_c(\mathbf{r})$ to add to our Hamiltonian through the envelope-function theory, as previously described in Sec. 5.1.2. Our choice is not device-specific, and instead aims at giving a general representation of a prototypical device. Consequently, for simplicity of the calculations, we decided to represent the SQDs and DQDs using a separable potential:

$$V_c(\mathbf{r}) = V_{c,x}(x) + V_{c,y}(y) + V_{c,z}(z). \quad (5.102)$$

For the SQD, we considered a harmonic confinement along both the in-plane directions x and y:

$$V_{c,x}(x) = \frac{1}{2}\kappa_x x^2\,, \quad V_{c,y}(y) = \frac{1}{2}\kappa_y y^2\,, \tag{5.103}$$

to which we can associate the HO frequencies and corresponding confinement lengths:

$$\omega_\alpha = \sqrt{\frac{\kappa_\alpha}{m^P_{eff}}} \quad L_\alpha = \sqrt{\frac{\hbar}{m^P_{eff}\omega_\alpha}}\,, \quad \alpha = x, y\,, \tag{5.104}$$

where m^P_{eff} is the effective mass previously introduced in Sec. 5.2.2. This confinement approximates the bottom of the gate-induced potential in a realistic FDSOI p-MOSFET transistor, as demonstrated through simulations with the GINESTRA® code in [189] (see Fig. 4.9(b) from Sec. 4.2.2). The only difference for the DQD is the shape of the potential along x, which is instead a quartic potential:

$$V_{c,x}(x) = \frac{1}{2}\kappa_x \frac{(x^2 - a^2)^2}{4a^2}\,, \tag{5.105}$$

where a is the half-distance parameter between the dots. Indeed, the two minima of this potential are located at $x = \pm a$, where the shape of the potential is approximately harmonic. By performing a Taylor expansion up to the second order, one gets

$$V_{c,x}(x) \approx \frac{1}{2}\kappa_x (x \pm a)^2\,, \tag{5.106}$$

showing that the parameter κ_x is the same elastic constant defining the strength of the confinement as in Eq. (5.103). A comparison between the quartic potential of the DQD and two harmonic potentials with the same κ_x located at $x = \pm a$ is shown in Fig. 5.1(a).

Instead, the out-of-plane confinement is the same for both SQDs and DQDs, and is modeled through a well of width L_z and height V_{bo}, either with sharp barriers,

$$V_{c,z}(z) = V_{bo}[\mathcal{H}(z - L_z/2) + \mathcal{H}(-z - L_z/2)]\,, \tag{5.107}$$

where $\mathcal{H}$ is the Heaviside step function:

$$\mathcal{H}(z) = \begin{cases} 0, & z < 0 \\ 1, & z \geq 0 \end{cases}\,, \tag{5.108}$$

or with smooth barriers,

$$V_{c,z}(z) = V_{bo}\left\{1 + \frac{1}{2}\tanh[(z - L_z/2)/S] + \frac{1}{2}\tanh[(-z - L_z/2)/S]\right\}\,, \tag{5.109}$$

where S is a parameter defining the slope of the potential barrier. The potentials in Eq. (5.107) and (5.109) reproduce the vertical confinement felt by a hole in a heterostructure, which is due to the band-offset V_{bo} between the different substrates. The latter, specifically, takes into account a more gradual transition at the interface between the substrates. In both situations, we introduce an additional out-of-plane electric field E_z, by summing a linear potential to the previous $V_{c,z}$'s:

$$V_{DC}(z) = -E_z z\,, \tag{5.110}$$

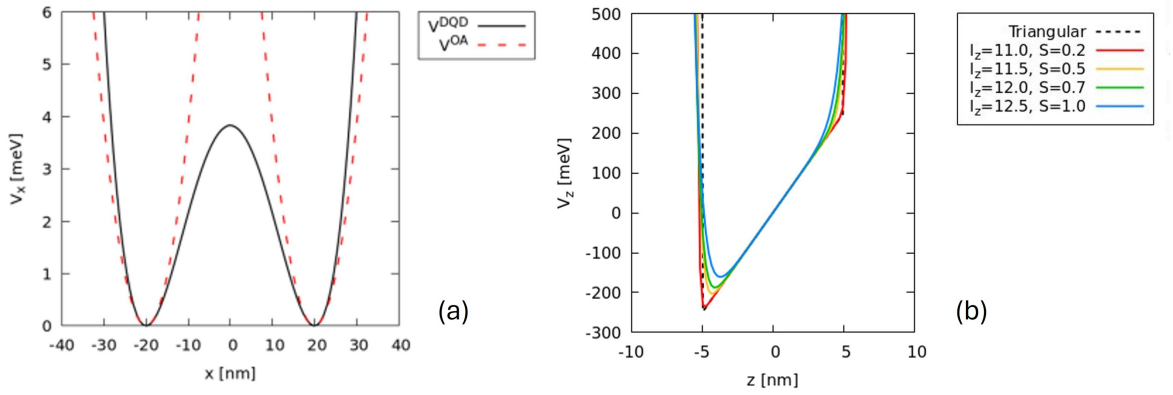


Figure 5.1: (a) An example of the shape of the quartic potential from Eq. (5.105) for the DQD (continuous line), with parameters $a = 20$ nm, and $k_x = 7.66 \cdot 10^{-2}$ meV/nm^2 ($\hbar\omega_x = 5$ meV). The dashed lines show the harmonic approximation from Eq. (5.106) close to the minima ($x = \pm a$), with the same parameters. (b) Comparison between the sharp triangular potential in Eq. (5.107) with $L_z = 10$ nm (dashed line) and the smooth potential in Eq. (5.109) (continuous curves), for different values of L_z (in nm) and S (in nm^{-1}). In all cases we fixed $E_z = 50$ mV/nm.

where DC stands for direct current, since it's a constant contribution in time to the confinement potential. This term breaks the orbital symmetry and allows for EDSR. Overall, the hole will feel the action of a triangular potential along z. Fig. 5.1(b) shows the comparison between the situations with sharp and smooth barriers in the presence of V_{DC}. Note that the higher the value of S is, the larger L_z must be to get a good enough approximation of the bottom of the sharp well. This is because in the smooth case L_z is the half-height width of the well, rather than the width at the bottom. Since the hole state tends to be located near the minimum of the potential, its behavior will generally be affected by the slope S.

5.3.2 Coulomb-induced modifications in the confinement

In this Section we look at ways to model the confinements and behaviors of SQDs and DQDs in the presence of a Coulomb potential caused by a charge Ze at position $\mathbf{r}_0$ close to the dots:

$$V_{Ze}(\mathbf{r}) = C\frac{Ze^2}{|\mathbf{r}-\mathbf{r}_0|} = C\frac{Ze^2}{\sqrt{(x-x_0)^2+(y-y_0)^2+(z-z_0)^2}}\,, \tag{5.111}$$

with

$$C = \frac{1}{4\pi\varepsilon_0\varepsilon_r}\,, \tag{5.112}$$

where ε_0 is the dielectric constant in vacuum and ε_r is the relative dielectric constant in the device. The models introduced here will be relevant in the next Chapter, in which we will study the effects of the electrostatic environment on our system and how to characterize such effects.

Effective curvature

The total potential felt by the hole in our device in the presence of an additional charge is

$$V_{tot}(\mathbf{r}) = V_c(\mathbf{r}) + V_{Ze}(\mathbf{r})\,. \tag{5.113}$$

If the Coulomb potential is small in the region defined by the quantum dots, the main effect of $V_{Ze}(\mathbf{r})$ will be to modify the position of the minima ($x_{min,1}$, $x_{min,2}$, ...) of the confinement potentials and the effective curvatures in their vicinity. Since the hole will be mainly localized near these minima, we can approximate the effective potential acting on the hole through a harmonic approximation of $V_{tot}(\mathbf{r})$ near $x_{min,1}$, $x_{min,2}$, and so on. To further simplify the treatment, we consider situations in which $L_z \ll l_x$, l_y, where l_x, l_y are the characteristic lengths of the harmonic confinements in-plane. In this case, to take account of the much stronger confinement along z, we state that in first approximation the hole will always be strongly localized near $z = 0$, independently of the strength of the Coulomb potential. That is, we consider the hole state to be a Dirac delta centered in 0 in z, $\delta(z)$. In this approximation, the potential felt by the hole is $V_{tot}(x, y, 0)$, and to find its minima in-plane we look at the solutions of the following equation:

$$\nabla_{(x,y)} V_{tot}(x, y, 0) = 0\,. \tag{5.114}$$

For a SQD, this translates to solving the following system of equations:

$$\begin{cases} \frac{\partial}{\partial x} V_{tot}^{SQD}(x, y, 0) = \kappa_x x - C\frac{Ze^2(x-x_0)}{[(x-x_0)^2+(y-y_0)^2+z_0^2]^{3/2}} = 0 \\ \frac{\partial}{\partial y} V_{tot}^{SQD}(x, y, 0) = \kappa_y y - C\frac{Ze^2(y-y_0)}{[(x-x_0)^2+(y-y_0)^2+z_0^2]^{3/2}} = 0 \end{cases}. \tag{5.115}$$

We now consider the condition for which $y_0 = 0$ and $Z < 0$. This greatly simplifies the second equation in Eq. (5.115), which now has only a trivial solution for $y_{min} = 0$. Replacing $y = y_{min} = 0$ into the first equation, the solution for x can then be found numerically. Specifically, we select the solution for which $x_{min} \approx 0$. Indeed, under the considered hypothesis of a small Coulomb potential in the SQD region, we expect the minimum to remain close to $x = 0$. At this point, the effective curvature of the potential in $(x_{min}, y_{min}) = (x_{min}, 0)$ is found by evaluating the eigenvalues of the Hessian matrix of $V_{tot}(x, y, 0)$ on the xy plane:

$$\begin{aligned} \mathbb{H}_{xy}^{SQD}(x_{min}, 0) &= \begin{pmatrix} \frac{\partial^2}{\partial x^2} V_{tot}^{SQD}(x, y, 0) & \frac{\partial^2}{\partial x \partial y} V_{tot}^{SQD}(x, y, 0) \\ \frac{\partial^2}{\partial x \partial y} V_{tot}^{SQD}(x, y, 0) & \frac{\partial^2}{\partial y^2} V_{tot}^{SQD}(x, y, 0) \end{pmatrix}\Bigg|_{(x_{min},0)} = \\ &= \begin{pmatrix} \kappa_x - C\frac{Ze^2[(x_{min}-x_0)^2+z_0^2]-3Ze^2(x_{min}-x_0)^2}{[(x_{min}-x_0)^2+z_0]^{5/2}} & 0 \\ 0 & \kappa_y - C\frac{Ze^2}{[(x_{min}-x_0)^2+z_0^2]^{3/2}} \end{pmatrix}. \end{aligned} \tag{5.116}$$

Since the in-plane Hessian matrix is diagonal at $(x_{min}, 0)$, its eigenvalues κ_x' and κ_y', i.e. the curvatures of the potential along x and y, are respectively the first and second diagonal elements. The same steps can be followed for a DQD, for which the system of equations to find the position of the minima is:

$$\begin{cases} \frac{\partial}{\partial x} V_{tot}^{SQD}(x, y, 0) = \frac{\kappa_x(x^2-a^2)x}{2a^2} - C\frac{Ze^2(x-x_0)}{[(x-x_0)^2+(y-y_0)^2+z_0^2]^{3/2}} = 0 \\ \frac{\partial}{\partial y} V_{tot}^{SQD}(x, y, 0) = \kappa_y y - C\frac{Ze^2(y-y_0)}{[(x-x_0)^2+(y-y_0)^2+z_0^2]^{3/2}} = 0 \end{cases}. \tag{5.117}$$

Again, for $y_0 = 0$ and $Z < 0$ the only solution for y is $y_{min} = 0$. Once we replace this into the first equation, we select the two solutions $x_{min,1} \equiv x_{D1} \approx a$ and $x_{min,2} \equiv x_{D2} \approx -a$, which are close to the original minima of the right and left dot, respectively. The Hessian matrix at the minima in this

case becomes:

$$\mathbb{H}_{xy}^{DQD}(x_{Di},0) = \begin{pmatrix} \frac{\partial^2}{\partial x^2}V_{tot}^{DQD}(x,y,0) & \frac{\partial^2}{\partial x\partial y}V_{tot}^{DQD}(x,y,0) \\ \frac{\partial^2}{\partial x\partial y}V_{tot}^{DQD}(x,y,0) & \frac{\partial^2}{\partial y^2}V_{tot}^{DQD}(x,y,0) \end{pmatrix}\Bigg|_{(x_{Di},0)} = \\ = \begin{pmatrix} \kappa_x\frac{(3x_{Di}^2-a^2)}{2a^2} - C\frac{Ze^2[(x_{Di}-x_0)^2+z_0^2]-3Ze^2(x_{Di}-x_0)^2}{[(x_{Di}-x_0)^2+z_0]^{5/2}} & 0 \\ 0 & \kappa_y - C\frac{Ze^2}{[(x_{Di}-x_0)^2+z_0^2]^{3/2}} \end{pmatrix}, \quad (5.118)$$

with $Di = D1$ or $D2$. The Hessian matrix for the DQD is once again diagonal, with eigenvalues $\kappa'_{x,Di}$ and $\kappa'_{y,Di}$, which generally differ between $D1$ and $D2$. Note that both for the SQD and DQD the effective curvature along y is always positive for $Z < 0$, which is our working hypothesis. However, the curvature along x can be either positive or negative depending on x_0, meaning that the solutions of Eqs. (5.115) and (5.117) can in general be either minimum or saddle points.

After all these considerations, we can rewrite the total potential felt by the hole state through a Taylor expansion to second order in both x and y. For the SQD:

$$\begin{aligned} V_{tot}(x,y,0) \approx & V_{min}^{SQD}(x,y) = \\ = & V_{tot}(x_{min},0,0) + \sum_{\alpha=x,y}\frac{\partial}{\partial\alpha}V_{tot}(x,y,0)\Big|_{(x_{min},0)}(\alpha-\alpha_{min}) \\ & + \frac{1}{2}\sum_{\alpha,\beta=x,y}\frac{\partial^2}{\partial\alpha\partial\beta}V_{tot}(x,y,0)\Big|_{(x_{min},0)}(\alpha-\alpha_{min})(\beta-\beta_{min}) = \\ = & V_{tot}(x_{min},0,0) + \frac{1}{2}\kappa'_x(x-x_{min})^2 + \frac{1}{2}\kappa'_y y^2\,, \end{aligned} \quad (5.119)$$

where we used that the first derivative of $V_{tot}(x,y,0)$ at $(x_{min},0)$ is zero, and the fact that the out-of-diagonal elements of the Hessiam matrix are zero at $(x_{min},0)$. Similarly, for each dot of the DQD we have:

$$\begin{aligned} V_{tot}(x,y,0) \approx & V_{Di}^{DQD}(x,y) = \\ = & V_{tot}(x_{Di},0,0) + \sum_{\alpha=x,y}\frac{\partial}{\partial\alpha}V_{tot}(x,y,0)\Big|_{(x_{Di},0)}(\alpha-\alpha_{Di}) \\ & + \frac{1}{2}\sum_{\alpha,\beta=x,y}\frac{\partial^2}{\partial\alpha\partial\beta}V_{tot}(x,y,0)\Big|_{(x_{Di},0)}(\alpha-\alpha_{Di})(\beta-\beta_{Di}) = \\ = & V_{tot}(x_{Di},0,0) + \frac{1}{2}\kappa'_{x,Di}(x-x_{Di})^2 + \frac{1}{2}\kappa'_{y,Di}y^2\,. \end{aligned} \quad (5.120)$$

Heavy-hole approximation

Overall, in the previous approximations, the 0th-order terms are the constant electrostatic biases felt by the hole at the potential minimum, while the 2nd-order terms give us the effective harmonic confinements. In first approximation, inside the Hamiltonian from (5.41) we can replace the total potential in Eq. (5.113) with the approximations in Eqs. (5.119-5.120) plus the z contribution, which at the beginning of the previous Section we decoupled from the in-plane one. Additionally, we know from previous studies that the first eigenstates of a single hole in Si quantum dots are predominantly of HH nature, with an HH band occupation higher that 98% [255]. Consequently,

the model can be further simplified by neglecting the coupling terms R and S in Eq. (5.41), which couple the HH bands to the LH and SO ones, since their occupation is much smaller. By doing so, we see that the envelope functions corresponding to the HH bands are now the solution of two decoupled equations. For the SQD:

$$\begin{cases} [P(\mathbf{k}) + Q(\mathbf{k}) + V_{min}^{SQD}(x,y) + V_{c,z}(z)]\phi_n^{\frac{3}{2},\frac{3}{2}}(\mathbf{r}) = E_n \phi_n^{\frac{3}{2},\frac{3}{2}}(\mathbf{r}) \\ [P(\mathbf{k}) + Q(\mathbf{k}) + V_{min}^{SQD}(x,y) + V_{c,z}(z)]\phi_n^{\frac{3}{2},-\frac{3}{2}}(\mathbf{r}) = E_n \phi_n^{\frac{3}{2},-\frac{3}{2}}(\mathbf{r}) \end{cases}, \tag{5.121}$$

where, in the absence of any external magnetic field, the solutions are the same. Thus, without loss of generality, we can call $\phi_n^{\frac{3}{2},\frac{3}{2}} = \phi_{HH}$ the HH eigenstate of the HH Hamiltonian:

$$H_{HH}^{SQD}(\mathbf{r}) = \sum_\alpha \left[\frac{\hbar^2}{2m_\alpha^{HH}}k_\alpha^2 + \frac{1}{2}\kappa'_\alpha(\alpha - \alpha_{min})^2\right] + \left[\frac{\hbar^2}{2m_z^{HH}}k_z + V_{c,z}(z)\right] + V_{tot}^{SQD}(x_{min},0,0)\,, \tag{5.122}$$

where we replaced the expressions of P and Q from Eqs. (5.28-5.29) and defined the HH effective masses as:

$$m_x^{HH} = m_y^{HH} \equiv \frac{m_0}{\gamma_1 + \gamma_2}\,, \quad m_z^{HH} \equiv \frac{m_0}{\gamma_1 - 2\gamma_2}\,. \tag{5.123}$$

Thanks to our approximations, the Hamiltonian in Eq. (5.122) is separable, so that its ground state energy E_0^{HH} is the sum of those along each direction plus the electrostatic bias:

$$E_0^{HH} = \frac{\hbar}{2}\left[\omega'_x + \omega'_y\right] + E_z + V_{tot}^{SQD}(x_{min},0,0)\,, \tag{5.124}$$

where ω'_x and ω'_y are the frequencies of the harmonic oscillators with constants κ'_x and κ'_y, and E_z is the ground state energy along z, approximately independent of the Coulomb potential from our previous considerations. Since the confinement along z is much stronger than the in-plane confinement, we can also say that the first excited state will correspond to either an excitation along x ($\Delta E^{HH} = \hbar\omega'_x$) or y ($\Delta E^{HH} = \hbar\omega'_x$), depending on the relative strength between them.

The same steps can be performed for the DQD, obtaining for each dot the following Hamiltonian:

$$H_{HH,Di}^{DQD}(\mathbf{r}) = \sum_\alpha \left[\frac{\hbar^2}{2m_\alpha^{HH}}k_\alpha^2 + \frac{1}{2}\kappa'_{\alpha,Di}(\alpha - \alpha_{Di})^2\right] + \left[\frac{\hbar^2}{2m_z^{HH}}k_z + V_{c,z}(z)\right] + V_{tot}^{DQD}(x_{Di},0,0)\,, \tag{5.125}$$

where the ground eigenenergies now depend on the dot through both the value of $V_{tot}(\mathbf{r})$ at the minimum and the effective confinement frequencies:

$$E_{0,Di}^{HH} = \frac{\hbar}{2}\left(\omega'_{x,Di} + \omega'_{y,Di}\right) + E_z + V_{tot}^{DQD}(x_{Di},0,0)\,. \tag{5.126}$$

In this case, the ground states of the two dots will in general have different energies. Recall that we are working under the hypothesis that the Coulomb potential is small with respect to the harmonic confinement in the region occupied by the dots. Thus, it's reasonable to assume that the energy difference between the ground states of the two dots,

$$\left|E_{0,D2}^{HH} - E_{0,D1}^{HH}\right| = \left|\frac{\hbar}{2}\left(\omega_x^{D2} + \omega_y^{D2} - \omega_x^{D1} - \omega_y^{D1}\right) + V_{tot}^{DQD}(x_{D2},0) - V_{tot}^{DQD}(x_{D1},0)\right|\,. \tag{5.127}$$

is lower than the quantum of oscillation in either dots. Consequently, the hole will occupy the lower-energy one in its ground state, and the higher-energy one in its first excited state.

Two-site Hubbard model

Another possible way to model the DQD system in the presence of an external charge is through a single-band two-site Hubbard model. In other to do so, we describe the two dots as two possible sites (1 and 2) that can be occupied by the hole. Like the model from the previous Section, this also does not take account of the coupling terms between bands, but the treatment is not dependent on which band we consider. As we have already seen, the presence of the defect makes the sites inequivalent. In fact, the Coulomb potential introduces a different shift on the bottom of the dots, so that the on-site energies $\mathcal{E}_1$ and $\mathcal{E}_2$ associated with each dot are different. By identifying site 1 as $x_{D1} = a$ and site 2 as $x_{D2} = -a$ we get:

$$\mathcal{E}_1 = C\frac{Ze^2}{\sqrt{(x_0 - a)^2 + y_0^2 + z_0^2}}, \qquad \mathcal{E}_2 = C\frac{Ze^2}{\sqrt{(x_0 + a)^2 + y_0^2 + z_0^2}}. \tag{5.128}$$

Then, we identify the hopping parameter t as the value of the energy gap between the bonding and anti-bonding states. That said, the Hubbard Hamiltonian for a single hole is an operator written as:

$$\hat{H}_{Hub} = -t(\hat{c}_1^\dagger \hat{c}_2 + \hat{c}_2^\dagger \hat{c}_1) + \mathcal{E}_1 \hat{n}_1 + \mathcal{E}_2 \hat{n}_2 \tag{5.129}$$

where we can neglect the spin degree of freedom since we are dealing with a single particle with a fixed spin. In Eq. (5.129), $\hat{c}_i^\dagger$ and $\hat{c}_i$ are the creation and annihilation operators on site i, and $\hat{n}_i = \hat{c}_i^\dagger \hat{c}_i$ is the number operator on site i. In matrix form, $\hat{H}_{Hub}$ can be written as a 2×2 matrix on the site basis:

$$\hat{H}_{Hub} = \begin{pmatrix} \mathcal{E}_1 & -t \\ -t^* & \mathcal{E}_2 \end{pmatrix} = \bar{\mathcal{E}} - \begin{pmatrix} \frac{\Delta}{2} & t \\ t^* & -\frac{\Delta}{2} \end{pmatrix} \tag{5.130}$$

where we have defined the quantities $\bar{\mathcal{E}} = (\mathcal{E}_1 + \mathcal{E}_2)/2$ and $\Delta = \mathcal{E}_2 - \mathcal{E}_1$. The eigenvalues and eigenvectors are then easily calculated:

$$e_\pm^{Hub} = \bar{\mathcal{E}} \pm \frac{\Delta}{2}\sqrt{1 + \sigma^2}, \qquad \sigma = \frac{2|t|}{\Delta}, \tag{5.131}$$

$$\left|\psi_\pm^{Hub}\right\rangle = \begin{pmatrix} c_1^\pm \\ c_2^\pm \end{pmatrix} = \frac{1}{\sqrt{2\Sigma}} \begin{pmatrix} \pm\frac{\sigma}{\sqrt{\Sigma \mp 1}} \\ \sqrt{\Sigma \mp 1} \end{pmatrix}, \qquad \Sigma = \sqrt{1 + \sigma^2}. \tag{5.132}$$

As we can see, this model does not take account of the shape of the confinement of each dot. As such, it can't give us any detail on how the behavior of our system is influenced by the interplay between the shape of the dots and the electrostatic environment. However, it gives us a metric of comparison to understand the generality of the phenomena we will be describing. We will see later in the next Chapter how this and the previous models can be helpful in the description of our system.

5.4 Definition of the qubit

After defining the single-hole Hamiltonian in Chapter 5 and the confining potentials characterizing our dots in Sec. 5.3, we can start modeling our qubit. Specifically, after the Kramers degeneracy has been lifted through the introduction of a static magnetic field (see Sec. 5.1.3), we identify the two states $|0\rangle$ and $|1\rangle$ of the qubit with the two states making up the ground doublet. Since one

state is the time-reversal conjugate of the other, we can associate opposite effective spins to them, which we will indicate as $\Downarrow$ and $\Uparrow$. In ket notation, we can write the states as the basis kets of a 2-dimensional Hilbert space:

$$|\Downarrow\rangle \equiv |0\rangle = \begin{pmatrix} 0 \\ 1 \end{pmatrix}, \quad |\Uparrow\rangle \equiv |1\rangle = \begin{pmatrix} 1 \\ 0 \end{pmatrix}. \tag{5.133}$$

Although the qubit is now defined from an effective spin degree of freedom of the hole states, the spin-orbit term from Eq. (5.23) inside our Hamiltonian allows us to manipulate its state directly through electrical means, as previously introduced in Sec. 4.2.2. In this Section, we give a brief analytical description of how this manipulation occurs.

5.4.1 SU(2) algebra

The usual way to graphically represent the state of a qubit is by means of the Bloch sphere [see Fig. 5.2(a)], where the states $|0\rangle$ and $|1\rangle$ are respectively at the north and south poles and any other state is defined by the polar angle θ_q and the azimuthal angle ϕ_q:

$$|\psi_q\rangle = \cos\left(\frac{\theta_q}{2}\right)|0\rangle + e^{i\phi_q}\sin\left(\frac{\theta_q}{2}\right)|1\rangle. \tag{5.134}$$

From this representation, it's clear to see how any operation acting on the qubit can be written as a combination of 3D rotations of the SU(2) algebra. The generators of this algebra are the Pauli matrices:

$$\hat{\sigma}_0 \equiv \hat{\mathbb{1}} = \begin{pmatrix} 1 & 0 \\ 0 & 1 \end{pmatrix}, \quad \hat{\sigma}_1 = \begin{pmatrix} 0 & 1 \\ 1 & 0 \end{pmatrix}, \quad \hat{\sigma}_2 = \begin{pmatrix} 0 & -i \\ i & 0 \end{pmatrix}, \quad \hat{\sigma}_3 = \begin{pmatrix} 1 & 0 \\ 0 & -1 \end{pmatrix}. \tag{5.135}$$

which are (i) traceless, (ii) Hermitian, and (iii) obey the following commutation relations:

$$\left[\hat{\sigma}_j, \hat{\sigma}_k\right] = 2i\sum_l \epsilon_{jkl}\hat{\sigma}_l, \quad j,k,l = 1,2,3, \tag{5.136}$$

where ϵ_{ijk} is the Levi-Civita symbol in three dimensions. A generic rotation in time of an angle $\alpha(t)$ around the axis of a unitary vector $\mathbf{n} \equiv (n_1, n_2, n_3)$ is:

$$\begin{aligned} \hat{R}[\alpha_{\mathbf{n}}(t)] =& e^{-\frac{i}{2}\hat{\boldsymbol{\sigma}}\cdot\mathbf{n}\alpha(t)} = \\ =& \begin{pmatrix} \cos[\alpha(t)/2] - in_3\sin[\alpha(t)/2] & (-n_1 + in_2)\sin[\alpha(t)/2] \\ (-n_1 - in_2)\sin[\alpha(t)/2] & \cos[\alpha(t)/2] + in_3\sin[\alpha(t)/2] \end{pmatrix}, \end{aligned} \tag{5.137}$$

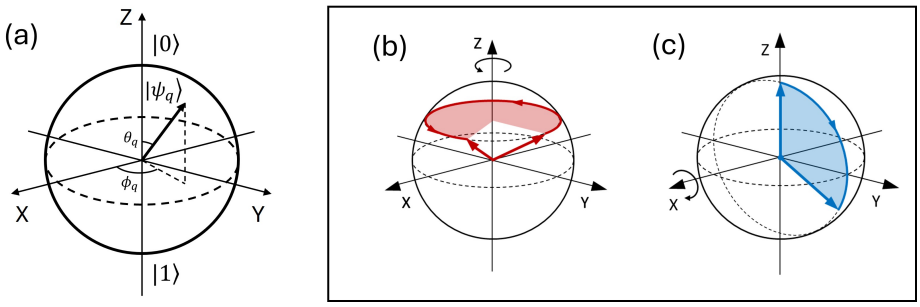


Figure 5.2: (a) Schematic representation of the qubit state $|\psi_q\rangle$ from Eq. (5.134), determined by angles θ_q and ϕ_q, on the Bloch sphere. (b) Precession of the qubit state around the Z axis of the Bloch sphere during free evolution. (c) Rotation of the qubit state around the X axis of the Bloch sphere during a transition between states $|0\rangle$ and $|1\rangle$. Panels (b) and (c) were adapted from [2].

where $\hat{\sigma} \equiv (\hat{\sigma_1}, \hat{\sigma_2}, \hat{\sigma_3})$ is the vector of Pauli matrices. We can now relate these rotations to the action of an external field. Indeed, any unitary operator acting in time on the qubit state is generated by a Hermitian operator $\hat{O}$:

$$\hat{U}(t) = e^{-i\hat{O}t/\hbar}. \tag{5.138}$$

Since it's a 2×2 operator, we can always represent $\hat{O}$ on the basis made of the four matrices from Eq. (5.135): from now on, we will refer to the coefficients of the linear combination as Rabi frequencies ω_n^R, up to a factor of $\hbar$.

$$\hat{O} = \sum_{n=0}^{3} \hbar\omega_n^R \hat{\sigma}_n = \hbar \begin{pmatrix} \omega_0^R + \omega_3^n & \omega_1^R - i\omega_2^R \\ \omega_1^R + i\omega_2^R & \omega_0^R - \omega_3^R \end{pmatrix}. \tag{5.139}$$

Note that the values of ω_1^R, ω_2^R and ω_3^R are the angular frequencies of rotation of the qubit around the axes X, Y and Z, corresponding to angles $\alpha_i(t) = \omega_i^R t$. Instead, the frequency $\hbar\omega_0^R$ is a global phase factor on the whole state. By now reversing the relations in Eq. (5.139), one is able to explicitly relate each Rabi frequency to the matrix elements of the operator $\hat{O}$:

$$\begin{aligned} \hbar\omega_0^R \equiv \hbar\omega_{\mathbb{1}}^R = \frac{O_{11} + O_{00}}{2}, \quad \hbar\omega_1^R \equiv \hbar\omega_X^R = \Re[O_{01}], \\ \hbar\omega_2^R \equiv \hbar\omega_Y^R = \Im[O_{01}], \quad \hbar\omega_3^R \equiv \hbar\omega_Z^R = \frac{O_{11} - O_{00}}{2}. \end{aligned} \tag{5.140}$$

5.4.2 Qubit evolution

Our aim now is to obtain the analytical expression of the evolution operator acting on the qubit under the presence of an external electric field. First of all, let's define another essential quantity, namely the Larmor frequency of the qubit. This quantity is the energy difference between the states $|1\rangle$ and $|0\rangle$ of the qubit:

$$\omega_L = \frac{e_1 - e_0}{\hbar}, \tag{5.141}$$

which in our case, recalling from Sec. 5.1.3, is the Kramers splitting induced by the introduction of a magnetic field inside our Hamiltonian in the first Kramers doublet:

$$\mathbf{B} = B(\sin\theta_B \cos\phi_B, \sin\theta_B \sin\phi_B, \cos\theta_B) = B\mathbf{b}, \tag{5.142}$$

where θ_B and ϕ_B are respectively the polar and azimuthal angle, this time with respect to the axes x, y and z in real space. With this quantity we can write the unperturbed, time-independent effective Hamiltonian of the qubit,

$$\hat{H}_0 = \begin{pmatrix} e_1 & 0 \\ 0 & e_0 \end{pmatrix} = \begin{pmatrix} e_{avg} + \frac{\hbar\omega_L}{2} & 0 \\ 0 & e_{avg} - \frac{\hbar\omega_L}{2} \end{pmatrix} = e_{avg}\hat{\mathbb{1}} + \frac{\hbar\omega_L\hat{\sigma}_3}{2}, \tag{5.143}$$

in which $e_{avg} = (e_1 + e_2)/2$ is the average energy of the system. In the Schrödinger picture, in the absence of any perturbing terms, the state evolution is found through the integration of the time-dependent Schrödinger equation:

$$i\hbar\frac{\partial |\psi_{q,S}(t)\rangle}{\partial t} = \hat{H}_0 |\psi_{q,S}(t)\rangle, \tag{5.144}$$

which we can integrate easily via variable separation, obtaining the following:

$$|\psi_{q,S}(t)\rangle = e^{-i\hat{H}_0 t/\hbar} |\psi_{q,S}(t_i)\rangle = e^{-ie_{avg}t/\hbar} \begin{pmatrix} e^{-i\omega_L t/2} c_1(t_i) \\ e^{i\omega_L t/2} c_0(t_i) \end{pmatrix}, \tag{5.145}$$

where we called $c_i(t_i)$ the coefficients of the state at time t_i, i.e. the initial condition of the system. Equation (5.145) shows that the quantity e_{avg} only introduces a global phase to $|\psi_{q,S}(t)\rangle$, and is therefore of no physical importance. On the other hand, the Larmor frequency ω_L induces a phase difference between the two components of the state vector, which increases linearly over time. On the Bloch sphere, this behavior corresponds to a precession around the Z axis [see Fig. 5.2(b)]. However, the action of this phase alone is not sufficient to change the coefficients c_0 and c_1 in module, i.e. the occupation probability of each basis state. Instead, to achieve a controlled variation in the occupation probability over time, we need to introduce a time-dependent perturbation in the Hamiltonian.

Action of a driving field

In this Section we consider the action of a time-dependent electric field $\hat{V}_{AC}(t)$ acting on the qubit. The notation AC stands for Alternating Current, which here is a name we use to distinguish it from the constant contribution in Eq. (5.110). With the addition of this term, the Schrödinger equation from Eq. (5.144) becomes:

$$i\hbar \frac{\partial |\psi_{q,S}(t)\rangle}{\partial t} = \left[\hat{H}_0 + \hat{V}_{AC}(t)\right] |\psi_{q,S}(t)\rangle \ . \tag{5.146}$$

The same equation can also be written in terms of the evolution operator $\hat{U}_S(t, t_0)$, which is a unitary operator that evolves the state from time t_0 to t:

$$|\psi_{q,S}(t)\rangle = \hat{U}_S(t, t_0) |\psi_{q,S}(t_0)\rangle \ . \tag{5.147}$$

Recall that the evolution operator is equal to the identity for $t = t_0$,

$$\hat{U}(t_0, t_0) = \hat{\mathbb{1}} \, , \tag{5.148}$$

and the composition of two evolution operators is still an evolution operator:

$$\hat{U}(t_2, t_1)\hat{U}(t_1, t_0) = \hat{U}(t_2, t_0). \tag{5.149}$$

By replacing Eq. (5.147) into Eq. (5.146), one obtains the Schrödinger equation for the evolution operator:

$$\mathrm{i}\hbar\partial_t \hat{U}_S(t, t_0) = \left[\hat{H}_0 + \hat{V}_{AC}(t)\right] \hat{U}_S(t, t_0) \, , \tag{5.150}$$

where we adopted the shorthand notation ∂_t for the time derivative. Solving either one of Eqs. (5.146) or (5.150) gives us the description of the evolution of the qubit in time. Consequently, from now on we decide to focus on Eq. (5.150), which doesn't depend on the initial condition of the qubit at time t_0. At this point, we notice that the total Hamiltonian of the system consists of a time-independent part, i.e. the unperturbed Hamiltonian $\hat{H}_0$, and a time-dependent perturbation, $\hat{V}_{AC}(t)$. Therefore, it's more convenient to study the time evolution of the system in the interaction picture. Here, the evolution is split between the state vector and the observables: while the former carries the evolution due to the perturbation term, the latter evolves through the unperturbed Hamiltonian. To pass from the Schrödinger picture to the interaction picture, one needs to perform the following transformation on the state:

$$|\psi_{q,I}(t)\rangle = e^{i\hat{H}_0 t/\hbar} |\psi_{q,S}(t)\rangle = e^{i\omega_L t\hat{\sigma}_3/2} |\psi_{q,S}(t)\rangle \ , \tag{5.151}$$

where we replaced the definition of $\hat{H}_0$ from Eq. (5.143) by setting $a_{avg} = 0$ without loss of generality. This transformation basically corresponds to a de-evolution of the state with respect to the unperturbed Hamiltonian. In addition, notice that it only adds phases to the components of the state vector, so that the occupation probabilities are the same in both pictures. In terms of the evolution operator, we can rewrite the one in the Schrödinger picture in terms of the one in the interaction picture:

$$\hat{U}_S(t,t_0) = \mathrm{e}^{-\mathrm{i}\hat{H}_0 t/\hbar}\,\hat{U}_\mathrm{I}(t,t_0)\,\mathrm{e}^{\mathrm{i}\hat{H}_0 t_0/\hbar} = \mathrm{e}^{-\mathrm{i}\omega_\mathrm{L} t\hat{\sigma}_3/2}\,\hat{U}_\mathrm{I}(t,t_0)\,\mathrm{e}^{\mathrm{i}\omega_\mathrm{L} t_0\hat{\sigma}_3/2}\,, \tag{5.152}$$

so that we can insert Eq. (5.152) into Eq (5.150) and obtain the Schrödinger equation for the evolution operator in the interaction picture:

$$i\hbar\partial_t\hat{U}_I(t,t_0) = e^{i\omega_L t\hat{\sigma}_3/2}\hat{V}_{AC}(t)e^{-i\omega_L t\hat{\sigma}_3/2}\hat{U}_I(t,t_0)\,. \tag{5.153}$$

As is apparent from Eq. (5.153), this Schrödinger equation only depends on the perturbative term $\hat{V}_{AC}(t)$.

In the following, we choose a driving field $\hat{V}_{AC}(t)$ that oscillates in time as a cosine, and whose shape in time is determined by an envelope function $F(t)$. Additionally, by comparison with the DC field defined in Eq. (5.110), we choose its amplitude to be linear in z through a factor of $-\delta E_z$. By setting $\delta E_z \ll E_z$, we can effectively treat $\hat{V}_{AC}(t)$ as a small oscillating perturbation of the constant out-of-plane potential $\hat{V}_{DC}$ applied on our system. Overall we write:

$$\hat{V}_{AC}(t) = -F(t)\cos(\omega_P t)\,\delta E_z\hat{z}\,, \tag{5.154}$$

where ω_P is the oscillation frequency of the pulse. Additionally, as we did previously for a general operator in Eq. (5.139), we write the time-independent amplitude of the perturbation as a linear combination of the Pauli matrices:

$$-\delta E_z\hat{z} = \sum_{n=0}^{3}\hbar\omega_n^R\hat{\sigma}_n\,, \tag{5.155}$$

where the Rabi frequencies are redefined as

$$\begin{aligned}
&\hbar\omega_0^R \equiv \hbar\omega_{\hat{\mathbb{1}}}^R = -\delta E_z\frac{\langle 1|\hat{z}|1\rangle + \langle 0|\hat{z}|0\rangle}{2}\,, \quad \hbar\omega_1^R \equiv \hbar\omega_X^R = -\delta E_z\Re\left[\langle 0|\hat{z}|1\rangle\right]\,,\\
&\hbar\omega_2^R \equiv \hbar\omega_Y^R = -\delta E_z\Im\left[\langle 0|\hat{z}|1\rangle\right]\,, \quad \hbar\omega_3^R \equiv \hbar\omega_Z^R = -\delta E_z\frac{\langle 1|\hat{z}|1\rangle - \langle 0|\hat{z}|0\rangle}{2}\,.
\end{aligned} \tag{5.156}$$

By inserting Eqs. (5.154-5.155) into Eq. (5.153), we rewrite the Schrödinger equation as:

$$i\hbar\partial_t\hat{U}_I(t,t_0) = F(t)\cos(\omega_P t)\sum_{n=0}^{3}\hbar\omega_n^R e^{i\omega_L t\hat{\sigma}_3/2}\hat{\sigma}_n e^{-i\omega_L t\hat{\sigma}_3/2}\hat{U}_I(t,t_0)\,. \tag{5.157}$$

Notice that only $\hat{\sigma}_0 = \hat{\mathbb{1}}$ and $\hat{\sigma}_3$ commute with the exponentials of $\hat{\sigma}_3$, which can then be simplified. Instead, we evaluate the other two terms explicitly:

$$e^{i\omega_L t\hat{\sigma}_3/2}\hat{\sigma}_1 e^{-i\omega_L t\hat{\sigma}_3/2} = \begin{pmatrix} 0 & e^{i\omega_L t} \\ e^{-i\omega_L t} & 0 \end{pmatrix}\,, \tag{5.158}$$

$$e^{i\omega_L t\hat{\sigma}_3/2}\hat{\sigma}_2 e^{-i\omega_L t\hat{\sigma}_3/2} = \begin{pmatrix} 0 & -ie^{i\omega_L t} \\ ie^{-i\omega_L t} & 0 \end{pmatrix} . \tag{5.159}$$

By replacing these expressions in Eq. (5.157) and simplifying a factor of $\hbar$, we obtain

$$i\partial_t \hat{U}_I(t,t_0) = F(t) \begin{pmatrix} (\omega_0^R + \omega_3^R)\cos(\omega_P t) & (\omega_+^R)^* \left(e^{-i(\omega_P-\omega_L)t} + e^{i(\omega_P+\omega_L)t}\right) \\ \omega_+^R \left(e^{i(\omega_P-\omega_L)t} + e^{-i(\omega_P+\omega_L)t}\right) & (\omega_0^R - \omega_3^R)\cos(\omega_P t) \end{pmatrix} \hat{U}_I(t,t_0) , \tag{5.160}$$

where we used Euler's formula to rewrite the cosine in the off-diagonal terms, and we introduced the complex frequency

$$\omega_+^R \equiv \omega_1^R + i\omega_2^R . \tag{5.161}$$

At this point, we have obtained an equation that corresponds to a system of two coupled differential equations, with boundary conditions imposed by Eq. (5.148). For simplicity, we will assume a rectangular envelope function,

$$F(t) = \mathcal{H}(t-t_i)\mathcal{H}(t_f-t) = \begin{cases} 1, & \text{for } t \in [t_i, t_f] \\ 0, & \text{for } t \notin [t_i, t_f] \end{cases} , \tag{5.162}$$

with $\mathcal{H}$ the Heaviside step function previously defined in Eq. (5.108). This shape for the envelope function $F(t)$ means that the external driving field is applied with fixed intensity only inside the interval $t \in [t_i, t_f]$. Instead, at all other times, we have $F(t) = 0$ and the system evolves freely. Consequently, for $t \in [t_0, t_i]$, the evolution operator in the interaction picture satisfies the trivial equation

$$\partial_t \hat{U}_{I,free}(t,t_0) = 0 , \tag{5.163}$$

which is solved as $\hat{U}_{I,free}(t,t_0) = \hat{\mathbb{1}}$ under the boundary condition $\hat{U}_{\text{I,free}}(t_0,t_0) = \hat{\mathbb{1}}$. Since the evolution operators combine as in Eq. (5.149), this means that for $t \in [t_i, t_f]$ we can write:

$$\hat{U}_I(t,t_0) = \hat{U}_I(t,t_i)\hat{U}_{I,free}(t_i,t_0) = \hat{U}_I(t,t_i) , \tag{5.164}$$

and we can focus on solving the Schrödinger equation for $t \in [t_i, t_f]$, with $F(t) = 1$:

$$i\partial_t \hat{U}_I(t,t_i) = \begin{pmatrix} (\omega_0^R + \omega_3^R)\cos(\omega_P t) & (\omega_+^R)^* \left(e^{-i(\omega_P-\omega_L)t} + e^{i(\omega_P+\omega_L)t}\right) \\ \omega_+^R \left(e^{i(\omega_P-\omega_L)t} + e^{-i(\omega_P+\omega_L)t}\right) & (\omega_0^R - \omega_3^R)\cos(\omega_P t) \end{pmatrix} \hat{U}_I(t,t_i) . \tag{5.165}$$

Rotating wave approximation

Let's now focus on solving Eq. (5.165) in resonant conditions, i.e. for

$$\omega_P \approx \omega_L . \tag{5.166}$$

We see that the matrix on the right-hand side contains terms that oscillate with one of three different frequencies: $(\omega_P - \omega_L) \equiv \Delta$; or ω_P; or $(\omega_P + \omega_L)$. Under the chosen resonant conditions, we have

$$|\Delta| \ll |\omega_P|, |\omega_P + \omega_L| , \tag{5.167}$$

so that it's possible to perform a rotating wave approximation (RWA) and neglect all terms but the ones oscillating at the lowest frequency Δ. The Schrödinger equation from Eq. (5.165) consequently reduces to

$$\partial_t \hat{U}_I(t,t_i) \approx -\frac{i}{2}\begin{pmatrix} 0 & (\omega_+^R)^* e^{-i\Delta t} \\ \omega_+^R e^{i\Delta t} & 0 \end{pmatrix} \hat{U}_I(t,t_i)\,. \tag{5.168}$$

Now, in order to solve Eq. (5.168), we start by defining a new operator $\breve{U}(t,t_i)$ for which:

$$\hat{U}_I(t,t_i) \equiv \begin{pmatrix} e^{-i\Delta t/2} & 0 \\ 0 & e^{i\Delta t/2} \end{pmatrix} \breve{U}(t,t_i)\,. \tag{5.169}$$

Using the chain rule, the left-hand side of Eq. (5.168) becomes:

$$\partial_t \hat{U}_I(t,t_i) = \begin{pmatrix} e^{-i\Delta t/2} & 0 \\ 0 & e^{i\Delta t/2} \end{pmatrix} \partial_t \breve{U}(t,t_i) - \frac{i}{2}\Delta \begin{pmatrix} e^{-i\Delta t/2} & 0 \\ 0 & -e^{i\Delta t/2} \end{pmatrix} \breve{U}(t,t_i)\,. \tag{5.170}$$

so that, after rearranging some terms, the equation of motion for operator $\breve{U}(t,t_i)$ becomes:

$$\begin{pmatrix} e^{-i\Delta t/2} & 0 \\ 0 & e^{i\Delta t/2} \end{pmatrix} \partial_t \breve{U}(t,t_i) = \frac{i}{2}\left[\Delta \begin{pmatrix} e^{-i\Delta t/2} & 0 \\ 0 & -e^{i\Delta t/2} \end{pmatrix} - \begin{pmatrix} 0 & (\omega_+^R)^* \\ \omega_+^R & 0 \end{pmatrix}\begin{pmatrix} e^{i\Delta t/2} & 0 \\ 0 & e^{-i\Delta t/2} \end{pmatrix}\right] \breve{U}(t,t_i)$$

$$\Rightarrow \partial_t \breve{U}(t,t_i) = \frac{i}{2}\begin{pmatrix} \Delta & -(\omega_+^R)^* \\ -\omega_+^R & -\Delta \end{pmatrix} \breve{U}(t,t_i)\,, \tag{5.171}$$

and can be straightforwardly integrated via variable separation. Specifically, notice that the boundary condition on $\breve{U}(t,t_i)$ is

$$\breve{U}(t_i,t_i) = \begin{pmatrix} e^{i\Delta t_i/2} & 0 \\ 0 & e^{-i\Delta t_i/2} \end{pmatrix}, \tag{5.172}$$

which follows from Eq. (5.169) after imposing $\hat{U}_I(t_i,t_i) = \hat{\mathbb{1}}$. Consequently, $\breve{U}(t,t_i)$ is not an evolution operator. The analytical solution of Eq. (5.171), with the boundary condition (5.172), is thus:

$$\breve{U}(t,t_i) = \exp\left\{ i \begin{pmatrix} \Delta & -(\omega_+^R)^* \\ -\omega_+^R & -\Delta \end{pmatrix} \frac{t-t_i}{2} \right\} \begin{pmatrix} e^{i\Delta t_i/2} & 0 \\ 0 & e^{-i\Delta t_i/2} \end{pmatrix}. \tag{5.173}$$

We can now evaluate the exponential of the matrix explicitly. First, we rewrite the complex Rabi frequency by factorizing the module and phase:

$$\omega_+^R \equiv |\omega_+^R| e^{i\theta_R} = |\omega_+^R|\left[\cos(\theta_R) + i\sin(\theta_R)\right]. \tag{5.174}$$

Then, we expand the exponential in (5.173) as a linear combination of Pauli matrices:

$$\begin{pmatrix} \Delta & -(\omega_+^R)^* \\ -\omega_+^R & -\Delta \end{pmatrix} \frac{t-t_i}{2} = -|\omega_+^R|\frac{t-t_i}{2}\left[\cos(\theta_R)\hat{\sigma}_1 + \sin(\theta_R)\hat{\sigma}_2\right] + \Delta\frac{t-t_i}{2}\hat{\sigma}_3 \equiv \boldsymbol{a}\cdot\hat{\boldsymbol{\sigma}}\,, \tag{5.175}$$

in which we defined the vector $\mathbf{a}$ as:

$$\boldsymbol{a} \equiv \left(-|\omega_+^R|\cos(\theta_R)\,, -|\omega_+^R|\sin(\theta_R)\,, \Delta\right)\frac{t-t_i}{2}\,, \tag{5.176}$$

with module

$$|\boldsymbol{a}| = \sqrt{|\omega_+^R|^2 + \Delta^2}\frac{t-t_i}{2} \equiv \Omega\frac{t-t_i}{2}\,. \tag{5.177}$$

In the last equation we defined an effective frequency Ω that depends on all the frequencies at play, that is, the pulse frequency ω_P, the complex Rabi frequency ω_+^R, and the Larmor frequency ω_L. At this point, using the following property of the Pauli matrices:

$$\exp\left\{i\left(\boldsymbol{a}\cdot\hat{\boldsymbol{\sigma}}\right)\right\} = \hat{\mathbb{1}}\cos\left(|\boldsymbol{a}|\right) + i\left(\frac{\boldsymbol{a}}{|\boldsymbol{a}|}\cdot\hat{\boldsymbol{\sigma}}\right)\sin\left(|\boldsymbol{a}|\right)\,, \tag{5.178}$$

we obtain the explicit expression of Eq. (5.173):

$$\begin{aligned}\breve{U}(t,t_i) &= \begin{pmatrix} C(t-t_i) + i\frac{\Delta}{\Omega}S(t-t_i) & -i\,e^{-i\theta_R}\frac{|\omega_+^R|}{\Omega}S(t-t_i) \\ -i\,e^{i\theta_R}\frac{|\omega_+^R|}{\Omega}S(t-t_i) & C(t-t_i) - i\frac{\Delta}{\Omega}S(t-t_i)\end{pmatrix}\begin{pmatrix} e^{i\Delta t_i/2} & 0 \\ 0 & e^{-i\Delta t_i/2}\end{pmatrix} \\ &= \begin{pmatrix} e^{i\frac{\Delta t_i}{2}}\left[C(t-t_i) + i\frac{\Delta}{\Omega}S(t-t_i)\right] & -ie^{-i\left(\frac{\Delta t_i}{2}+\theta_R\right)}\frac{|\omega_+^R|}{\Omega}S(t-t_i) \\ -ie^{i\left(\frac{\Delta t_i}{2}+\theta_R\right)}\frac{|\omega_+^R|}{\Omega}S(t-t_i) & e^{-i\frac{\Delta t_i}{2}}\left[C(t-t_i) - i\frac{\Delta}{\Omega}S(t-t_i)\right]\end{pmatrix}\,,\end{aligned} \tag{5.179}$$

where we defined the shorthands

$$C(t-t_i) \equiv \cos\left(\frac{\Omega\,(t-t_i)}{2}\right)\,, \quad S(t-t_i) \equiv \sin\left(\frac{\Omega\,(t-t_i)}{2}\right)\,. \tag{5.180}$$

We can now find the expression $\hat{U}_I(t,t_i)$ valid in the RWA via the definition in Eq. (5.169):

$$\hat{U}_I(t,t_i) = \begin{pmatrix} e^{-i\frac{\Delta(t-t_i)}{2}}\left[C(t-t_i) + i\frac{\Delta}{\Omega}S(t-t_i)\right] & -ie^{-i\left(\frac{\Delta(t+t_i)}{2}+\theta_R\right)}\frac{|\omega_+^R|}{\Omega}S(t-t_i) \\ -ie^{i\left(\frac{\Delta(t+t_i)}{2}+\theta_R\right)}\frac{|\omega_+^R|}{\Omega}S(t-t_i) & e^{i\frac{\Delta(t-t_i)}{2}}\left[C(t-t_i) - i\frac{\Delta}{\Omega}S(t-t_i)\right]\end{pmatrix}\,. \tag{5.181}$$

Now that we have finally obtained the expression of the evolution operator in the interaction picture under the action of the external driving field $\hat{V}_{AC}(t)$, let's see how the state of the qubit is affected. Specifically, let's consider a state vector in the ground state at time t_i, i.e. at the beginning of the pulse:

$$\left|\psi_{q,I}(t_i)\right\rangle = |\Downarrow\rangle = \left|0\right\rangle \equiv \begin{pmatrix}0\\1\end{pmatrix}\,, \tag{5.182}$$

then the occupation probability of state $|\Uparrow\rangle = \left|1\right\rangle$ at time t during the action of the rectangular pulse is

$$\left|\left\langle 1|\psi_{q,I}(t)\right\rangle\right|^2 = \left|U_I^{\Uparrow\Downarrow}(t,t_i)\right|^2 = \left|U_I^{10}(t,t_i)\right|^2 = \frac{|\omega_+^R|^2}{\Omega^2}\sin^2\left(\frac{\Omega(t-t_i)}{2}\right)\,. \tag{5.183}$$

Consequently, the occupation probability of state $|1\rangle$ oscillates in time with amplitude given by the ratio between $|\omega_+^R|$ and Ω. Thus, in the conditions close to resonance that we considered to perform the RWA, the amplitude of the oscillation is $\lesssim 1$ and a transition occurs. Specifically, when the pulse is in perfect resonance and $\Delta = 0$, the transition frequency is equal to the module of the complex Rabi frequency, $\Omega = |\omega_+^R|$, and the state oscillates periodically between states $|0\rangle$

and $|1\rangle$. Notice that this transition can be viewed on the Bloch sphere as a rotation around an axis lying on the XY plane, which brings the state vector from one pole of the sphere to the other and vice versa [see Fig. 5.2(c)]. The orientation of such axis on the XY plane is given by the angle θ_R which defines the phase of the complex frequency ω_+^R from Eq. (5.161). Indeed, θ_R is related to the ratio between ω_2^R and ω_1^R, which respectively characterize rotations around the X and Y axes. That said, the orientation of the X and Y axes themselves in the qubit space is arbitrary. Therefore, we can always choose a reference system for which $\theta_R = 0$, and identify the complex Rabi frequency from Eq. (5.161) with ω_1^R. By doing so, we can rewrite a simpler expression for the evolution operator from Eq. (5.181):

$$\hat{U}_I(t,t_i) = \begin{pmatrix} e^{-i\frac{\Delta(t-t_i)}{2}}\left[C(t-t_i) + i\frac{\Delta}{\Omega}S(t-t_i)\right] & -ie^{-i\frac{\Delta(t+t_i)}{2}}\frac{\omega_1^R}{\Omega}S(t-t_i) \\ -ie^{i\frac{\Delta(t+t_i)}{2}}\frac{\omega_1^R}{\Omega}S(t-t_i) & e^{i\frac{\Delta(t-t_i)}{2}}\left[C(t-t_i) - i\frac{\Delta}{\Omega}S(t-t_i)\right] \end{pmatrix}, \tag{5.184}$$

where now the effective frequency of the $|0\rangle \leftrightarrow |1\rangle$ transition is defined as

$$\Omega = \sqrt{(\omega_1^R)^2 + \Delta^2}. \tag{5.185}$$

"You've given me answers all right; but they were all different.
What I want to know is, out of all the stories you told me,
which ones were true and which ones weren't?"
"My dear Doctor, they're all true."

$\sim$ Dr. Julian Bashir and Elim Garak in *The Wire*,
Star Trek: Deep Space Nine, S2E22

Chapter 6

Quantum sensing applied to integrated hole-spin qubits in MOSFET technology

In this Chapter we consider the use of a hole-spin qubit inside a DQD for quantum-sensing applications in the presence of an additional charge inside the device. We start in Sec. 6.1 with the analysis of the single-hole states, and describe the Coulomb-induced polarization due to the external charge in Sec. 6.1.1. Then, in Sec. 6.2 we consider a first, static approach to quantum sensing. We study the possibility of discriminating between the configurations in the presence and absence of charge in Sec. 6.2.1 with the help of the Helstrom bound. Then, we define the quantum Fisher information and a way to compute it numerically in Sec. 6.2.2. We subsequently apply it in Sec. 6.2.3 to our system for estimating the parameter of the distance x_0 of the charge from the qubit. We also describe in Sec. 6.3 how the charge modifies the evolution in time of a qubit, by looking at the characteristic figures of merit of the Larmor and Rabi frequencies in Sec. 6.3.1. In Sec. 6.4 we translate the qubit's sensitivity to the charge into a second, more accurate dynamic approach to quantum sensing. In Sec. 6.4.1 we apply the Rabi scheme to state discrimination by analyzing the discrimination probability corresponding to a measurement of the outcomes of $\hat{\sigma}_3$. We then describe the Fisher information for the same measurement in Sec. 6.4.2, and give its analytical expression for both a Rabi and Ramsey scheme. Lastly, in Sec. 6.4.3 we compare the Fisher information for parameter estimation inside SQDs and DQDs, for both schemes.

The parameters of our simulations define a band offset of $V_{bo} = 4\,\text{eV}$ for a sharp quantum well in z, with $L_z = 5\,\text{nm}$. We also set $\hbar\omega_{x,y} = 5\,\text{meV}$ for the in-plane characteristic confinement energy. Unless specified otherwise, we fix the position of the charge ($Z = -1$) along y and z to $y_0 = z_0 = 0$. Finally, we fixed $E_z = 0\,\text{mV/nm}$ for the static analysis and $E_z = 50\,\text{mV/nm}$ for the dynamic analysis.

6.1 State characterization

We start our analysis by first characterizing the behavior of hole states in DQDs. Figures 6.1(a) shows the energies of the single-hole ground ($\alpha = 1$) and first-excited ($\alpha = 3$) states as a function of the interdot distance $D = 2a$ in Si. The parameter a also determines the strength of the interdot coupling, since the latter is related to the height of the interdot barrier:

$$h = V_c^{DQD}(\mathbf{r} = \mathbf{0}) = \kappa_x a^2/8\,. \tag{6.1}$$

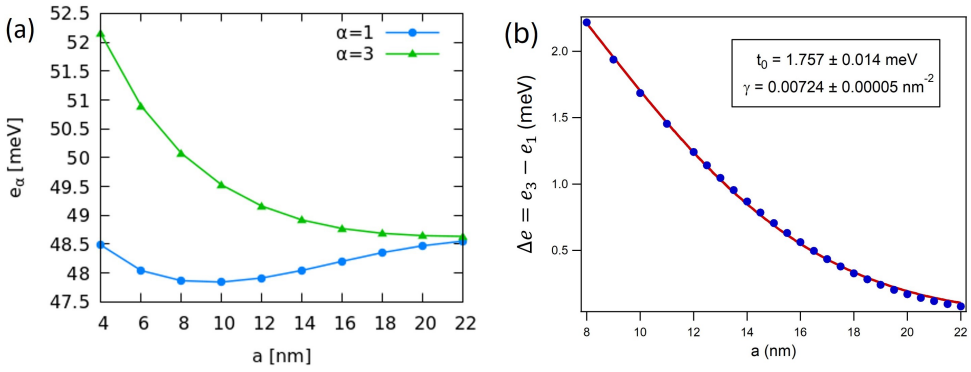


Figure 6.1: (a) Energies of the ground doublet ($\alpha = 1$) and first-excited doublet ($\alpha = 3$) in a Si DQD as a function of the interdot half-distance a. (b) Energy gaps Δe between the ground- and first-excited doublet (dots) fitted through Eq. (6.4) (continuous line). The results of the fit are reported in the inset. Panel (b) is adapted from [2].

Notice that when the value of the half-distance a is large the interdot barrier increases quadratically, and interdot coupling soon becomes negligible. As a consequence, the energy gap between the first two Kramers doublets, $\Delta e = e_3 - e_1$, quickly approaches zero, and both the energies e_1 and e_3 approach the ground-state energy of the corresponding isolated SQD. Instead, when the dots' minima get closer and the interdot coupling increases, Δe increases as well. This behavior tells us that the DQD system behaves similarly to a diatomic molecule: the degeneracy of the ground states of the isolated 'atoms' is progressively lifted as the distance between them decreases. This is further confirmed by the shape of the states $\Phi_1(\mathbf{r})$ and $\Phi_3(\mathbf{r})$, as can be seen in Fig. 6.2. When the interdot distance is large [Fig. 6.2(c)], the shapes of the charge densities along direction x resemble the bonding-antibonding behavior typical of a diatomic molecule. In fact, both the ground state and first-excited state are maximal near the minima of the dots, and $|\Phi_3(\mathbf{r} = \mathbf{0})|^2 = 0$. As the interdot distance decreases [Fig. 6.2(b)], the maxima of the ground-state eigenfunction get closer and the value of $|\Phi_1(\mathbf{r} = \mathbf{0})|^2$ also increases, until the separate contributions from each dot are no longer distinguishable [Fig. 6.2(a)].

In Sec. 5.3.2 we introduced a Hubbard Hamiltonian to describe the DQD as a two-site system, where the sites are identified with the two dots $D1$ and $D2$. We mentioned that the energy difference between the bonding and antibonding states is strictly related to the hopping parameter t. Specifically, it's clear from Eq. (5.131) that when there is no bias between the dots, i.e. for $\mathcal{E}_1 = \mathcal{E}_2$, we can identify:

$$\Delta e \equiv e_+^{Hub} - e_-^{Hub} = 2|t| \,. \tag{6.2}$$

Analytically, we consider t to be real and to decrease exponentially as the height of the potential barrier between the dots increases:

$$t = t_0 e^{-h/\beta} \,, \tag{6.3}$$

where the height h is the one defined in Eq. (6.1). By comparing Eqs. (6.2-6.3), we can now obtain the parameters for t in the DQD we simulated by performing a numerical fit of $\Delta e = e_3 - e_1$ obtained numerically:

$$\Delta e = 2|t| = 2|t_0| e^{-\gamma a^2} \,, \tag{6.4}$$

when we defined $\gamma = \kappa_x / 8\beta$. As reported in Fig. 6.1(b) and by looking at the results of the fit obtained with the least-squares method, the numerical data reproduces the behavior of the

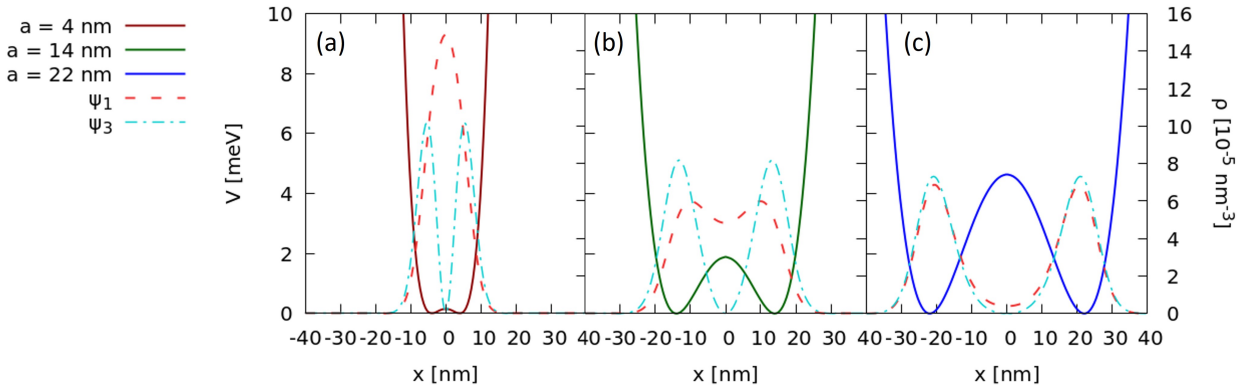


Figure 6.2: Potential profiles (continuous line) of Si DQDs for half-distance parameters (a) $a = 4$ nm, (b) $a = 14$ nm, and (c) $a = 22$ nm, with fixed confining energy $\hbar\omega_x = 5$ meV. The charge densities (dotted lines) for the ground state (red) and first-excited state (light blue) are reported as well.

analytical curve with high accuracy and for a wide range of values of a.

6.1.1 Coulomb-induced polarization

Now that we have seen how a hole behaves inside a DQD with no bias between the dots, we can start considering the action of an external charge inside of our device. This charge, as mentioned in Sec. 5.3.2, introduces a Coulomb potential which induces a bias between $D1$ and $D2$, and slightly modifies the effective confinement of each dot. Figure 6.3 shows the effective shape of the DQD along the x axis, and the consequent shapes of the ground- and first-excited states. As we can see from Fig. 6.3(a), the effective potential profile has different effects on the states of the DQD, depending on the half-distance a and the coupling parameter between the dots. More specifically, when the two dots are close to each other (e.g. $a = 8$ nm) and highly coupled, the shape of $\Phi_1(x)$ and $\Phi_2(x)$ is only slightly modified with respect to the case with zero bias (see Fig. 6.2 for comparison): the maximum of $\Phi_1(x)$ moves towards the lower minimum (right dot), while the maximum of $\Phi_3(x)$ towards the higher one (left dot). As the distance increases ($a = 14$ nm) though, the coupling decreases. As a consequence, $\Phi_1(x)$ is much more localized in the right dot, while $\Phi_3(x)$ in the left one. Finally, for even higher distances ($a = 22$ nm), the system is completely polarized: $\Phi_1(x)$ is completely localized in the right dot, $\Phi_3(x)$ in the left one, and both resemble the ground state of a single dot. Interestingly, this polarization process is highly sensitive to the presence of smaller charges as well. Figure 6.3(b) shows the shapes of $\Phi_1(x)$ and $\Phi_3(x)$ as the charge $q = |Z|e$ increases. For $a = 22$ nm, one can see that, already at an absolute charge as small as $q = 0.04\,e$, the percentage of $\Phi_1(x)$ in the left dot is significantly smaller than the one on the right [vice versa for $\Phi_3(x)$]. At $q = 0.10\,e$ both states are almost completely localized in the respective dots, and the remaining part of the wave function is negligible from $q \sim 0.40\,e$ onward. Finally, Fig. 6.3(c) shows how the dots are less and less polarized as the charge moves away from the system. And yet, to re-obtain states that are more or less localized over both dots we need to consider a charge as far as hundreds of nanometers from the origin.

The presence of a charge in the DQD system also changes the energy gap $\Delta e = e_3 - e_1$ between the two first Kramers doublets. As a reference variable, in this paragraph we will use the distance between the charge and the DQD system as a whole, calling x_{D1} the minimum of the dot closer to

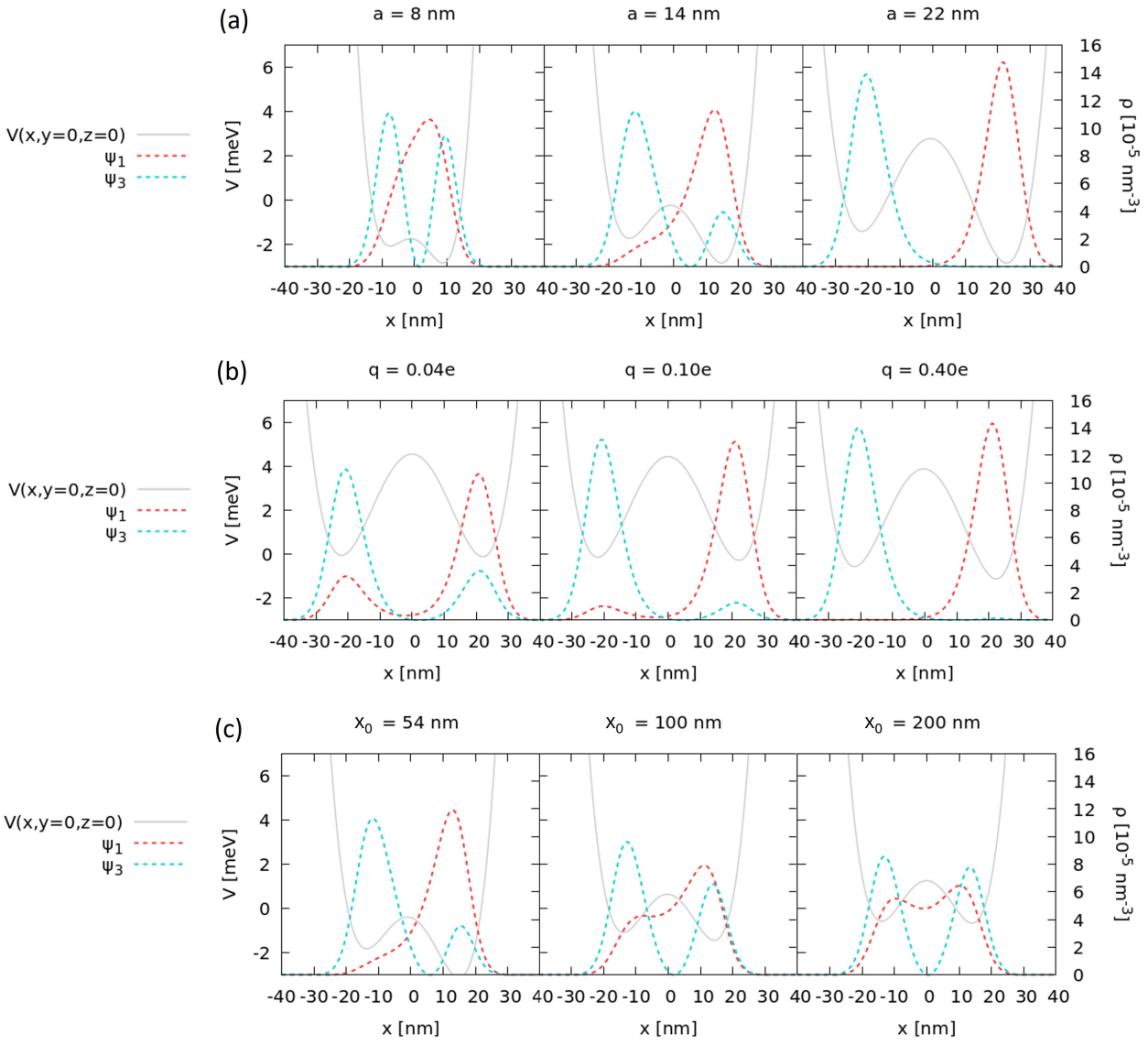


Figure 6.3: Charge densities (dashed lines) of the ground state (red) and first-excited state (blue) of a Si DQD in the presence of an external charge along the x axis. In grey is the shape of the potential at $y = 0$ and $z = 0$. (a) Trials performed with different values of a at fixed charge $q = |Z|e = e$ and distance $x_0 - x_{D1} = 44$ nm between the charge and the right dot. (b) Trials performed with different charges q at fixed $a = 22$ nm and $x_0 - x_{D1} = 44$ nm. (c) Trials performed with different charge positions x_0 at fixed $a = 14$ nm and $q = e$.

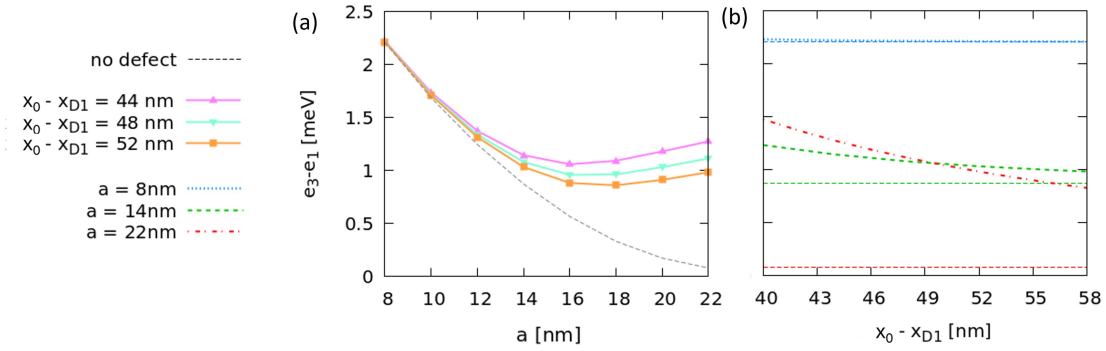


Figure 6.4: Energy gaps between the first-excited doublet ($\alpha = 3$) and the ground doublet ($\alpha = 1$) in a Si DQD (a) as a function of the interdot half-distance a by fixing the distance $x_0 - x_{D1}$ between charge and right dot and (b) vice versa, by fixing a and varying $x_0 - x_{D1}$.

x_0 (i.e. the right dot $D1$). Most notably, Δe is no longer monotone as a function of a, as it was in the case with no charge [see Fig. 6.1(b) for comparison]. Instead, as we can see in Fig. 6.4(a), Δe starts increasing for the largest a's, more and more notably as $x_0 - x_{D1}$ decreases. To analyze this behavior, we can also look at Fig. 6.4(b), where we compare the curves of $\Delta e = e_3 - e_1$ as a function of the distance $x_0 - x_{D1}$. Notice the scale of the change in Δe: when a is small and the coupling is strong, Δe is a few meV without charge and only increases of ~ 10 meV in the range we simulated. For $a = 8$ nm for example, the relative change is only $\sim 3\%$ in the closest simulated case, for $x_0 - x_{D1} = 40$ nm. This tells us that in this case the effect of the coupling wins over the presence of the charge: this is further confirmed by our analysis of Fig. 6.3(a) in the previous Section, where the shape of Φ_1 and Φ_3 for $a = 8$ nm is only slightly changed with respect to the case without charge. On the contrary, Δe increases significantly when the distance is large. For example, for the case of $a = 22$ nm in Fig. 6.4(b), Δe goes from a value of 0.082 meV with no charge to 1.475 meV for $x_0 - x_{D1} = 40$ nm: approximately 17 times as much. In this case, it is the effect of the charge that wins over the coupling between the dots, as confirmed by the polarizing process discussed in the previous section. The overall effect is the non-monotone behaviour shown in Fig. 6.4(a).

Comparison with heavy-hole model

Overall, what we said in the previous Sections, both with respect to the wave functions and Δe, suggests the presence of two competing effects: the coupling between the dots, dictated by the half-distance parameter a, and the strength of the Coulomb potential, which depends on the distance $x_0 - x_{Di}$, with $i = 1, 2$. In Sec. 5.3.2, we saw how to model the latter effect and find the bias and effective curvature of each dot $D1$ and $D2$ by approximating the total potential V_{tot}^{DQD} felt by the hole. Specifically, in the heavy-hole approximation we were able to find in Eq. 5.127 the energy difference between the ground states of the two dots. In the case of a polarized DQD, i.e. when the interdot coupling is negligible, this energy corresponds to the gap between bonding and anti-bonding states. To see the validity of such a model, we compare it in Fig. 6.5 with other possible approximations, at fixed $a = 22$ nm.

- (GS) $E_{D2} - E_{D1}$: the energy difference between the ground states of the separated dots in the presence of the charge. To obtain this value we simulated the two dots separately. We used a harmonic confining potential in x, reproducing the Taylor approximation in Eq. (5.106) near

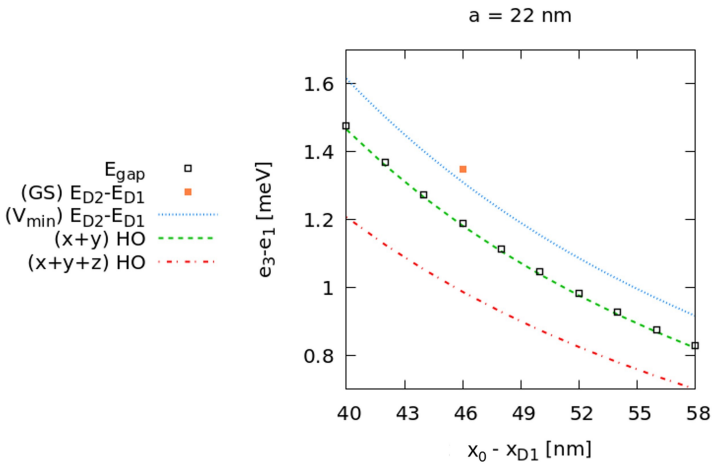


Figure 6.5: Energy gap $e_3 - e_1$ for a Si DQD with half-distance $a = 22$ nm in the presence of an external charge, as a function of the distance $x_0 - x_{D1}$ between the charge and the right dot. Comparison between the numerical data (black dots) and various analytical models (see explanation in the main text).

the minima of V_x^{DQD}. This method takes into account the effect of the Coulomb potential on the curvature near both minima, however it neglects the coupling between the dots.

- (V_{min}) $E_{D2} - E_{D1}$: the energy difference between the electrostatic potential of the charge at $x = \pm a$, i.e. at the original minima of V_x^{DQD}. This value does not consider the modification of the effective confining potential V_{tot}^{DQD}, nor the coupling between dots.

- $(x + y)$ HO: the harmonic approximation previously illustrated in Eq. 5.127, which considers the curvature of the effective confining potential V_{tot}^{DQD} near its new minima. The formula also takes into account the absolute values of V_{tot} at its minima. That said, the model still doesn't take into account the coupling between dots.

- $(x + y + z)$ HO: the same as the previous point, adding an additional harmonic approximation for the potential along the z direction. This model includes the curvature at the bottom of the modified square well along z, at the cost of neglecting the much stronger confinement caused by the well itself.

From Fig. 6.5 we see that our model, which considers the harmonic approximation of V_{tot}^{DQD} only in the x and y direction, reproduces the numerical data of Δe the best for $a = 22$ nm, i.e. when the dots are far away from each other and polarizable. However, the model fails as soon as the DQD is no longer polarized by the charge and the interdot coupling becomes significant. As one can see from Fig. 6.6, the discrepancy between the numerical data and the curve from our model tends to increase in all cases as the charge gets farther away and its influence on the DQD decreases. Moreover, it's immediate to see that the energy gap Δe can never be lower than its original value in the absence of the charge, and will tend to the latter asymptotically. Instead, the charge-induced polarization can very clearly decrease the energy gap even further. Consequently, as was to be expected, our model is not able to correctly reproduce relatively highly-coupled systems.

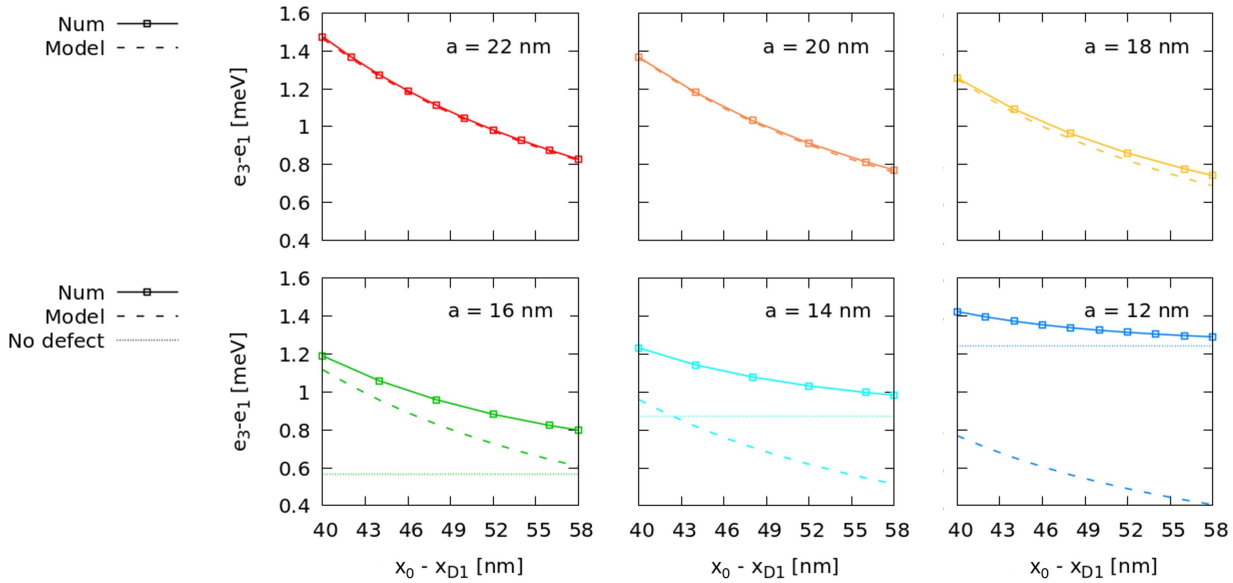


Figure 6.6: Energy gap $e_3 - e_1$ for Si DQDs with various half-distances in the presence of an external charge, as a function of the distance $x_0 - x_{D1}$ between the charge and the right dot. Comparison between the numerical data (continuous line) and the analytical model (dotted line) considering the harmonic approximation along x and y of the total potential near the minima (see explanation in text). When included, the horizontal line represents $\Delta e = e_3 - e_1$ in the same case in the absence of charge.

Comparison with the Hubbard model

On the other hand, the Hubbard model introduced in Sec. 5.3.2 does not take account of the effective curvature induced by the Coulomb potential, but it does take account of the bias between dots $D1$ and $D2$ through the on-site energies $\mathcal{E}_1$ and $\mathcal{E}_2$. Additionally, it introduces the interdot coupling t previously studied in Sec. 6.1.1 as the hopping parameter between the two sites. Consequently, we can see if this model is better than the previous one at reproducing highly-coupled regimes. In general, all parameters (i.e. $\mathcal{E}_1$, $\mathcal{E}_2$, and t) will depend on the position of the electrostatic charge. However, as an approximation, we can neglect the effect of the charge on the potential barrier between the dots, and fix the hopping parameter t to its value in the absence of the charge. With the values obtained from the fit from Fig. 6.1(b), we are then able to solve the Hubbard Hamiltonian and evaluate its eigenstates and eigenvalues. We first plot in Fig. 6.7(a) the occupation probabilities of sites 1 and 2 for the ground state, namely $|c_1^-|^2$ and $|c_2^-|^2$ from Eq. (5.132), respectively (the probabilities are switched for the excited state). As we can see, the ground state gets progressively more polarized in site 1 as the interdot half-distance a increases. Additionally, the closer the charge is to the system and the more the polarization occurs. Since we identified site 1 with the dot closer to the charge, this is in qualitative agreement with the results previously reported and shown in Fig. 6.3.

That said, we can also assess the accuracy of the results from the Hubbard model by comparing the energies $e_\pm^{Hub}$ obtained with the fitted expression of t with the numerical energies $e_1 = e_2$ and $e_3 = e_4$, respectively of the first and second Kramers doublet of the simulated DQD. We report the comparison between both the absolute energies and the energy gaps in Fig. 6.7(b-e). Contrarily to

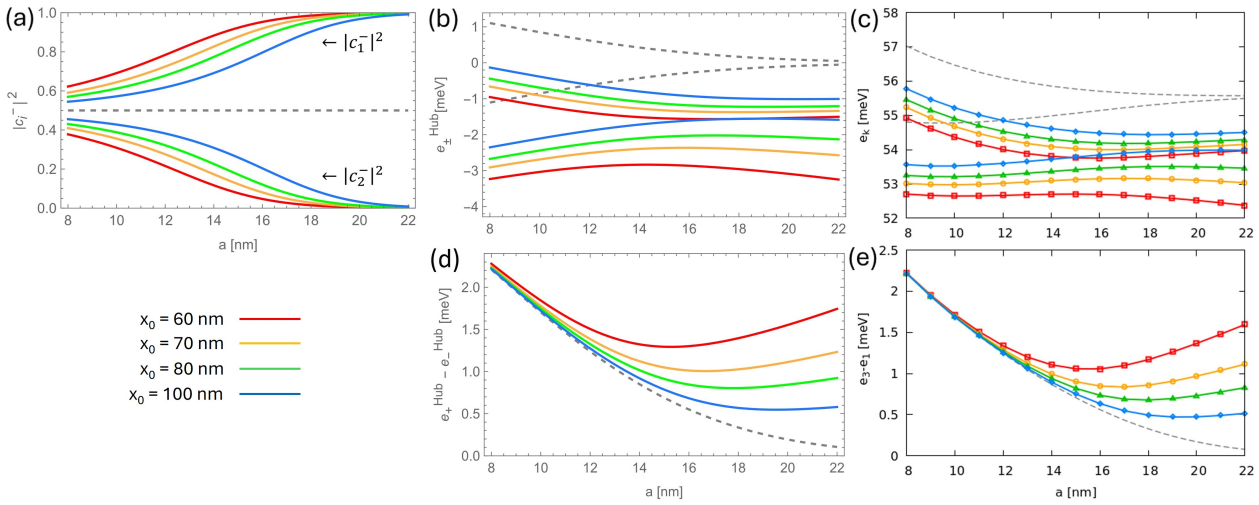


Figure 6.7: Results of the analytical Hubbard model from Sec. 5.3.2 and comparison to the numerical simulations, as a function of the interdot half-distance a in the absence (dashed grey curves) and in presence of an external charge (continuous curves), with distance from the origin $x_0 = 60\,\text{nm}$ (red lines), $x_0 = 70\,\text{nm}$ (yellow lines), $x_0 = 80\,\text{nm}$ (green lines) and $x_0 = 100\,\text{nm}$ (blue lines). Panel (a) shows the occupation probabilities $|c_1^-|^2$ and $|c_2^-|^2$ of the ground state of the Hubbard model, respectively in sites 1 and 2, as found in Eq. (5.132). Panel (b) shows the absolute energies $e_+^{Hub} > e_-^{Hub}$ of the Hubbard model from Eq. (5.131); panel (c) shows the energy gap $e_+^{Hub} - e_-^{Hub}$. Panels (d) shows the energies of the ground and first-excited Kramers doublets of the simulated DQD, $e_3 > e_1$; panel (e) shows the energy gap $e_3 - e_1$. Panels (b-e) are adapted from [2].

the plot in Fig. 6.4(a), here we show the curves by fixing the absolute value of x_0 rather than its distance from the right dot. However, the qualitative behavior is the same. From Fig. 6.7(b,c) we see a clear anticrossing behavior between the ground and excited energies, which is present in both the Hubbard model and the numerical six-band results. Consequently, as previously mentioned, the energy gaps in Fig. 6.7(d,e) present a clear minimum which was not present in the case without charge. Anticrossing comes from the interplay between the Coulomb bias between the two sites and the quantum tunneling. The avoided crossing occurs at a_{min}, and signals a transition between the delocalized case (at small a) and the more localized one (at large a). Notice that in this case both the bias and t depend on a, which causes the shape of the anticrossing to be slightly different than the usual one. Overall, from Fig. 6.7 we see that the single-band two-site Hubbard model is able to represent the behavior of the DQD qualitatively well, with a striking resemblance between the values of Δe obtained numerically and from the model. Indeed, the energy gaps in Fig. 6.7(d) are also quantitatively similar to the numerical values in Fig. 6.7(f). Overall, this result, along with the fact that the Hubbard model does not depend on the shape of the sites, indicates that our treatment can be easily extended to DQDs with arbitrary confinement.

6.2 Static approach to quantum sensing

6.2.1 State discrimination through the Helstrom bound

At this point, we can exploit the process of charge-induced polarization to try and infer the presence or absence of a charge inside of the system. The method that we consider here is formalized

within the framework of quantum state discrimination [268, 269]. In general, the ground states of the DQD with charge, $|\Phi_c\rangle$, and with no charge, $|\Phi_{nc}\rangle$, are not orthogonal to one another, meaning that they can't be distinguished with certainty. We start by saying that these two states are generally associated with certain *a priori* probabilities, p_c and p_{nc}, which are the probabilities of them occurring independently of each other. Then, we can try and guess which state the system is in by performing an alternative measurement. That is, instead of measuring the charge directly, we consider a general measurement procedure with two possible outcomes, and associate each of them to either c or nc. These kinds of *strong* measurements on a quantum system are known to be destructive, meaning that the state of the system after the procedure will depend on the outcome itself. We can view this as the application of a projective measurement with projectors on an orthogonal basis, $\{|o_c\rangle, |o_{nc}\rangle\}$. However, we are not interested on the state at the end of the procedure, and are instead only concerned with the possibility of identifying the characteristics of the system's environment, i.e. the presence or absence of the charge.

That said, given a state of the system, the probability of guessing correctly is found through the conditional probability of obtaining outcome o_c (o_{nc}) for state $|\Phi_c\rangle$ ($|\Phi_{nc}\rangle$), which we name $p(o_c|\Phi_c)$ ($p(o_{nc}|\Phi_{nc})$). Putting these probabilities together, the overall discrimination probability that we get from a correct guess is

$$\begin{aligned} p_d =& p_c p(o_c|\Phi_c) + p_{nc} p(o_{nc}|\Phi_{nc}) = \\ =& p_c \left|\langle o_c|\Phi_c\rangle\right|^2 + p_{nc} \left|\langle o_{nc}|\Phi_{nc}\rangle\right|^2 . \end{aligned} \tag{6.5}$$

One can show that the maximal discrimination probability is obtained by performing a Von Neumann measurement [268, 270], which gives the so-called Helstrom bound:

$$p_{d,max} = \frac{1}{2} + \frac{1}{2}\left[1 - 4 p_c\, p_{nc} |\langle\Phi_c|\Phi_{nc}\rangle|^2\right]^{1/2} . \tag{6.6}$$

In our case, we fix $p_c = p_{nc} = 1/2$, since there's no reason to consider one case more probable than the other. Understandably, we see that the quantity defined in Eq. (6.6) is strictly dependent on the overlap between the two states $|\Phi_c\rangle$ and $|\Phi_{nc}\rangle$. Indeed, when this overlap is close to one, the states are practically indistinguishable, and on the contrary, smaller overlaps indicate states that are more and more different from one another. Numerically, the overlap between two states can be evaluated through the coefficients of the expansion on the HO basis. Looking at Eq. (5.90) and considering the spinorial form of the eigenstates from Eq. (5.43), one can write:

$$\langle\Phi_c|\Phi_{nc}\rangle = \sum_b \langle\phi_c^b|\phi_{nc}^b\rangle = \sum_{\{\mathbf{n}^{HO}\}} (\eta^b_{c,\mathbf{n}^{HO}})^* \eta^b_{nc,\mathbf{n}^{HO}} . \tag{6.7}$$

Additionally, we can also obtain the overlap expected from the Hubbard model. Indeed, by looking at the ground state with charge $\left|\Phi_c^{Hub}\right\rangle = \left|\psi_-^{Hub}\right\rangle$ from Eq. (5.132), and knowing that the ground state with no charge is equally distributed between the two sites:

$$\left|\Phi_{nc}^{Hub}\right\rangle = \frac{1}{\sqrt{2}}\begin{pmatrix} -1 \\ 1 \end{pmatrix} , \tag{6.8}$$

we can evaluate:

$$\langle\Phi_c^{Hub}|\Phi_{nc}^{Hub}\rangle = \frac{1}{2\sqrt{\Sigma}}\left(\frac{\sigma}{\sqrt{\Sigma+1}} + \sqrt{\Sigma+1}\right) . \tag{6.9}$$

We compare the numerical results and the Hubbard model in Fig. 6.8, where we show the overlap and $p_{d,max}$ as a function of the distance D of the charge. Here we fixed the interdot half-distance at

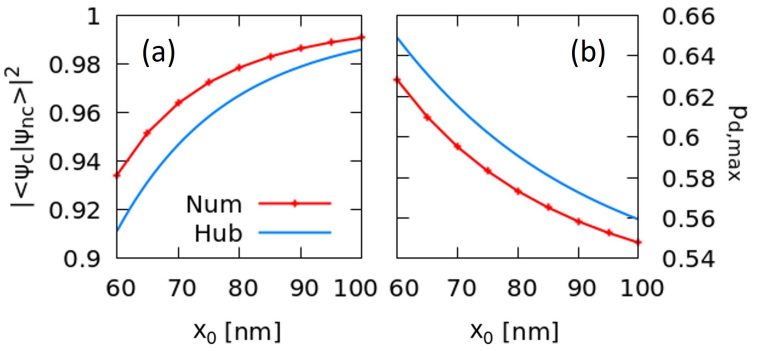


Figure 6.8: (a) Squared overlap between the hole states of a Si DQD with $a = 12\,\text{nm}$ in the presence ($|\psi_c\rangle$) and absence ($|\psi_{nc}\rangle$) of the external charge. The results are reported as a function of the distance x_0 of the charge from the origin of the system, found numerically (red) and through the Hubbard model (blue). (b) Corresponding maximum discrimination probability found through the Helstrom bound as in Eq. (6.6). The figure is adapted from [2].

$a = 12\,\text{nm}$ to study a representative case. Indeed, in this case the interdot coupling is small enough to allow for polarization even when the charge is relatively far away from the system. At the same time, the distance between the dots remains in a range that is reasonable for DQD implementation in realistic devices. Notice from Fig. 6.8 that the Hubbard model (blue curves) always slightly overestimates the numerical values of $p_{d,max}$ obtained by diagonalizing the Luttinger-Kohn Hamiltonian (red curves). However, the curves behave similarly, and the relative discrepancy is limited between 2% and 3% in the whole investigated range of x_0, meaning that the generality of our Hubbard model still stands.

That said, we see that at the smallest distance considered in our simulated range, i.e. $x_0 = 60\,\text{nm}$, the hole wave function is only slightly modified from its counterpart with no charge, yielding a discrimination probability around 0.63. As the charge-induced bias further decreases and the interdot coupling dominates, the state is more and more delocalized, and the discrimination probability approaches its theoretical minimum, i.e. $1/2$, corresponding to a random guess. Of course, the discrimination probability can be increased by either considering a larger a, and consequently a weaker coupling, or by considering a closer charge. However, the maximum value of $p_{d,max}$ in our system as evaluated from Eq. (6.6) will never reach 1. Indeed, even in the limit of small x_0 and large a, one state will occupy both sites while the other will occupy only one. Consequently, the minimum squared overlap that can be reached is $1/2$, and the Helstrom bound will be $p_{d,max} = \frac{1}{2}(1 + 1/\sqrt{2}) \approx 0.854$. However, note that the obtained values of $p_{d,max}$ represented in the curves in Fig. 6.8(b) correspond to a single measurement. Consequently, one could in principle always increase the discrimination probability by performing repeated measurements [271].

6.2.2 Quantum Fisher information for parameter estimation

Another declination of quantum sensing consists in parameter estimation, i.e. in determining the value of a parameter on which the system's state is dependent. Specifically, for our problem at hand, we can imagine exploiting the sensitivity of the DQD system to determine the position x_0 of the charge itself. Since the parameter of interest is in general not associated with any measurable observable, one needs to resort once again to alternative projective measurements. This approach is addressed in classical estimation theory through the definition of an estimator on the parameter

of interest λ, defined as a statistical property on a set of samples $\{f_i\}$ obtained from measurements on a variable f. The objective of estimation theory is to minimize the mean square error $\mathcal{V}(\lambda)$ on such estimator, thus saturating the Cramer-Rao bound [272],

$$\mathcal{V}(\lambda) \geq \frac{1}{M\mathcal{F}(\lambda)}, \tag{6.10}$$

where M is the number of measurements and $F(\lambda)$ is the so-called Fisher information, defined for discrete outcomes as

$$\mathcal{F}(\lambda) = \sum_{f_i} \frac{1}{p(f_i|\lambda)} \left[\frac{\partial p(f_i|\lambda)}{\partial \lambda}\right]^2 . \tag{6.11}$$

Being $\mathcal{F}(\lambda)$ inversely proportional to the minimal variance of the measurement, one can view the Fisher information as the quantity of information intrinsically contained in the system, and which can be extracted through the chosen measurement and estimator. The same concepts can be straightforwardly generalized in quantum mechanics through the definition of the quantum Cramer-Rao bound, which further minimizes the variance on the estimated parameter λ over all possible measurements on the system. By doing so, this concept now provides an ultimate lower bound to the variance of the estimation, which only depends on the specific system of interest and does not define a measurement *a priori*. In this context, the generalization of $F(\lambda)$ takes the name of quantum Fisher information (QFI), and is evaluated for a pure state as [272]:

$$\mathscr{H}(\lambda) = 4\left(\langle \partial_\lambda \psi_\lambda | \partial_\lambda \psi_\lambda \rangle + \langle \partial_\lambda \psi_\lambda | \psi_\lambda \rangle^2\right) . \tag{6.12}$$

In the following, we will evaluate the QFI as a generalized quantifier of the dependence of the system on the parameter λ. Instead, we will not state the optimal observable that saturates the quantum Cramer-rao bound, as this objective goes beyond the scope of this Thesis. That said, notice that the quantity in Eq. (6.12) is not related to a specific observable, however, it is still gauge-invariant. Indeed, an arbitrary gauge transformation on the Hamiltonian introduces an additional coordinate-dependent phase on its eigenstates:

$$|\psi_\lambda\rangle \to |\psi'_\lambda\rangle = e^{ih_\lambda(\mathbf{r})} |\psi_\lambda\rangle , \tag{6.13}$$

where the real scalar function $h_\lambda(\mathbf{r})$ may in general also depend on the parameter λ to estimate, so that:

$$|\partial_\lambda \psi'_\lambda\rangle = e^{ih_\lambda(\mathbf{r})} |\partial_\lambda \psi_\lambda\rangle + i[\partial_\lambda h(\mathbf{r})] e^{ih_\lambda(\mathbf{r})} |\psi_\lambda\rangle \tag{6.14}$$

and by evaluating the QFI for the new gauge, we obtain [273]:

$$\begin{aligned}\mathscr{H}'(\lambda) =& 4\Big(\langle \partial_\lambda \psi_\lambda | \partial_\lambda \psi_\lambda \rangle + i[\partial_\lambda h(\mathbf{r})] \left(\langle \partial_\lambda \psi_\lambda | \psi_\lambda \rangle - \langle \psi_\lambda | \partial_\lambda \psi_\lambda \rangle\right) + [\partial_\lambda h(\mathbf{r})]^2 \\ &+ \langle \partial_\lambda \psi_\lambda | \psi_\lambda \rangle^2 - 2i[\partial_\lambda h(\mathbf{r})] \langle \partial_\lambda \psi_\lambda | \psi_\lambda \rangle - [\partial_\lambda h(\mathbf{r})]^2 \Big) = \\ =& 4\Big(\langle \partial_\lambda \psi_\lambda | \partial_\lambda \psi_\lambda \rangle + \langle \partial_\lambda \psi_\lambda | \psi_\lambda \rangle^2 - i[\partial_\lambda h(\mathbf{r})] \underbrace{[\partial_\lambda \langle \psi_\lambda | \psi_\lambda \rangle]}_{=0} \Big) \equiv \mathscr{H}(\lambda) ,\end{aligned} \tag{6.15}$$

where we used the hypothesis that λ does not influence the unitariety of the eigenstate. In our case, we identify $\lambda = x_0$ and $|\psi_\lambda\rangle$ with the ground state $|\Phi_0\rangle$ of the hole inside our system.

Numerical evaluation of the QFI

The main difficulty of evaluating the QFI from Eq. (6.12) numerically consists in the calculation of the derivative of $|\psi_\lambda\rangle$. A possible way to approach this problem is through the finite-difference method:

$$|\partial_\lambda \psi_\lambda\rangle \approx \frac{|\psi_{\lambda+\delta\lambda/2}\rangle - |\psi_{\lambda-\delta\lambda/2}\rangle}{\delta\lambda}\,. \tag{6.16}$$

The formula in Eq. (6.16) requires the evaluation of the ground state both at $\lambda \pm \delta\lambda/2$, with sufficiently small values of $\delta\lambda$. That is, it requires two separate simulations. Other than being a computationally demanding method, we also know that the state $|\psi_\lambda\rangle$ is in general given with a global phase factor (unrelated to the gauge-fixing procedure previously mentioned). This phase is randomly generated by the code during diagonalization, so that there is no guarantee that it is the same for both $|\psi_{\lambda\pm\delta\lambda/2}\rangle$. One possible solution to this problem would be to fix this phase, for example by requiring that the scalar product of the state of interest with a fixed reference (basis) state is real. However, there is another drawback to this procedure. Indeed, the final outcome of $|\partial_\lambda\psi_\lambda\rangle$ may very well depend on the value of $\delta\lambda$ itself, and consequently be inaccurate. If $\delta\lambda$ is too large, the finite difference method does not provide a good approximation. However, if $\delta\lambda$ is too small, the states $|\psi_{\lambda\pm\delta\lambda/2}\rangle$ may be too similar and their numerical difference could be subjected to machine errors.

Instead, the derivative of state $|\psi_\lambda\rangle$ can be evaluated through the extended Hellmann-Feynman (HF) theorem [274]. We consider the Schrödinger equation

$$\hat{H}_\lambda |\psi^n_\lambda\rangle = e^n_\lambda |\psi^n_\lambda\rangle\,, \tag{6.17}$$

where the Hamiltonian $\hat{H}_\lambda$, the eigenstates and eigenvalues all depend on parameter λ. The extended HF theorem then states that the derivatives of the eigenvalues are the matrix elements of the derivative of operator $\hat{H}_\lambda$:

$$\partial_\lambda e^n_\lambda = (\partial_\lambda H_\lambda)_{n,n}\,, \tag{6.18}$$

where from now on we call $(\partial_\lambda H_\lambda)_{i,j} = \langle\psi^i_\lambda|(\partial_\lambda \hat{H}_\lambda)|\psi^j_\lambda\rangle$. Additionally, the derivative of eigenstate $|\psi^n_\lambda\rangle$ is a specific linear combination of all eigenstates of $\partial_\lambda \hat{H}_\lambda$:

$$|\partial_\lambda \psi^n_\lambda\rangle = i w_n |\psi^n_\lambda\rangle + \sum_{m\neq n} \frac{(\partial_\lambda H_\lambda)_{m,n}}{e_n - e_m} |\psi^m_\lambda\rangle\,, \tag{6.19}$$

in which w_n is an undetermined real number, dependent on the numerical phase of the eigenstate. The value of w_n can be set to zero by imposing $\langle\partial_\lambda\psi^n_\lambda|\psi^n_\lambda\rangle = 0$, thus fixing the phase.

The expression in Eq. (6.19) allows one to evaluate $|\partial_\lambda\psi_\lambda\rangle$, i.e. the derivative of the ground state of $\hat{H}_\lambda$, after a single simulation with parameter λ. The only requirement is that we are able to evaluate the derivative of $\hat{H}_\lambda$ with respect to λ. In our case this is easily done since the only λ-dependent term in our Hamiltonian is the Coulomb potential from Eq. (5.111). Deriving its analytical expression with respect to $\lambda \equiv x_0$ we get:

$$\partial_\lambda \hat{H}_\lambda(\mathbf{r}) = \frac{\partial V_{Ze}(\mathbf{r})}{\partial x_0}\hat{\mathbb{1}} = C\frac{Ze^2(x-x_0)}{[(x-x_0)^2+(y-y_0)^2+(z-z_0)^2]^{3/2}}\hat{\mathbb{1}}\,, \tag{6.20}$$

where $\hat{\mathbb{1}}$ is the identity matrix on the band-index degree of freedom, since V_{Ze} is inside the diagonal of $\hat{H}_\lambda$. Inserting Eq. (6.19) for $n = 1$ inside the expression of the QFI in Eq. (6.12), we finally obtain:

$$\mathscr{H}(\lambda) = 4\sum_{m\neq 1}\frac{(\partial_\lambda H)_{1,m}(\partial_\lambda H)_{m,1}}{(e_m - e_1)^2} \tag{6.21}$$

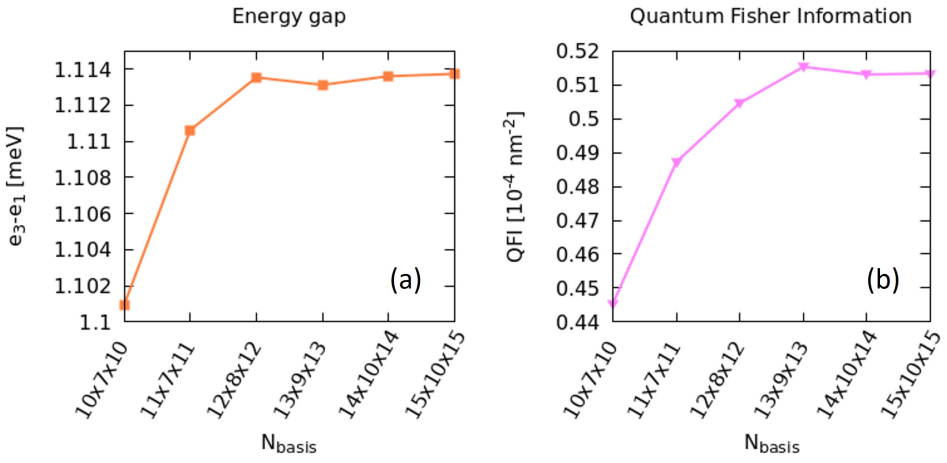


Figure 6.9: Convergence as a function of the number of basis states $N_{tot}^{HO} = N_x^{HO} \times N_y^{HO} \times N_z^{HO}$ of (a) the energy gap $e_3 - e_1$ between the ground- and first-excited doublet and (b) the quantum Fisher information as evaluated in Eq. (6.21) for a Si DQD with half-distance $a = 22\,\text{nm}$, in presence of a charge at position $x_0 = 70\,\text{nm}$.

This expression of the QFI is independent of any numerical phase returned by the code, i.e. w_n. Thus, we don't have to worry about fixing the phase inside of our simulation, as it instead happened for the finite-difference method.

Notice that even though the QFI evaluated in Eq. (6.21) is written in terms of a sum on all the eigenfunctions of the system, it is still possible to evaluate it on a truncated computational basis for which only the first states reach convergence. In fact, the only hypothesis considered during the demonstration is that the ground state vector $|\psi_\lambda^1\rangle$ be an eigenstate of the Hamiltonian of interest. Thus, for the numerical evaluation of the derivative of the ground state via Eq. (6.19), it is sufficient that only the ground state has achieved convergence. This concept is illustrated in Fig. 6.9, where we show that the value of the QFI obtained from Eq. (6.21) converges with the energy difference $\Delta e = e_3 - e_1$ of the system. More specifically, the relative errors for $N_{tot}^{HO} = 14 \times 10 \times 14$ with respect to the reference case $N_{tot}^{HO} = 15 \times 10 \times 15$ are respectively $\delta_{\Delta e} = 1.2 \cdot 10^{-4}$ and $\delta_{QFI} = 5 \cdot 10^{-4}$. Considering the problem from the point of view of the computational cost, Eq. (6.21) now requires the computation of the matrix elements of $\partial_\lambda \hat{H}_\lambda$. Since the eigenstates of the system are written in the harmonic basis, this requires a basis transformation for the derivative of V_{Ze}. This operation is quite heavy, and increases the cost of a single simulation, which now requires two basis changes other than the diagonalization of $\hat{H}_\lambda$. However, the cost is still not as much as the one required by the finite-difference method. Indeed, this asked to perform two separate simulations at different λ's, with a total of two basis changes for V_0 and *two* diagonalizations instead of one. Overall, the extended HF theorem is less costly than the finite-difference method, and provides more numerically stable results.

6.2.3 Behaviour of the QFI

In this Section we study the QFI evaluated with Eq. (6.21), to study the precision with which we can determine the position of the external charge inside of our DQD device. Specifically, we identify λ with the position of the charge along the x axis, $\lambda = x_0$. We define δ as the relative

error we want to have on a measurement on x_0. Once we have the value $\mathscr{H}(x_0)$ of the QFI, the number of measurements necessary to obtain δ as the relative error with a confidence interval of 99.9% (three standard deviations around the mean of a Gaussian distribution) is [272]:

$$M_\delta(x_0) = \frac{9}{\delta^2 x_0^2 \mathscr{H}(x_0)} \,. \tag{6.22}$$

Notice that $\Delta = \delta \cdot x_0$ is the absolute error on the measurement. In our case it is more convenient to fix the value of Δ rather than δ. In fact, x_0 may range in a large interval, and an equal relative error would imply widely different measurement precisions. That said, we can instead consider the following formula:

$$M_\Delta(x_0) = \frac{9}{\Delta^2 \mathscr{H}(x_0)} \,. \tag{6.23}$$

Figure 6.10(a) shows the results for the QFI as a function of the half-distance a. As we can see, when the dots are either very close (small a) or far away (large a) the QFI is smaller with respect to the intermediate case ($a \sim 14\,\text{nm}$). In fact, the latter case is the most sensitive to the polarizability induced by the strength of the Coulomb potential, as previously hinted in Sec. 6.1.1. The same behavior seems to hold for different x_0's. However, the effect of a charge farther away is less significant, and better polarizes less-coupled dots. Consequently, the maximal sensitivity is obtained for larger values of a, and the maximal QFI decreases as x_0 increases. From Fig. 6.10(a) one can also see that after a certain threshold the QFI increases again, e.g. for $x_0 = 60$ nm and $a > 20$ nm: in this situation (i.e. $x_0 - x_{D1} \lesssim 40$ nm) the charge is so close to the dots that its influence on the ground state is high, even though the system is far from the polarizable regime. In Fig. 6.10(b) are then shown both the values of the QFI and M_Δ as a function of the distance $x_0 - x_{D1}$ between the charge and the right dot. We can see that the QFI decreases more or less exponentially as the charge

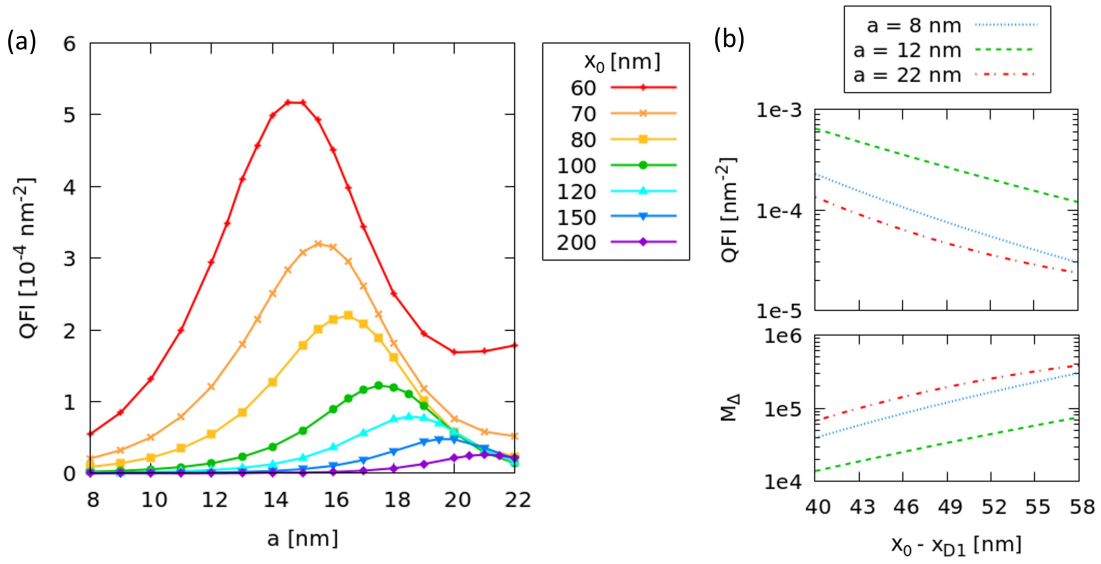


Figure 6.10: (a) QFI evaluated as in Eq. (6.21) for a Si DQD in the presence of a charge as a function of the half-distance a for different positions x_0. (b) Behaviour of the QFI and number of measurements M_Δ necessary to obtain an absolute error of $\Delta = 1$ nm on the charge position x_0 with a confidence interval of 99.9%, as a function of the distance $x_0 - x_{D1}$ between the charge and the right dot.

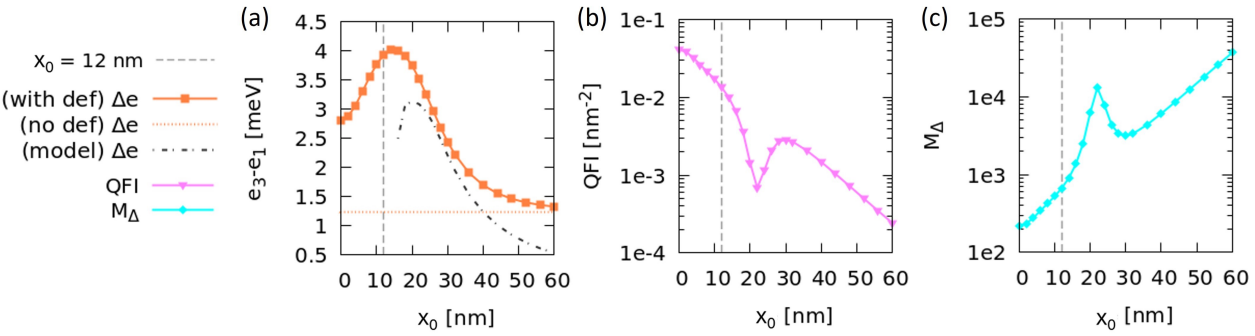


Figure 6.11: Behaviour of a Si DQD with half-distance $a = 12$ nm in presence of a charge with different x_0's at fixed $z_0 = 10$ nm. The vertical dotted line shows the x coordinate of the right dot $D1$. (a) Energy gap $\Delta e = e_3 - e_1$ between the ground- and first-excited doublet of the system. The dotted horizontal line is the gap obtained with no charge; in black is the curve obtained from the model in Sec. 5.3.2. (b) Quantum Fisher information obtained through Eq. (6.21), and (c) number of measurements M_Δ necessary to obtain an absolute error $\Delta = 1$ nm on the charge position x_0 with a confidence interval of 99.9%.

gets farther away, but even with a charge as close as 40 nm it remains of the order of $10^{-4}\,\mathrm{nm}^{-2}$. Coherently, M_Δ increases exponentially, and is in the order of $10^4 \div 10^5$ in the considered interval once we require an absolute error of $\Delta = 1$ nm.

We performed additional simulations in which we considered a charge moving along the x direction, but fixing its z coordinate to $z_0 = 10$ nm. This allowed us to move the charge closer to the center of the DQD while still keeping it outside the simulated space. Figure 6.11 shows the energy gap $\Delta e = e_3 - e_1$, the QFI and M_Δ in this situation, when the half-distance is fixed at $a = 12$ nm. Notice that Δe is non-monotone [Fig. 6.11(a)], and has a maximum at around $x_0 \simeq 14$ nm, near the minimum of the original confining potential $V_{c,x}$ along x. It makes sense that this is the case, since the charge is the closest to one of the dots and thus influences the system gap the most. After that, the gap keeps decreasing as the charge gets closer to the origin of the system and influences the two dots similarly at the same time. The model we introduced in Sec. 5.3.2 is only valid for large x_0's. In fact, it fails as soon as the charge gets too close to the DQD system ($a \lesssim 22$ nm). Moreover, for $a \lesssim 14$ nm and below, the Coulomb potential modifies the confining potential too much to recognize the two original minima of $V_{c,x}$, and the model is no longer applicable. The QFI in Fig. 6.11(b) also possesses a non-trivial behavior: since its maximum value is for $x_0 = 0$, we can imagine that this is the region in which the shape of the wave function is the most sensitive to the position of the charge. Then, it decreases and has a local minimum at around $x_0 = 22$ nm. After a local maximum at $x_0 \sim 30$ nm, it finally decreases exponentially, as x_0 keeps increasing and the charge no longer influences the shape of $\Phi_1(\mathbf{r})$. This behavior seems to suggest that there is a region at around $x_0 \sim 30$ nm in which the DQD system is more sensitive to the position of the charge than for similar x_0 around it. Coherently, Fig. 6.11(c) shows that M_Δ is the smallest at $x_0 = 0$ nm, has a peak at $x_0 \sim 22$ nm, a local minimum in $x_0 \sim 30$ nm, and then increases exponentially. That said, in the considered interval the QFI is still always in the order of $10^{-4} \div 10^{-2}\,\mathrm{nm}^{-2}$, while M_Δ is $10^2 \div 10^4$ for absolute error $\Delta = 1$ nm.

QFI estimated through the Hubbard model

The results of the QFI obtained numerically can once again be compared to the more generic and simple Hubbard model introduced in Sec. 5.3.2. In order to do so, we can replace the state $|\psi_\lambda\rangle$ used in the definition from Eq. (6.12) with the ground state from the Hubbard model, $|\psi_-^{Hub}\rangle$, as introduced in Eq. (5.132). The result is:

$$\mathscr{H}^{Hub}(\lambda) = 4[(\partial_\lambda c_1^-)^2 + (\partial_\lambda c_2^-)^2 + (c_1^- \partial_\lambda c_1^- + c_2^- \partial_\lambda c_2^-)^2], \tag{6.24}$$

where we used the fact that both coefficients c_1^- and c_2^- are real. Notice that to obtain Eq. (6.24) we considered the basis states (i.e. in which the hole is completely localized in dot 1 and 2) to be independent of $\lambda = x_0$. Additionally, we fix $Z = -1$, $y_0 = 0$ and $z_0 = 0$, and, as we did before, we consider t to be independent of parameter λ, and equal to the value in the absence of the external charge. Specifically, we consider the analytical formula in Eq. (6.4) and the fitting parameters previously reported in Fig. 6.7(a). By doing so, we only take into account the contribution of the on-site energies on the QFI. Consequently, the expression of the QFI in Eq. (6.24) becomes relatively simple:

$$\mathscr{H}^{Hub}(\lambda) = \left[\frac{2e^2\, a\, |t|\, 4\pi\varepsilon_r\varepsilon_0\, x_0}{a^2e^4 + |t|^2(4\pi\varepsilon_r\varepsilon_0)^2(x_0^2 - a^2)^2}\right]^2. \tag{6.25}$$

We thus calculated the QFI analytically as in Eq. (6.25) and shown in Fig. 6.12(a). The curves as a function of the half-distance a and for different x_0 are shown in Fig. 6.12(b) and compared to the numerical results previously reported in Fig. 6.10(a). Although the position of the maxima is shifted at lower a for each x_0, the order of magnitude is the same, as well as the general behavior of

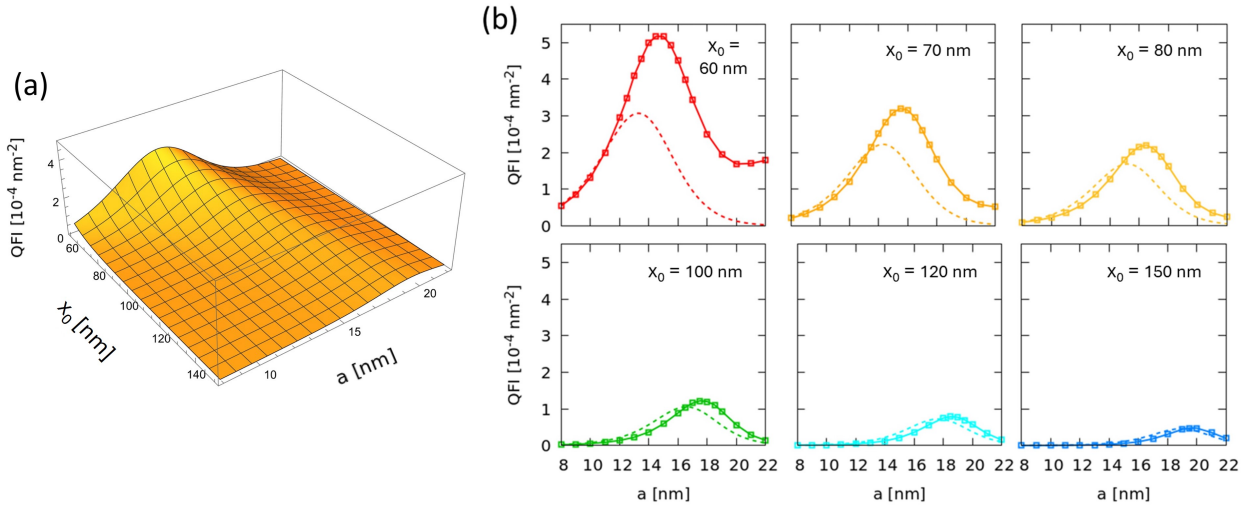


Figure 6.12: (a) 3D plot of the quantum Fisher information from Eq. (6.25) obtained with the Hubbard model, as a function of the half-distance a and charge position x_0. The parameters for the hopping parameter t are the ones obtained from the fit in Fig. 6.1(b). (b) Comparison between the QFI obtained from the Hubbard model (dotted lines) and the numerical data (continuous lines) for different positions of the charge x_0 as a function of the half-distance a.

the curves. Indeed, the Hubbard model is able to reproduce the interplay between the Coulombian potential and interdot coupling quite well, by showing a maximal QFI in between the polarized and unpolarized regimes. However, as the charge approaches the dots ($x_0 \lesssim 80$ nm) the discrepancy between the numerical and model curves increases, as the Hubbard model neglects some aspects of the problem, e.g. how the charge influences the interdot barrier. For one, the model is not able to reproduce the increase of the QFI for $x_0 = 60$ nm [red curve in Fig. 6.12(c)] and $a > 20$ nm.

Through the Hubbard model we obtained, we are able to approximately extrapolate the position of the maxima of the QFI. In this sense, we need to distinguish maxima with respect to a and with respect to λ. That is, we can consider either fixed half-distance a or charge position $x_0 = \lambda$, and find the global maximum along the corresponding direction. More specifically, if we want to find the maximum QFI at fixed a, we can find the value of parameter λ that maximizes the analytical expression of $\mathscr{H}(\lambda)$ in Eq. (6.25). In this way, we find the value of λ for which a specific DQD configuration is the most sensitive. In order to do so we neglect once again the dependence of t on λ. By setting the derivative of $\mathscr{H}(\lambda)$ with respect to λ equal to zero:

$$\lambda_a^{max} = \sqrt{\frac{a}{3}\left(a + \sqrt{4a^2 + \frac{3e^4}{(4\pi\varepsilon_r\varepsilon_0)^2|t|^2}}\right)}. \tag{6.26}$$

Similarly, the half-distance a for which the QFI is maximized for fixed values of λ is found by setting the derivative of $\mathscr{H}(\lambda)$ with respect to a equal to zero. Notice that t is dependent on a through Eq. (6.4). Although there exists no analytical expression for the solution a_λ^{max}, we can

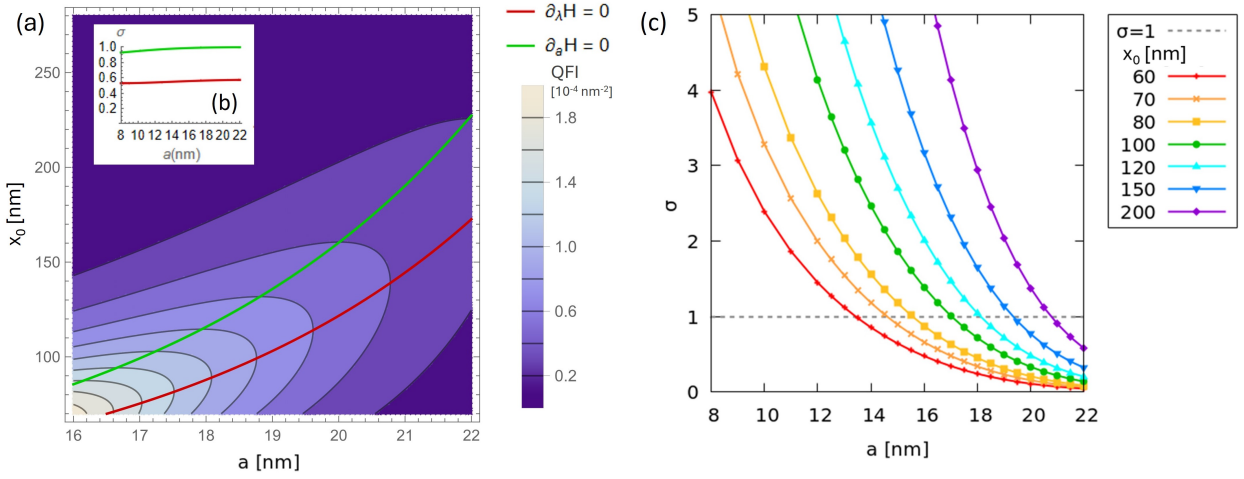


Figure 6.13: (a) Contour plot of the quantum Fisher information from Eq. (6.25) obtained with the Hubbard model, as a function of the half-distance a and charge position x_0. The parameters for the hopping parameter t are the ones obtained from the fit in Fig. 6.1(b). The red and green lines correspond to Eq. (6.26) and (6.27) respectively, representing the position of the maxima with respect to parameters $\lambda = x_0$ and a. Sub-panel (b) shows the values of the ratio $\sigma = 2|t|/\Delta$ along the red and green curves from panel (a). (c) Values of σ obtained from the numerical values of $e_3 - e_1 = 2|t|$ in the absence of charge. The curves are plotted for different values of x_0 as a function of a. The dotted line shows the reference at $\sigma = 1$.

write an implicit relation:

$$\lambda = \frac{a_\lambda^{max}}{\sqrt{1+2(a_\lambda^{max})^2\alpha}}\sqrt{2(a_\lambda^{max})^2\alpha - 1 + \sqrt{4 + \frac{e^4}{(a_\lambda^{max})^2(4\pi\varepsilon_r\varepsilon_0)^2|t|^2}(1+2(a_\lambda^{max})^2\alpha)^2}}\,, \quad (6.27)$$

which is then solved numerically. The set of points denoted in Eqs. (6.26-6.27) are plotted in Fig. 6.13(a), alongside a contour plot of the QFI. As we can see from the picture, the two curves are distinct and never cross: on the contrary, the distance between them increases as both a and λ increase.

It is also interesting to study the value of $\sigma = 2|t|/\Delta$ defined in Eq. (5.131) in the points in Eqs. (6.26-6.27). Indeed, σ is the ratio between the tunneling energy between the dots (which is the gap $\Delta e_{31} = 2|t|$ in the absence of charge) and the Coulomb bias Δ, both of which in turn can be evaluated analytically. The values of σ obtained from the analytical model are reported in Fig. 6.13(b): as we can see, these are more or less constant, $\sigma \sim 0.5$ for the solutions in Eq. (6.26) and $\sigma \sim 1.0$ for Eq. (6.27). This means that there are specific values of σ at which the QFI is maximal, i.e. corresponding to the transition between the polarizable and non-polarizable regimes. To further confirm this, we have also plotted the values of σ for every trial previously shown in Fig. 6.12(c): since these results are shown as a function of a, the maxima are found through Eq. (6.27), corresponding to $\sigma \sim 1$. As we can see from Fig. 6.13(c), the crossing between each curve and $\sigma = 1$ provides a good estimate of the positions of the maxima from Fig. 6.12(c).

Finally, we briefly report in Fig. 6.14(a) the effect of screening phenomena inside of the device by varying the value of ε_r from Eq. (5.111). We vary the ratio between the considered dielectric constant in the presence of screening and the one in bulk, and see that the behavior of the QFI is once again well reproduced by the Hubbard model. That said, notice from the formula in Eq. (5.111) that the dependence of the QFI on the dielectric constant cannot be absorbed in a redefinition of the distance λ. However, as we can see from Fig. 6.14, the main effect of an increase in $\varepsilon = \varepsilon_r\varepsilon_0$ is to shift the position of the maximum, whose value however remains more or less constant in a wide range of $\varepsilon_{bulk}/\varepsilon$. Consequently, all phenomena that we described for ε_{bulk} can be generalized for a system with screening.

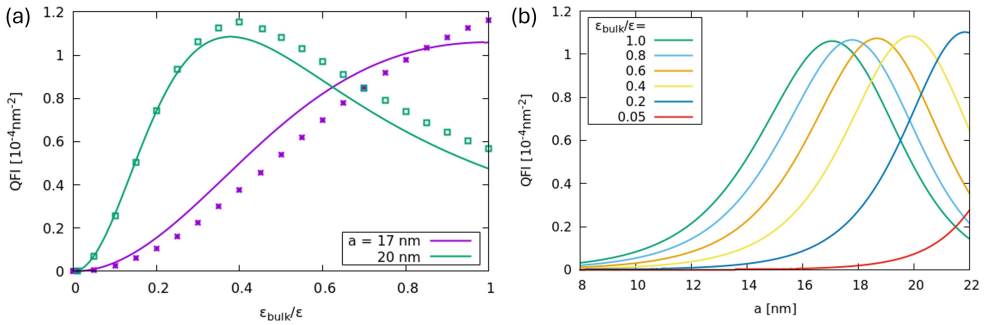


Figure 6.14: Quantum Fisher information as a function of (a) the screening constant ε, normalized to the value in bulk Si ε_{bulk}, and (b) the interdot half-distance a, at fixed distance $x_0 = 100\,\text{nm}$ between the charge and the qubit.

6.3 Charge-induced effects on qubit manipulation

The results shown in the previous Section imply that the information obtainable from the whole ground state of the DQD system is not enough to expect a high precision on the position of the charge. At least, if we want to limit the number of measurements M_Δ below the hundreds/thousands. However, we can try and enhance the sensitivity of our measurements on the system by exploring different protocols for quantum sensing. Specifically, here we analyze the change in the manipulation properties of a qubit encoded into the hole states.

6.3.1 Modification to the Larmor and Rabi frequencies of the qubit

We briefly recall what we previously introduced in Sec. 5.4.2 for the manipulation frequencies that characterize the evolution in time of a qubit. Firstly, the Larmor frequency is defined for our system as the splitting energy of the first Kramers doublet, $\Delta e_{12} = e_2 - e_1 = \hbar\omega_L$, in presence of a magnetic field $\mathbf{B} = B(\sin\theta\cos\phi, \sin\theta\sin\phi, \cos\theta) = B\mathbf{b}$. The value of Δe_{12} is proportional to $\mathbf{B}$ through an effective factor g^*, whose value is dependent on the orientation of $\mathbf{b}$ [170]:

$$\Delta e_{12} = h f_L = \hbar\omega_L = g^*\mu_B B\,, \tag{6.28}$$

$$g^* = |\hat{g}\mathbf{b}|\,, \tag{6.29}$$

where μ_B is the Bohr magneton and $\hat{g}$ is the 3×3 g-tensor, which in turn depends on the total electrostatic potential $V_c(\mathbf{r}) + V_{DC}(z)$ acting on the system. The Larmor frequency describes the precession around the Z axis of the Bloch sphere during free evolution, as we showed in Fig. 5.2(b). In the following, we will refer either to the actual Larmor frequency f_L (measured in Hz) or to the angular frequency ω_L (measured in rad/s). The relation between the two is $\omega_L = 2\pi f_L$. Secondly, the Rabi frequencies are defined as the coupling between states, and are evaluated through the matrix elements of the driving field $\hat{V}_{AC} = -\delta E_z\hat{z}$:

$$\omega_X^R = |\delta E_z \Re\left[\langle 0|\,\hat{z}\,|1\rangle\right]|\,, \quad \omega_Y^R = |\delta E_z \Im\left[\langle 0|\,\hat{z}\,|1\rangle\right]|\,, \quad \omega_Z^R = \left|\delta E_z \frac{\langle 1|\,\hat{z}\,|1\rangle - \langle 0|\,\hat{z}\,|0\rangle}{2}\right|\,. \tag{6.30}$$

Specifically, the frequencies along the X and Y axes of the Bloch sphere correspond to transverse rotations of the qubit which induce transitions from qubit state $|\Downarrow\rangle \equiv |0\rangle$ to $|\Uparrow\rangle \equiv |1\rangle$, as illustrated previously in Fig. 5.2(c). Since the value of these frequencies is dependent on the global phase of the qubit states, we can also define the complex quantity $\omega_+^R = \omega_X^R + i\omega_Y^R$ and focus on its modulus. Then, the frequency along the Z axis of the Bloch sphere corresponds to a longitudinal rotation, which further modifies the relative phase between the components on states $|\Uparrow\rangle$ and $|\Downarrow\rangle$ in the precession of the qubit state around the Z axis [Fig. 5.2(b)]. Overall, we can take account of both the values of $|\omega_+^R|$ and ω_Z^R by defining the following quantity:

$$\omega_{+Z}^R = \left(\frac{1}{|\omega_+^R|} + \frac{1}{\omega_Z^R}\right)^{-1} = \frac{|\omega_+^R|\omega_Z^R}{|\omega_+^R| + \omega_Z^R}\,, \tag{6.31}$$

which still has the units of a frequency. Since the quantity $1/|\omega_+^R|$ ($1/|\omega_Z^R|$) can be interpreted as the characteristic time for a transverse (longitudinal) rotation, we can think of $1/\omega_{+Z}^R$ as the time necessary to perform the two rotations one after another. As a consequence, the optimal orientation of $\mathbf{B}$ to consider will be the one that maximizes ω_{+Z}^R, which allows for a trade-off between making transverse and longitudinal rotations both as fast as possible [189].

Larmor frequencies

Before studying how f_L is modified by the presence of an additional charge into the device, let's see how it behaves without it. Figures 6.15(a) and (b) show the values of Δe_{12} as a function of the orientation of $\mathbf{B}$ on the xz plane for different ratios between the characteristic frequencies of the confinement potentials along x and y. Since these frequencies define the elastic constants $\kappa_{x,y}$ and effective lengths $l_{x,y}$ of the in-plane harmonic confinement, this overall corresponds to considering different ratios between the x and y dimensions of the channel which defines our DQD system. These trials were performed by fixing $\hbar\omega_x = 5$ meV for the confinement along x, and varying $\hbar\omega_y$ for y. We did not see any difference in the curves' behavior by considering the same ratios with a different $\hbar\omega_x$. Figure 6.15(a) shows the behaviour of the Larmor frequency when $\mathbf{B}$ lies on the xy plane ($\theta = 90°$). As we can see, $\Delta e_{12} = \hbar\omega_L$ generally increases as the width of the channel in y decreases (i.e. the confining energy ω_y increases), and its value remains approximately unaffected by the orientation of the field with respect to the x and y axes. Then, Fig. 6.15(b) shows the values of Δe_{12} when $\mathbf{B}$ lies on the xz plane (i.e. $\phi = 0°$). Coherently with the previous graph, we noticed no significant difference in the case of a field $\mathbf{B}$ lying on the yz plane (i.e. $\phi = 90°$). More specifically, Δe_{12} decreases for all ratios ω_y/ω_x as the angle θ with the z axis increases. Additionally, as confirmed in Fig. 6.15(c), when θ is small enough ($\lesssim 60°$) then ω_L decreases monotonically as ω_y decreases and the ratio ω_y/ω_x increases. Instead, the opposite behavior occurs for larger angles ($\gtrsim 60°$). The same trials were also performed for a single quantum dot system (not shown), with no significant variations in the behavior of the curves. For reference, a previous work describing the behavior of the Rabi frequency in integrated hole-spin qubits in SQD is [189].

At this point, we can introduce the charge-induced Coulomb potential into our system. From the slope of the curves in Fig. 6.16(a) we can see that the presence and position of the charge change the value of the factor g^* in Eq. (6.28), and consequently the values of f_L. Fig. 6.16(b) then shows the change in hf_L with respect to their values in the absence of charge, at fixed $B = 1$ T and $x_0 = 60$ nm, for different values of a. Overall, hf_L is always smaller than its value in the absence of charge, but we see that it changes the most at $a \simeq 18$ nm, close to where in Sec. 6.1.1 we observed the system to be the most polarizable. In Fig. 6.16(b) we report both the curves evaluated with

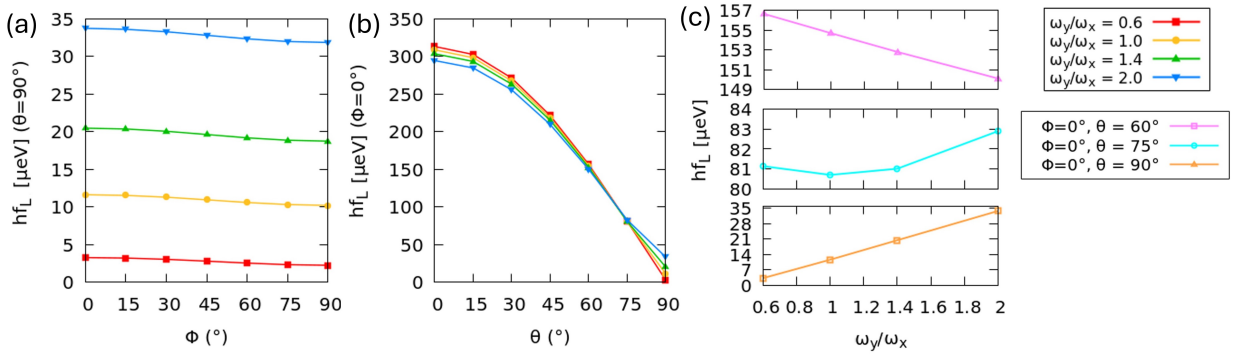


Figure 6.15: Larmor frequency $\hbar\omega_L = hf_L = e_2 - e_1$ of a Si DQD with half-distance $a = 12$ nm with no charge, and with a constant magnetic field of module $B = 1$ T. Panels (a) and (b) show the Larmor frequency as a function of the orientation of $\mathbf{B}$, respectively when the field lies on the xy plane ($\theta = 90°$) and on the xy plane ($\phi = 0°$). Panel (c) shows the Larmor frequency for different orientations of $\mathbf{B}$ as a function of the ratio ω_y/ω_x between the confining energies along y and x.

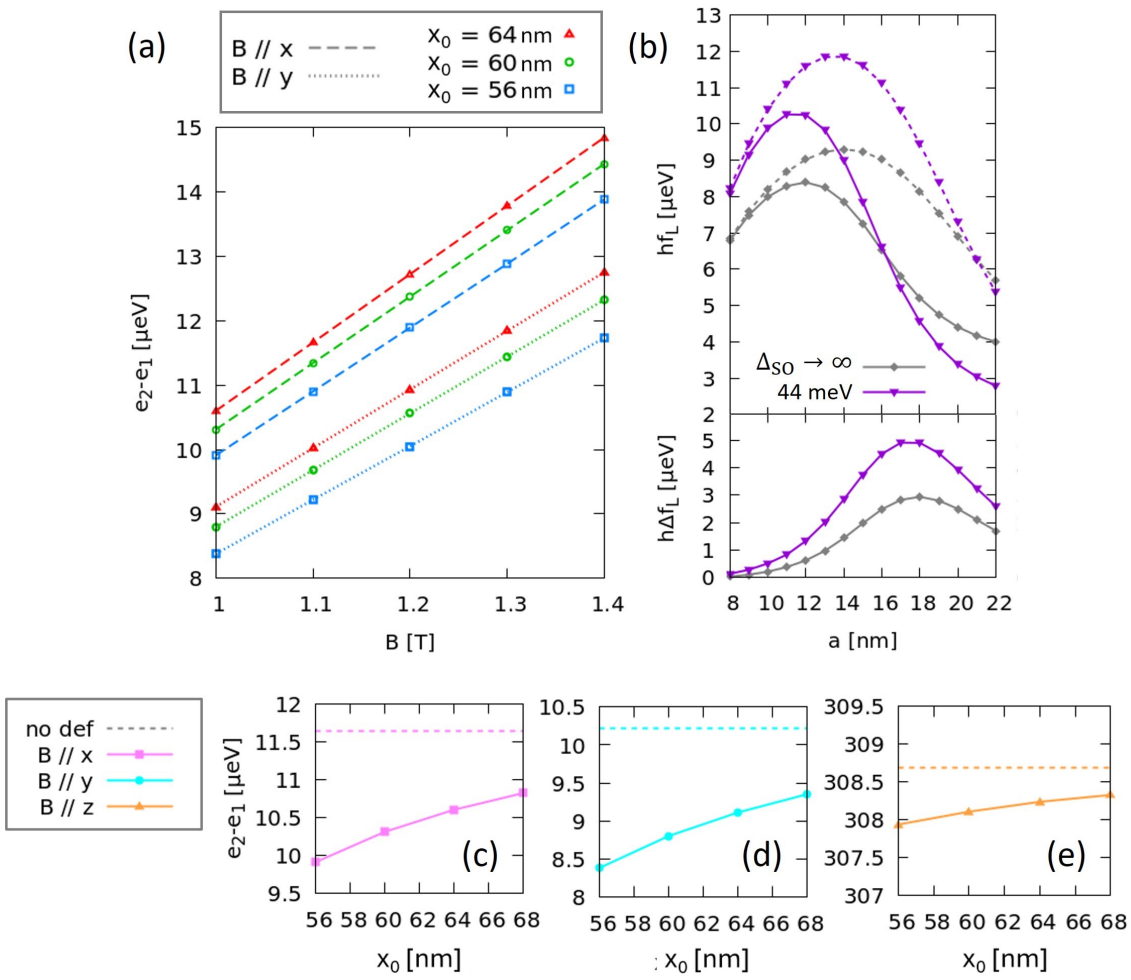


Figure 6.16: Larmor frequency of a Si DQD in the presence of a charge. (a) Trials as a function of the intensity of the magnetic field B for different positions x_0 of the charge, for a DQD with fixed half-distance $a = 12$ nm. (b) Trials as a function of a at fixed $B = 1$ T parallel to the x axis. On the top panel are the curves in the absence (dotted line) and presence (continuous line) of the charge at $x_0 = 60$ nm; on the bottom panel is the difference between the two curves, which gives the variation in the Larmor frequency, Δf_L. The curves in purple are obtained from six-band simulations with the real spin-orbit coupling of Si, i.e. $\Delta_{SO} = 44$ meV, while the curves in grey represent the limit for $\Delta_{SO} \to \infty$. (c-e) Variation of the Larmor frequency as a function of x_0 (continuous line) with respect to the case with no charge (dotted line), for three orientations of the magnetic field: (c) $\mathbf{B} \parallel \hat{x}$, (d) $\mathbf{B} \parallel \hat{y}$, and (e) $\mathbf{B} \parallel \hat{z}$. Panels (b-e) were adapted from [2].

6-band simulations with the real spin-orbit coupling in Si, $\Delta_{SO} = 44$ meV, and those in the limit for $\Delta_{SO} \to \infty$, corresponding in practice to 4-band simulations. By doing so we show that the split-off bands are necessary to accurately represent f_L, and thus the behavior of the qubit under manipulation. The Larmor frequency is in fact not only dependent on the interplay among the interdot coupling, the Coulomb interaction, and the magnetic field, but also on band mixing, which can be accurately reproduced by considering the appropriate number of bands.

For completeness, we also performed 6-band simulations with $\Delta_{SO} = 0$, obtaining a constant value of $hf_L = 115.77\,\mu$eV which does not depend on a, x_0 or $\mathbf{b}$. This value corresponds to a g-factor equal to the free electron-spin g-factor, $g_s \sim 2$. In this case, the absence of spin-orbit makes it so that the orbital and spin degrees of freedom do not couple, and the Hamiltonian in Eq. (5.62) can be written as the sum of the separate orbital and spinorial contributions, $H_{TOT} = H_{orb} + H_{ZB}$, where H_{ZB} is the Zeeman-Bloch Hamiltonian for spin 1/2. Thus, the eigenstates forming the first Kramers doublets are factorized, with an equal orbital part corresponding to the ground state of H_{orb}:

$$\Phi_1(\mathbf{r}) = \phi^{orb}_{GS}(\mathbf{r})\chi_{\Downarrow}(\mathbf{r})\,, \quad \Phi_2(\mathbf{r}) = \phi^{orb}_{GS}(\mathbf{r})\chi_{\Uparrow}(\mathbf{r})\,. \tag{6.32}$$

The corresponding eigenenergies are $e_{1,2} = E^{orb}_{GS} \mp g_s\mu_B B/2$. In practice, the orbital term cancels out and the Larmor frequency is completely determined by the Zeeman contribution, which only depends on the magnitude of B. Overall, the spin-orbit coupling is necessary to observe a dependence of f_L on the electrostatic environment, i.e. it is of crucial importance for quantum sensing.

We then look at how the charge affects g^* for different orientations of the magnetic field. With respect to this, in Fig. 6.16(f-h) we can see the behavior of $g^*\mu_B$ (the total proportionality factor, obtained from a measure of $e_2 - e_1 = hf_L$ with fixed $B = 1\,T$) as a function of x_0 for three different orientations of $\mathbf{B}$, along the x, y or z axis. As we can see, in all cases the effect of the charge is stronger when the value of g^* itself is smaller, i.e. along directions x and y. Instead, it becomes almost negligible in comparison along the z direction, where f_L is the largest. That is to say that the values of f_L change in a larger range for large angles θ, although the values of f_L themselves are smaller. That said, in all cases, the presence of the Coulomb potential always influences the values of $g^*\mu_B$ in a range of approximately $\sim 0.1\,\mu$eV/T per nm, or lower. However, as we will see in the following Sections, this variation will be large enough to discriminate between different values of x_0, and thus obtain information from the system.

We can also compare these results with analog trials with single dots. For this case, we considered the same harmonic confinement with $\hbar\omega = 5$ meV both in the x and y direction. Fig. 6.17(a) shows the linear dependence between $\hbar\omega_L$ and B for a magnetic field along x and y, while Fig. 6.17(b) shows the the same quantity as a function of x_0. First of all, the presence of the charge does not necessarily lower the Larmor frequency, as it did for the double dot. Instead, $\hbar\omega_L$ is always higher than its value without charge when $\mathbf{B} \parallel \hat{x}$. We relate this behavior to the symmetry breaking between the x and y induced by the Coulomb interaction. In fact, the average between the values for $\mathbf{B} \parallel \hat{x}$ and $\hat{y}$ is always equal to the value of $\hbar\omega_L$ with no charge. Overall, this means that the two curves in Fig. 6.17(b) are correlated, and consequently the single dot system presents fewer degrees of freedom than the double dot system.

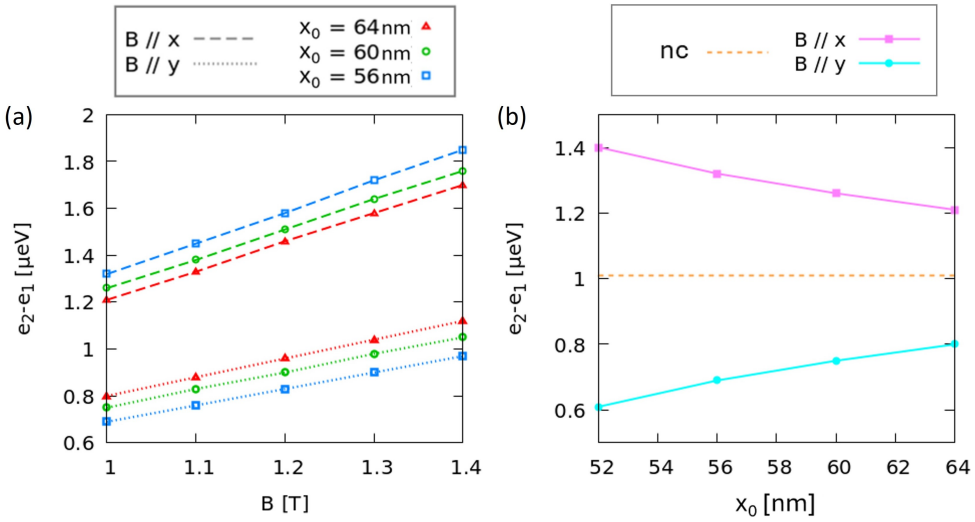


Figure 6.17: Larmor frequency of a Si SQD in the presence of a charge. (a) Trials as a function of the intensity of the magnetic field B for different positions x_0 of the charge. (c) Variation of the Larmor frequency as a function of x_0 (continuous line) with respect to the case with no charge (dotted line), for $\mathbf{B} \parallel \hat{x}$ and $\mathbf{B} \parallel \hat{y}$.

Rabi frequencies

We now pass to analyzing the Rabi frequencies. Notice from Eq. (6.30) that the Rabi frequencies are linear in δE_z, meaning that we can consider a reference value of $\delta E_z = 1\,\mathrm{mV/nm}$ and then, if we want to change δE_z, straightforwardly multiply the obtained values. As for the Larmor frequencies, we start by looking at the behavior without the additional charge. In this specific case, the numerical calculations with our code automatically fix the qubit phase for which $\omega_Y^R = 0$, so that ω_+^R coincides with ω_X^R and $\omega_{+Z}^R = \omega_{XZ}^R$. From Fig. 6.18(a) we see that in the case for $\theta = 45°$ and $\phi = 90°$ the Rabi frequencies ω_X^R and ω_Z^R reach values as high as ~ 100 Mrad/s for high enough DC electric fields E_z. However, it seems that for values larger than $E_z \simeq 50\,\mathrm{mV/nm}$ the Rabi frequencies start decreasing. Then, once we fix the value of E_z, Fig. 6.18(b) and (c) show results obtained by varying the intensity of the magnetic field B. Specifically, we choose $E_z = 50\,\mathrm{mV/nm}$, by comparison with previous simulations of the confinement potentials felt inside a MOSFET [189]. Figure 6.18(b) shows the crossing between the gaps $\Delta e_{21} = e_2 - e_1$ of the first Kramers doublet, which increases linearly with B, and $\Delta e_{31} = e_3 - e_1$ between the first two Kramers doublets, which instead remains more or less constant. This panel indicates that the working regime for manipulation with $a = 12\,\mathrm{nm}$ must maintain $B \ll 5\,\mathrm{T}$, so that the first two states of the system in which we encode the qubit remain energetically separate from the second Kramers doublets, and can be considered isolated. Notice that a larger half-interdot distance a implies a smaller Δe_{31} [see Fig. 6.1(a)]: consequently, the larger is the value of a, the smaller must be B for the same condition to be satisfied. For example, we saw that for $a = 22$ nm (not shown) the inversion between states 2 and 3 happens as soon as $B \simeq 1$ T. That said, Fig. 6.18(c) shows how both ω_X^R and ω_Z^R increase approximately linearly with a magnetic field as high as 4 T, coherently with what previously reported in literature [170, 189].

In the next calculations we fix $B = 1\,\mathrm{T}$. For $a = 12$ nm, this condition along with $E_z = 50\,\mathrm{mV/nm}$ corresponds to a ratio between energy gaps of $\Delta e_{31}/\Delta e_{21} \sim 5.30$, sufficiently large

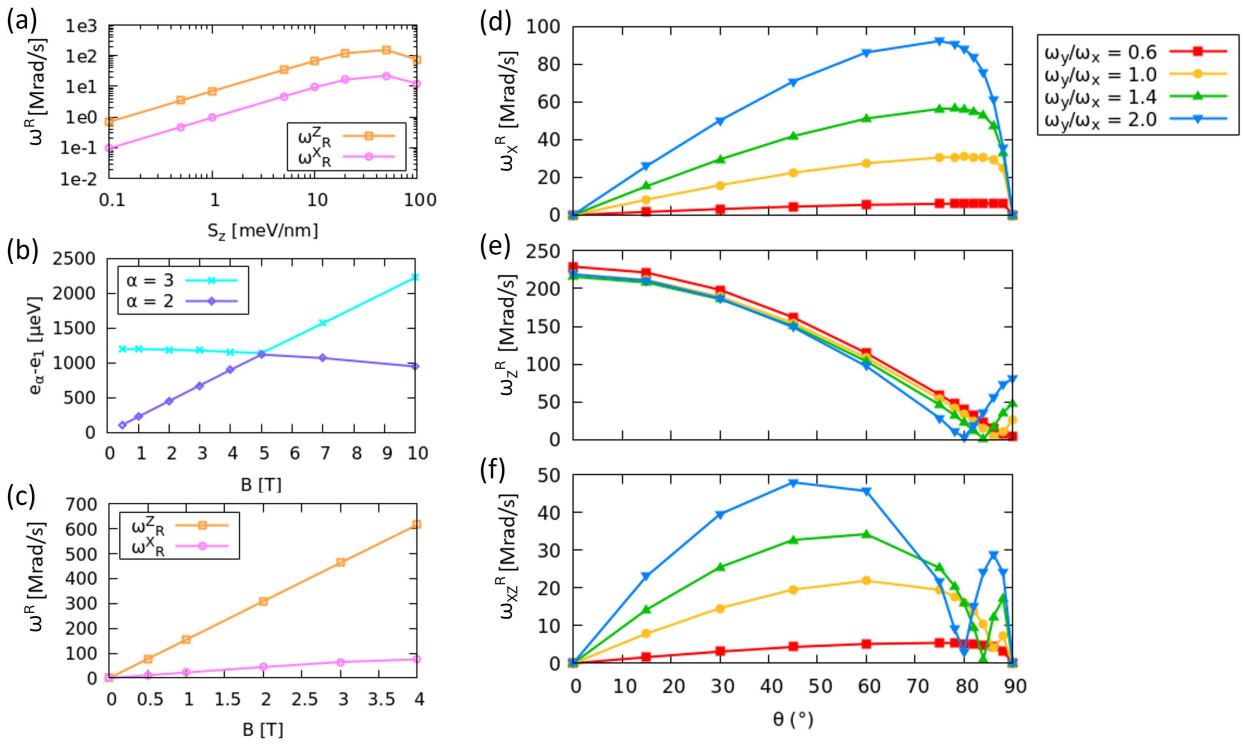


Figure 6.18: (a) Rabi frequencies ω_X^R and ω_Z^R as a function of the out-of-plane electric field E_z, at fixed $B = 1$ T ($\theta = 45°$, $\phi = 90°$). (b) Energy gaps between the first two Kramers doublet ($e_3 - e_1$) and the states $|\Uparrow\rangle$ and $|\Downarrow\rangle$ of the qubit ($e_2 - e_1$), and (c) Rabi frequencies ω_X^R and ω_Z^R as a function of the magnetic field intensity at $\theta = 45°$, $\phi = 90°$, with fixed $E_z = 50$ mV/nm. (d-f) Rabi frequencies (d) ω_X^R, (e) ω_Z^R and (f) ω_{XZ}^R as a function of the angle θ between $\mathbf{B}$ and the z axis, at fixed $\phi = 90°$ and with $B = 1$ T and $E_z = 50$ mV/nm; different curves were obtained by varying the value of the confining energy $\hbar\omega_y$ along y, thus changing the ratio ω_y/ω_x. All calculations were performed on a Si DQD with half-distance $a = 12$ nm without charge, and confining energy $\hbar\omega_x = 5$ meV for the quartic potential along x. Panels (a-c) were obtained with $\omega_y/\omega_x = 1$.

to guarantee a good isolation of the first Kramers doublet with respect to the next ones. Figures 6.18(d), (e) and (f) respectively show the Rabi frequencies ω_X^R, ω_Z^R and ω_{XZ}^R as a function of the orientation of $\mathbf{B}$ with respect to the angle θ with respect to the z axis, for different ratios ω_y/ω_x between the confining energies along y and x. The influence of the angle ϕ is instead negligible (not shown), and we choose an arbitrary value of $\phi = 90°$. These curves are again similar to those obtained for a realistic SQD in a Si MOSFET [189]. Specifically, ω_X^R is generally higher as θ increases, but falls to zero when $\mathbf{B}$ lays on one of the spatial axes, i.e. for $\theta = 0°$ or $\theta = 90°$. Instead, ω_Z^R reaches zero at a specific angle and is different from zero for either very small or large θ. Overall, ω_{XZ}^R is maximal for an intermediate value of θ, which depends on the ratio between the confining energies. Unless specified otherwise, for the following simulations we fix a magnetic field orientation of $\theta = 60°$ and $\phi = 90°$. At this orientation indeed the value of ω_{XZ}^R is maximized for the reference value of the channel ratio $\omega_y/\omega_x = 1$.

Figure 6.19 shows the behavior of the Rabi frequencies in the presence of the charge. The main effect caused by the presence of a charge is the modification of the qubit phase returned by our

numerical calculations. Overall this behavior is related to two separate phases, one for each of the basis vectors. Our numerical code automatically fixes specific phases for $|\Downarrow\rangle$ and $|\Uparrow\rangle$ during the calculation of the eigenstates of the system's Hamiltonian. In the absence of Coulomb potential, the code-defined phases define a real matrix element $(V_{AC})_{\Downarrow,\Uparrow}$, and $\omega_Y^R = 0$. Apparently, the situation changes when we introduce the Coulomb potential. This is probably due to a symmetry breaking with respect to the real-space x axis of the system. However, the relative phase is not measurable, and does not influence our system's observables, since it can be arbitrarily changed with a rotation in the qubit space, as previously mentioned in Sec. 5.4.2. Consequently, this phase has no physical significance, but, for completeness, in the Figures we report both the results obtained by considering ω_X^R and ω_Y^R separately and the whole complex frequency ω_+^R.

From Fig. 6.19(a,c,e), we can see that the Rabi frequencies behave similarly to the Larmor frequency as a function of the parameter x_0. Specifically, both $|\omega_+^R|$ and ω_Z^R, as well as their combination ω_{+Z}^R, tend to the respective values in the absence of charge for $x_0 \to \infty$. Figures 6.19(b,d,f) show the same frequencies as a function of the angle θ formed by $\mathbf{B}$ with the z axis. By comparing the curves with and without charge, we see that $|\omega_+^R|$ and ω_{+Z}^R no longer go to zero for $\theta = 0°$. This behavior is surprising, since we know that the g-tensor goes to zero whenever $\mathbf{B}$ lies on a coordinate plane. Thus, we deduce that the symmetry-breaking along x introduced by the charge at $(x_0, 0, 0)$ causes a shift in the plane at which such frequency is null.

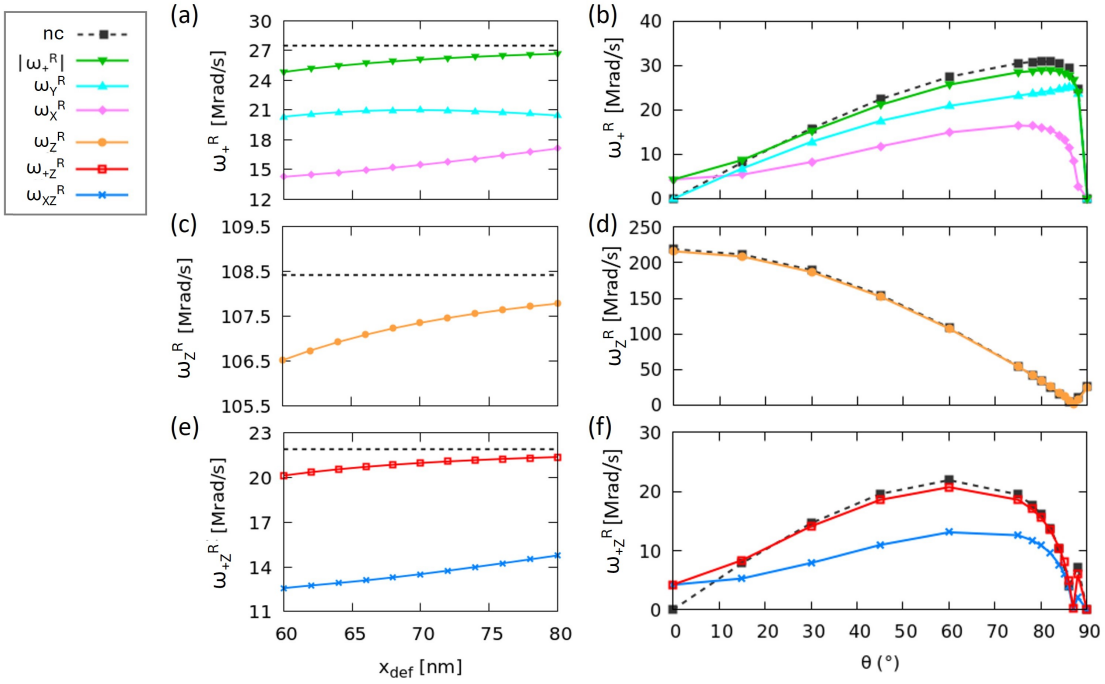


Figure 6.19: Comparison of the Rabi frequency inside a Si DQD with $a = 12\,\text{nm}$ in the absence (dashed lines) and presence (continuous lines) of a charge. All panels on the left plot the Rabi frequencies as functions of the charge position x_0, for a fixed orientation of $\mathbf{B}$: $\theta = 60°$, $\phi = 90°$. All panels on the right are as a function of the angle θ, for fixed $\phi = 90°$ and $x_0 = 66\,\text{nm}$. Panels (a,b) show the behavior of ω_X^R, ω_Y^R and $\omega_+^R = \omega_X^R + i\omega_Y^R$. Panels (c,d) show ω_Z^R, and panels (e,f) show ω_{XZ}^R and ω_{+Z}^R, as defined in the text. The magnetic field was fixed at $B = 1\,\text{T}$.

6.4 Dynamic approaches to quantum sensing

We can now apply our considerations from the previous Section to study operative approaches to quantum sensing with qubits. Since we can exploit the time-dependent evolution of the qubit as described by the final expression of $\hat{U}_I$ from Eq. (5.184), we refer to these approaches as *dynamic*, in opposition to the static approaches described in Sec. 6.2 for sensing on the hole ground state. From here on out we fix $E_z = 50\,\mathrm{mV/nm}$ and $\delta E_z = 3\,\mathrm{mV/nm}$. Following our considerations on the Larmor and Rabi frequencies from Sec. 6.3.1, we fix a magnetic field $B = 1\,\mathrm{T}$ oriented with angles $\theta = 60°$ and $\phi = 90°$, and set the interdot half-distance to $a = 12\,\mathrm{nm}$ for the DQD simulations. The confining energies of the potentials along x and y are fixed to $\hbar\omega_x = \hbar\omega_y = 5\,\mathrm{meV}$ for both the SQD and DQD. Finally, in this Section we once and for all fix the qubit phase for which $\omega_+^R = \omega_X^R$.

6.4.1 Rabi scheme applied to state discrimination

Overall, the operator $\hat{U}_I$ found from Eq. (5.184) shows that the qubit evolution in the RWA only depends on the Larmor frequency ω_L and the Rabi frequency ω_X^R of the system. All the other quantities are either arbitrary and do not depend on the system configuration (ω_P, t, t_i) or derived quantities (Ω, Δ). In this Section, we start by approaching the problem of state discrimination through the use of a Rabi scheme. In this kind of manipulation, the qubit is initialized in state $|0\rangle = (0\ 1)^T$ at time $t_i = 0$. Subsequently, the qubit is (ideally) rotated by an angle π on the Bloch sphere by applying an external pulse. In this way, the final state in an ideal experiment corresponds to state $|1\rangle = (1\ 0)^T$. Here we generalize the duration of the pulse to an arbitrary time T, so that, considering a rectangular pulse during the interval $[0, T]$, and recalling from Sec. 5.4.2, the final probability of outcome 1 from a $\hat{\sigma}_3$ measurement becomes

$$p_1^{Rabi} = |U_I^{1,0}(T,0)|^2 = \frac{(\omega_X^R)^2}{\Omega^2}\sin^2\left(\frac{\Omega T}{2}\right). \tag{6.33}$$

Since in real-life experiments T is usually much smaller than the lifetime associated with decoherence processes acting on the qubit, for now we neglect them and instead focus on coherent manipulation. Notice that the value of p_1^{Rabi} presents a strong dependence on the quantity $\Delta = \omega_P - \omega_L$ through the effective frequency Ω. Indeed, for $\omega_P \approx \omega_L$, we are in resonant conditions, and the $|0\rangle \leftrightarrow |1\rangle$ transition is driven with amplitude ≈ 1. Consequently, at $T \approx \pi/\omega_X^R$ the state $|1\rangle$ is

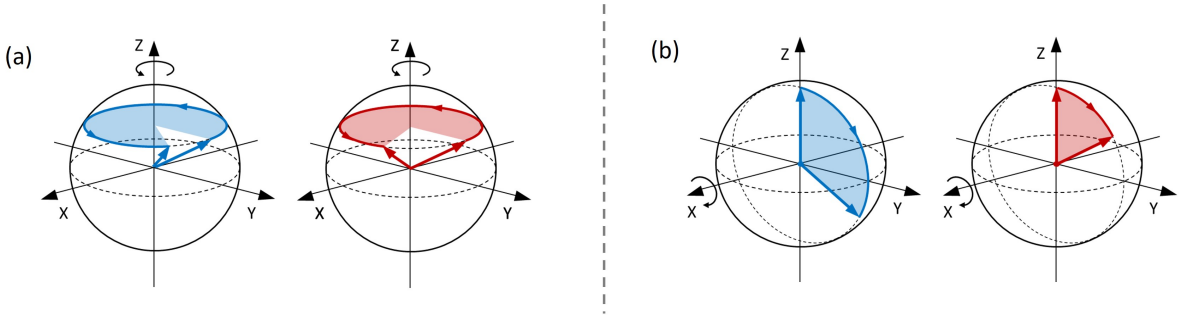


Figure 6.20: Schematic representation of how two different electrostatic environments (blue vs. red) can influence (a) the Larmor precession of the qubit vector state around the Z axis of the Bloch sphere and (b) the rotation induced by a Rabi pulse around the X axis of the Bloch sphere. The figure was adapted from [2].

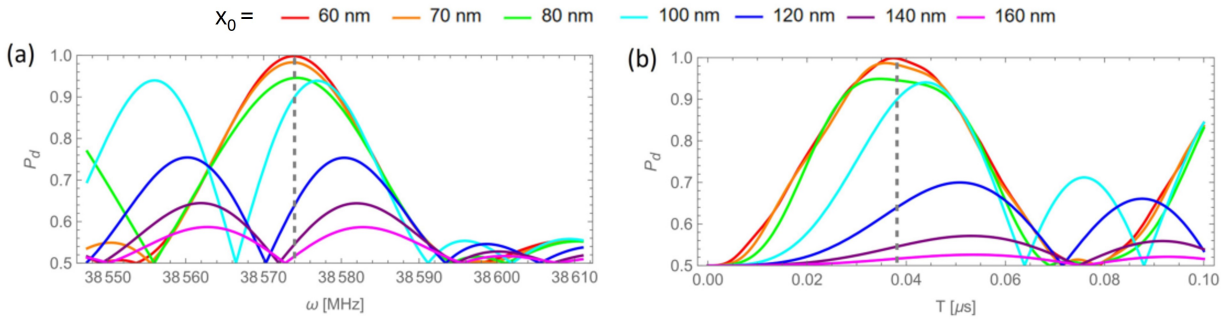


Figure 6.21: Discrimination probability from Eq. (6.34), evaluated on a Rabi measurement as a function of (a) the pulse frequency ω with fixed pulse duration $T = \pi/\omega^R_{X,ref}$, where $\omega^R_{X,ref}$ is the Rabi frequency in the absence of charge; and (b) the pulse duration T with fixed $\omega_P = \omega_L^{ref}$, where ω_L^{ref} is the Larmor frequency in the absence of charge. The gray dashed line corresponds to a π rotation in the conditions without charge. The figure was adapted from [2].

almost completely occupied. On the contrary, out of resonance, for $|\Delta| \gg 0$, the amplitude of the Rabi oscillations falls to zero, and state $|1\rangle$ is never occupied. Consequently, considering a reference value of ω_L^{ref} and $\omega^R_{X,ref}$, the state of the qubit at time $T \approx \pi/\omega^R_{X,ref}$ tells us whether or not a driving field with $\omega_P = \omega_L^{ref}$ is in resonance with the qubit transition, and helps us discriminate between the resonant and out of resonance conditions. This is directly translated to our problem of charge sensing by fixing, for instance, the reference frequency to the Larmor frequency with no charge, $\omega_P = \omega_L^{nc}$. In this case, the discrimination probability between states with and without charge leads back to the formula in Eq. (6.5), where we identify outcomes $o_{nc} = 1$ and $o_c = 0$ respectively with resonant (no charge) and out of resonance (charge) conditions:

$$p_d = \frac{1}{2}p(0|\psi^c_{q,I}(T)) + \frac{1}{2}p(1|\psi^{nc}_{q,I}(T)) = \frac{1}{2}p^{Rabi}_{0,nc} + \frac{1}{2}p^{Rabi}_{1,c}\,, \tag{6.34}$$

where we fixed the *a priori* probabilities to $p_c = p_{nc} = 1/2$. The quantity in Eq. (6.34) is shown in Fig. 6.21 as a function of both ω_P and T. Here, at the reference case that we illustrated, for $\omega_P = \omega_L^{nc}$ and $T = \pi/\omega^R_{X,nc}$, we see that the discrimination probability is able to reach values as high as $p_d = 1$ for a charge close enough to the qubit, $x_0 \lesssim 100\,\text{nm}$. This implies an improvement in the discrimination probability with respect to the maximal one found from the static approach from Sec. 6.2.1. Consequently, this dynamic approach proves to be superior with respect to the static one already at the stage of state discrimination.

6.4.2 Fisher information on an evolved state

The same dependency of the evolved state on the Larmor and Rabi frequencies, and consequently on the position x_0 of the charge, is naturally encoded into the definition of the Fisher information defined in Sec. 6.2.2. Indeed, identifying the general occupation probabilities of states $|0\rangle$ and $|1\rangle$ after manipulation as:

$$p_i(t;\lambda) = |c_i(t;\lambda)|^2\,, \quad i = 0,1\,, \tag{6.35}$$

where in our case $\lambda = x_0$, the Fisher information relative to a projective measurement on $\hat{\sigma}_3$ becomes:

$$\mathcal{F}(\lambda) = \sum_{i=\{0,1\}} \frac{(\partial_\lambda p_i)^2}{p_i} = \frac{(\partial_\lambda p_0)^2 p_1 + (\partial_\lambda p_1)^2 p_0}{p_0 p_1} = \frac{(\partial_\lambda p_1)^2}{p_1(1-p_1)}\,, \tag{6.36}$$

in which we used the fact that there are only two outcomes, $i = 0, 1$, with $p_0 + p_1 = 1$, and consequently $(\partial_\lambda p_0) = -(\partial_\lambda p_1)$. Inside Eq. (6.36), p_1 is dependent on the Larmor and Rabi frequencies, so that through the chain rule we get:

$$\partial_\lambda p_1 = \frac{\partial p_1}{\partial \lambda} = \frac{\partial p_1}{\partial \omega_L}\frac{\partial \omega_L}{\partial \lambda} + \frac{\partial p_1}{\partial \omega_X^R}\frac{\partial \omega_X^R}{\partial \lambda} + \frac{\partial p_1}{\partial \omega_Z^R}\frac{\partial \omega_Z^R}{\partial \lambda}\,. \tag{6.37}$$

Although not shown here, the derivatives of the Larmor and Rabi frequencies are also gauge-invariant, as provable through similar steps as in Eq. (6.15). At this point, since we do not have any analytic formula expressing the dependence of the Larmor and Rabi frequencies on λ, their derivatives need to be evaluated numerically. Firstly, the evaluation of the derivative of ω_L is straightforward from the Hellmann-Feynman theorem:

$$\hbar \partial_\lambda \omega_L = (\partial_\lambda H)_{1,1} - (\partial_\lambda H)_{0,0}\,. \tag{6.38}$$

As for the Rabi frequencies, we use the statement of the extended Hellmann-Feynman theorem in Eq. (6.19) to evaluate the derivative of the matrix elements of $\hat{V}_{AC}$:

$$\begin{aligned}
\hbar\partial_\lambda \omega_Z^R =& \frac{1}{2}\partial_\lambda[(V_{AC})_{1,1} - (V_{AC})_{0,0}] = \Re\left[\langle 1|\hat{V}_{AC}|\partial_\lambda 1\rangle - \langle 0|\hat{V}_{AC}|\partial_\lambda 0\rangle\right] = \\
=& \Re\Bigg[i w_1 (V_{AC})_{1,1} - i w_0 (V_{AC})_{0,0} + \frac{(V_{AC})_{1,0}(\partial_\lambda H)_{0,1}}{e_1 - e_0} \\
& - \frac{(V_{AC})_{0,1}(\partial_\lambda H)_{1,0}}{e_0 - e_1} + \sum_{m=2}^{+\infty}\left(\frac{(V_{AC})_{1,m}(\partial_\lambda H)_{m,1}}{e_1 - e_m} - \frac{(V_{AC})_{0,m}(\partial_\lambda H)_{m,0}}{e_0 - e_m}\right)\Bigg] = \\
=& \Re\left[2\frac{(V_{AC})_{0,1}(\partial_\lambda H)_{1,0}}{\hbar\omega_L} + \sum_{m=2}^{+\infty}\left(\frac{(V_{AC})_{1,m}(\partial_\lambda H)_{m,1}}{e_1 - e_m} - \frac{(V_{AC})_{0,m}(\partial_\lambda H)_{m,0}}{e_0 - e_m}\right)\right],
\end{aligned} \tag{6.39}$$

$$\begin{aligned}
\hbar\partial_\lambda \omega_X^R =& \partial_\lambda |(V_{AC})_{0,1}| = \frac{1}{|(V_{AC})_{0,1}|}\Re\left[(V_{AC})_{1,0}\partial_\lambda (V_{AC})_{0,1}\right] = \\
=& \frac{1}{|(V_{AC})_{0,1}|}\Re\left[(V_{AC})_{1,0}\langle 0|\hat{V}_{AC}|\partial_\lambda 1\rangle + (V_{AC})_{0,1}\langle 1|\hat{V}_{AC}|\partial_\lambda 0\rangle\right] = \\
=& \frac{1}{|(V_{AC})_{0,1}|}\Re\Bigg[i(w_1 + w_0)|(V_{AC})_{0,1}|^2 - \frac{(V_{AC})(\partial_\lambda H)_{1,0}}{e_1 - e_0}((V_{AC})_{1,1} - (V_{AC})_{0,0}) \\
& + \sum_{m=2}^{+\infty}\left(\frac{(V_{AC})_{0,m}(\partial_\lambda H)_{m,1}}{e_1 - e_m} - \frac{(V_{AC})_{1,m}(\partial_\lambda H)_{m,0}}{e_0 - e_m}\right)\Bigg] = \\
=& \frac{1}{|(V_{AC})_{0,1}|}\Re\left[-2\hbar\omega_Z^R\frac{(V_{AC})_{0,1}(\partial_\lambda H)_{1,0}}{\hbar\omega_L} + \sum_{m=2}^{+\infty}\left(\frac{(V_{AC})_{0,m}(\partial_\lambda H)_{m,1}}{e_1 - e_m} - \frac{(V_{AC})_{1,m}(\partial_\lambda H)_{m,0}}{e_0 - e_m}\right)\right].
\end{aligned} \tag{6.40}$$

In Eqs. (6.39-6.40) we used the fact that both $\delta\hat{V}$ and $\hat{\mathcal{H}}$ are hermitian operators, and $w_n \in \mathbb{R}\,\forall\, n$.

Expressions of the Fisher information for a Rabi and Ramsey scheme

Now that we have the general expression of the Fisher information on an evolved state, we can first replace the expression in Eq. (6.33) into Eq. (6.36), and explicitly find the Fisher information after a Rabi manipulation:

$$\mathcal{F}^{Rabi} = \frac{\left[T\cos\left(\frac{\Omega T}{2}\right)\omega_X^R\Omega\left(\omega_X^R\partial_\lambda\omega_X^R - \Delta\partial_\lambda\omega_L\right) + 2\Delta\sin\left(\frac{\Omega T}{2}\right)\left(\omega_X^R\partial_\lambda\omega_L + \Delta\partial_\lambda\omega_X^R\right)\right]^2}{\Omega^4\left[\Delta^2 + (\omega_X^R)^2\cos^2\left(\frac{\Omega T}{2}\right)\right]}. \tag{6.41}$$

Then, we can generalize the same concept to a Ramsey experiment, which instead consists of two separate pulses instead of a single one. In the ideal experiment, the π-rotation from the Rabi scheme is split into two $\pi/2$-rotations. These pulses are separated by a waiting time, during which the qubit state vector evolves freely. Consequently, its components acquire a relative phase that depends on the detuning Δ between the pulse frequency and the Larmor frequency of the system. Overall, the final probability p_1 of finding the state in $|1\rangle$ will also depend on this additional phase. In our case, we consider once again rectangular pulses, each of which has duration T in time, and we call the waiting time τ. Eventually, the overall envelope function of the pulse entering the definition of the driving pulse from Eq. (5.154) is

$$F(t) = \mathcal{H}(T-t)\mathcal{H}(t) + \mathcal{H}(2T+\tau-t)\mathcal{H}(t-T-\tau)\,, \tag{6.42}$$

and the total evolution operator can be written as the product of three operators. In the coherent case, $\hat{U}_I^{TOT}$ is:

$$\hat{U}_{I,coh}^{TOT}(2T+\tau,0) = \hat{U}_I(2T+\tau,T+\tau)\hat{U}_I^{free}(T+\tau,T)\hat{U}_I(T,0)\,, \tag{6.43}$$

where we recall that the free evolution operator in the interaction picture is the identity, $\hat{U}_I^{free} = \mathbb{1}$. Consequently, the qubit state after a coherent Ramsey manipulation reads

$$\left|\psi_{q,I}^{coh}(2T+\tau)\right\rangle = \hat{U}_I(2T+\tau,T+\tau)\hat{U}_I(T,0)\,|0\rangle\,, \tag{6.44}$$

and the probability of outcome 1 is

$$p_{1,coh}^{Ramsey} = |U_I^{1,1}(2T+\tau,T+\tau)U_I^{1,0}(T,0) + U_I^{1,0}(2T+\tau,T+\tau)U_I^{0,0}(T,0)|^2 = X^2A^2\,, \tag{6.45}$$

in which we defined

$$A \equiv \cos\left(\frac{1}{2}\tau\Delta\right)\sin\left(T\Omega\right) - Y\sin\left(\frac{1}{2}\tau\Delta\right)\left(1-\cos\left(T\Omega\right)\right)\,, \tag{6.46}$$

and $X \equiv \omega_X^R/\Omega$ and $Y \equiv \Delta/\Omega$ are dimensionless quantities such that $X^2+Y^2=1$. Inserting the expression from Eq. (6.45) into Eq. (6.36), we arrive to the Fisher information:

$$\mathcal{F}_{coh}^{Ramsey}(\lambda) = \frac{4B^2}{1-X^2A^2}\,, \tag{6.47}$$

in which we defined

$$\begin{aligned} B \equiv&(\partial_\lambda X)A + X(\partial_\lambda A) = \\ =&A\frac{(\partial_\lambda\omega_X^R - X\partial_\lambda\Omega)}{\Omega} + A_1\frac{1}{2}\tau(\partial_\lambda\omega_L) + A_2T(\partial_\lambda\Omega) + A_3\frac{(\partial_\lambda\omega_L + Y\partial_\lambda\Omega)}{\Omega}\,. \end{aligned} \tag{6.48}$$

The quantities A_1, A_2 and A_3 in Eq. 6.48 are defined as

$$A_1 \equiv \sin\left(\frac{1}{2}\tau\Delta\right)\sin\left(T\Omega\right) + Y\cos\left(\frac{1}{2}\tau\Delta\right)\left(1-\cos\left(T\Omega\right)\right)\,; \tag{6.49}$$

$$A_2 \equiv \cos\left(\frac{1}{2}\tau\Delta\right)\cos\left(T\Omega\right) - Y\sin\left(\frac{1}{2}\tau\Delta\right)\sin\left(T\Omega\right)\,; \tag{6.50}$$

$$A_3 \equiv \sin\left(\frac{1}{2}\tau\Delta\right)\left(1-\cos\left(T\Omega\right)\right)\,. \tag{6.51}$$

In Ramsey experiments, however, usually the waiting time τ is varied in a range much larger than the one of the duration T of the pulses. Thus, τ can reach values that are comparable to the characteristic lifetimes related to decoherence processes. Consequently, these processes are no longer negligible in the treatment of a Ramsey manipulation, and it is necessary to include them. Specifically, here we focus on the process that most affects the free evolution of a spin qubit in Si, that is, the hyperfine interaction between the spin and the magnetic nuclei inside the device [182]. Let's first define the population contrast of a general state as $\chi_{coh} = p_{0,coh} - p_{1,coh}$, such that

$$p_{0,coh} = \frac{1+\chi_{coh}}{2}\,, \qquad p_{1,coh} = \frac{1-\chi_{coh}}{2}\,. \tag{6.52}$$

Notice that the Fisher information can be rewritten entirely as a function of χ_{coh}. Indeed, by replacing the expression of $p_{1,coh}$ from Eq. (6.52) inside Eq. (6.36), one gets:

$$\mathcal{F}_{coh}(\lambda) = \frac{(\partial_\lambda \chi_{coh})^2}{1-\chi_{coh}^2}\,. \tag{6.53}$$

A dephasing process acting during time τ causes a Gaussian decay of the outcome probabilities in time to $1/2$, which is equivalent to saying that the population contrast decays do zero for $\tau \to \infty$:

$$p_0 = e^{-(\tau/T_2^*)^2}p_{0,coh} + \frac{1}{2}\left(1-e^{-(\tau/T_2^*)^2}\right) = \frac{1+e^{-(\tau/T_2^*)^2}\chi_{coh}}{2} \xrightarrow{\tau\to\infty} \frac{1}{2}\,, \tag{6.54}$$

$$p_1 = e^{-(\tau/T_2^*)^2}p_{1,coh} + \frac{1}{2}\left(1-e^{-(\tau/T_2^*)^2}\right) = \frac{1-e^{-(\tau/T_2^*)^2}\chi_{coh}}{2} \xrightarrow{\tau\to\infty} \frac{1}{2}\,. \tag{6.55}$$

Equivalently, one can model such a dephasing process as the decay of the density matrix of the qubit to half the identity. Calling $\hat{\rho}_{coh} = |\psi_{coh}\rangle\langle\psi_{coh}|$ the density matrix in the coherent case,

$$\hat{\rho} = e^{-(\tau/T_2^*)^2}\hat{\rho}_{coh} + \frac{1-e^{-(\tau/T_2^*)^2}}{2}\mathbb{1} \xrightarrow{\tau\to\infty} \frac{\mathbb{1}}{2}\,. \tag{6.56}$$

Finally, one obtains the Fisher information in the presence of dephasing processes by replacing the expression of p_1 from Eq. (6.55) into Eq. (6.36). Noticing that neither τ nor T_2^* depend on parameter λ, one obtains that

$$\mathcal{F}(\lambda) = \frac{(\partial_\lambda\chi_{coh})^2}{e^{2(\tau/T_2^*)^2}-\chi_{coh}^2} = \mathcal{F}_{coh}(\lambda)\frac{1-\chi_{coh}^2}{e^{2(\tau/T_2^*)^2}-\chi_{coh}^2}\,. \tag{6.57}$$

Thus, the Fisher information in the presence of dephasing is equal to its coherent equivalent up to a multiplicative factor that decays with $e^{-2(\tau/T_2^*)^2}$ for large waiting time τ.

Combining Eqs. (6.57) and (6.47), the final expression of the Fisher information for the Ramsey experiment in the presence of decoherence processes reads:

$$\mathcal{F}^{Ramsey}(\lambda) = \frac{16X^2A^2B^2}{(e^{2(\tau/T_2^*)^2}-1)+4X^2A^2(1-X^2A^2)}\,. \tag{6.58}$$

6.4.3 Dynamic parameter estimation

We now apply the formulas for the Fisher information found in the previous Section to the estimation of the parameter $\lambda = x_0$. As previously said, the value of the Larmor frequency ω_L depends on the parameter we want to estimate. Thus, if we know that a charge is present inside of a device, it is not possible to tune the pulse frequency ω_P to be in exact resonance with the qubit *a priori*. Instead, in a real-life situation, the experimenter working on a collection of devices $\{i\}$ would know nominal values of the Larmor and Rabi frequencies, which describe the collection in an average way. For example, if the qubit interacts in each device i with a charge positioned in $x_0^i \in [x_0^{min}, x_0^{max}]$, we can identify such nominal values with the integral averages $\bar{\omega}_L$ and $\bar{\omega}_X^R$ determined by our calculations in the considered domain, and fix $\omega_P = \bar{\omega}_L$.

In the top row of Fig. 6.22 we show the numerical values of the Larmor and Rabi frequencies (dots) for both a DQD and SQD, for 11 evenly spaced values of $x_0 \in [140, 160]$ nm. We then interpolated these values with a cubic spline (continuous line), and evaluated the integral averages $\bar{\omega}_L$ and $\bar{\omega}_X^R$ (dashed line). We also evaluated and interpolated the derivatives of ω_L and ω_X^R in the same points, as shown in Fig. 6.22 (bottom row). As previously mentioned, we use the average value of the Larmor frequency $\bar{\omega}_L$ to define the frequency ω_P of the external pulses acting on the qubit. Then, we consider the average value of the Rabi frequency $\bar{\omega}_X^R$ to define a reference time equal to

$$T_{Rabi} = \frac{\pi}{\bar{\omega}_X^R} \,. \tag{6.59}$$

Indeed, this duration of the pulse corresponds to an ideal angle π obtained at resonance. We also

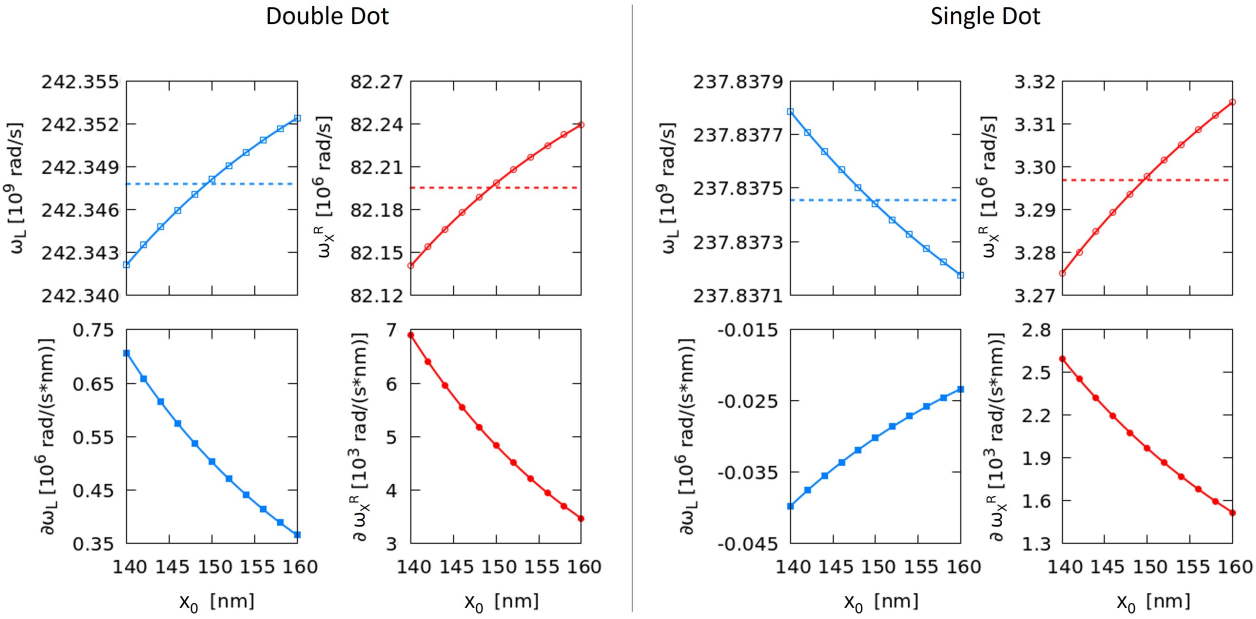


Figure 6.22: Values of the Larmor frequency (blu curves, top row) and its derivative (blue curves, bottom row), and of the Rabi frequency (red curves, top row) and its derivative (red curves, bottom row) inside the DQD (left panel) and the SQD (right panel). We report the numerical results (dots), the cubic spline interpolation of the curves (continuous line) and, for the frequencies, the integral average obtained through the trapezoidal rule (dashed line).

	$\bar{\omega}_L$ (10^9 rad/s)	$\bar{\omega}_X^R$ (10^6 rad/s)	$\lvert\omega_L - \bar{\omega}_L\rvert^{max}$ (10^6 rad/s)	$\lvert\omega_X^R - \bar{\omega}_X^R\rvert^{max}$ (10^3 rad/s)	T_{Rabi} (μs)	T_{Ramsey} (μs)	ΩT_{Ramsey} (rad)
DQD	242.35	82.196	5.7000	55.152	0.03822	0.01911	$[0.9996 \div 1.0021]\,\pi/2$
SQD	237.84	3.2968	0.3329	21.773	0.95292	0.47646	$[0.9985 \div 1.0091]\,\pi/2$

Table 6.1: Numerical values of the quantities that characterize the manipulation of the qubit state. All results refer to a simulated interval of $x_0 \in [140, 160]$ nm. The barred quantities refer to integral averages over the whole interval. T_{Rabi} and T_{Ramsey} are the pulse durations corresponding to ideal rotations of the qubit of respectively π and $\pi/2$; $\Omega T_{Ramsey} = \Omega T_{Rabi}/2$ is the expression that enters at the argument of the oscillating functions for p_1 in Eq. (6.33) and (6.45).

define $T_{Ramsey} = T_{Rabi}/2$ as the duration of each pulse during the Ramsey experiment, in which the ideal rotation angle is $\pi/2$.

We report the values of $\bar{\omega}_L$ and $\bar{\omega}_X^R$ for both the DQD and SQD in Table 6.1, along with the maximal values of $|\omega_L - \bar{\omega}_L|$ and $|\omega_X^R - \bar{\omega}_X^R|$ obtained for $x_0 \in [140, 160]$ nm. These values show the maximal discrepancy from the reference values of the Larmor and Rabi frequencies, and consequently give us an idea of how far the system can get from the resonance condition as the charge changes its position in the considered interval. Table 6.1 also reports the values of T_{Rabi} and T_{Ramsey}, and the minimal and maximal values of $\Omega T_{Rabi}/2 = \Omega T_{Ramsey}$. The latter angle is the argument of the sines and cosines that define the probabilities p_1 after both a Rabi [Eq. (6.33)] and Ramsey [Eq. (6.45)] experiment, thus they allow us to infer the general quality of the schemes' implementation inside the considered interval. The numerical values in Table 6.1 confirm that the Rabi and Ramsey schemes are implemented reasonably well within the interval we choose for x_0. Indeed, the system is never too far from resonance, as the maximum of $|\Delta| = |\bar{\omega}_L - \bar{\omega}_L|$ is at least three orders of magnitude lower than $\bar{\omega}_L$ itself. Additionally, the dispersion of ω_X^R is also several orders of magnitude lower than the value of $\bar{\omega}_X^R$, so that the reference values of T_{Rabi} and T_{Ramsey} allow to obtain rotations that are very close to the ideal angle, with discrepancy always smaller than 1%. It is also worth noticing that the times T_{Rabi} and T_{Ramsey} are approximately 25 times smaller for the DQD than the SQD, due to the larger Rabi frequencies it presents. Thus, the DQD appears to be generally a more suitable system for our problem. Firstly, because the hypothesis that the pulse duration T must be much smaller than T_2^* is more easily satisfied, decoherence effects can effectively be neglected during the application of the pulses. Secondly, and more generally, the possibility to apply gates in a shorter time is fundamental for the implementation of complex algorithms that require a large number of operations performed on the qubit.

Estimation with Rabi experiment

We first show in Fig. 6.23 the results of the Rabi manipulation on the hole-spin qubit inside both a DQD (top row) and a SQD (bottom row). The occupation probabilities p_1^{Rabi} [Fig. 6.23(a,d)] show that the quality of the Rabi experiment is quite high inside the whole interval we considered. Indeed, p_1^{Rabi} displays a negligible dependence on the parameter x_0, and the rotation angle is very close to π for every x_0 at $T = T_{Rabi}$ (black dashed line). The periodicity of p_1^{Rabi} with respect to T is also reflected in the Fisher information [Fig. 6.23(b,d)], which shows local maxima whenever $\bar{\omega}_X^R T \approx (2n+1)\pi$. However, we focus only on the case for $n = 0$, since it better satisfies the condition $T \ll T_2^*$, for which we can neglect decoherence effects during the pulse. Panels (c,f) in Fig. 6.23 thus show sections of the Fisher information close to the rotation angle $\bar{\omega}_X^R T \approx \pi$ (i.e. close

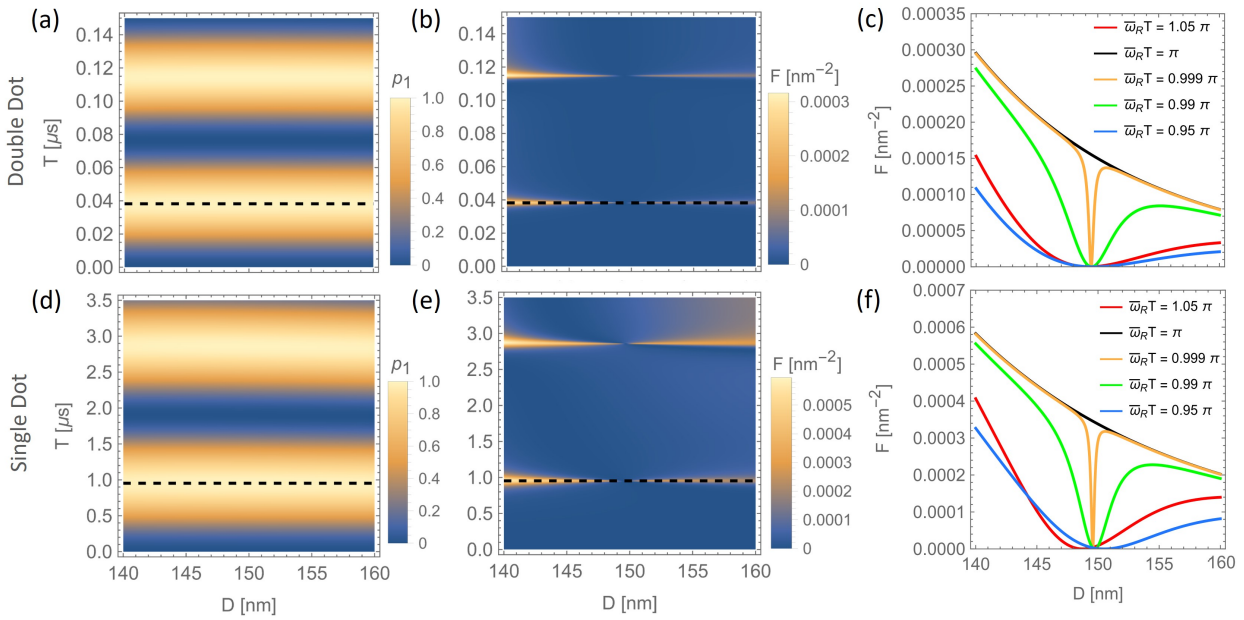


Figure 6.23: Color plots, related to the Rabi measurement, of the probability p_1^{Rabi} [panels (a), (d)] and of the Fisher information $\mathcal{F}_{Rabi}$ [panels (b), (e)] for a Si DQD with half-distance $a = 12$ nm (top row) and a SQD (bottom row), as functions of the charge position x_0 and the pulse duration T. The dashed black line in panels (a,b,d,e) shows the values of T_{Rabi} for both systems, as defined in Eq. (6.59). Panels (c) and (f) show the profile of $\mathcal{F}_{Rabi}$ as a function of x_0 for selected values of T close to T_{Rabi}, respectively for the DQD and the SQD.

to $T \approx T_{Rabi}$). Generally, $\mathcal{F}^{Rabi}$ decreases as x_0 increases. However, we see that a discrepancy as small as 5% with respect to $\bar{\omega}_X^R T = \pi$ in either direction causes the Fisher information to decrease significantly close to resonance. Additionally, all curves with $\bar{\omega}_X^R T \neq \pi$ maintain a downward peak at resonance which narrows as the angle approaches π. For the exact case of $\bar{\omega}_X^R T = \pi$ (i.e. $T = T_{Rabi}$) instead, the Fisher information is not defined under the condition of exact resonance. Indeed, the limit of $\mathcal{F}_{Rabi}$ for $\Delta \to 0$,

$$\lim_{\Delta \to 0} \mathcal{F}^{Rabi} = T^2 (\partial_\lambda \omega_X^R)^2 \,, \tag{6.60}$$

is generally different from the one obtained in other directions. Specifically, if we perform a limit on Eq. (6.41) for both $\Delta \to 0$ and $T \to T_{Rabi}$ at the same time, we get an undetermined form of the kind $0/0$. Luckily, this is a zero-dimensional locus of points, and does not affect the validity of the formula for the Fisher information of the Rabi measurement overall.

The behavior of the Fisher information can be loosely explained as follows. During the Rabi experiment that we described, we expect to observe a rotation angle of $\bar{\omega}_X^R T$, something which is only true at resonance. Thus, for $\Delta = 0$, an expected angle close to π brings the qubit near the south pole of the Bloch sphere, and almost every measurement results in outcome 1. If $\Delta \approx 0$, the probability of obtaining 1 is still very close to the unity, so a large number of measurements is needed in order to recognize that we are not at resonance. The Fisher information is consequently small, and we observe the downward peaks in Fig. 6.23(c,f). Only when we get further away from the resonance condition, the outcome statistics will have varied enough to require a smaller num-

ber of measurements. Thus, the Fisher information will be higher. The closer we are to a perfect π angle [e.g. the yellow line in Fig. 6.23(e,f)], the more outcomes 1 we will expect at resonance, and the sooner it becomes clear if $\Delta \neq 0$. Consequently, the peak narrows and the Fisher information tends to the limit curve for $\bar{\omega}_X^R T = \pi$ [black line in Fig. 6.23(e,f)]. The general decrease with x_0 of the Fisher information outside the peaks comes from the higher and higher difficulty in distinguishing the exact value of x_0 out of resonance. Indeed, for higher x_0 the variation of both ω_L and ω_X^R decreases, and the evolution of the qubit is less affected by small variations of x_0.

The comparison between the SQD and DQD cases does not show any advantage in terms of the magnitude of the Fisher information. Indeed, in both cases $\mathcal{F}^{Rabi}$ stays of the order of $10^{-4}\,\mathrm{nm}^{-2}$ or lower, similarly to the QFI we found for the ground state (see Sec. 6.2.3). However, as we said before, the DQD presents a much higher $\bar{\omega}_X^R$. Consequently, as can be seen from the time scale of the graphs, the DQD has the advantage of a much smaller manipulation time T that is necessary to observe the characteristic Rabi oscillations for both p_1^{Rabi} and $\mathcal{F}^{Rabi}$.

Estimation with Ramsey experiment

Figure 6.24 then shows the results for the Ramsey scheme. All the results were obtained by fixing the pulse duration time to $T_{Ramsey} = T_{Rabi}/2$. The presence of decoherence processes was taken into account by considering the expressions in Eq. (6.55) and (6.58) with lifetime $T_2^* = 2.5\,\mu$s. This quantity approximately corresponds to the calculated dephasing time due to hyperfine interactions for a hole-spin qubit in Si [182, 254]. The graphs are strikingly different from those in the Rabi case. Indeed, the typical Ramsey fringes [275] that can be observed in Fig. 6.24(a) for a DQD now show a non-negligible dependence on the parameter x_0. This aspect is reflected in the Fisher information as well [Fig. 6.24(b)]. Indeed, $\mathcal{F}^{Ramsey}$ oscillates both as a function of τ and x_0, as can be clearly seen by the sections plotted in Fig. 6.24(c) at different waiting times τ. Here we see that the periodicity increases with τ, because the sensitivity of the accumulated phase on the exact value of ω_L (and thus of x_0) increases with its value. Without decoherence, the peaks would also increase indefinitely. However, as we said in Sec. 4.1.2 and as shown in Fig. 6.25(a-d), the decoherence causes the probability p_1 to decay to $1/2$ for $\tau \gg T_2^*$. Consequently, p_1 presents lower and lower contrast as τ increases (or T_2^* decreases), and the Fisher information [Fig. 6.25(e-h)] decays to zero.

The Fisher information in Fig. 6.25(e-h) also shows a qualitative change between the cases with and without decoherence. Indeed, $\mathcal{F}^{Ramsey}$ without decoherence [Fig. 6.25(e)] is smooth, and increases monotonically towards the upper left of the graph, i.e. for higher τ and lower x_0. Instead, the addition of decoherence processes induces the oscillations previously described, and causes the Fisher information to fall to zero at precise values, and more importantly at resonance. The oscillations become more and more prominent as T_2^* decreases. By looking at the shape of Eqs. (6.47) and (6.58), we understand that this change in behavior is caused by the additional oscillating factor

$$4X^2A^2 = 4X^2\left[\cos\left(\frac{1}{2}\tau\Delta\right)\sin\left(T\Omega\right) - Y\sin\left(\frac{1}{2}\tau\Delta\right)\left(1-\cos\left(T\Omega\right)\right)\right]^2, \tag{6.61}$$

which simplifies when $T_2^* \to \infty$ and $e^{2(\tau/T_2^*)^2} - 1 \to 0$. Since realistic systems will always present finite decoherence lifetimes T_2^*, the Fisher information will always show this oscillatory behaviour.

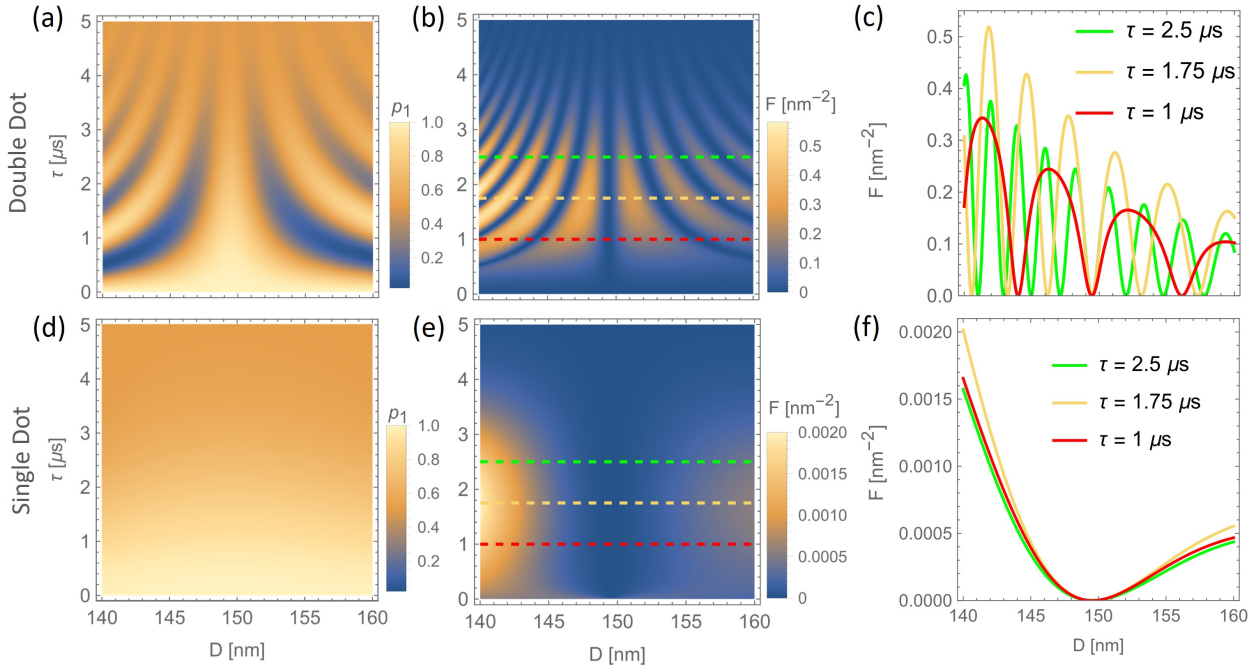


Figure 6.24: Color plots, related to the Ramsey measurement, of the probability p_1^{Ramsey} [panels (a), (d)] and of the Fisher Information $\mathcal{F}_{Ramsey}$ [panels (b), (e)] for a Si DQD with half-distance $a = 12$ nm (top row) and a SQD (bottom row), as functions of the charge coordinate x_0 and the waiting time τ. All results take account of decoherence, with decay lifetime $T_2^* = 2.5\,\mu$s. The pulse duration is fixed for all cases at $T = T_{Ramsey}$, as defined in the text. The dashed lines in panels (b,e) correspond to fixed values of $\tau = 1\,\mu$s (red line), $\tau = 1.75\,\mu$s (yellow line) and $2.5\,\mu$s (green line). Panels (c) and (f) show the profile of $\mathcal{F}_{Ramsey}$ as a function of x_0 for the selected values of τ, respectively for the DQD and the SQD.

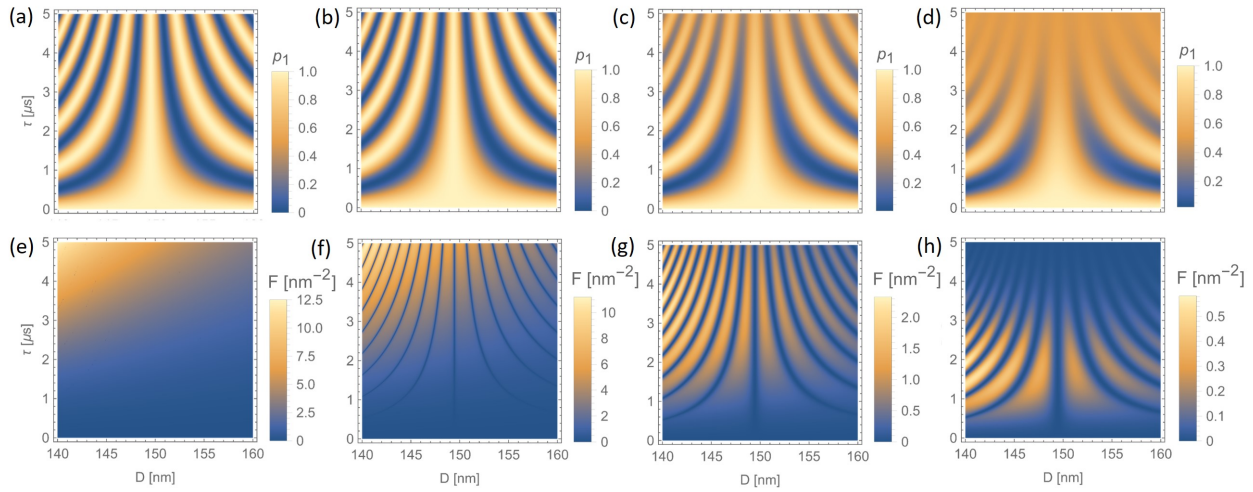


Figure 6.25: Occupation probability p_1^{Ramsey} (top row) and corresponding Fisher information $\mathcal{F}_{Ramsey}$ (bottom row) as a function of x_0 and τ, in the absence of decoherence (a,e) and for T_2^* equal to 25 (b,f), 5 (c,g), and $2.5\,\mu$s (d,h). All the calculations refer to a Si DQD with half-distance $a = 12$ nm.

The graphs for the SQD [Fig. 6.24(d-f)] do not show the same features as clearly as the DQD. The reason for this comes from the weaker dependence of ω_L on x_0, which consequently causes a smaller detuning Δ with respect to the pulse frequency. Thus, we do not observe the same Ramsey fringes in p_1^{Ramsey} that the DQD shows in the chosen interval, and similarly the Fisher information is smoother. If we were to choose a larger interval to simulate, we would observe similar oscillations for the SQD as well, just with a smaller frequency with respect to the DQD.

Finally, we can focus on the magnitude of the Fisher information in the Ramsey experiment. As seen in Fig. 6.25(e-h), this is another factor that depends on T_2^*: the smaller T_2^*, the sooner $\mathcal{F}_{Ramsey}$ starts decaying to zero and the smaller said maximum will be. That said, even with the smallest considered value of $T_2^* = 2.5\,\mu$s, the Fisher information remains several orders of magnitude larger than the one found for a Rabi measurement [seen by comparing Figs. 6.23(b,e) and Fig. 6.24(b,e)]. Specifically, $\mathcal{F}_{Ramsey}$ is approximately 10 times larger than $\mathcal{F}^{Rabi}$ for a SQD, while it is more than 10^3 times larger for a DQD. To understand where the advantage comes from, we can study approximations of Eqs. (6.41) and (6.58) and compare the resulting expressions. More specifically, the numerical values reported in Table 6.1 show that the most reasonable approach is to impose $\Omega T_{Rabi}/2 = \Omega T_{Ramsey} \approx \pi/2$. In this way, the Fisher information of a Rabi experiment corresponding to pulse duration $T = T^{Rabi}$ becomes:

$$\mathcal{F}^{Rabi} \approx \frac{4(\omega_X^R)^2(\partial_\lambda \omega_L)^2}{\Omega^4}\,, \tag{6.62}$$

where we also used that $\omega_X^R \partial_\lambda \omega_L \gg \Delta \partial_\lambda \omega_X^R$, which is true in the whole interval we considered. Then, the Fisher information of a Ramsey experiment with pulse duration $T = T^{Ramsey}$ is:

$$\mathcal{F}^{Ramsey} \approx C\frac{4(\omega_X^R)^2(\partial_\lambda \omega_L)^2}{\Omega^4}(\omega_X^R \tau)^2\,, \tag{6.63}$$

where we also considered $|\partial_\lambda \omega_L \tau| \gg |\partial_\lambda X|, |\partial_\lambda Y|$. In Eq. (6.63) we defined

$$C = \frac{\left[\cos\left(\frac{\Delta\tau}{2}\right) - \sin\left(\frac{\Delta\tau}{2}\right) Y\right]^2 \left[\cos\left(\frac{\Delta\tau}{2}\right) Y + \sin\left(\frac{\Delta\tau}{2}\right)\right]^2}{e^{2\left(\tau/T_2^*\right)^2} - \left\{1 - 2X^2\left[\cos\left(\frac{\Delta\tau}{2}\right) - \sin\left(\frac{\Delta\tau}{2}\right) Y\right]^2\right\}^2}\,. \tag{6.64}$$

In total, Eq. (6.63) has three terms. The first one [expanded in Eq. (6.64)] oscillates with $\Delta\tau$, and remains limited in the whole simulated interval, as shown in Fig. 6.26(a). This is the term that includes the Gaussian decay, and as such it is the cause for which the Fisher information decays for $\tau \gg T_2^*$. The second term coincides with the approximated expression of $\mathcal{F}^{Rabi}$ in Eq. (6.62), while the third term increases quadratically with τ. Since we know $\omega_X^R T_{Ramsey} \approx \pi/2$, whenever $T_{Ramsey} \ll \tau \ll T_2^*$ the factor $(\omega_X^R \tau)$ becomes very large while C has not decayed to zero yet. Consequently, the maximal values of $\mathcal{F}^{Ramsey}$ are higher than those of $\mathcal{F}^{Rabi}$. Unexpectedly, Eq. (6.63) also tells us that the discriminating factor determining the magnitude of $\mathcal{F}^{Ramsey}$ is the Rabi frequency ω_X^R, rather than the Larmor frequency that drives the free evolution of the qubit. As the DQD allows to observe values of ω_X^R an order of magnitude larger than the SQD (see Table 6.1), this explains the factor of ~ 100 between the $\mathcal{F}^{Ramsey}$ in Fig. 6.24(b,e).

In view of all previous considerations, the best strategy for quantum parameter estimation, among those we considered, is a dynamic Ramsey measurement inside a DQD. The dynamic approach on a manipulated state, rather than the static one on the hole ground state, allows the

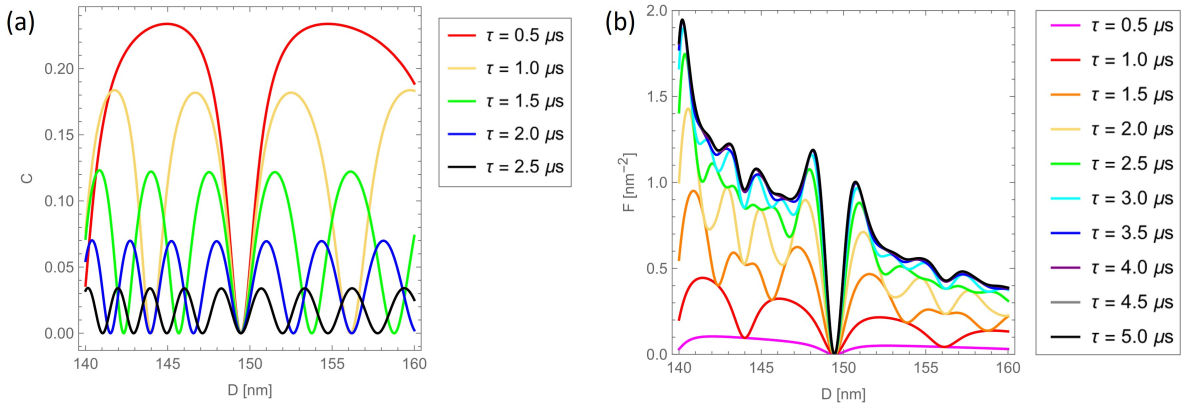


Figure 6.26: (a) Factor C expressed in Eq. (6.64) for different values of the free evolution time τ. (b) Fisher information for subsequent Ramsey measurements performed with different τ's. Each curve is the sum of the contribution to the Fisher information at time τ plus all the previously plotted contributions. All results are reported for a Si DQD with $a = 12\,\text{nm}$, in presence of decoherence with lifetime $T_2^* = 2.5\,\mu\text{s}$.

exploitation of dynamical quantities such as ω_L and ω_X^R, as well as their derivatives. The Ramsey measurement introduces an additional sensitivity to the phase acquired by the qubit during a free evolution of duration τ, and is thus more efficient than the Rabi measurement. Finally, the DQD presents a stronger dependence of the characteristic quantities ω_L and ω_X^R on the parameter x_0 that we want to estimate. Consequently, it provides larger values of the Fisher information. The only problem of $\mathcal{F}^{Ramsey}$ inside a DQD is its frequent oscillations as a function of x_0. Indeed, at fixed τ there are always values of x_0 that correspond to a small Fisher information, and that are consequently difficult to estimate. At the same time, though, values of x_0 that correspond to a small $\mathcal{F}^{Ramsey}$ at a certain τ may correspond to peaks of $\mathcal{F}^{Ramsey}$ at another time τ', as can be inferred by comparing the different curves in Fig. 6.24(c). Consequently, the problem can be bypassed by performing many sets of measurements at different τ's.

The total Fisher information from subsequent measurements is the sum of the Fisher information of each experiment. For example, we considered $n = 10$ equally distant values of τ in the interval $[0.5, 2T_2^*]$ and summed the curves of the Fisher information from all the contributing terms. The resulting curve, shown in black in Fig. 6.26(b), is much smoother than all of its contributions, and reaches values of $\mathcal{F}^{Ramsey}$ of the order of the unity in the whole interval. Such a procedure increases the total number of measurements by a factor of n, since each experiment needs to be repeated n times. However, it is able to maintain a stable precision on every value of x_0 in the studied interval, unless it is exactly at resonance, in which case every contribution is identically zero.

Moving of th' earth brings harms and fears,
Men reckon what it did, and meant;
But trepidation of the spheres,
Though greater far, is innocent.

$\sim$ from *A Valediction: Forbidding Mourning*,
by John Donne

Chapter 7

Characterization of single-hole excited states to enhance qubit manipulation

In this Chapter we study the manipulation of a hole state beyond the 2-dimensional Hilbert space of the qubit. We start in Sec. 7.1 with the generalization of the qubit to a higher dimensionality d. In Sec. 7.1.1 we describe the general SU(d) algebra, while in Sec. 7.1.2 we extend the treatment for the time evolution of a qubit to the case for $d = 4$. Then, in Sec. 7.2 we characterize the first four hole levels in a SQD, by reporting the main characteristic quantities as a function of the degree of anisotropy of the SQD. Specifically, in Sec. 7.2.1 we investigate the behavior of the energy splittings and intra- and inter-doublet couplings. Then, in Sec. 7.2.2 we relate such properties to the degree of band vs. orbital excitations of the hole states. Finally, in Sec. 7.2.3 we compare the obtained results with those for a DQD.

Unless specified otherwise, we simulated a system with parameters $V_{bo} = 4\,\text{eV}$ as the band offset, $B = 1\,\text{T}$ as the intensity of the magnetic field, $E_z = 50\,\text{mV/nm}$ as the constant out-of-plane electric field and $\delta E_z = 1\,\text{mV/nm}$ as the driving amplitude.

7.1 Generalization to higher dimensionality

Just like we were able to identify the states $|0\rangle$ and $|1\rangle$ which defined the basis of a 2-dimensional Hilbert space for the qubit, we can extend the same definition to any dimensionality d. In this case we talk about *qudits*, which can be modeled within a d-dimensional Hilbert space with a basis made up of the first d hole states, $\{|0\rangle, |1\rangle, \ldots, |d-1\rangle\}$. Specifically, we choose to focus on the case $d = 4$, i.e. a *ququart*, corresponding to the first two Kramers doublets of the hole system. This situation is more convenient than $d = 3$, since the latter would necessitate isolating the treatment of one of the two states of the first-excited doublet from its time-reversal conjugate.

7.1.1 SU(d) algebra

The same description of the SU(2) algebra reported in Sec. 5.4.1 can be straightforwardly extended to d dimensions. Specifically, now the qudit state can be represented on a d-dimensional hypersphere in a $(d+1)$-dimensional space, and the operations acting on the qudit state can be led back to the SU(d) algebra. Its generators $\hat{\lambda}_n$ are the generalization of the Pauli matrices from Eq. (5.135), called generalized Gell-Mann matrices [276, 277]. By calling the d-dimensional elementary

matrices $\{\hat{e}_j^k | j,k = 0,\dots d-1\}$, with only one non-zero element equal to one:

$$(e_j^k)_{l,m} = \delta_{j,m}\delta_{k,l}\,, \quad 0 \leq l,m \leq d-1\,, \tag{7.1}$$

the d^2-1 generalized Gell-Mann matrices are defined as:

$$\begin{cases} \hat{\lambda}_{j^2+2k} = e_j^k + e_k^j & 0 \leq k < j \leq d-1\,, \\ \hat{\lambda}_{j^2+2k+1} = -i(e_j^k - e_k^j) & 0 \leq k < j \leq d-1\,, \\ \hat{\lambda}_{j^2+2j} = \sqrt{\frac{2}{j(j+1)}}\left(-\sum_{k=0}^{j-1} e_k^k + j e_j^j\right) & 1 \leq j \leq d-1\,. \end{cases} \tag{7.2}$$

Just like the Pauli matrices, these are (i) traceless, (ii) Hermitian, and (iii) obey the following commutation relation:

$$[\hat{\lambda}_j, \hat{\lambda}_k] = 2i\sum_k f_{jkl}\hat{\lambda}_l\,, \tag{7.3}$$

where f_{jkl} is the d-dimensional Levi-Civita symbol, whose elements are defined by

$$4i f_{jkl} = Tr\{\hat{\lambda}_l[\hat{\lambda}_j, \hat{\lambda}_k]\}\,. \tag{7.4}$$

Just like the Levi-Civita symbol in 3 dimensions, f_{jkl} is real and totally antisymmetric. It's immediate to see how for, $d = 2$, one retrieves the definition and properties of the Pauli matrices from Eq. 5.135, with $\hat{\lambda}_n \equiv \hat{\sigma}_n$ for $n = 1,2,3$. Instead, for $d = 4$, one gets:

$$\hat{\lambda}_1 = \begin{pmatrix} 0&0&0&0\\0&0&0&0\\0&0&0&1\\0&0&1&0 \end{pmatrix}, \hat{\lambda}_2 = \begin{pmatrix} 0&0&0&0\\0&0&0&0\\0&0&0&-i\\0&0&i&0 \end{pmatrix}, \hat{\lambda}_3 = \begin{pmatrix} 0&0&0&0\\0&0&0&0\\0&0&1&0\\0&0&0&-1 \end{pmatrix},$$

$$\hat{\lambda}_4 = \begin{pmatrix} 0&0&0&0\\0&0&0&1\\0&0&0&0\\0&1&0&0 \end{pmatrix}, \hat{\lambda}_5 = \begin{pmatrix} 0&0&0&0\\0&0&0&-i\\0&0&0&0\\0&i&0&0 \end{pmatrix}, \hat{\lambda}_6 = \begin{pmatrix} 0&0&0&0\\0&0&1&0\\0&1&0&0\\0&0&0&0 \end{pmatrix}, \hat{\lambda}_7 = \begin{pmatrix} 0&0&0&0\\0&0&-i&0\\0&i&0&0\\0&0&0&0 \end{pmatrix}, \hat{\lambda}_8 = \frac{1}{\sqrt{3}}\begin{pmatrix} 0&0&0&0\\0&2&0&0\\0&0&-1&0\\0&0&0&-1 \end{pmatrix},$$

$$\hat{\lambda}_9 = \begin{pmatrix} 0&0&0&1\\0&0&0&0\\0&0&0&0\\1&0&0&0 \end{pmatrix}, \hat{\lambda}_{10} = \begin{pmatrix} 0&0&0&-i\\0&0&0&0\\0&0&0&0\\i&0&0&0 \end{pmatrix}, \hat{\lambda}_{11} = \begin{pmatrix} 0&0&1&0\\0&0&0&0\\1&0&0&0\\0&0&0&0 \end{pmatrix}, \hat{\lambda}_{12} = \begin{pmatrix} 0&0&-i&0\\0&0&0&0\\i&0&0&0\\0&0&0&0 \end{pmatrix},$$

$$\hat{\lambda}_{13} = \begin{pmatrix} 0&1&0&0\\1&0&0&0\\0&0&0&0\\0&0&0&0 \end{pmatrix}, \hat{\lambda}_{14} = \begin{pmatrix} 0&-i&0&0\\i&0&0&0\\0&0&0&0\\0&0&0&0 \end{pmatrix}, \hat{\lambda}_{15} = \frac{1}{\sqrt{6}}\begin{pmatrix} 3&0&0&0\\0&-1&0&0\\0&0&-1&0\\0&0&0&-1 \end{pmatrix}. \tag{7.5}$$

Additionally, the terms f_{jkl} for $d = 4$ are reported in Table 7.1. Along with the 4-dimensional identity $\hat{\mathbb{1}}^{(4)} \equiv \hat{\lambda}_0$, the matrices in Eq. (7.5) form the basis of the operation space. Note that in our 4-dimensional system one can identify a total of six separate SU(2) sub-algebras, corresponding to rotations between each pair of levels, and whose generators can be obtained through a linear combination of the Gell-Mann matrices:

$$1 \leftrightarrow 0 : \{\hat{\lambda}_1, \hat{\lambda}_2, \hat{\lambda}_3\}\,, \quad 2 \leftrightarrow 0 : \left\{\hat{\lambda}_4, \hat{\lambda}_5, \left(\hat{\lambda}_3 + \sqrt{3}\hat{\lambda}_8\right)/2\right\}, \quad 2 \leftrightarrow 1 : \left\{\hat{\lambda}_6, \hat{\lambda}_7, \left(-\hat{\lambda}_3 + \sqrt{3}\hat{\lambda}_8\right)/2\right\},$$

$$3 \leftrightarrow 0 : \left\{\hat{\lambda}_9, \hat{\lambda}_{10}, \left(\frac{3}{2}\hat{\lambda}_3 + \frac{\sqrt{3}}{2}\hat{\lambda}_8 + \sqrt{6}\hat{\lambda}_{15}\right)/3\right\}, \quad 3 \leftrightarrow 1 : \left\{\hat{\lambda}_{11}, \hat{\lambda}_{12}, \left(-\frac{3}{2}\hat{\lambda}_3 + \frac{\sqrt{3}}{2}\hat{\lambda}_8 + \sqrt{6}\hat{\lambda}_{15}\right)/3\right\},$$

$$3 \leftrightarrow 2 : \left\{\hat{\lambda}_{13}, \hat{\lambda}_{14}, \left(-\sqrt{3}\hat{\lambda}_8 + \sqrt{6}\hat{\lambda}_{15}\right)/3\right\}. \tag{7.6}$$

jkl	f_{jkl}	jkl	f_{jkl}	jkl	f_{jkl}	jkl	f_{jkl}	jkl	f_{jkl}
$(1,2,3)$	1	$(2,5,7)$	$-\frac{1}{2}$	$(3,11,12)$	$-\frac{1}{2}$	$(6,7,8)$	$\frac{\sqrt{3}}{2}$	$(8,11,12)$	$\frac{\sqrt{3}}{6}$
$(1,4,7)$	$-\frac{1}{2}$	$(2,9,11)$	$-\frac{1}{2}$	$(4,5,8)$	$\frac{\sqrt{3}}{2}$	$(6,11,14)$	$-\frac{1}{2}$	$(8,13,14)$	$-\frac{\sqrt{3}}{3}$
$(1,5,6)$	$\frac{1}{2}$	$(2,10,12)$	$-\frac{1}{2}$	$(4,9,14)$	$-\frac{1}{2}$	$(6,12,13)$	$\frac{1}{2}$	$(9,10,15)$	$\frac{\sqrt{6}}{3}$
$(1,9,12)$	$-\frac{1}{2}$	$(3,4,5)$	$\frac{1}{2}$	$(4,10,13)$	$\frac{1}{2}$	$(7,11,13)$	$-\frac{1}{2}$	$(11,12,15)$	$\frac{\sqrt{6}}{3}$
$(1,10,11)$	$\frac{1}{2}$	$(3,6,7)$	$-\frac{1}{2}$	$(5,9,13)$	$-\frac{1}{2}$	$(7,12,14)$	$-\frac{1}{2}$	$(13,14,15)$	$\frac{\sqrt{6}}{3}$
$(2,4,6)$	$-\frac{1}{2}$	$(3,9,10)$	$\frac{1}{2}$	$(5,10,14)$	$-\frac{1}{2}$	$(8,9,10)$	$\frac{\sqrt{3}}{6}$		

Table 7.1: Nonzero values of the generalized Levi-Civita symbol f_{jkl} as obtained from Eq. (7.4), for $d = 4$. All odd permutations of the three indices change the sign of f_{jkl}.

At this point, recalling what we said for $d = 2$, we can also write a general operator acting on the ququart as a linear combination of the Gell-Mann matrices:

$$\hat{O}^{(4)} = \sum_{n=0}^{15} \hbar \Omega_n^R \hat{\lambda}_n \,. \tag{7.7}$$

As before, the coefficients of the combination in Eq. (7.7) are directly related to the system's Rabi frequencies. More specifically, those corresponding to non-diagonal Gell-Mann matrices can be identified as either the X or Y Rabi frequency of the respective SU(2) sub-algebra they belong to:

$$\begin{aligned} &\Omega_1^R \equiv \omega_X^{1\leftrightarrow 0},\ \Omega_2^R \equiv \omega_Y^{1\leftrightarrow 0},\ \Omega_4^R \equiv \omega_X^{2\leftrightarrow 0},\ \Omega_5^R \equiv \omega_Y^{2\leftrightarrow 0},\ \Omega_6^R \equiv \omega_X^{2\leftrightarrow 1},\ \Omega_7^R \equiv \omega_Y^{2\leftrightarrow 1}, \\ &\Omega_9^R \equiv \omega_X^{3\leftrightarrow 0},\ \Omega_{10}^R \equiv \omega_Y^{3\leftrightarrow 0},\ \Omega_{11}^R \equiv \omega_X^{3\leftrightarrow 1},\ \Omega_{12}^R \equiv \omega_Y^{3\leftrightarrow 1},\ \Omega_{13}^R \equiv \omega_X^{3\leftrightarrow 2},\ \Omega_{14}^R \equiv \omega_Y^{3\leftrightarrow 2}\,, \end{aligned} \tag{7.8}$$

and as such are related to the matrix elements of $\hat{O}$ in the same way as illustrated in Eq. (5.140). As for the diagonal Gell-Mann matrices, i.e. $\hat{\lambda}_3$, $\hat{\lambda}_8$, $\hat{\lambda}_{15}$ and $\hat{\lambda}_0 \equiv \hat{\mathbb{1}}$, we have:

$$\Omega_3^R = \frac{1}{2\hbar}\left[O_{11}^{(4)} - O_{00}^{(4)}\right], \tag{7.9}$$

$$\Omega_8^R = \frac{\sqrt{3}}{3\hbar}\left[O_{22}^{(4)} - \frac{O_{11}^{(4)} + O_{00}^{(4)}}{3}\right], \tag{7.10}$$

$$\Omega_{15}^R = \frac{\sqrt{6}}{4\hbar}\left[O_{33}^{(4)} - \frac{O_{22}^{(4)} + O_{11}^{(4)} + O_{00}^{(4)}}{2}\right], \tag{7.11}$$

$$\Omega_0^R = \frac{O_{33}^{(4)} + O_{22}^{(4)} + O_{11}^{(4)} + O_{00}^{(4)}}{4}, \tag{7.12}$$

which correspond to the angular frequencies with which state $j > 1$ rotates with respect to the ensemble of states with $k < j$. These last frequencies are related to the Z and $\hat{\mathbb{1}}$ Rabi frequencies of the six sub-algebras from Eq. (7.6), but the relation is not univocal. Indeed, of the 12 Rabi frequencies $\hbar\omega_{\hat{\mathbb{1}}}^{j\leftrightarrow k}$ and $\hbar\omega_Z^{j\leftrightarrow k}$, only 4 are independent, and the others can be obtained through their combination. For example:

$$\begin{aligned} &\hbar\omega_Z^{2\leftrightarrow 1} = \hbar(\omega_Z^{2\leftrightarrow 0} - \omega_Z^{1\leftrightarrow 0})\,, \quad \hbar\omega_Z^{3\leftrightarrow 1} = \hbar(\omega_Z^{3\leftrightarrow 0} - \omega_Z^{1\leftrightarrow 0})\,, \quad \hbar\omega_Z^{3\leftrightarrow 2} = \hbar(\omega_Z^{3\leftrightarrow 0} - \omega_Z^{2\leftrightarrow 0})\,, \\ &\hbar\omega_{\hat{\mathbb{1}}}^{2\leftrightarrow 1} = \hbar(\omega_Z^{2\leftrightarrow 0} + \omega_{\hat{\mathbb{1}}}^{1\leftrightarrow 0})\,, \quad \hbar\omega_{\hat{\mathbb{1}}}^{3\leftrightarrow 1} = \hbar(\omega_Z^{3\leftrightarrow 0} + \omega_{\hat{\mathbb{1}}}^{1\leftrightarrow 0})\,, \quad \hbar\omega_{\hat{\mathbb{1}}}^{3\leftrightarrow 2} = \hbar(\omega_Z^{3\leftrightarrow 0} - \omega_Z^{2\leftrightarrow 0} - \omega_Z^{1\leftrightarrow 0} + \omega_{\hat{\mathbb{1}}}^{1\leftrightarrow 0})\,, \\ &\hbar\omega_{\hat{\mathbb{1}}}^{2\leftrightarrow 0} = \hbar(\omega_Z^{2\leftrightarrow 0} - \omega_Z^{1\leftrightarrow 0} + \omega_{\hat{\mathbb{1}}}^{1\leftrightarrow 0})\,, \quad \hbar\omega_{\hat{\mathbb{1}}}^{3\leftrightarrow 0} = \hbar(\omega_Z^{3\leftrightarrow 0} - \omega_Z^{1\leftrightarrow 0} + \omega_{\hat{\mathbb{1}}}^{1\leftrightarrow 0})\,. \end{aligned} \tag{7.13}$$

Overall, we can use the Rabi frequencies describing the six sub-algebras to write the operator $\hat{O}^{(4)}$ in an alternative way:

$$\hat{O}^{(4)} = \hbar\left(\omega_{\hat{\mathbb{1}}}^{1\leftrightarrow 0} - \omega_Z^{1\leftrightarrow 0}\right)\hat{\mathbb{1}} + \hbar\begin{pmatrix} 2\omega_Z^{3\leftrightarrow 0} & \omega_X^{3\leftrightarrow 2} - i\omega_X^{3\leftrightarrow 2} & \omega_X^{3\leftrightarrow 1} - i\omega_X^{3\leftrightarrow 1} & \omega_X^{3\leftrightarrow 0} - i\omega_X^{3\leftrightarrow 0} \\ \omega_X^{3\leftrightarrow 2} + i\omega_X^{3\leftrightarrow 2} & 2\omega_Z^{2\leftrightarrow 0} & \omega_X^{2\leftrightarrow 1} - i\omega_X^{2\leftrightarrow 1} & \omega_X^{2\leftrightarrow 0} - i\omega_X^{2\leftrightarrow 0} \\ \omega_X^{3\leftrightarrow 1} + i\omega_X^{3\leftrightarrow 1} & \omega_X^{2\leftrightarrow 1} + i\omega_X^{2\leftrightarrow 1} & 2\omega_Z^{1\leftrightarrow 0} & \omega_X^{1\leftrightarrow 0} - i\omega_X^{1\leftrightarrow 0} \\ \omega_X^{3\leftrightarrow 0} + i\omega_X^{3\leftrightarrow 0} & \omega_X^{2\leftrightarrow 0} - i\omega_X^{2\leftrightarrow 0} & \omega_X^{1\leftrightarrow 0} + i\omega_X^{1\leftrightarrow 0} & 0 \end{pmatrix}. \tag{7.14}$$

With respect to this, we underline that the SU(2) algebra of the qubit was gauge-independent, where the gauge corresponded to the global phase added to both the states of the 2-dimensional system. Instead, the six SU(2) sub-algebras for $d > 2$ are not gauge-independent, since a global phase added to two of the states of the qudit causes a relative phase with respect to the other levels. Therefore, we need to always consider the whole SU(d) algebra when performing operations on a qudit. Consequently, in the remaining part of this Section we will refer directly to the frequencies in Eq. (7.7). Indeed, these fix the rotation of each state with respect to all the others, since the Ω^R's refer to the generators of the total SU(4) algebra of the ququart.

7.1.2 Ququart evolution

We can now generalize our previous considerations on qubit evolution to $d = 4$. The generalization of the unperturbed Hamiltonian from Eq. (5.143) in terms of the 4-dimensional Gell-Mann matrices from Eq. (7.5) is:

$$\hat{H}_0 = \begin{pmatrix} e_3 & 0 & 0 & 0 \\ 0 & e_2 & 0 & 0 \\ 0 & 0 & e_1 & 0 \\ 0 & 0 & 0 & e_0 \end{pmatrix} = e_{avg}\hat{1} + \frac{\hbar\Omega_L^1}{2}\hat{\lambda}_3 + \frac{\hbar\Omega_L^2}{3}\sqrt{3}\hat{\lambda}_8 + \frac{\hbar\Omega_L^3}{4}\sqrt{6}\hat{\lambda}_{15}\,, \tag{7.15}$$

where $e_{avg} = (e_0 + e_1 + e_2 + e_3)/4$ is the average energy of the system, and new Larmor frequencies are defined as:

$$\hbar\Omega_L^1 \equiv e_1 - e_0\,, \quad \hbar\Omega_L^2 \equiv e_2 - \frac{e_1 + e_0}{2}\,, \quad \hbar\Omega_L^3 \equiv e_3 - \frac{e_2 + e_1 + e_0}{3}\,. \tag{7.16}$$

Similarly to the Rabi frequencies defined in Eq. (7.9-7.12), these new Larmor frequencies describe rotations of each state $j > 1$ with respect to the ensemble $k < j$. We now see this clearly by integrating the Schrödinger equation in the Schrödinger picture, for which we get:

$$\begin{aligned} \psi_S(t) = e^{-i\hat{H}t/\hbar}\psi_S(0) &= \left(e^{-i\Omega_L^1\hat{\lambda}_3 t} + e^{-i\Omega_L^2\hat{\lambda}_8 t} + e^{-i\Omega_L^3\hat{\lambda}_{15}t}\right)\psi_S(0) = \\ &= \begin{pmatrix} e^{-i\frac{3}{4}\Omega_L^3 t}c_3(0) \\ e^{\frac{i}{4}\Omega_L^3 t}c_2(0) \\ e^{\frac{i}{4}\Omega_L^3 t}c_1(0) \\ e^{\frac{i}{4}\Omega_L^3 t}c_0(0) \end{pmatrix} + \begin{pmatrix} 0 \\ e^{-i\frac{2}{3}\Omega_L^2 t}c_2(0) \\ e^{\frac{i}{3}\Omega_L^2 t}c_1(0) \\ e^{\frac{i}{3}\Omega_L^2 t}c_0(0) \end{pmatrix} + \begin{pmatrix} 0 \\ 0 \\ e^{-\frac{i}{2}\Omega_L^1 t}c_1(0) \\ e^{\frac{i}{2}\Omega_L^1 t}c_0(0) \end{pmatrix}, \end{aligned} \tag{7.17}$$

where we fixed $E_{avg} = 0$ without loss of generality, since its value carries a global phase on all 4 states which has no physical importance. Notice that in Eq. (7.17) we factorized the exponential thanks to the fact that $\hat{\lambda}_3$, $\hat{\lambda}_8$ and $\hat{\lambda}_{15}$ all commute among themselves and with the identity.

Transitions induced by a driving field

Let's now take the same steps as in Sec. 5.4.2 to describe the evolution of the ququart under the action of a driving field $\hat{V}_{AC}(t)$. We recall the time-dependent Schrödinger equation for the evolution operator in the interaction picture:

$$i\hbar\partial_t\hat{U}_I(t,t_0) = e^{i\hat{H}_0 t/\hbar}\hat{V}_{AC}(t)e^{-i\hat{H}_0 t/\hbar}\hat{U}_I(t,t_0)\,. \tag{7.18}$$

We now choose the same pulse described in Eq. (5.154). This time, the amplitude of the perturbation must be written on the complete basis of d-dimensional Gell-Mann matrices generating the SU(4) algebra:

$$-\delta E_z\hat{z} = \sum_{n=0}^{15}\hbar\Omega_n^R\hat{\lambda}_n\,. \tag{7.19}$$

By replacing Eqs. (5.154) and (7.19) into Eq. (7.18) we get:

$$i\hbar\hat{U}_I(t,t_0) = F(t)\cos(\omega_P t)\sum_{n=0}^{15}\hbar\Omega_n^R\hat{\Lambda}_n\hat{U}_I(t,t_i)\,, \tag{7.20}$$

where we defined

$$\begin{aligned}\hat{\Lambda}_n \equiv& e^{i\hat{H}_0 t/\hbar}\hat{\lambda}_n e^{-i\hat{H}_0 t/\hbar} = \\ =& e^{i\Omega_L^1\hat{\lambda}_3 t/2}e^{i\Omega_L^2\sqrt{3}\hat{\lambda}_8 t/3}e^{i\Omega_L^3\sqrt{6}\hat{\lambda}_{15}t/4}\hat{\lambda}_n e^{-i\Omega_L^1\hat{\lambda}_3 t/2}e^{-i\Omega_L^2\sqrt{3}\hat{\lambda}_8 t/3}e^{-i\Omega_L^3\sqrt{6}\hat{\lambda}_{15}t/4}\,.\end{aligned} \tag{7.21}$$

We now evaluate each $\hat{\Lambda}_n$ explicitely, and consider the relations from Eq. 7.3. By doing so, we get:

$$\sum_{n=0}^{15}\Omega_n^R\hat{\Lambda}_n = \begin{pmatrix} \Omega_0^R+\sqrt{\frac{3}{2}}\Omega_{15}^R & (\omega_+^{3\leftrightarrow 2})^* e^{i\left(\Omega_L^3-\frac{2}{3}\Omega_L^2\right)t} & (\omega_+^{3\leftrightarrow 1})^* e^{i\left(\Omega_L^3+\frac{1}{3}\Omega_L^2-\frac{1}{2}\Omega_L^1\right)t} & (\omega_+^{3\leftrightarrow 0})^* e^{i\left(\Omega_L^3+\frac{1}{3}\Omega_L^2+\frac{1}{2}\Omega_L^1\right)t} \\ \omega_+^{3\leftrightarrow 2}e^{-i\left(\Omega_L^3-\frac{2}{3}\Omega_L^2\right)t} & \Omega_0^R+\frac{2}{\sqrt{3}}\Omega_8^R-\frac{1}{\sqrt{6}}\Omega_{15}^R & (\omega_+^{2\leftrightarrow 1})^* e^{i\left(\Omega_L^2-\frac{1}{2}\Omega_L^1\right)t} & (\omega_+^{2\leftrightarrow 0})^* e^{i\left(\Omega_L^2+\frac{1}{2}\Omega_L^1\right)t} \\ \omega_+^{3\leftrightarrow 1}e^{-i\left(\Omega_L^3+\frac{1}{3}\Omega_L^2-\frac{1}{2}\Omega_L^1\right)t} & \omega_+^{2\leftrightarrow 1}e^{-i\left(\Omega_L^2-\frac{1}{2}\Omega_L^1\right)t} & \Omega_0^R+\Omega_3^R-\frac{1}{\sqrt{3}}\Omega_8^R-\frac{1}{\sqrt{6}}\Omega_{15}^R & (\omega_+^{1\leftrightarrow 0})^* e^{i\Omega_L^1 t} \\ \omega_+^{3\leftrightarrow 0}e^{-i\left(\Omega_L^3+\frac{1}{3}\Omega_L^2+\frac{1}{2}\Omega_L^1\right)t} & \omega_+^{2\leftrightarrow 0}e^{-i\left(\Omega_L^2+\frac{1}{2}\Omega_L^1\right)t} & \omega_+^{1\leftrightarrow 0}e^{-i\Omega_L^1 t} & \Omega_0^R-\Omega_3^R-\frac{1}{\sqrt{3}}\Omega_8^R-\frac{1}{6}\Omega_{15}^R \end{pmatrix}, \tag{7.22}$$

in which we defined the complex frequencies

$$\omega_+^{j\leftrightarrow k} \equiv \omega_X^{j\leftrightarrow k} + i\omega_Y^{j\leftrightarrow k}\,, \quad 0\leq k<j\leq 3\,. \tag{7.23}$$

Notice that the off-diagonal elements (j,k) of the obtained matrix contain each an exponential with the energy difference between the states j and k, which allows us to define a Larmor frequency for each pair of states:

$$\begin{aligned} 1\leftrightarrow 0: \Omega_L^1 = \frac{(e_1-e_0)}{\hbar} \equiv \omega_L^{1\leftrightarrow 0}\,, \quad 2\leftrightarrow 0: \Omega_L^2+\frac{1}{2}\Omega_L^1 = \frac{(e_2-e_0)}{\hbar} \equiv \omega_L^{2\leftrightarrow 0} \\ 3\leftrightarrow 0: \Omega_L^3+\frac{1}{3}\Omega_L^2+\frac{1}{2}\Omega_L^1 = \frac{(e_3-e_0)}{\hbar} \equiv \omega_L^{2\leftrightarrow 0}\,, \quad 2\leftrightarrow 1: \Omega_L^2-\frac{1}{2}\Omega_L^1 = \frac{(e_2-e_1)}{\hbar} \equiv \omega_L^{2\leftrightarrow 1}\,, \\ 3\leftrightarrow 1: \Omega_L^3+\frac{1}{3}\Omega_L^2-\frac{1}{2}\Omega_L^1 = \frac{(e_3-e_1)}{\hbar} \equiv \omega_L^{3\leftrightarrow 1}\,, \quad 3\leftrightarrow 2: \Omega_L^3-\frac{2}{3}\Omega_L^2 = \frac{(e_3-e_2)}{\hbar} \equiv \omega_L^{3\leftrightarrow 2}\,, \end{aligned} \tag{7.24}$$

so that we can rewrite the same matrix in a more straightforward manner:

$$\sum_{n=0}^{15}\Omega_n^R\hat{\Lambda}_n = \begin{pmatrix} \Omega_0^R+\sqrt{\frac{3}{2}}\Omega_{15}^R & (\omega_+^{3\leftrightarrow 2})^* e^{i\omega_L^{3\leftrightarrow 2}t} & (\omega_+^{3\leftrightarrow 1})^* e^{i\omega_L^{3\leftrightarrow 1}t} & (\omega_+^{3\leftrightarrow 0})^* e^{i\omega_L^{3\leftrightarrow 0}t} \\ \omega_+^{3\leftrightarrow 2}e^{-i\omega_L^{3\leftrightarrow 2}t} & \Omega_0^R+\frac{2}{\sqrt{3}}\Omega_8^R-\frac{1}{\sqrt{6}}\Omega_{15}^R & (\omega_+^{2\leftrightarrow 1})^* e^{i\omega_L^{2\leftrightarrow 1}t} & (\omega_+^{2\leftrightarrow 0})^* e^{i\omega_L^{2\leftrightarrow 0}t} \\ \omega_+^{3\leftrightarrow 1}e^{-i\omega_L^{3\leftrightarrow 1}t} & \omega_+^{2\leftrightarrow 1}e^{-i\omega_L^{2\leftrightarrow 1}t} & \Omega_0^R+\Omega_3^R-\frac{1}{\sqrt{3}}\Omega_8^R-\frac{1}{\sqrt{6}}\Omega_{15}^R & (\omega_+^{1\leftrightarrow 0})^* e^{i\omega_L^{1\leftrightarrow 0}t} \\ \omega_+^{3\leftrightarrow 0}e^{-i\omega_L^{3\leftrightarrow 0}t} & \omega_+^{2\leftrightarrow 0}e^{-i\omega_L^{2\leftrightarrow 0}t} & \omega_+^{1\leftrightarrow 0}e^{-i\omega_L^{1\leftrightarrow 0}t} & \Omega_0^R-\Omega_3^R-\frac{1}{\sqrt{3}}\Omega_8^R-\frac{1}{6}\Omega_{15}^R \end{pmatrix}. \tag{7.25}$$

We once again consider the rectangular envelope function $F(t)$ from Eq. (5.162), so that the problem reduces to solving the following equation for $t > t_i$:

$$\partial_t \hat{U}_I(t, t_i) = -i \cos(\omega_P t) \sum_{n=0}^{15} \Omega_n^R \hat{\Lambda}_n \hat{U}_I(t, t_i) \,. \tag{7.26}$$

As before, this equation requires some manipulation and can only be solved through the RWA. Specifically, we now have many more oscillating frequencies to take into account. Indeed, for each of the Larmor frequencies $\omega_L^{j\leftrightarrow k}$ defined in Eq. (7.24), we have terms oscillating with frequencies $\omega_P - \omega_L^{j\leftrightarrow k} \equiv \Delta^{j\leftrightarrow k}$ and $\omega_P + \omega_L^{j\leftrightarrow k}$, while the diagonal terms all oscillate with frequency ω_P. In this case, the RWA neglects all terms but those oscillating with the lowest $\Delta^{j\leftrightarrow k}$'s. Specifically, we can set the pulse frequency to be in resonance with one transition at a time. If the corresponding Larmor frequency is different from the ones of all the other transitions, we can imagine that the evolution operator will act only on the two states participating in the considered transition, as all other $\Delta^{j\leftrightarrow k}$'s will be much higher. All transitions for which these conditions apply can be considered to be *isolated* from the others. For example, if we set $\omega_P \approx \omega_L^{1\leftrightarrow 0}$, the problem reduces to the one we studied previously for the qubit, and the evolution operator can be written as a block operator:

$$\hat{U}_{\mathrm{I}}(t, t_i) = \begin{pmatrix} 0_{2\times 2} & 0_{2\times 2} \\ 0_{2\times 2} & \hat{U}_{\mathrm{I}}^{\mathrm{qubit}}(t, t_i) \end{pmatrix} . \tag{7.27}$$

where the block on the bottom right is the evolution operator on the 2-dimensional space of a qubit. Similarly for all the other transitions. The situation is more complex when instead more than one transition has the same (or similar) Larmor frequency. In these cases, the transitions are not isolated and the evolution operator will present a more complicated form, coupling more than two states at the same time.

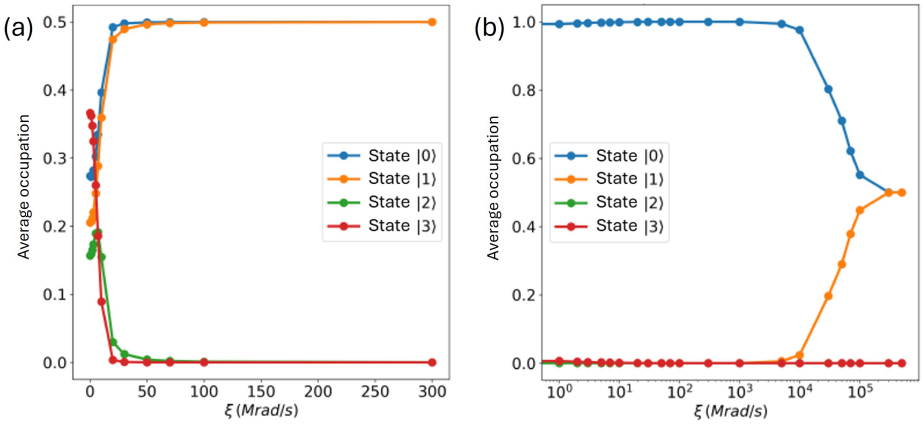


Figure 7.1: Average occupation of the first four hole states in a Si SQD characterized by confining frequencies $\hbar\omega_x = 5\,\mathrm{meV}$ and $\hbar\omega_y = 6\,\mathrm{meV}$ and channel width $L_z = 5\,\mathrm{nm}$. The qubit is subjected to a constant magnetic field $B = 1\,\mathrm{T}$ oriented with $\theta = 75°$ and $\phi = 90°$ and an electric field $E_z = 50\,\mathrm{mV/nm}$ and a driving field of amplitude $\delta E_z = 1\,\mathrm{mV/nm}$. The numerical integration was performed by fixing all Larmor frequencies equal to $\omega_L^{1\leftrightarrow 0} = 1.23 \cdot 10^5\,\mathrm{Mrad/s}$ and setting (a) all Rabi frequencies equal to $\omega_+^{1\leftrightarrow 0}$ or (b) the Rabi frequencies reported in Table 7.2.

$j \setminus k$	3	2	1	0
3	$7.77 \cdot 10^5$	$1.23 \cdot 10^2$	$1.77 \cdot 10^2$	$1.36 \cdot 10^3$
2	$1.23 \cdot 10^2$	$7.77 \cdot 10^5$	$1.28 \cdot 10^3$	$6.95 \cdot 10^2$
1	$1.77 \cdot 10^2$	$1.28 \cdot 10^3$	$7.75 \cdot 10^5$	8.93
0	$1.36 \cdot 10^3$	$6.95 \cdot 10^2$	8.93	$7.75 \cdot 10^5$

Table 7.2: Moduli of the Rabi frequencies $|\omega_+^{j\leftrightarrow k}|$ in units of Mrad/s, used for the simulation in Fig. 7.1(b).

This behavior can be seen in the curves reported in Fig. 7.1. Here, we show the average occupation probabilities of the first four states during a time-dependent evolution with the driving field at resonance with the first transition, $\omega_P \equiv \omega_L^{1\leftrightarrow 0}$. These curves are obtained through the Runge-Kutta integration of Eq. (7.26), in which we fixed an equal Kramers splitting for the first two doublets, $\omega_L^{1\leftrightarrow 0} = \omega_L^{3\leftrightarrow 2}$, and varying the difference between the energetic separation between states $\{|0\rangle, |1\rangle\}$ and $\{|1\rangle, |2\rangle\}$, by defining

$$\xi \equiv \omega_L^{2\leftrightarrow 1} - \omega_L^{1\leftrightarrow 0}. \tag{7.28}$$

First of all, from Fig. 7.1(a) we have the confirmation that it's possible that for small ξ the pulse is in resonance with all the possible transitions involving adjacent levels, and all the states possess an average occupation in time different from zero. Instead, for large ξ, the occupation of the excited doublet falls to zero, meaning that it's no longer involved in the transition and the system is appropriately described by the evolution operator in Eq. (7.27). However, the behavior of the four-level system is highly dependent on the ratio of the Rabi frequencies as well. Indeed, in Fig. 7.1(b) we fixed all Rabi frequencies involving the higher doublet to be much higher than $|\omega_+^{1\leftrightarrow 0}|$ (see Table 7.2), and observed no significant occupation of the excited states until a much higher value of ξ, at which once again the evolution could be described by the operator in Eq. (7.27). This kind of behavior is due to the high oscillation frequencies of all the involved transitions, which overall oscillate too rapidly to induce a non-negligible change in the occupation probabilities over time.

7.2 Four-level characterization in a SQD

In view of a possible addressing of the transitions between hole states, we report the key quantities represented by the Larmor frequencies $\omega_L^{j\leftrightarrow k}$ from Eq. (7.24) and Rabi frequencies from Eq. (7.14) previously introduced in Sec. 7.1 for a higher-dimensional 4-level system. In the following, these quantities are correlated with the properties of the ground-state doublet and first-excited doublet, specifically with the band occupation and with their symmetry-related character. In the SQD, the ground- and first-excited doublets present different features in terms of band occupation and/or symmetries. As one can imagine, these differences depend both qualitatively and quantitatively on the relative strength between the in-plane confinement, along x and y, and the out-of-plane along z. In order to highlight such dependencies, we compare in the following a reference geometry, referred to SQD1, to two others: these are SQD2, characterized by a stronger in-plane confinement (higher $\hbar\omega_\alpha$, $\alpha = x, y$), and SQD3, with a weaker out-of-plane confinement (larger L_z). As mentioned in Sec. 5.3.1, the static out-of-plane electric field E_z also contributes to the hole confinement along the z direction, and modifies the hole states as well as the behavior of the qubit. Consequently, some of the relevant quantities in SQD3 are also plotted as a function of E_z. The sets of parameters that define the three dots are reported in Table 7.3.

	$\hbar\omega_x$ (meV)	L_x (nm)	$\hbar\omega_y$ (meV)	L_y (nm)	L_z (nm)	E_z (mV/nm)	L_E (nm)
SQD1	5	8.08	6	7.38	5	50	1.48
SQD2	10	5.71	12	5.22	5	50	1.48
SQD3	5	8.08	6	7.38	10	50	1.48
DQD1	5	8.08	10	5.71	5	50	1.48

Table 7.3: Parameters that define the confining potential for the three representative SQDs and DQD considered in Sec. 7.2.

7.2.1 Effects of the degree of anisotropy on the manipulation frequencies

Energy levels and Larmor frequencies

We start by considering the dependence of the energy levels on the orientation of the magnetic field with respect to the z axis, which is specified by the angle θ [Fig. 7.2(a)]. In all simulations, the angle ϕ is set to 90°, so that the magnetic field always lies on the yz plane. This choice does not affect the numerical results significantly [189], as we also observed in Sec. 6.3.1. As seen in Fig. 7.2(b), the splittings within the ground- ($\omega_L^{1\leftrightarrow 0}$) and first-excited ($\omega_L^{3\leftrightarrow 2}$) Kramers doublets display similar values and a similar dependence on θ, apart from the case where the magnetic field is oriented along the y axis ($\theta = 90°$). Here, unlike $\omega_L^{1\leftrightarrow 0}$, the Larmor frequency $\omega_L^{3\leftrightarrow 2}$ is nonzero. This implies that the Kramers degeneracy of the first-excited doublet is broken independently of the orientation of **B**, while the ground-doublet degeneracy is only broken through an out-of-plane field. The plot of the inter-doublet energy gaps in Fig. 7.2(c) completes the picture, and gives an estimate of the spectral resolution required to resolve the whole set of transitions within the four-dimensional subspace formed by the two lowest doublets. Notice that in this case the frequencies $\omega_L^{2\leftrightarrow 0}$ and $\omega_L^{3\leftrightarrow 1}$, respectively connecting the two lower or upper states of each doublet, almost coincide, due to the similarity of the Kramers splittings. Consequently, the $2 \leftrightarrow 0$ and $3 \leftrightarrow 2$ transitions, as well as the $1 \leftrightarrow 0$ and $3 \leftrightarrow 1$ ones, are not perfectly decoupled from each other. Thus, the manipulation field may be in resonance with multiple transitions at once, independently of the value of θ, as we briefly explained at the end of Sec. 7.1.2. Depending on the chosen manipulation scheme, this may constitute a problem.

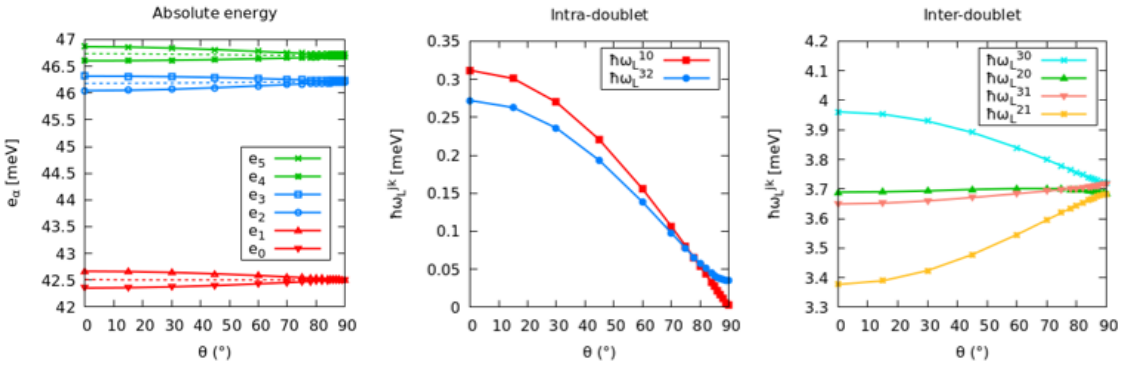


Figure 7.2: (a) Six lowest energy levels and (b-c) Larmor frequencies corresponding to transitions between the four lowest eigenstates for SQD1, plotted as a function of the magnetic-field tilting angle θ and for $\phi = 90°$.

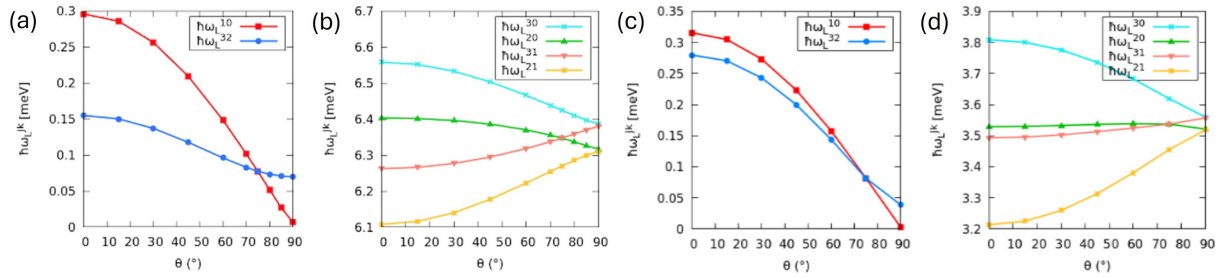


Figure 7.3: Larmor frequencies corresponding to intra- [panels (a), (c)] and inter-doublet [panels (b), (d)] transitions as a function of the magnetic-field tilting angle θ and for $\phi = 90°$, for SQD2 [panels (a), (b)] and SQD3 [panels (c), (d)].

In order to verify the dependence of the energy gaps on the confinement potential, and try to bypass the aforementioned problem during manipulation, we compare the above results with those obtained for larger values of $\hbar\omega_{x/y}$ (SQD2) or of L_z (SQD3). In both cases, the ratio between the confinement lengths defined in-plane (L_x, L_y) and out-of-plane (L_z) is closer to 1 with respect to SQD1, meaning that we are dealing with slightly more isotropic dots. In the case of SQD2 [Fig. 7.3(a,b)], the symmetry between the Larmor frequencies defined within the two doublets is clearly removed, suggesting a significant difference between the two doublets in terms of state composition, i.e. band mixing between HH and LH contributions (see the discussion in Sec. 7.2.2). Also, the transition energies differ from each other by at least the order of a tenth of meV. The qualitative differences with respect to the reference dot (SQD1) are not so significant instead in the case of SQD3. This is also due to the electric field, which limits the effect of the well-width enhancement, so that the strength of the confinement along the z direction relative to that along x and y does not change as much as for SQD2. Indeed, the effective confinement length due to the electric field can be evaluated as [278]:

$$L_E = \left(\frac{\hbar^2}{2m^P_{eff} e E_z} \right)^{1/3} \tag{7.29}$$

which in all considered SQDs is much smaller than the confinement length L_z due to the heterostructure (see Table 7.3). The effect of E_z and L_E is further studied in Fig. 7.4. Here, we see that E_z produces a moderate effect on the energy splittings related to intra-doublet transitions ($\omega_L^{1\leftrightarrow 0}$ and $\omega_L^{3\leftrightarrow 2}$), while it significantly and nonlinearly affects the energy splittings between the ground and the first-excited doublets, reflecting the difference between these two pairs of states in terms of orbital components. Notice that the intra-doublet splittings $\omega_L^{1\leftrightarrow 0}$ and $\omega_L^{3\leftrightarrow 2}$ differ from each other the most for $E_z \sim 10\,\mathrm{mV/nm}$ ($l_E \sim 2.54\,\mathrm{nm}$). In this situation, the ratio between the in-plane and effective out-of-plane confinement is $l_{x/y}/l_E \approx 3$, which is similar to the one obtained for SQD2 ($L_x/L_E \approx 3.9$ and $L_y/L_E \approx 3.5$).

These first results already show the high degree of tunability available in the manipulation of the first-excited doublet with respect to the ground- one. Indeed, through considerations of the relative confinement strengths along the in-plane and out-of-plane directions, one can engineer the energy splittings between the levels of a considered manipulation scheme, and consequently search for the operative regime in which each transition is isolated from the others, and can be manipulated separately with specific pulse frequencies.

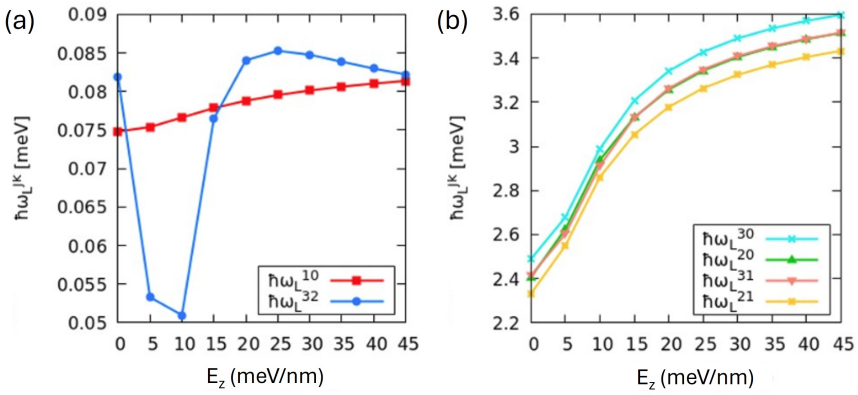


Figure 7.4: Dependence on the electric field E_z of the Larmor frequencies corresponding to intra- (left) and inter-doublet (right) transitions in SDQ3. The orientation of the magnetic field is $\theta = 75°$ and $\phi = 90°$.

Rabi frequencies

The other key quantities that describe the transitions between the hole eigenstates are the Rabi frequencies $\omega_+^{j\leftrightarrow k}$ and $\omega_Z^{j\leftrightarrow k}$ previously introduced in Sec. 7.1.1. In particular, our results show that the transitions between the states of the excited doublet ($2 \leftrightarrow 3$), or between any two states belonging to different doublets, present transition amplitudes that largely exceed those between the states of the ground doublet. The reported Rabi frequencies are obtained for a specific value of the magnetic field ($B = 1$ T), in a regime where these frequencies vary linearly with B.

We start by considering the transverse Rabi frequencies, $\omega_+^{j\leftrightarrow k}$, as defined in Eq. (7.23) and reported in Fig. 7.5. As for the qubit frequencies, the relevant quantities are their moduli. However, now it's not possible to fix an arbitrary gauge for each transition, since rotations described by the SU(4) algebra don't allow for it (see the discussion at the end of Sec. 7.1.1). Consequently, contrary to what we did for the qubit, we can't identify $|\omega_+^{j\leftrightarrow k}|$ with the corresponding Rabi frequency along X. As shown in Fig. 7.5, the dependence of $\omega_+^{1\leftrightarrow 0}$ and $\omega_+^{3\leftrightarrow 2}$ on the orientation of the magnetic field qualitatively coincides with that found in the literature for different geometries [189] and also reported in Sec. 6.3.1. In particular, these Rabi frequencies vanish for $\theta = 0$ and $\theta = \pi/2$, and display a maximum for large, but lower than $\pi/2$, tilting angles. That said, the intra-doublet transition involving the first-excited doublets ($\omega_+^{3\leftrightarrow 2}$) is, in all the considered cases, one order of magnitude larger than $\omega_+^{1\leftrightarrow 0}$. The ratio between the two is particularly high in the case of SQD2, which is characterized by the strongest in-plane confinement relative to that in the z direction. Moving from intra- to inter-doublet transitions, two main features emerge. First, the transverse Rabi frequencies, especially those involving the ground state ($\omega_+^{2\leftrightarrow 0}$ and $\omega_+^{3\leftrightarrow 0}$), achieve values that are one order of magnitude larger than the highest intra-doublet frequency ($\omega_+^{3\leftrightarrow 2}$). Second, the dependency on the tilting angle θ is qualitatively different from that characterizing $\omega_+^{1\leftrightarrow 0}$ and $\omega_+^{3\leftrightarrow 2}$, and changes significantly from one dot to the other.

Moving from the longitudinal rotations around the Z axis, some of the above features are confirmed, while others change. In particular, the Rabi frequency for the states belonging to the excited doublet ($\omega_Z^{3\leftrightarrow 2}$) is generally, though not always, larger than that involving the ground states ($\omega_Z^{1\leftrightarrow 0}$). On the other hand, the transition amplitudes associated with the states belonging to different dou-

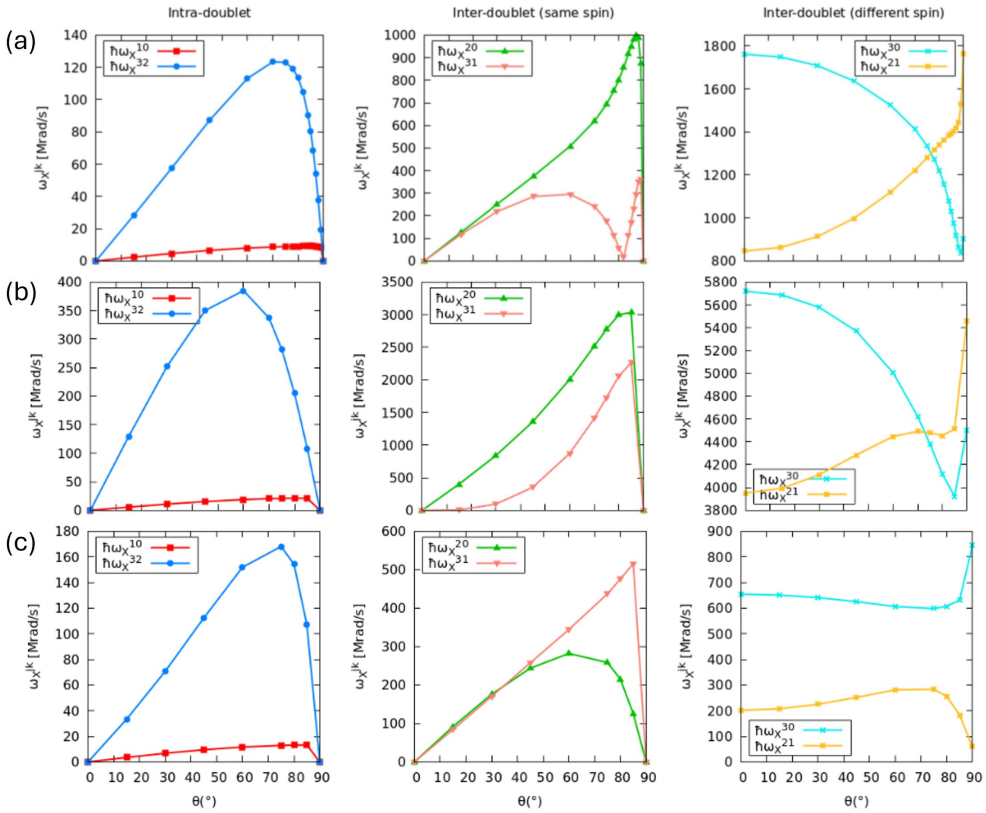


Figure 7.5: Rabi frequencies $\omega_X^{j\leftrightarrow k}$ of the intra-doublet transitions (left), inter-doublet, spin-preserving transitions (center) and inter-doublet, spin-non-preserving transitions (right) as a function of the magnetic-field tilting angle θ and for $\phi = 90°$ for (a) SQD1, (b) SQD2, and (c) SQD3.

blets are one order of magnitude larger than $\omega_Z^{3\leftrightarrow 2}$ and $\omega_Z^{1\leftrightarrow 0}$. The analysis of the dependence on the electric field, in Fig. 7.7, shows qualitatively similar trends for all the Rabi frequencies. In particular, these trends are characterized by a very pronounced peak at $E_z \sim 5\,\mathrm{mV/nm}$ ($L_E \sim 3.20\,\mathrm{nm}$), in agreement with behaviors reported in previous studies on similar systems [278]. While in some cases a stronger $\omega_Z^{j\leftrightarrow k}$ allows for faster rotations, and consequently gates, in other cases one may want to decrease it in order to suppress dephasing processes. In this sense, the high tunability with respect to the confinement strength showed in the curves of $\omega_Z^{j\leftrightarrow k}$ both in absolute and relatively to $\omega_+^{j\leftrightarrow k}$ is a great advantage.

7.2.2 Band occupation vs. orbital excitation

The tunability of the transitions involving the first-excited doublet with respect to the ratio between the in-plane and out-of-plane confinements can be related to the composition of the states in terms of band occupation. Indeed, as we described in Sec. 5.1.2, the hole eigenstates can be written within the envelope-function approach as the sum of the contributions from each of the six bands making up the top of the valence band. In Fig. 7.8 we show the contributions from the HH, LH and SO components for all the simulated cases. Starting from SQD1 we see that the states from both the ground- and first-excited doublets are prevalently HH, however, the LH and SO components of states $|2\rangle$ and $|3\rangle$ are higher of a factor of ~ 3 with respect to their counterparts

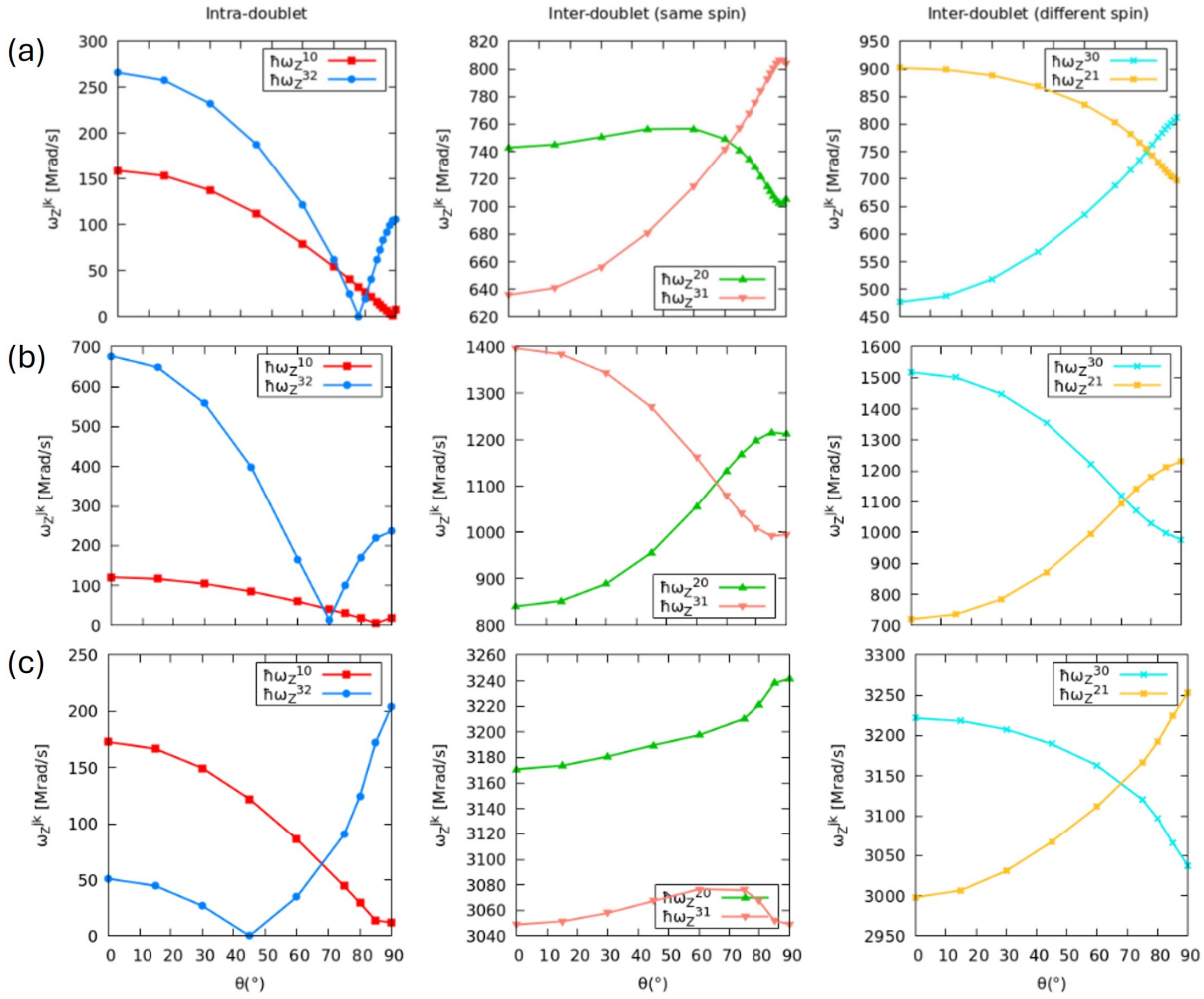


Figure 7.6: Rabi frequencies $\omega_Z^{j\leftrightarrow k}$ of the intra-doublet transitions (left), inter-doublet, spin-preserving transitions (center) and inter-doublet, spin-non-preserving transitions (right) as a function of the magnetic-field tilting angle θ and for $\phi = 90^\circ$ for (a) SQD1, (b) SQD2, and (c) SQD3.

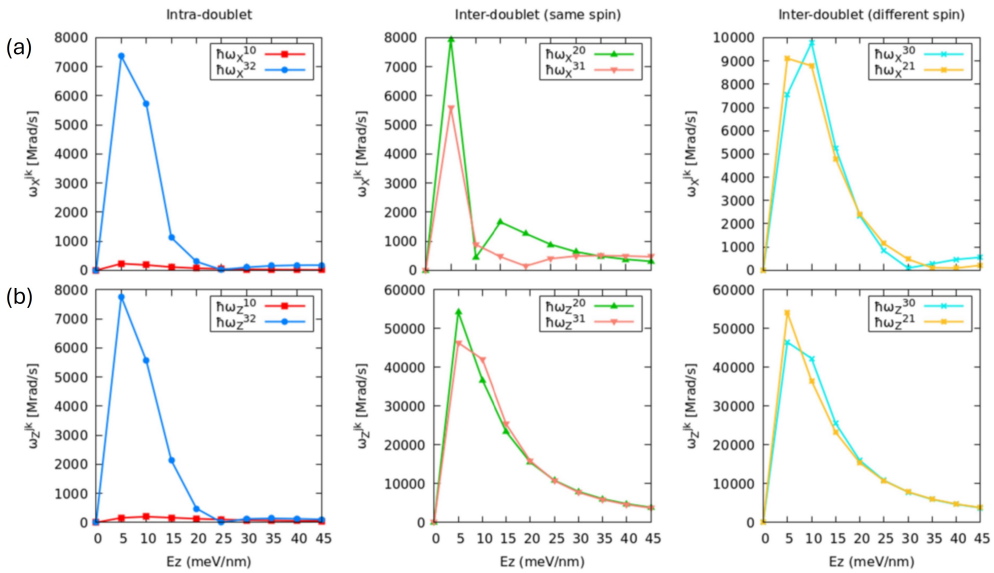


Figure 7.7: Rabi frequencies (a) $\omega_X^{j\leftrightarrow k}$ and (b) $\omega_Z^{j\leftrightarrow k}$ of the intra-doublet transitions (left), inter-doublet, spin-preserving transitions (center) and inter-doublet, spin-non-preserving transitions (right) as a function of the out-of-plane electric field E_z for SQD3. The orientation of the magnetic field is $\theta = 75°$ and $\phi = 90°$.

from the first doublet, and present a significantly stronger dependence on the orientation of **B**. This behavior is enhanced by increasing the strength of the in-plane confinement relative to the out-of-plane confinement, as we can see by comparing SQD1 and SQD2. Indeed, the band mixing of both doublets increases, plus the LH and SO components of states $|2\rangle$ and $|3\rangle$ are now a factor of $4 \div 6$ higher than those of states $|0\rangle$ and $|1\rangle$. As for SQD3, similarly to what we described in Sec. 7.2.1, the same effect is not as prominent when increasing the width of the well L_z. Instead, it's the effective confinement felt through E_z that influences the results the most. Indeed, the applied electric field induces a transition in the excited doublet, which is not apparent in the ground doublet. More specifically, the states $|2\rangle$ and $|3\rangle$ undergo a transition from a predominantly HH to a LH character for $E_z \gtrsim 5\,\mathrm{mV/nm}$. This confirms the above consideration on the much larger tunability of the first-excited doublet with respect to the ground doublet. Note that the transition region is the same one where we observed the marked peaks in the Rabi frequencies (see Fig. 7.7). This behavior further confirms a relation between the band mixing and manipulation properties of the hole eigenstates.

At this point, we can also analyze the degree of symmetry of the hole eigenstates, which provides further insight into their properties and on the character of the transition that takes place in SQD3 as a function of the applied electric field. Overall, none of the eigenstates has a well-defined mirror or inversion symmetry. Indeed, the Hamiltonian is not invariant under any of the parity operations defined in Sec. 5.2.3: that is, the inversion around the origin, called P, and around axis $\alpha = x, y, z$, called P_α. However, the expectation values of P, P_x and P_y reported in Fig. 7.9(a,c) show that the states belonging to the ground doublet are always approximately even, being $\langle P\rangle_n, \langle P_x\rangle_n, \langle P_y\rangle_n \sim 1$ for $n = 0, 1$. On the contrary, the states belonging to the excited doublets present expectation values of $\hat{P}$ and $\hat{P}_x$ that are relatively close to -1, as can be seen in Fig. 7.9(b,d), and with a significant dependence on the direction of the magnetic field. These plots also confirm

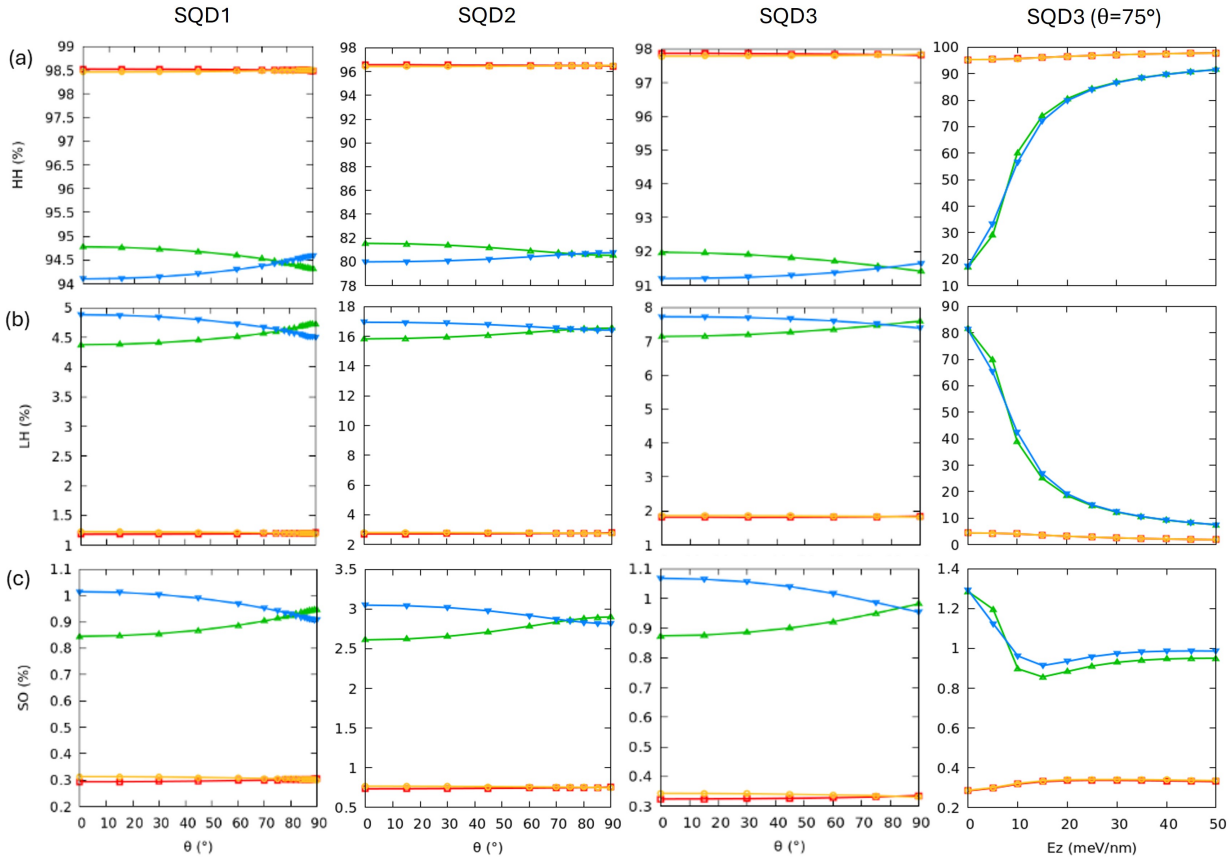


Figure 7.8: Band composition of the single quantum dots SQD1, SQD2, and SQD3. Different colors correspond to different eigenstates: 0 (red), 1 (yellow), 2 (green), 3 (blue). (a) HH, (b) LH and (c) SO occupation percentages as a function of the tilting angle θ for $E_z = 50\,\mathrm{mV/nm}$ (first three columns) and as a function of E_z for $\theta = 75°$. In all cases we fixed $\phi = 90°$.

that the differences between the states belonging to the excited doublet are much more pronounced than those belonging to the ground doublet. As to the dependence on the electric field, the expectation values of the symmetry operators point to the occurrence of a sharp transition (from an even to an odd state) that parallels the one shown by the band occupations. This behavior further proves the presence of two different regimes: the first one, for high E_z, in which the out-of-plane confinement is much stronger than the in-plane confinement and the excited doublet presents an orbital excitation. In this case, the symmetry character of the state along x resembles a p-like atomic orbital. In the second regime, the confinements felt by the hole along all directions are comparable, and the excited doublet has the same parity as an s-like orbital. Instead, the excited states here present a *band excitation*, since their band character is prominently LH, in opposition to the prevalently HH ground doublet. The tunability of the excited hole states, their energy splittings and Rabi frequencies is intrinsically related to the tunability between these regimes.

Note that in all simulated cases the expectation values of P_y and P_z (not shown) are close to 1, meaning that orbital excitations only occur along the x direction. This is to be expected in the SQD we simulated, since the confinement along x is smaller with respect to the other directions (see parameters in Table 7.3).

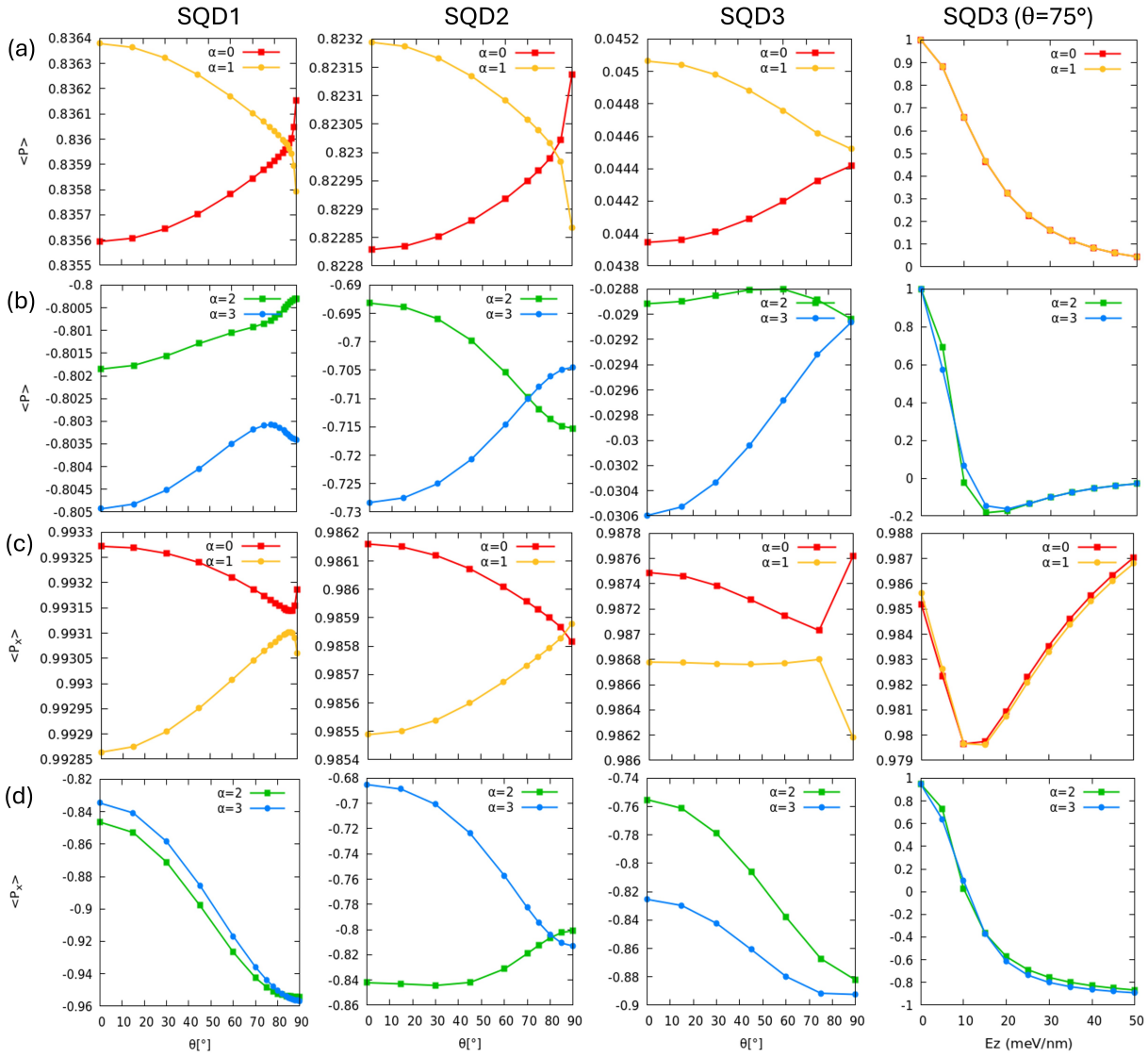


Figure 7.9: Expectation values of (a,b) the parity operator around the origin P on the (a) ground- and (b) first-excited doublet; and of (c,d) the parity operator P_x around x on the (c) ground- and (d) first-excited [panel (d)] doublet. Different colors correspond to different eigenstates: 0 (red), 1 (yellow), 2 (green), 3 (blue). The results are reported as a function of the tilting angle θ for $E_z = 50\,\mathrm{mV/nm}$ (first three columns) and as a function of E_z for $\theta = 75°$. In all cases we fixed $\phi = 90°$.

7.2.3 Comparison to the DQD states

In this Section we study an example of DQD with the parameters reported in Table 7.3. This system, as we studied previously in Chapter 6, possesses an additional degree of freedom with respect to the SQD, namely the half-interdot distance a, which determines the coupling strength between dots. From this, it turns out that the first-excited doublet in the DQD presents qualitative differ-

ences with respect to that in the SQD. In fact, the lowest excitation is related to the motion along the tunneling direction (x), rather than to the band composition or parity character of the hole states. Thus, when a is high and the coupling low, the states belonging to the first-excited doublet can resemble the ground states much more in terms of band mixing and parity than in the case of the SDQs discussed above. This is already clear in Fig. 7.10(a) from the level scheme (left panel), and from the energy splittings defined within the ground- ($\omega_L^{1\leftrightarrow 0}$) and first-excited doublets ($\omega_L^{3\leftrightarrow 2}$) (middle panel), which for large a become more and more similar to one another. This behavior is independent of the magnetic field orientation (not shown).

The higher degree of resemblance between the states belonging to the two doublets is also reflected in the similar values of the Rabi frequencies. Indeed, we can compare in Fig. 7.10(b) those related to the intra-doublet transitions ($\omega_X^{1\leftrightarrow 0}$ and $\omega_X^{3\leftrightarrow 2}$) or the inter-doublet, "spin-preserving" ones ($\omega_X^{2\leftrightarrow 0}$ and $\omega_X^{3\leftrightarrow 1}$), or the inter-doublet, "spin-non-preserving" ones ($\omega_X^{2\leftrightarrow 1}$ and $\omega_X^{3\leftrightarrow 0}$) between each other, and see that their value starts to differ significantly only for $a \lesssim 8$. Further confirmation is given by the band occupations [Fig. 7.11(a)]. These show that both the ground- and first-excited doublets are characterized by a predominantly HH character, which starts to differ of a few percentages only for small a. Instead, the expectation values of the parity operators P and P_x show the symmetrical/antisymmetrical nature typical of the bonding/antibonding states inside of a DQD,

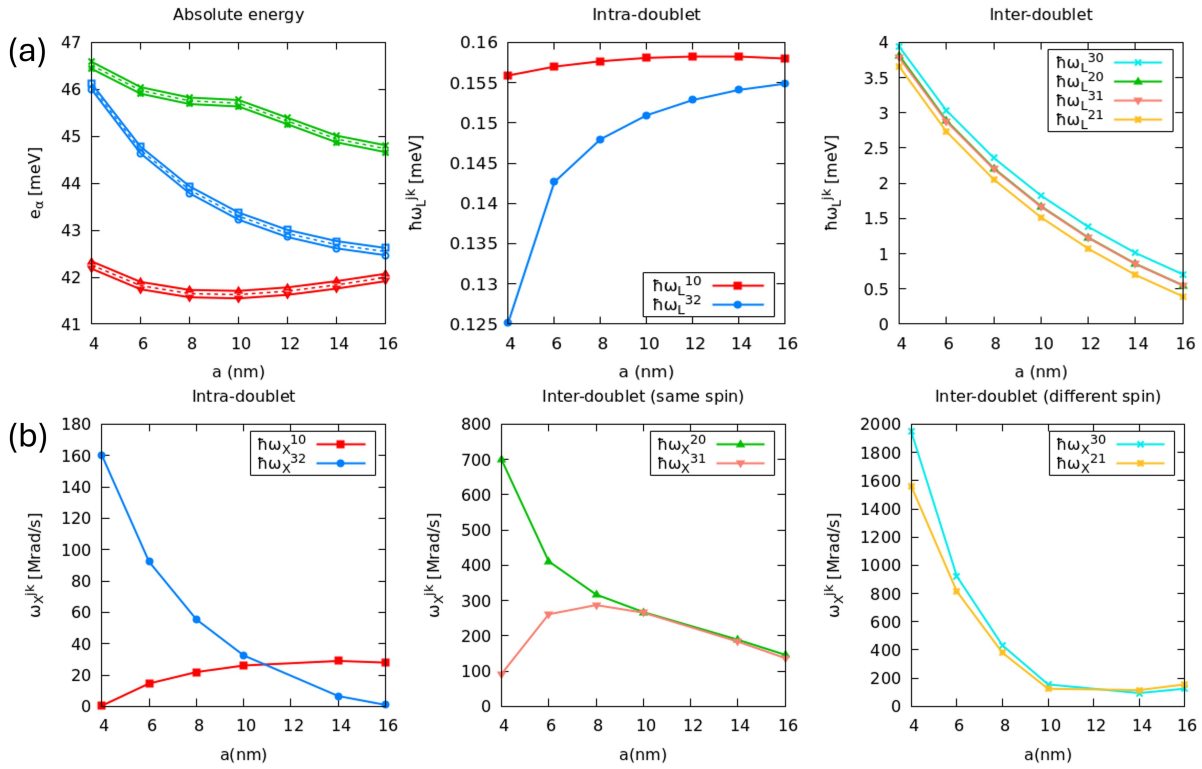


Figure 7.10: (a) Six lowest energy levels (left) and Larmor frequencies corresponding to transitions between the four lowest eigenstates (center and right) for DQD1. (b) Rabi frequencies $\omega_X^{j\leftrightarrow k}$ of the intra-doublet transitions (left), inter-doublet, spin-preserving transitions (center) and inter-doublet, spin-non-preserving transitions (right) for DQD1. All results are plotted as a function of the interdot half-distance a. The orientation of the magnetic field is $\theta = 75^\circ$ and $\phi = 90^\circ$.

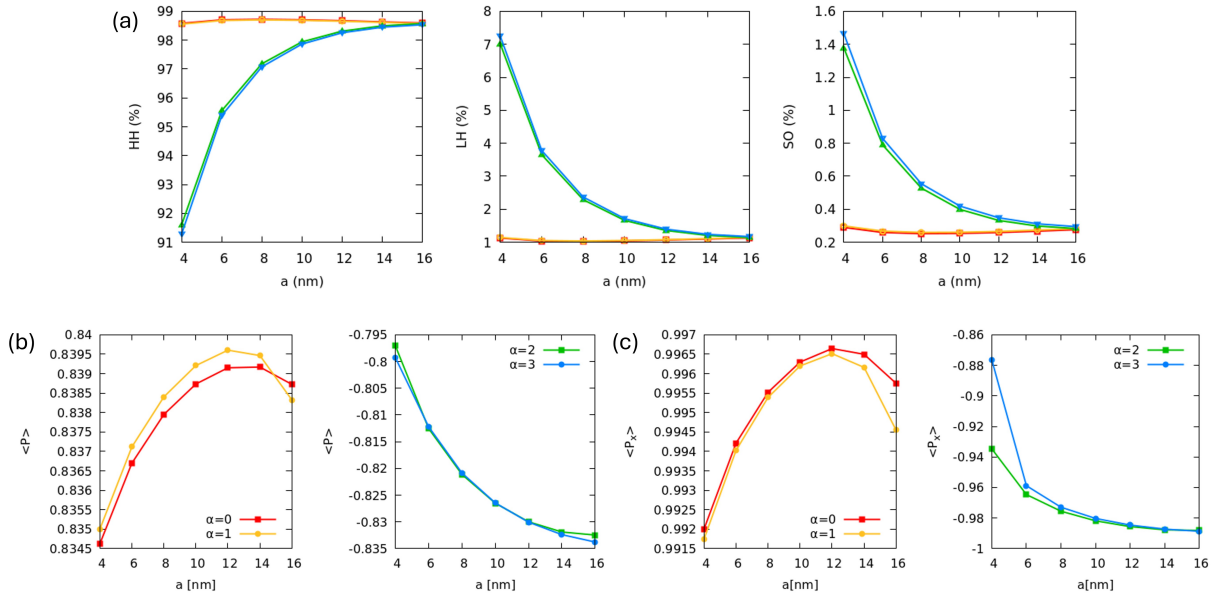


Figure 7.11: (a) Band composition of DQD1, showing the HH (left), LH (center) and SO (right) occupation percentages. (b) From left to right: expectation values of P on the ground- and first-excited doublet; expectation values of P_x on the ground- and first-excited doublet. Different colors correspond to different eigenstates: 0 (red), 1 (yellow), 2 (green), 3 (blue). All results are plotted as a function of the interdot half-distance a. The orientation of the magnetic field is $\theta = 75^\circ$ and $\phi = 90^\circ$.

with $\langle P \rangle_n, \langle P_x \rangle_n \approx 1$ for both $n = 0, 1$ and $\langle P \rangle_n, \langle P_x \rangle_n \approx -1$ for $n = 2, 3$. This is all in agreement with our considerations of Sec. 7.2.2. As before, no special behavior is observed for P_y and P_z, which are always ≈ 1 in all cases.

All of these considerations overall tell us that DQDs, as expected, can be tuned more easily than SQDs in regards to the values of the Larmor and Rabi frequencies for manipulation. Specifically, here we showed that the half-interdot distance is the determining factor in regulating the coupling strength between dots, and consequently the difference in the manipulation properties between the ground- and first-excited doublets. The same reasoning can be easily generalized to any parameter that modifies the tunneling t between dots. For example, by increasing the interdot barrier directly through the use of an additional gate between dots. This would allow us to obtain isolated transitions for every pair of levels even at larger a, thus further confirming the superior tunability of the DQD system with respect to the SQD.

Part III

Conclusions

Correlazioni

Non ho più riferimenti in questi specchi
Di onde, che parlano e si scambiano
E si annientano nel nulla.
Credevo di conoscere ogni possibilità,
Credevo di capire gli ingranaggi del mio mondo.

E poi mi hai distrutto con grazia ineffabile,
Mi hai trascinato in assurdi intrighi.
Ed io non resisto all'indecifrabile:
Volevo carpire i tuoi oscuri segreti,
Desideravo armonie dal tuo caos.

Devo imparare a invitare l'assurdo,
Seguire l'ignoto, cercare e trovare
La luce nei vuoti del nostro silenzio.
Ma adesso confondo presenza ed assenza,
Ed esiste per forza la causalità?

Ti ho conosciuto per solo un istante,
Nel quale mi hai illuso di memorizzarti.
Ma un solo futuro è infiniti passati,
E la ragione appesantisce la cadenza dei ricordi.

Tutto sommato io non ti capisco,
E questo mi spinge a rincorrerti
In gorghi di illusioni.
Ma ancora mi voto assurdamente a te,
Nella speranza
Di un giorno poterti comprendere davvero.

The past is latent, is submerged, but still there,
capable of rising to the surface once the later imprinting
unfortunately – and against ordinary experience – vanished.

$\sim$ from *Ubik*, by Philip K. Dick

Conclusions

The simulations performed in this Thesis showed the potential of various semiconductor-based platforms for applications in the field of quantum information processing. Indeed, the available manufacturing techniques of semiconductor devices guarantee a high degree of integration and control over these systems, enabling the miniaturization and scalability required for practical quantum computation. Specifically, computation based on DiVincenzo's criteria requires both stationary and flying qubits [23]. That is, one must be able to encode and manipulate quantum information locally, as well as transmit it at a distance. In this Thesis, we presented approaches to both problems, studying suitable systems that show promising perspectives in terms of robustness and integrability with the existing modern technology.

The first part of this Thesis focused on the use of graphene devices in the integer quantum Hall (IQH) regime for quantum communication. Thanks to the presence of massless Dirac fermions, graphene shows unique properties that can be exploited for the implementation of flying qubits in electron quantum optics. By solving the exact 2D Schrödinger equation of carriers in graphene in the IQH regime, we studied the interplay between a magnetic field orthogonal to a graphene monolayer and the confinement due to the armchair edge of a nanoribbon or to an electrostatic potential generated by metal gates on top of the device. We extended the treatment of the split-step Fourier method in Chapter 2, to take account of both the sublattice and valley degrees of freedom of a localized wavepacket in graphene.

Semiconductor materials offer the possibility of interfacing single-electron sources with 2D electron gases in the IQH regime, with a recent demonstration of a single-electron source in graphene [127]. Consequently, in Chapter 3 we studied the coherent evolution of a Gaussian state, in view of possible future implementations of single-particle interferometers acting as logical gates for flying qubits. We considered a particle initialized inside our simulated device at the edge of the nanoribbon, as a linear combination of edge states with mixed valley quantum number. The possibility of manipulating such valley quantum number opens the opportunity of operating graphene devices in the scope of valleytronics [11], a new kind of electronics that encodes the information on the valley degree of freedom of the electron. Then, we analyzed the carrier's behavior in terms of shape retention and center of mass velocity, and reported the single-particle regimes at which it's possible to observe edge-state versus snake-state behavior. We were also able to show the reflection against a smooth electrostatic barrier and the known phenomenon of Klein tunneling, typical of Dirac fermions. We observed a general good coherence of the carrier in the edge-state regime, mainly dependent on the shape of the Landau level dispersion, thus confirming the optimal characteristics of Dirac fermions for the transport of quantum information.

We later studied the energy-dependent scattering of the wavepacket due to a quantum point contact (QPC) and a valley beam splitter (VBS). In the literature, this is usually done through the definition of a scattering matrix acting on a stationary state in an effective 1D geometry. Instead, we directly addressed the transmission and reflection probabilities of the traveling particle through

the wave packet method, by defining the actual 2D potential profile present in a realistic device. This allowed us to obtain a more realistic description of the interplay between the energy resolution of the wavepacket and the geometry of the QPC/VBS. After this, we tuned the QPC/VBS to act as ideal semireflective mirrors ($\sim$50-50% splitting) and built single-particle Mach-Zehnder interferometers. We observed Aharonov-Bohm oscillations with high visibilities with both the implementations through QPCs and VBSs. The obtained visibilities were comparable to those observed experimentally with delocalized currents in graphene, which in turn can get much higher than those obtainable in GaAs/AlGaAs implementations.

We found that the main detrimental factors lowering the visibilities were different depending on the implementation. Although the use of QPCs can create back-scattering below the gates, this effect could be suppressed with an appropriately designed potential landscape. However, the arms of an interferometer based on QPCs were spatially separated, and phase averaging caused a significant suppression of the Aharonov-Bohm oscillations when the difference in the optical path was large. Instead, this effect was negligible in valley-based interferometers, in which the edge channels propagated alongside the same potential barrier. Indeed, as cleaner and cleaner graphene samples get realized, the energetic gap between the involved Landau levels gets smaller and smaller, and the edge channels can be only a few nanometers away from each other. On the other hand, we found that the inter-channel distance oscillated along the zigzag direction of the honeycomb lattice, thus causing the visibility to drop to zero when it vanished.

In the second part of the Thesis we studied foundry-compatible Si-based devices for the implementation of hole-spin qubits. We referred to the Loss-DiVincenzo scheme, in which a particle with spin is localized inside a gate-defined single quantum dot (SQD) or double quantum dot (DQD). Single- and two-qubit gates for holes in group-IV semiconductors specifically can be implemented completely by electrical means, thanks to the natural large spin-orbit coupling, which is instead much smaller for electrons. We base our simulations on the full 6-band Luttinger-Kohn Hamiltonian, based on the $\mathbf{k} \cdot \mathbf{p}$ method and the envelope-function theory.

Due to the presence of spin-orbit coupling, confined holes are particularly sensitive to variations in their electrostatic environment, and are consequently subjected to electrostatic noise [252]. However, this same sensitivity can be exploited in the field of quantum sensing, to gain information about the same device in which the qubit is implemented. Consequently, in Chapter 6, we considered the hole-spin qubit as a quantum sensor of an electrostatic charge, the presence of which may be due to defects at the interface with the top gates defining the SQD/DQD and providing manipulation on the hole state. We further enhanced the effect of the external charge by considering a DQD, in which the hole state is more easily polarized depending on the charge presence and distance from the system. Due to the Kramers theorem, which applies to the single-hole Hamiltonian in the absence of an external magnetic field, the hole states are organized in Kramers doublets. By using a Hubbard model to describe the eigenfunction and eigenenergy of the first two Kramers doublets inside a DQD, we were able to qualitatively reproduce the interplay between the Coulomb-induced bias and the interdot coupling of the DQD. Consequently, despite having to choose a specific shape of the DQD confinement for our simulations, we showed that our results were qualitatively independent of the specific DQD implementation, and could consequently be generalized.

A static approach to quantum sensing was then introduced, based on measurements applied on the hole ground state. We showed that both state discrimination and parameter estimations were possible, and were respectively quantified by the maximal discrimination probability obtained through the Helstrom bound, and the quantum Fisher information. Specifically, the latter quantity confirmed that the maximal sensitivity is obtained when the interdot coupling and Coulomb

bias are comparable in energy. However, both quantities were relatively small and would require several measurements on the quantum state to obtain significative confidence in the results, even considering an optimal projective measurement. On the contrary, a dynamic approach allowed us to exploit the dependence of both the Larmor and Rabi frequencies on the charge, thus significantly enhancing the discrimination probability and Fisher information on a $\hat{\sigma}_3$ measurement. Specifically, a Ramsey measurement better suited the process of quantum estimation with respect to a Rabi scheme, due to the presence of a free precession phase during the evolution. Indeed, in this way it exploited the Larmor frequency in a more efficient way, considering its stronger dependence on the charge distance with respect to the Rabi frequency. Our results were further generalized by obtaining the expressions of the Fisher information for both manipulation schemes, which are independent of the physical implementation of the qubit.

Finally, in Chapter 7 we analyzed the possibility of exploiting states of the first-excited Kramers doublet for qubit manipulation. Indeed, there exist several manipulation schemes that involve the higher energy levels beyond the ground doublet as auxiliary states [279]. We showed how the manipulation frequencies involving the first-excited doublets were usually one or two orders of magnitude larger than those only involving the ground doublet. Additionally, they showed a much higher degree of tunability by means of the external fields acting on the device, as well as the effective confinement ratios felt by the hole state inside of the SQD/DQD. Specifically, we related the behavior of the manipulation frequencies to the symmetries of the hole eigenstates and their composition in terms of band occupation. Thanks to this, we identified a regime in which the Rabi frequencies are maximized, corresponding to transitions in the character of the eigenstates.

Overall, in this Thesis we reported on theoretical methods and practical applications to study two problems. The first was the implementation of coherent transport of electronic flying qubits in graphene; the second was the use of hole-spin qubits in Si for quantum sensing and the fast local manipulation of quantum information. Our methods allowed us to simulate the whole potential landscape of the systems in both situations, thus providing a straightforward, one-to-one correspondence with realistic devices. In this way, we were able to account for the interplay between all the crucial aspects of the problems, from the real-space resolution of the particles to their composition, to the energy scales and interactions at play. In the future, our simulations may also serve as a starting point for the study of few-particle applications. These could include the simulation of two-particle interferometers for the implementation of two-qubit gates with flying qubits [35, 36, 41], by exploiting the strong and tunable Coulomb interaction between localized electrons. Another possibility is the use of few-hole states for spin-qubits in SQD/DQD, which would exploit the exchange and Coulomb interactions to provide additional enhancements and tunability of the manipulation properties [280–282]. Finally, the two prototypical systems studied in this Thesis could be potentially coupled with each other, with the aim of ultimately converting quantum information from stationary qubits into flying qubits and vice versa [56].

Le lacune sono i Nessuno degli elettroni
ma a Valencia invece che al mare

$\sim$ cit. Fre

Acknowledgments

The majority of the work in this Thesis was made possible thanks to the collaboration with the CNR Institute of Nanosciences in Modena, in the scope of the IQubits project. I also acknowledge the CINECA award under the ISCRA initiative, for the availability of high-performance computing resources and support.

That said, I would like to first thank my supervisors, Prof. Paolo Bordone, Dr. Andrea Bertoni and Dr. Filippo Troiani, for their fundamental support during this journey. Their guidance and experience have been invaluable in navigating this new (and more often than not overwhelming) world of scientific research that I only first entered three years ago. In the same way I also thank Dr. Andrea Secchi, who constantly helped me with his insights, for encouraging me and providing irreplaceable advice. Without them all I would not have been able to grow in my abilities, as I hope I did. I thank Prof. Daniel Loss and Dr. Stefano Bosco, for hosting me at the Department of Physics of the University of Basel, and for investing precious time in our collaboration during my last year of PhD. And I thank the rest of the group in Basel and all the people I met there, for including me in their discussions and making me feel welcome during my stay.

I am grateful to all my colleagues in Modena, and to all the lunches and coffee breaks we shared. I believe we were able to support each other through our common hardships, even just by being there and joking together. I am thankful for all the friendships I made during the years I spent at Unimore, which I hope to keep cultivating in the future, even in the chance that our paths may separate. I especially thank the *Giollo* group, with whom I shared most, if not all, of my academic career up to this point. I thank Chiara and Alessia, who share my passion for music and fandoms, and probably some of my craziness as well. I thank Edoardo and Adamo, whose opinions are the best when arguing in the group chat. And I thank Lorenzo, who shared my same journey all the way, and endured my lunacy for three more years. I will always remember our outings, as well as the afternoon playdates and the nights spent together: you all made even the quarantine bearable! Know that I will always consider Pinguini Tattici Nucleari as *our* band, and think of their concert in Reggio Emilia as one of my fondest memories with all of you.

I then wish to thank all my friends in Carpi: from *la Compagnia del Rosmarino*, who will always have a special place in my heart, even if it takes ages to see one another and catch up; to *i Pistacchi* & Co. My friendship with you all supported me immensely when I needed it most, and when I felt the most lost. To the latter specifically I give a very special thanks. Even if I met you only relatively recently, you had a great impact on my life. You met me as a shy and solitary person, and allowed me to break free of my shell, by making me feel comfortable to express myself with no judgment. I thank Raffaella and Agnese, who have always perpetually put up with me and my bad sense of humor; who have convinced me to exercise and to maintain a social life. I thank Francesca, aka my *Nobody*, for being there when I felt nostalgic away from home, and for ranting

together on everything that we would obsess over, especially Kingdom Hearts, TWEWY, Megaman, frogs crashing, and anything else. I thank Myri and Guerzo, for basically adopting me as one of their cats during the drafting of this Thesis. I thank everyone else, too many to list, who made me feel comfortable enough in my skin to give me a home away from home. For the late nights and the visits to the *pastaro*; for the political movies watched together at Dave's house (as well as other movies of questionable taste...); for the book clubs and the Star Trek nights, and the plans of building a *Borghetto* together; and generally for all of our gatherings, which I always look forward to. Last but not least, I thank Jimmy, who has been my strongest cornerstone during this past year; for his understanding, for his kindness, for his stubbornness (one of his best qualities of course), and for his fierce sense of justice. For being different from everyone else, and for truly and deeply loving all the people who are close to him. I am infinitely grateful to be considered among them.

Finally, I thank my relatives, from my mother and father, to their spouses, and to my whole extended family. We are a complicated bunch, but you have always been there for me along my journey, ever since the first time that I showed interest in Maths and the other hard sciences. You never discouraged me, you always helped me along every step of the way up to here, and it's thanks to you that I can now consider myself part of the scientific community. Thanks to my sister, one of my favorite persons in the world, for not hating me even though I never watch the reels she sends me, and instead asking me to watch them together whenever we can; for always being willing to spend time with me, no matter how many times I screw something up. Thank you all, for supporting me in my every endeavor; for bearing with my idiosyncrasies, and for always accepting me as I am.

Bibliography

[1] E. Fanucchi, G. Forghieri, A. Secchi, et al., arXiv.2411.05526 (2024).

[2] G. Forghieri, A. Secchi, A. Bertoni, et al., Phys. Rev. Res. **5**, 043159 (2023).

[3] G. Forghieri, P. Bordone, and A. Bertoni, Phys. Rev. B **106**, 165402 (2022).

[4] E. Fanucchi, "Exploiting excited states for the manipulation of Hole-Spin qubits in silicon Quantum Dots", Master Thesis (University of Modena and Reggio Emilia, 2023).

[5] J. Preskill, "Quantum computing 40 years later", in *Feynman lectures on computation*, edited by T. Hey (CRC Press, Boca Raton, FL, 2023), p. 52.

[6] G. Cariolaro, *Quantum communications*, Vol. 2 (Springer, 2015).

[7] A. M. J. Zwerver, T. Krähenmann, T. F. Watson, et al., Nature Electronics **5**, 184 (2022).

[8] H. Edlbauer, J. Wang, T. Crozes, et al., EPJ Quantum Technology **9** (2022).

[9] P. Roulleau, F. Portier, P. Roche, et al., Phys. Rev. Lett. **100**, 126802 (2008).

[10] K. S. Novoselov, A. K. Geim, S. V. Morozov, et al., Nature **438**, 197 (2005).

[11] J. Schaibley, H. Yu, G. Clark, et al., Nature Reviews Materials **1**, 16055 (2016).

[12] D. Loss and D. P. DiVincenzo, Phys. Rev. A **57**, 120 (1998).

[13] G. Burkard, T. D. Ladd, A. Pan, et al., Rev. Mod. Phys. **95**, 025003 (2023).

[14] L. C. Camenzind, S. Geyer, A. Fuhrer, et al., Nature Electronics **5**, 178 (2022).

[15] S. D. Liles, F. Martins, D. S. Miserev, et al., Phys. Rev. B **104**, 235303 (2021).

[16] C. L. Degen, F. Reinhard, and P. Cappellaro, Rev. Mod. Phys. **89**, 035002 (2017).

[17] J. Weis and K. von Klitzing, Philosophical Transactions of the Royal Society A: Mathematical, Physical and Engineering Sciences **369**, 3954 (2011).

[18] K. v. Klitzing, G. Dorda, and M. Pepper, Phys. Rev. Lett. **45**, 494 (1980).

[19] H. L. Stormer, A. Chang, D. C. Tsui, et al., Phys. Rev. Lett. **50**, 1953 (1983).

[20] P. Bordone, L. Bellentani, and A. Bertoni, Semiconductor Science and Technology **34**, 103001 (2019).

[21] M. Büttiker, Phys. Rev. B **38**, 9375 (1988).

[22] E. Bocquillon, V. Freulon, F. D. Parmentier, et al., Annalen der Physik **526**, 1 (2014).

[23] D. P. DiVincenzo, Fortschritte der Physik: Progress of Physics **48**, 771 (2000).

[24] P. Lodahl, Quantum Science and Technology **3**, 013001 (2017).

[25] P. Kok, W. J. Munro, K. Nemoto, et al., Rev. Mod. Phys. **79**, 135 (2007).

[26] A. Bertoni, Journal of Computational Electronics **6**, 67 (2007).

[27] A. Bertoni, "Charge-based solid-state flying qubits", in *Encyclopedia of complexity and systems science*, edited by R. A. Meyers (Springer New York, New York, NY, 2009), pp. 1011–1027.

[28] Y. J. Chung, A. Gupta, K. W. Baldwin, et al., Phys. Rev. B **106**, 075134 (2022).

[29] I. Neder, N. Ofek, Y. Chung, et al., Nature **448**, 333 (2007).

[30] L. Bellentani, P. Bordone, X. Oriols, et al., Phys. Rev. B **99**, 245415 (2019).

[31] Y. Ji, Y. Chung, D. Sprinzak, et al., Nature **422**, 415 (2003).

[32] L. Bellentani, G. Forghieri, P. Bordone, et al., Physical Review B **102**, 035417 (2020).

[33] M. Henny, S. Oberholzer, C. Strunk, et al., Science **284**, 296 (1999).

[34] W. D. Oliver, J. Kim, R. C. Liu, et al., Science **284**, 299 (1999).

[35] R. H. Brown and R. Twiss, The London, Edinburgh, and Dublin Philosophical Magazine and Journal of Science **45**, 663 (1954).

[36] C. K. Hong, Z. Y. Ou, and L. Mandel, Phys. Rev. Lett. **59**, 2044 (1987).

[37] E. Bocquillon, V. Freulon, J.-M. Berroir, et al., Science **339**, 1054 (2013).

[38] D. Marian, E. Colomés, and X. Oriols, Journal of Physics: Condensed Matter **27**, 245302 (2015).

[39] V. Giovannetti, F. Taddei, D. Frustaglia, et al., Phys. Rev. B **77**, 155320 (2008).

[40] L. Bellentani, A. Beggi, P. Bordone, et al., Phys. Rev. B **97**, 205419 (2018).

[41] A. Bertoni, P. Bordone, R. Brunetti, et al., Phys. Rev. Lett. **84**, 5912 (2000).

[42] S. Takada, H. Edlbauer, H. V. Lepage, et al., Nature Communications **10**, 4557 (2019).

[43] L. Freise, T. Gerster, D. Reifert, et al., Phys. Rev. Lett. **124**, 127701 (2020).

[44] F. Stein, H. Scherer, T. Gerster, et al., Metrologia **54**, S1 (2016).

[45] J. Dubois, T. Jullien, F. Portier, et al., Nature **502**, 659 (2013).

[46] G. Fève, A. Mahé, J.-M. Berroir, et al., Science **316**, 1169 (2007).

[47] S. Ryu, M. Kataoka, and H.-S. Sim, Phys. Rev. Lett. **117**, 146802 (2016).

[48] L. S. Levitov, H. Lee, and G. B. Lesovik, Journal of Mathematical Physics **37**, 4845 (1996).

[49] M. Büttiker, H. Thomas, and A. Prêtre, Physics Letters A **180**, 364 (1993).

[50] T. Jonckheere, J. Rech, C. Wahl, et al., Phys. Rev. B **86**, 125425 (2012).

[51] D. Ferraro, B. Roussel, C. Cabart, et al., Phys. Rev. Lett. **113**, 166403 (2014).

[52] M. D. Blumenthal, B. Kaestner, L. Li, et al., Nature Physics **3**, 343 (2007).

[53] Y. Yin, Journal of Physics: Condensed Matter **31**, 245301 (2019).

[54] C. Emary, L. A. Clark, M. Kataoka, et al., Phys. Rev. B **99**, 045306 (2019).

[55] M. Kataoka, J. D. Fletcher, and N. Johnson, physica status solidi (b) **254**, 1600547 (2017).

[56] V. Thiney, P.-A. Mortemousque, K. Rogdakis, et al., Phys. Rev. Res. **4**, 043116 (2022).

[57] D. C. Glattli, J. Nath, I. Taktak, et al., arXiv.2002.03947 (2020).

[58] P. R. Wallace, Phys. Rev. **71**, 622 (1947).

[59] K. S. Novoselov, A. K. Geim, S. V. Morozov, et al., Science **306**, 666 (2004).

[60] A. A. Balandin, Nature Materials **10**, 569 (2011).

[61] M. Sang, J. Shin, K. Kim, et al., Nanomaterials **9**, 374 (2019).

[62] M. Cao, D.-B. Xiong, L. Yang, et al., Advanced Functional Materials **29**, 1806792 (2019).

[63] A. K. Geim, Science **324**, 1530 (2009).

[64] H. O. Pierson, in *Handbook of carbon, graphite, diamonds and fullerenes*, edited by H. O. Pierson (William Andrew Publishing, Oxford, 1993), pp. 244–277.

[65] M. Cutini, G. Forghieri, M. Ferrario, et al., Carbon **203**, 601 (2023).

[66] A. C. Neto, F. Guinea, and N. M. Peres, Physics World **19**, 33 (2006).

[67] M. I. Katsnelson, K. S. Novoselov, and A. K. Geim, Nature Physics **2**, 620 (2006).

[68] M. Katsnelson and K. Novoselov, Solid State Communications **143**, Exploring graphene, 3 (2007).

[69] O. Klein, Zeitschrift für Physik **53**, 157 (1929).

[70] X. Jiang, C. Shi, Z. Li, et al., Science (New York, N.Y.) **370**, 1447 (2020).

[71] A. K. Geim and K. S. Novoselov, Nature Materials **6**, 183 (2007).

[72] K. Bolotin, K. Sikes, Z. Jiang, et al., Solid State Communications **146**, 351 (2008).

[73] S. Rakheja, V. Kumar, and A. Naeemi, Proceedings of the IEEE **101**, 1740 (2013).

[74] P. Neugebauer, M. Orlita, C. Faugeras, et al., Phys. Rev. Lett. **103**, 136403 (2009).

[75] L. Banszerus, M. Schmitz, S. Engels, et al., Nano Letters **16**, 1387 (2016).

[76] M. Jo, J.-Y. M. Lee, A. Assouline, et al., Nature Communications **13**, 5473 (2022).

[77] A. Assouline, M. Jo, P. Brasseur, et al., Nature Physics **17**, 1 (2021).

[78] L. Zhang, N. Schwertfager, T. Cheiwchanchamnangij, et al., Phys. Rev. B **86**, 245430 (2012).

[79] Y. Zhang, Y.-W. Tan, H. Stormer, et al., Nature **438**, 201 (2005).

[80] J. Ho, Y. Lai, Y.-H. Chiu, et al., Physica E-low-dimensional Systems & Nanostructures - PHYSICA E **40**, 1722 (2008).

[81] X. Wu, Y. Hu, M. Ruan, et al., Applied Physics Letters **95**, 223108 (2009).

[82] S. Fujita and A. Suzuki, International Journal of Theoretical Physics **55**, 4830 (2016).

[83] K. S. Novoselov, Z. Jiang, Y. Zhang, et al., Science **315**, 1379 (2007).

[84] D. A. Abanin, B. E. Feldman, A. Yacoby, et al., Phys. Rev. B **88**, 115407 (2013).

[85] A. F. Young, C. R. Dean, L. Wang, et al., Nature Physics **8**, 550 (2012).

[86] J. J. Cuozzo and E. Rossi, Phys. Rev. B **110**, 024518 (2024).

[87] X.-C. Jiang, Y.-Y. Zhao, and Y.-Z. Zhang, Phys. Rev. B **105**, 115106 (2022).

[88] V. I. Fal'ko, Philosophical Transactions of the Royal Society A: Mathematical, Physical and Engineering Sciences **366**, 205 (2008).

[89] Y. Kim, P. Moon, K. Watanabe, et al., Nano Letters **21**, 4249 (2021).

[90] L. Brey and H. A. Fertig, Phys. Rev. B **73**, 195408 (2006).

[91] L. Brey and H. A. Fertig, Phys. Rev. B **73**, 235411 (2006).

[92] K. Wakabayashi, K.-i. Sasaki, T. Nakanishi, et al., Science and Technology of Advanced Materials **11**, 054504 (2010).

[93] H. Wang, H. S. Wang, C. Ma, et al., Nature Reviews Physics **3**, 791 (2021).

[94] D. Jariwala, A. Srivastava, and P. M. Ajayan, J Nanosci Nanotechnol. **11(8)**, 6621 (2011).

[95] M. Ishigami, J. H. Chen, W. G. Cullen, et al., Nano Letters **7**, 1643 (2007).

[96] S. V. Morozov, K. S. Novoselov, M. I. Katsnelson, et al., Phys. Rev. Lett. **100**, 016602 (2008).

[97] C. R. Dean, A. F. Young, I. Meric, et al., Nature Nanotechnology **5**, 722 (2010).

[98] J. Wang, F. Ma, and M. Sun, RSC Advances **7**, 16801 (2017).

[99] C. Dean, A. Young, L. Wang, et al., Solid State Communications **152**, Exploring Graphene, Recent Research Advances, 1275 (2012).

[100] G. Giovannetti, P. A. Khomyakov, G. Brocks, et al., Phys. Rev. B **76**, 073103 (2007).

[101] K. Watanabe, T. Taniguchi, and H. Kanda, Nature Materials **3**, 404 (2004).

[102] M. Šiškins, C. Mullan, S.-K. Son, et al., Applied Physics Letters **114**, 123104 (2019).

[103] J. Jung, A. M. DaSilva, A. H. MacDonald, et al., Nature Communications **6**, 6308 (2015).

[104] M. Kindermann, B. Uchoa, and D. L. Miller, Phys. Rev. B **86**, 115415 (2012).

[105] C. Díaz, F. Calleja, A. L. Vázquez de Parga, et al., Surface Science Reports **77**, 100575 (2022).

[106] F. Liu, P. Li, H. An, et al., Advanced Functional Materials **32**, 2203191 (2022).

[107] N. Mishra, J. Boeckl, N. Motta, et al., physica status solidi (a) **213**, 2277 (2016).

[108] C. Berger, Z. Song, T. Li, et al., The Journal of Physical Chemistry B **108**, 19912 (2004).

[109] S. Eigler, M. Enzelberger-Heim, S. Grimm, et al., Advanced Materials **25**, 3583 (2013).

[110] N. F. Ahmad, K. Komatsu, T. Iwasaki, et al., Scientific Reports **9**, 3031 (2019).

[111] C. Handschin, "Quantum transport in encapsulated graphene "pn" junctions", PhD thesis (University of Basel, 2017).

[112] S. Morikawa, S. Masubuchi, R. Moriya, et al., Applied Physics Letters **106**, 183101 (2015).

[113] D. S. Wei, T. van der Sar, J. D. Sanchez-Yamagishi, et al., Science Advances **3**, e1700600 (2017).

[114] M. Jo, P. Brasseur, A. Assouline, et al., Phys. Rev. Lett. **126**, 146803 (2021).

[115] F. Amet, J. R. Williams, K. Watanabe, et al., Phys. Rev. Lett. **112**, 196601 (2014).

[116] P. Makk, C. Handschin, E. Tóvári, et al., Phys. Rev. B **98**, 035413 (2018).

[117] P. Marconcini, D. Logoteta, M. Fagotti, et al., in 2010 14th international workshop on computational electronics (2010), pp. 1–4.

[118] D. A. Abanin, K. S. Novoselov, U. Zeitler, et al., Phys. Rev. Lett. **98**, 196806 (2007).

[119] S. Xiang, A. Mre ńca-Kolasi ńska, V. Miseikis, et al., Phys. Rev. B **94**, 155446 (2016).

[120] A. Marguerite, J. Birkbeck, A. Aharon-Steinberg, et al., Nature **575**, 628 (2019).

[121] N. Moreau, B. Brun, S. Somanchi, et al., Nature Communications **12**, 4265 (2021).

[122] R. Kumar, S. K. Srivastav, C. Spånslätt, et al., Nature Communications **13**, 213 (2022).

[123] R. Quhe, J. Zheng, G. Luo, et al., NPG Asia Materials **4**, e6 (2012).

[124] L. Trifunovic and P. W. Brouwer, Phys. Rev. B **99**, 205431 (2019).

[125] C. W. Johnson, A. E. Turner, and B. J. McMorran, Phys. Rev. Research **3**, 043009 (2021).

[126] I. M. Flór, A. Lacerda-Santos, G. Fleury, et al., Phys. Rev. B **105**, L241409 (2022).

[127] A. Assouline, L. Pugliese, H. Chakraborti, et al., Science **382**, 1260 (2023).

[128] P. Giannozzi, S. Baroni, N. Bonini, et al., Journal of Physics: Condensed Matter **21**, 395502 (2009).

[129] F. Utermohlen, *Tight-binding model for graphene*, (2018) [Online].

[130] Y. Hancock, A. Uppstu, K. Saloriutta, et al., Phys. Rev. B **81**, 245402 (2010).

[131] J. L. Lado, J. W. González, and J. Fernández-Rossier, Phys. Rev. B **88**, 035448 (2013).

[132] M. O. Goerbig, Rev. Mod. Phys. **83**, 1193 (2011).

[133] J. Lado, N. García-Martínez, and J. Fernández-Rossier, Synthetic Metals **210**, Reviews of Current Advances in Graphene Science and Technology, 56 (2015).

[134] P. Ruffieux, S. Wang, B. Yang, et al., Nature **531**, 489 (2016).

[135] S. Chen, Z. Han, M. M. Elahi, et al., Science **353**, 1522 (2016).

[136] K. Kolasi ński, A. Mre nca-Kolasi ńska, and B. Szafran, Phys. Rev. B **95**, 045304 (2017).

[137] A. Beggi, P. Bordone, F. Buscemi, et al., Journal of Physics: Condensed Matter **27**, 475301 (2015).

[138] G. Yamahata, S. Ryu, N. Johnson, et al., Nature Nanotechnology **14**, 1019 (2019).

[139] Y. Arakawa and M. J. Holmes, Applied Physics Reviews **7**, 021309 (2020).

[140] T. Kramer, C. Kreisbeck, and V. Krueckl, Physica Scripta **82**, 038101 (2010).

[141] M. Frigo and S. Johnson, in Proceedings of the 1998 ieee international conference on acoustics, speech and signal processing, icassp '98 (cat. no.98ch36181), Vol. 3 (1998), pp. 1381–1384.

[142] R. F. W. Bader and P. M. Beddall, The Journal of Chemical Physics **56**, 3320 (1972).

[143] H. Wiseman, New Journal of Physics **9**, 165 (2007).

[144] J. Fankhauser and P. M. Dürr, Studies in History and Philosophy of Science Part A **85**, 16 (2021).

[145] N. Stander, *Graphene - the missing link*, (2007) [Online].

[146] L. Oroszlány, P. Rakyta, A. Kormányos, et al., Physical Review B **77**, 081403 (2008).

[147] J. R. Williams and C. M. Marcus, Phys. Rev. Lett. **107**, 046602 (2011).

[148] P. Carmier, C. Lewenkopf, and D. Ullmo, Physical Review B **84**, 195428 (2011).

[149] M. Barbier, G. Papp, and F. M. Peeters, Applied Physics Letters **100**, 163121 (2012).

[150] S. P. Milovanović, M. Ramezani Masir, and F. M. Peeters, Applied Physics Letters **105**, 123507 (2014).

[151] T. Taychatanapat, J. Y. Tan, Y. Yeo, et al., Nature Communications **6**, 6093 (2015).

[152] P. Rickhaus, P. Makk, M.-H. Liu, et al., Nature Communications **6**, 6470 (2015).

[153] *See supplemental material of [3]*, [Online].

[154] K. Zimmermann, A. Jordan, F. Gay, et al., Nature Communications **8**, 14983 (2017).

[155] A. F. Young and P. Kim, Nature Physics **5**, 222 (2009).

[156] T. Tudorovskiy, K. J. A. Reijnders, and M. I. Katsnelson, Physica Scripta **T146**, 014010 (2012).

[157] A. Beggi, A. Bertoni, and P. Bordone, Journal of Physics: Conference Series **647**, 012023 (2015).

[158] Y. Zeng, J. I. A. Li, S. A. Dietrich, et al., Phys. Rev. Lett. **122**, 137701 (2019).
[159] H. Polshyn, H. Zhou, E. M. Spanton, et al., Phys. Rev. Lett. **121**, 226801 (2018).
[160] Y. Ronen, T. Werkmeister, D. Haie Najafabadi, et al., Nature Nanotechnology **16**, 563 (2021).
[161] C. Déprez, L. Veyrat, H. Vignaud, et al., Nature Nanotechnology **16**, 555 (2021).
[162] V. S.-W. Chung, P. Samuelsson, and M. Büttiker, Phys. Rev. B **72**, 125320 (2005).
[163] M. Mirzakhani, N. Myoung, F. Peeters, et al., Carbon **201**, 734 (2023).
[164] W. Luo, L. Cao, Y. Shi, et al., Light: Science & Applications **12**, 175 (2023).
[165] K. Wintersperger, F. Dommert, T. Ehmer, et al., EPJ Quantum Technology **10**, 32 (2023).
[166] O. Ezratty, The European Physical Journal A **59**, 94 (2023).
[167] D. Jirovec, A. Hofmann, A. Ballabio, et al., Nature Materials **20**, 1106 (2021).
[168] M. Feng, L. H. Zaw, and T. S. Koh, npj Quantum Information **7**, 112 (2021).
[169] R. C. Ashoori, Nature **379**, 413 (1996).
[170] B. Venitucci, L. Bourdet, D. Pouzada, et al., Phys. Rev. B **98**, 155319 (2018).
[171] F. H. L. Koppens, C. Buizert, K. J. Tielrooij, et al., Nature **442**, 766 (2006).
[172] J. J. Pla, K. Y. Tan, J. P. Dehollain, et al., Nature **489**, 541 (2012).
[173] M. Veldhorst, C. H. Yang, J. C. C. Hwang, et al., Nature **526**, 410 (2015).
[174] A. Hosseinkhani and G. Burkard, Phys. Rev. B **106**, 075415 (2022).
[175] G. Dresselhaus, Phys. Rev. **100**, 580 (1955).
[176] J. M. Elzerman, R. Hanson, L. H. Willems van Beveren, et al., Nature **430**, 431 (2004).
[177] A. Saraiva, W. H. Lim, C. H. Yang, et al., Advanced Functional Materials **32**, 2105488 (2022).
[178] A. Jayashankar and P. Mandayam, Journal of the Indian Institute of Science **103**, 497 (2023).
[179] A. Noiri, K. Takeda, T. Nakajima, et al., Nature **601**, 338 (2022).
[180] X. Xue, M. Russ, N. Samkharadze, et al., Nature **601**, 343 (2022).
[181] W. Lawrie, M. Rimbach-Russ, F. v. Riggelen, et al., Nature Communications **14**, 3617 (2023).
[182] P. Stano and D. Loss, Nature Reviews Physics **4**, 672 (2022).
[183] A. Abragam, *The Principles of Nuclear Magnetism* (Oxford University Press, 2016).
[184] I. I. Rabi, J. R. Zacharias, S. Millman, et al., Phys. Rev. **53**, 318 (1938).
[185] N. F. Ramsey, Phys. Rev. **78**, 695 (1950).
[186] E. L. Hahn, Phys. Rev. **80**, 580 (1950).
[187] J. R. Petta, A. C. Johnson, J. M. Taylor, et al., Science **309**, 2180 (2005).
[188] W. Yang, W.-L. Ma, and R.-B. Liu, Reports on Progress in Physics **80**, 016001 (2016).
[189] L. Bellentani, M. Bina, S. Bonen, et al., Phys. Rev. Applied **16**, 054034 (2021).
[190] S. G. J. Philips, M. T. Madzik, S. V. Amitonov, et al., Nature **609**, 919 (2022).
[191] D. A. Lidar and T. A. Brun, *Quantum Error Correction* (Cambridge University Press, 2013).
[192] J. Yoneda, K. Takeda, T. Otsuka, et al., Nature Nanotechnology **13**, 102 (2018).
[193] D. Fernández-Fernández, Y. Ban, and G. Platero, Phys. Rev. Appl. **18**, 054090 (2022).

[194] A. R. Mills, C. R. Guinn, M. J. Gullans, et al., Science Advances **8**, eabn5130 (2022).
[195] C. H. Yang, K. W. Chan, R. Harper, et al., Nature Electronics **2**, 151 (2019).
[196] G. Zheng, N. Samkharadze, M. L. Noordam, et al., Nature Nanotechnology **14**, 742 (2019).
[197] X. Xue, B. Patra, J. P. G. van Dijk, et al., Nature **593**, 205 (2021).
[198] L. Petit, M. Russ, G. H. Eenink, et al., Communications Materials **3**, 82 (2022).
[199] L. Petit, H. G. J. Eenink, M. Russ, et al., Nature **580**, 355 (2020).
[200] J. P. G. Van Dijk, B. Patra, S. Subramanian, et al., IEEE Journal of Solid-State Circuits **55**, 2930 (2020).
[201] K. Wu, S. Kindel, T. Descamps, et al., Phys. Rev. Appl. **21**, 054052 (2024).
[202] X. Yan, S. Gitt, B. Lin, et al., APL Photonics **6**, 070901 (2021).
[203] M. Spethmann, X.-P. Zhang, J. Klinovaja, et al., Phys. Rev. B **106**, 115411 (2022).
[204] A. Tosato, V. Levajac, J.-Y. Wang, et al., Communications Materials **4**, 23 (2023).
[205] B. Hetényi, A. Mook, J. Klinovaja, et al., Phys. Rev. B **106**, 235409 (2022).
[206] D. Degli Esposti, B. Paquelet Wuetz, V. Fezzi, et al., Applied Physics Letters **120**, 184003 (2022).
[207] L. A. Tracy, E. H. Hwang, K. Eng, et al., Phys. Rev. B **79**, 235307 (2009).
[208] T. Tanttu, B. Hensen, K. W. Chan, et al., Phys. Rev. X **9**, 021028 (2019).
[209] K. Takeda, A. Noiri, T. Nakajima, et al., Nature **608**, 682 (2022).
[210] R. Maurand, X. Jehl, D. Kotekar-Patil, et al., Nature communications **7**, 13575 (2016).
[211] S. Geyer, B. Hetényi, S. Bosco, et al., Nature Physics, 1152 (2024).
[212] N. Hendrickx, D. Franke, A. Sammak, et al., Nature **577**, 487 (2020).
[213] F. N. M. Froning, L. C. Camenzind, O. A. H. van der Molen, et al., Nature Nanotechnology **16**, 308 (2021).
[214] K. Wang, G. Xu, F. Gao, et al., Nature Communications **13**, 206 (2022).
[215] Y. Liu, S. Guan, J.-W. Luo, et al., Advanced Functional Materials **34**, 2304725 (2024).
[216] S. J. Angus, A. J. Ferguson, A. S. Dzurak, et al., Nano letters **7**, 2051 (2007).
[217] W. H. Lim, F. Zwanenburg, H. Huebl, et al., Applied Physics Letters **95**, 242102 (2009).
[218] D. Sabbagh, N. Thomas, J. Torres, et al., Phys. Rev. Appl. **12**, 014013 (2019).
[219] C. Yang, A. Rossi, R. Ruskov, et al., Nature communications **4**, 2069 (2013).
[220] J. K. Gamble, P. Harvey-Collard, N. T. Jacobson, et al., Applied Physics Letters **109**, 253101 (2016).
[221] C. H. Yang, R. Leon, J. Hwang, et al., Nature **580**, 350 (2020).
[222] W. I. L. Lawrie, H. G. J. Eenink, N. W. Hendrickx, et al., Applied Physics Letters **116**, 080501 (2020).
[223] E. Paladino, Y. Galperin, G. Falci, et al., Reviews of Modern Physics **86**, 361 (2014).
[224] K. Chan, W. Huang, C. Yang, et al., Physical Review Applied **10**, 044017 (2018).
[225] N. W. Hendrickx, W. I. L. Lawrie, M. Russ, et al., Nature **591**, 580 (2021).
[226] G. Scappucci, C. Kloeffel, F. A. Zwanenburg, et al., Nature Reviews Materials **6**, 926 (2021).

[227] X. Mi, T. M. Hazard, C. Payette, et al., Phys. Rev. B **92**, 035304 (2015).
[228] M. Lodari, O. Kong, M. Rendell, et al., Applied Physics Letters **120**, 122104 (2022).
[229] X. Mi, J. V. Cady, D. M. Zajac, et al., Applied Physics Letters **110**, 043502 (2017).
[230] M. Failla, J. Keller, G. Scalari, et al., New Journal of Physics **18**, 113036 (2016).
[231] F. Borsoi, N. W. Hendrickx, V. John, et al., Nature Nanotechnology **19**, 21 (2024).
[232] A. S. Ivlev, H. Tidjani, S. D. Oosterhout, et al., Applied Physics Letters **125**, 023501 (2024).
[233] V. N. Ciriano-Tejel, M. A. Fogarty, S. Schaal, et al., PRX Quantum **2**, 010353 (2021).
[234] S. Conesa-Boj, A. Li, S. Koelling, et al., Nano letters **17**, 2259 (2017).
[235] J. J. Zhang, G. Katsaros, F. Montalenti, et al., Phys. Rev. Lett. **109**, 085502 (2012).
[236] F. Gao, J.-H. Wang, H. Watzinger, et al., Advanced Materials **32**, 1906523 (2020).
[237] L. Vukušić, J. Kukučka, H. Watzinger, et al., Nano letters **17**, 5706 (2017).
[238] S. Bosco and D. Loss, Phys. Rev. Lett. **127**, 190501 (2021).
[239] B. Paquelet Wuetz, M. P. Losert, S. Koelling, et al., Nature Communications **13**, 7730 (2022).
[240] F. Kondev, M. Wang, W. Huang, et al., Chinese Physics C **45**, 030001 (2021).
[241] F. A. Zwanenburg, A. S. Dzurak, A. Morello, et al., Rev. Mod. Phys. **85**, 961 (2013).
[242] T. Abedadze, W. E. Saunders, M. Y. Wachs, et al., U.S. pat. (CERADYNE EPB Inc, Ceradyne Inc, and Goldman Sachs Credit Partners LP, Nov. 14, 2000).
[243] M. Asen-Palmer, K. Bartkowski, E. Gmelin, et al., Phys. Rev. B **56**, 9431 (1997).
[244] A. J. Sigillito, R. M. Jock, A. M. Tyryshkin, et al., Phys. Rev. Lett. **115**, 247601 (2015).
[245] J. R. Chelikowsky and M. L. Cohen, Phys. Rev. B **10**, 5095 (1974).
[246] A. Hamilton, R. Danneau, O. Klochan, et al., Journal of Physics: Condensed Matter **20**, 164205 (2008).
[247] Y. Sun, S. Thompson, and T. Nishida, Journal of Applied Physics - J APPL PHYS **101**, 104503 (2007).
[248] Y. A. Bychkov and É. I. Rashba, JETP lett **39**, 78 (1984).
[249] R. Winkler, Phys. Rev. B **62**, 4245 (2000).
[250] A. Imamogłu, D. D. Awschalom, G. Burkard, et al., Phys. Rev. Lett. **83**, 4204 (1999).
[251] W. Gilbert, T. Tanttu, W. H. Lim, et al., Nature Nanotechnology **18**, 131 (2023).
[252] A. Bermeister, D. Keith, and D. Culcer, Applied Physics Letters **105**, 192102 (2014).
[253] D. V. Bulaev and D. Loss, Phys. Rev. Lett. **95**, 076805 (2005).
[254] N. Piot, B. Brun, V. Schmitt, et al., Nature Nanotechnology **17**, 1072 (2022).
[255] A. Secchi, L. Bellentani, A. Bertoni, et al., Phys. Rev. B **104**, 035302 (2021).
[256] G. L. Bir and G. E. Pikus, *Symmetry and strain-induced effects in semiconductors* (Wiley, 1974).
[257] F. Maier, C. Kloeffel, and D. Loss, Phys. Rev. B **87**, 161305 (2013).
[258] C. Kloeffel, M. J. Ran či ć, and D. Loss, Phys. Rev. B **97**, 235422 (2018).
[259] R. Winkler, D. Culcer, S. Papadakis, et al., Semiconductor science and technology **23**, 114017 (2008).

[260] A. Secchi, L. Bellentani, A. Bertoni, et al., Phys. Rev. B **104**, 205409 (2021).

[261] A. Secchi and F. Troiani, Phys. Rev. B **107**, 155411 (2023).

[262] A. Secchi and F. Troiani, Phys. Rev. B **110**, 045420 (2024).

[263] S. Bonen, U. Alakusu, Y. Duan, et al., IEEE Electron Device Letters **40**, 127 (2019).

[264] F. Bloch, Zeitschrift für Physik **52**, 555 (1929).

[265] S. M. Sze, Y. Li, and K. K. Ng, *Physics of semiconductor devices* (John wiley & sons, 2021).

[266] M. Willatzen and L. C. L. Y. Voon, *The kp method: electronic properties of semiconductors*, Vol. 1 (Springer, 2009).

[267] J. M. Luttinger and W. Kohn, Phys. Rev. **97**, 869 (1955).

[268] C. W. Helstrom, Journal of Statistical Physics **1**, 231 (1969).

[269] J. Bae and L.-C. Kwek, Journal of Physics A: Mathematical and Theoretical **48**, 083001 (2015).

[270] S. M. Barnett and S. Croke, Adv. Opt. Photon. **1**, 238 (2009).

[271] F. Troiani, E. Rotunno, S. Frabboni, et al., Phys. Rev. A **102**, 043510 (2020).

[272] M. G. A. Paris, International Journal of Quantum Information **07**, 125 (2009).

[273] A. Secchi, *Private discussion*.

[274] R. D. Levine and C. A. Coulson, Proceedings of the Royal Society of London. Series A. Mathematical and Physical Sciences **294**, 467 (1966).

[275] Y. Wang, V. Bushmakin, G. A. Stein, et al., Optica **9**, 374 (2022).

[276] M. Gell-Mann, in *The eightfold way* (CRC Press, 2018), pp. 216–233.

[277] R. T. Thew, K. Nemoto, A. G. White, et al., Phys. Rev. A **66**, 012303 (2002).

[278] S. Bosco, M. Benito, C. Adelsberger, et al., Phys. Rev. B **104**, 115425 (2021).

[279] N. V. Vitanov, A. A. Rangelov, B. W. Shore, et al., Reviews of Modern Physics **89**, 015006 (2017).

[280] B. Hetényi, S. Bosco, and D. Loss, Phys. Rev. Lett. **129**, 116805 (2022).

[281] W. I. L. Lawrie, N. W. Hendrickx, F. van Riggelen, et al., Nano Letters **20**, PMID: 32833455, 7237 (2020).

[282] X. Liu, G. Farahi, C.-L. Chiu, et al., Science **375**, 321 (2022).

What you do in this world is a matter of no consequence.
The question is what can you make people believe you have done.

∼ Sherlock Holmes in *A Study in Scarlet*,
by Sir Arthur Conan Doyle